BULGARIAN CHEMICAL COMMUNICATIONS

Schizocommunin analogues and derivatives as G-quadruplex ligands and anticancer agents

S. M. Bakalova, J. Kaneti*

Institute of Organic Chemistry with Centre of Phytochemistry, Bulgarian Academy of Sciences, Acad. G. Bonchev Str., Block 9, 1113 Sofia, Bulgaria

G-quadruplexes (GQs) have become valid targets for anticancer efforts in the recent couple of decades due to their extremely multifaceted biological functions. Our goal is to quantify interactions within GQs, as well as their interactions with potential ligands (Ls). As secondary nucleic acid (NA) structures, GQs may be understood as a central channel of stacked G-quartets, interlinked into a G-stem (GS) with nucleotide loops. Computational data on full GQ energetics are, however, increasingly noisy. Therefore, we have chosen to simplify our GQ model by stripping it off all nucleotide residues into a "naked" GQ. The GQ-L stacking model allows computing of intrinsic interaction energies, as well as external ligand stacking affinities with "chemical precision". To relate computed ligand – G4 affinities to their biological activity, we use published inhibitory activities (IC_{50} values) of several groups of heterocycles. Some of our results provide a good linear relationship between ligand stacking affinities to GQ, calculated by quantum chemical DFT methods, and corresponding $\log(IC_{50})$ values. Herewith we discuss the obtained results in terms of a mechanism of anticancer activity of heterocyclic ligands *via* complexation with GQs and thereby control of GQ cell regulatory activity.

Keywords: G-quadruplexes, nitrogen heterocyclic ligands, stacking interactions, IC_{50} *vs*. G4-affinity relationship

INTRODUCTION

Alkaloids and their chemical analogues have long been among the most popular and sought for organic natural, laboratory and industrial products for a leading reason – their beneficial physiological activity on human health [1]. Recently, their activity and use has increasingly been related to their capability to interact with a special category of nucleic acids (NAs) – the four stranded G-quadruplexes [1]. While not being directly involved in the preservation and transfer of genetic information, G-quadruplexes have been disclosed as decisive participants in a plethora of cellular processes as NA biosynthesis, replication, transcription, oncogenesis, etc. Telomeres are a known site accumulating G-quadruplexes, which are thereby essential to telomere functioning in cancer, aging and genetic stability. A G-quadruplex may inhibit telomerase activity, which directly affects cancer cells and primary tumors [2]. A G-quadruplex may dissociate telomere-binding proteins thus leading to dysfunction and finally to apoptosis or senescence [3]. A G-quadruplex interferes with telomeric replication by impairing replication fork progression [4]. Knowledge of ligand structures stabilizing G-quadruplexes allows for the specific design of heterocyclic structures targeting the cancer cell function [1, 5].

The recent decade has seen quite a number of efforts to quantify anticancer activities of series of selected heterocycles on cultivated cancer cell cultures [1, 6, 7]. The results of these efforts outline important structure – activity trends in series of quinazoline derivatives [6], indenoisoquinoline derivatives, including an isolated MYC-cancer promoter [7], and more generally in G-quadruplexes of various functions, structures and sizes, as well as various quadruplex targeting heterocyclic ligands [8]. On the other hand, the belief that G4-ligands lack selectivity due to targeting multiple quadruplexes and thus many different sites in the genome still has a significant place in the literature [9]. This requires additional efforts to reduce effects of different binding of G4-ligands [9 and references therein], which remain very attractive therapeutic agents nevertheless [10]. Moreover, one might consider a G-quadruplex itself as determining selectivity and attracting (larger size) heterocycles to stack to its large G4 plane. In these terms, G-quadruplex selectivity with respect to crescent-shaped planar ligand chromophores has repeatedly been noticed [1, 8] and exploited in the search of novel anticancer heterocycles [11], even though the terms G-quadruplex and mechanism of action have not been mentioned together in the latter review [11]. The pressing demand to all anticancer activity studies is then the generalization of their biochemical pharmacology data in the form of IC_{50}, that is, their structure – activity information, into quantitative form. Half-maximal inhibitory concentration (IC_{50}) is the most widely used and

---

* To whom all correspondence should be sent:
E-mail: *jose.kaneti@orgchm.bas.bg*

informative measure of a drug's efficacy. It indicates how much drug is needed to inhibit a biological process by half, thus providing a measure of potency of an antagonist drug in pharmacological research. The value of IC_{50} of a ligand regarded as its inhibition constant [12] should exponentially depend on ligands' G4 affinity. The latter value is conveniently computable theoretically.

We have ventured into the field while discussing the mechanism of biological activity of some quinazoline-4-one derivatives [13]. The latter has introduced us to the possible involvement of G-quadruplexes in the problem, and the necessity to bring up adequate computational methodologies to its solution. Traditional molecular mechanics MM and molecular dynamics MD approaches do not seem capable of bringing sufficiently accurate results for G-quadruplex structures [14]. This problem is related to both intrinsic lack of accuracy, and technical numerical noise accumulating with slow energy convergence for polyatomic structures as G-quadruplexes [14, 15]. The necessary theoretical and computational accuracy only looks achievable using large-scale quantum chemical calculations [15]. To reduce the computational problem to affordable limits and improve accuracy as much as possible, we strip our G-quadruplex model off all nucleotide residues [13]. This leaves the model a core of stacked guanine tetrads with a central channel containing the pertinent stabilizing K^+ or Na^+ ions [8]. With a size of 130 to 260 and more atoms, of which 64 for a single G4 quartet (C, H, N, O) atoms plus a K+ per layer, the core-G4 system is relatively easily amenable to quantum chemical calculations using density functional theory, DFT [16]. Improved "chemical precision" molecular orbital post-Hartree-Fock calculations, are feasible as well [17].

SELECTION OF HETEROCYCLIC COMPOUNDS AS POTENTIAL GQ-LIGANDS

Our initial work has been oriented to computational design and directed synthesis of N---H---N heterocycles, with emphasis on their capability to undergo intramolecular proton transfer, possibly related to biological activity. In this respect, quinazolines and derivatives have been considered promising. 4-Amino-quinazolines [6, 18] and perimidines [19] (entries 5, 7, 8; Table 1) have been selected as potentially convenient synthetic targets, based on extensive literature data. The interest to derivatives of schizocommunin [1], however, also stems directly from their biological mechanisms,

related to G-quadruplexes. Further structural speculations, related to GQ-drug design, led us to benzimidazolo[1.2-a] quinolines [20, 21], which are also given some attention here.

COMPUTATIONAL MODELING

To obtain the required DFT affinities of heterocyclic ligands to a model G-quadruplex, we mostly use the wB97XD functional, chosen for its reasonable treatment of long-range and dispersion interactions [22, 23] at the 6-31G(d,p) basis set level, as implemented in the Gaussian program system [24]. This corresponds to the expected stacking type of interactions in the layered secondary NA structures. We also test the general purpose M06-2X functional, where the hydrogen bonding and long-range interactions are well covered, but dispersion is not explicitly accounted for. We follow the routine protocol for location of minima on the potential energy surface of G4-quadruplex – ligand complexes by computing the matrix of vibrational force constants and ensuring that it has no negative eigenvalues, i.e. frequencies, at the final optimization point [24]. We have chosen the simplest G-quadruplex model, consisting of two guanine quartet layers and a single stabilizing potassium ion [13]. As pointed out in this earlier paper of ours [13], even this simplest G-quadruplex model has 129 atoms, including K^+, to which number the atoms of the corresponding ligand have to be added. This size prevents use of higher-level explicit electron correlated methods like CCSD, and even MP2, which we use under the resolution of identity approximation, RI MP2 [13].

With the above definitions, the ligand affinity has the simple form of
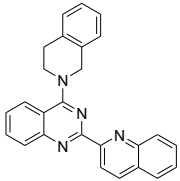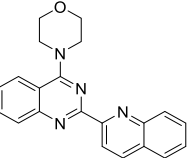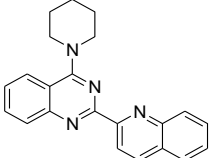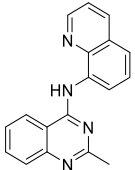
$$A_{QL} = E_{QL} - (E_Q + E_L),$$
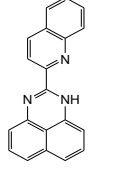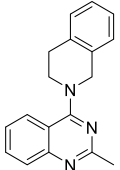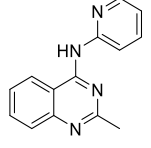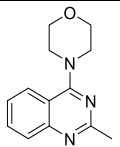
where E_{QL}, E_Q, E_L are the computed total energies in vacuum for the quadruplex-ligand complex, free quadruplex, and free ligand, each completely optimized at the chosen theoretical level. Computed ligand affinities have the meaning of stability constants of their G4 complexes and may be related as such to their thermodynamics. The results with the series of heterocycles [18, 19, 29] are summarized in Table 1.
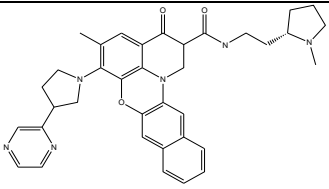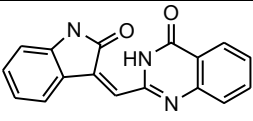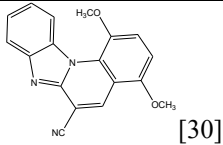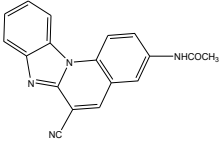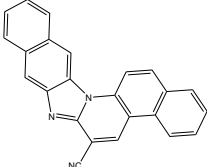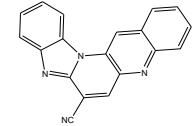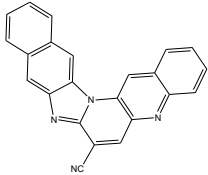
A logarithmic plot of experimental IC_{50} values [18, 19, 29] against computed DFT ligand affinities is shown in Fig. 1. Table 2 summarizes computed ligand affinities for substituted schizocommunin derivatives and their experimental biological activities [1, 28].
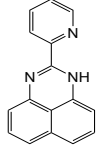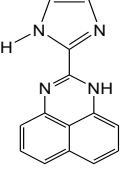
Table 1. Computed wB97XD/6-31G(d,p) total electronic energies, *hartrees*, and ligand affinities, *kcal.mol^{-1}*, against experimentally determined **IC_{50}** values, *mol*, tested against the A375 line [29] entries 1-10. Some known (entries 11-14)

and hypothetical structures 15-17 illustrate trends in calculated affinities. The model quadruplex total energy E[Q2K] equals -4939.424743 *hartrees*. E_L – ligand energy, a. u.; Q_L – ligand-quadruplex energy, a. u.; A_{QL} – affinity, *kcal.mol^{-1}*.

No	Ligands	E_L, a.u.	Q_L, a.u.	A_{QL}, kcal.mol^{-1}	IC$_{50}$, *mol*
1		-1221.484259	-6160.971209	-39.04	1.43×10^{-5}
2		-1104.982776	-6044.467535	-37.66	2.9×10^{-5}
3		-1069.087694	-6008.596043	-37.63	3.19×10^{-5}
4		-913.106098	-5852.581625	-35.20	9.8×10^{-5}
5		-933.966342	-5873.446834	-34.98	4.47×10^{-5}
6		-860.183549	-5799.660935	-33.03	5.8×10^{-5}
7		-780.369285	-5719.845155	-32.08	9.37×10^{-5}
8		-758.318366	-5697.793309	-31.53	6.05×10^{-5}
9		-759.521386	-5698.995996	-31.33	1.61×10^{-4}
10		-743.685384	-5683.152521	-26.64	1.28×10^{-4}

11	Quarfloxin CX3543 [25]	-2007.047343	-6946.550902	-49.42	>10⁻⁸
12	Schizocommunin [28]	-968.888943	-5908.369172	-34.82	>50.10⁻⁵
13	[30]	-1008.097477	-5947.581345	-37.10	1.10⁻⁶ HeLa [30]
14	[31]	-987.084237	-5926.572842	-40.11	3.10⁻⁶ HeLa [30]
15		-1086.312979	-6025.805852	-42.79	
16		-948.751257	-5888.237078	-38.33	
17		-1102.341603	-6041.834300	-42.68	
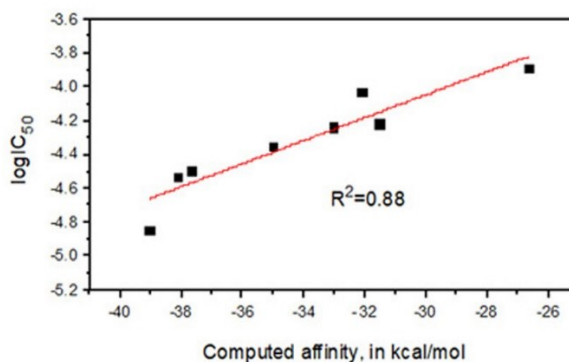
Figure 1. Plot of calculated wB97XD ligand affinities against the logarithm of the 50% inhibitory concentrations IC_{50} (in mol) for compounds 1–8, tested against the A375 melanoma cell line; R=0.9357, R^2=0.8756 [29].

Table 2. Computed M06-2x/6-31G** total electronic energies in atomic units; 1 a. u. (*hartree*) = 627.51 kcal.mol⁻¹ [1] of alkaloids and schizocommunin derivatives [1, 28]. E[Q2K] = 4939.111267 *hartrees*. Affinities are in kcal.mol⁻¹.

IC$_{50}$ in µmol from ref. [28]. HeLa – breast cancer cell line; U2OS – osteosarcoma cell line [28, 30]. The used compound numbering Che*mn* follows the original paper [28].
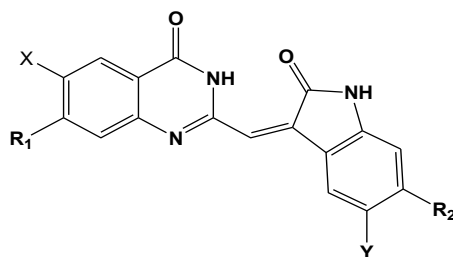
Substituent R$_n$	Orig. # [28] Substit. X, Y	Ligand energy E$_L$, a.u.	Q2K-quadruplex energy, a.u.	Affinity ΔE, kcal.mol^{-1}	IC$_{50}$ HeLa, µmol	IC$_{50}$ U2OS, µmol
R$_1$= -NH-(CH$_2$)$_3$-NMe$_2$ R$_2$=H	Che07 X=Y=R$_2$=H	-1275.942614	-6215.111074	-35.51	42.5	20.4
R$_1$=-NH-(CH$_2$)$_3$-NMe$_2$ R$_2$=H	Che08 X=F, Y=R$_2$=H	-1375.147425	-6314.317092	-36.27	13.4	18.7
R$_1$=-NH-(CH$_2$)$_3$-N-morpholyl	Che10 X=F, Y=R$_2$=H	-1527.727970	-6466.872389	-20.43	>50	>50
R$_1$=-NH-(CH$_2$)$_3$-NMe$_2$ R$_2$=-N$_1$N$_4$Me-piperazyl	Che12 X=Y=H	-1581.866729	-6521.028646	-31.41	49	14.1
R$_1$=-NH-(CH$_2$)$_2$-NMe$_2$ R$_2$=-N$_1$N$_4$Me-piperazyl	Che13 X=F,Y=H	-1681.071588	-6620.233579	-31.45	15.7	6.3
R$_1$=-NH-(CH$_2$)$_2$-tetrahydro-pyrrolyl; R$_2$=-N$_1$N$_4$Me-piperazyl	Che14 X=F,Y=H	-1719.170498	-6658.332508	-31.46	17.4	6.4
R$_1$=-N-hexahydro-pyridyl; R$_2$=-N$_1$N$_4$Me-piperazyl	Che15 X=F,Y=H	-1758.462551	-6697.626406	-32.62	20.5	3.6
R$_1$=-NH-(CH$_2$)$_3$-NMe$_2$; R$_2$=-N$_1$N$_4$Me-piperazyl	Che16 X=F,Y=H	-1681.071588	-6620.233579	-31.45	3.8	3.2
R$_1$=-NH-(CH$_2$)$_3$-NEt$_2$; R$_2$=-N$_1$N$_4$Me-piperazyl	Che17 X=F,Y=H	-1759.662809	-6698.826612	-32.59	10.0	7.6
R$_1$=-NH-(CH$_2$)$_3$-NMe$_2$; R$_2$=N-morpholyl	Che22 X=Y=F	-1760.839282	-6700.001404	-31.53	34.3	32.4
R$_1$=-NH-(CH$_2$)$_2$-tetrahydro-pyrrolyl; R$_2$=N-morpholyl	Che23 X=Y=F	-1838.228542	-6777.394694	-34.06	>50	>50
R$_1$=-NH-(CH$_2$)$_2$-N-morpholyl; R$_2$=N-morpholyl	Che24 X=Y=F	-1913.419817	-6852.581597	-31.32	>50	>50
R$_1$=-N$_1$N$_4$Me-piperazyl; R$_2$=N-morpholyl	Che25 X=Y=F	-1759.641803	-6698.802843	-30.86	>50	>50
R$_1$=-NH-(CH$_2$)$_3$-NMe$_2$; R$_2$=-N$_1$N$_4$Me-piperazyl	Che30 X=Y=F	-1780.272927	-6719.435916	-32.08	17.6	9.0
R$_1$=-NH-(CH$_2$)$_3$-NEt$_2$; R$_2$=-N$_1$N$_4$Me-piperazyl	Che31 X=Y=F	-1858.863115	-6798.028849	-33.80	9.6	6.1

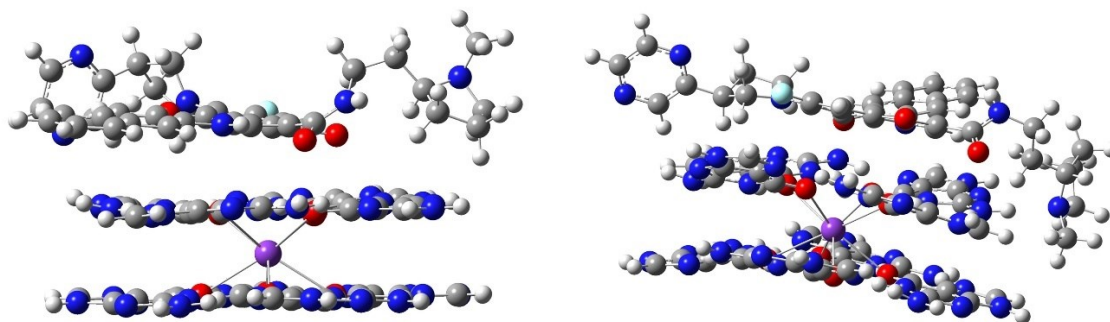| R₁=-NH-(CH₂)₃-tetrahydro-pyrrolyl; R₂=-N₁N₄Me-piperazyl	Che32 X=Y=F	-1857.666276	-6796.829178	-32.02	9.0	16.4
R₁=-NH-(CH₂)₃-N-imidazolyl; R₂=-N₁N₄Me-piperazyl	Che33 X=Y=F	-1871.307737	-6810.469544	-31.34	>50	>50
R₁=-NH-(CH₂)₃N₁N₄-Me- piperazyl; R₂=-N₁N₄Me-piperazyl	Che34 X=Y=F	-1952.286514	-6891.449523	-32.09	8.8	12.7
R₁=-NH-(CH₂)₃-NMe₂; R₂=-N₁N₄Me-piperazyl	Che35 X=F, Y=H	-1720.357156	-6659.530943	-38.85	14.0	12.5

Figure 2. Two modes of attachment of quarfloxin [25] to a model bilayered G-quadruplex. Left: total energy -6946.550919 *hartrees*, right: total energy -6946.563341 *hartrees*. These values correspond to a difference between calculated ligand affinities of 49.5, left, and 57.3, right, *kcal.mol⁻¹*, of *ca.* 8 kcal.mol⁻¹, which is *ca.* 15% of the affinity value, defining the stacking mechanism used here. Further, more examples to this point are given by derivatives of schizocommunin, Table 2 [28].

DISCUSSION

The clear trend revealed between experimental IC₅₀ (Inhibitory Concentration for 50% tumor suppression in present cases) of some of studied small heterocyclic ligands, Fig. 1 [29] indicates at first sight the good likeliness of the suggested stacking mechanism of their interactions with G-quadruplexes. Thus, the stacking of relatively small heterocyclic molecules to the model quadruplex "core" is probably a valid interaction mechanism, apart of known modes of NA interaction with relatively larger anticancer ligands, targeting telomeres [26, 29]. This suggestion does not eliminate by any means different modes of attachment of small heterocycles to G4 quadruplexes. The multidimensional problem of finding the minima of potential energy surfaces for these interactions has no unique solution even from the purely mathematical viewpoint. Some optimism in this direction may be found in the earlier observation that molecular dynamics G4 quadruplex potential energy surfaces are relatively flat with deep global minima for bound ligands [27]. We may then

10

concentrate on structural properties of small ligands and the variations of their quadruplex interaction energies elicited by ligand characteristics. A case of variations of interaction energy may arise from internal structural variations of a given ligand – the possibility of tautomeric forms and rotational isomerism. Important among the latter variations would be the changes, leading to loss of planarity of ligands, and thus to reduced affinity to G-quadruplex core stacking and deviations from the mechanism of biological interference, discussed here. An example is given on Figure 2, with two modes of attachment of CX-3543, quarfloxin [25], to a model Q2 core.

Introduction of mostly hydrophilic long-chain substituents to the leading alkaloid molecule brings additional rotatable bonds, greatly complicating the corresponding energy surface. At the same time, we attempt to find relationships between computed ligand affinities to the telomeric G-quadruplex, which is most probably responsible to observed activities of these more than thirty molecules, Table 2 [28]. These computations use the more general M06-2X/6-31G** density functional. Computed M06-2X ligand affinities are similar to these of

compounds 1 – 10 (Table 1) but do not correlate with reported biological activities [28]. In fact, one has to keep in mind that our model quadruplex cannot describe the complete binding capability of this NA structure and only represents its part capable of dispersion and/or correlation interactions. There is only a part of the native quadruplex, or its model here, which is accessible by the heterocyclic ligand, which is part of the large planar surface of its internal G4 core. The surrounding part of native quadruplex can bind heterocycles too, in particular their hydrophilic substituents. This part of the affinity is comparable or possibly even larger than the part of it, which we calculate here as stacking, or dispersion, or correlation contribution to complete ligand bonding interaction, see Figure 2 for an example. Specifically, in the case of extended hydrophilic substituents, their potential interactions with pentose and phosphate residues of G4 are not covered by the present computational model. Thus, we might further be confronted with the necessity to introduce also "quadruplet accessibility" by ligands, which would give limits to their potential participation in G4 regulated bioprocesses.

CONCLUSION

The mechanism of exerting biological activity of some aromatic heterocyclic compounds *via* formation of ligand adducts to G-quadruplexes (GQ.L) certainly finds a lot of reliable examples in biological and pharmaceutical experiments. We add to the so far formulated requirements to such heterocyclic molecules, namely crescent-like form and a number of annelated aromatic rings, preferably three or more, a quantitative measure of possible activity - the ligand affinity of heterocycles to G-quadruplexes. The latter quantitative requirement offers explanations also in cases where planarity of ligands is compromised, which reduces affinity to the G-quadruplex plane. The consequence is reduced stacking energy of the potential complex. Thus, in cases of conforming to the formulated qualitative requirements, and computed good quantitative affinity to a model G-quadruplex, we may recommend the potentially synthetically achievable molecules like entries 15 – 17 of Table 1 for further experimental studies.

REFERENCES

1. T. Che, Y.-Q. Wang, Z.-L. Huang, J.-H. Tan, Z.-S. Huang, S.-B. Chen, *Molecules,* **23**, 493 (2018).
2. C. Chadeneau, K. Hay, H. W. Hirte, S. Gallinger, S. Bacchetti, *Cancer Res.,* **55**, 2533 (1995).
3. P. Phatak, J. C. Cookson, F. Dai, V. Smith, R. B. Gartenhaus, M. F. Stevens, A. M. Burger, *Br. J. Cancer*, **96**, 1223 (2007).
4. G. N. Parkinson, M. P. Lee, S. Neidle, *Nature*, **417**, 876 (2002).
5. M.-H. Hu, S.-B. Chen, B. Wang, T.-M. Ou, L.-Q. Gu, J.-H. Tan, Z.-S. Huang, *Nucleic Acids Res.,* **45**, 1606 (2016).
6. Y. OuYang, C. Wang, B. Zhao, H. Xiong, Z. Xiao, B. Zhang, P. Zheng, J. Hu, Y. Gao, M. Zhang, W. Zhu, S. Xu, *New J. Chem.*, **42**, 17203 (2018).
7. K.-B. Wang, M. Elsayed, G. Wu, N. Deng, M. Cushman, D. Yang, *J. Am. Chem. Soc.,* **141** (28), 11059 (2019).
8. S. Neidle, *Curr. Op. Struct. Biol.*, **19**, 239 (2009); S. Balasubramanian, L. H. Hurley, Neidle, S., *Nature Reviews Drug Discovery,* **10**, 261 (2011); S. Neidle, *J. Med. Chem.*, **59**, 5987 (2016).
9. N. Kosiol, S. Juranek, P. Brossart, A. Heine, K. Paeschke, *Molecular Cancer,* **20 (**40), (2021), https://doi.org/10.1186/s12943-021-01328-4.
10. I. Alessandrini, M. Recagni, N. Zaffaroni, M. Folini, *Int. J. Mol. Sci.,* **22**, 5947 (2021).
11. T. Liang, X. Sun, W. Li, G. Hou, F. Gao, *Front. Pharmacol.*, **12**: 661173 (2021).
12. S. Lazareno, N. J. Birdsall, *Brit. J. Pharmacol.,* **109** (4), 1110 *(*1993*).*
13. J. Kaneti, M. Georgieva, M. Rangelov, I. Philipova, B. Vasileva, I. Angelov, D. Staneva, G. Miloshev, S. Bakalova, *BBA - General Subjects*, **1865,** 129773 (2021).
14. B. Islam, P. Stadlbauer, S. Neidle, S. Haider, J. Sponer, *J. Phys. Chem. B,* **120**, 2899 (2016).
15. J. Sponer, A. Mladek, N. Spackova, X. Cang, T. E. Grimme, S. Cheatham III, *J. Am. Chem. Soc.*, **135**, 9785 *(*2013**).**
16. P. Hohenberg, W. Kohn, *Phys. Rev.*, **136**, B864 (1964). W. Kohn, L. J. Sham, *Phys. Rev.*, **140**, A1133 (1965).
17. W. Hehre, L. Radom, P. Schleyer, J. A. Pople von R., *Ab Initio* Molecular Orbital Theory, Wiley-Interscience, 1986.
18. T. N. Moshkina, E. V. Nosova, J. V. Permyakova, G. N. Lipunova, M. S. Valova, P. Slepukhin, L. Sadieva, V. Charushin, *Dyes and Pigments,* **204**, 110592 (2022), https://doi.org/10.1016/j.dyepig.2022.110592
19. M. Lamperti, A. M.Giani, A. Maspero, G. Vesco, A. Cimino, R. Negri, G. B. Giovenzana, G. Palmisano, M. Mella, L. Nardo, *Journal of Fluorescence,* **29**, 495 (2019).

20. M. Hranjec, G. Pavlović, M. Marjanović, M. Kralj, G. Karminski-Zamola, *European Journal of Medicinal Chemistry*. **45**, 2405 (2010).
21. N. Perin, L. Uzelac, I. Piantanida, G. Karminski-Zamola, M. Kralj, M. Hranjec, *Bioorganic & Medicinal Chemistry*. **19**, :6329 (2011).
22. S. Grimme, *J. Chem. Phys.*, **118**, 9095 (2003).
23. J.-D. Chai, M. Head-Gordon, *Phys. Chem. Chem. Phys.,* **10**, 6615 (2008).
24. Gaussian 16, Revision C.01, M. J. Frisch, G. W. Trucks; H. B. Schlegel, G. E. Scuseria, M. A. Robb, J. R. Cheeseman, G. Scalmani, V. Barone, G. A. Petersson, H. Nakatsuji, X. Li, M. Caricato, A. V. Marenich, J. Bloino, B. G. Janesko, R. Gomperts, B. Mennucci, H. P. Hratchian, J. V. Ortiz, A. F. Izmaylov, J. L. Sonnenberg, D. Williams-Young, F. Lipparini, F. Egidi, J. Goings, B. Peng, A. Petrone, T. Henderson, D. Ranasinghe, V. G. Zakrzewski, J. Gao Ding, N. Rega, G. Zheng, W. Liang, M. Hada, M. Ehara, K. Toyota, R. Fukuda, J. Hasegawa, M. Ishida, T. Nakajima, Y. Honda, O. Kitao, H. Nakai, T. Vreven, K. Throssell, J. A. Montgomery Jr., J. E. Peralta, F. Ogliaro, M. J. Bearpark, J. J. Heyd, E. N. Brothers, K. N. Kudin, V. N. Staroverov, T. A. Keith, R. Kobayashi, J. Normand, K. Raghavachari, A. P. Rendell, J. C. Burant, S. S. Iyengar, J. Tomasi, M. Cossi, J. M. Millam, M. Klene, C. Adamo, R. Cammi, J. W. Ochterski, R. L. Martin, K. Morokuma, O. Farkas, J. B. Foresman, D. J. Fox, Gaussian, Inc., Wallingford CT, 2019.
25. D. Drygin, A. Siddiqui-Jain, S. O'Brien, M. Schwaebe, A. Lin, J. Bliesath, C. B. Ho, C. Proffitt, K. Trent, J. P. Whitten, J. K. C. Lim, D. Von Hoff, K. Anderes, W. G. Rice, *Cancer Res.,* **69**(19), 7653 (2009).
26. S. Asamitsu, S. Obata, Z. Yu, T. Bando, H. Sugiyama, *Molecules,* **24**, 429 (2019).
27. B. Machireddy, H.-J. Sullivan, C. Wu, *Molecules,* **24**, 1010 (2019).
28. T. Che, S.-B. Chen, J.-L. Tu, B. Wang, Y.-Q. Wang, Y. Zhang, J. Wang, Z.-Q. Wang, Z.-P. Zhang, T.-M. Ou, Y. Zhao, J.-H. Tan, Z.-S. Huang, *J. Med. Chem.*, **61**, 3436 (2018).
29. J. Kaneti, V. Kurteva, M. Georgieva, N. Krasteva, G. Miloshev, N. Tabakova, Z. Petkova, S. Bakalova, *Molecules*, **27**, 7577 (2022).
30. M. Hranjec, G. Pavlovic, M. Marjanovic, M. Kralj, G. Karminski-Zamola, *Eur. J. Med. Chem*., **45**, 2405 (2010).
31. N. Perin, L. Uselac, I. Piantanida, G. Karminski-Zamola, M. Kralj, M. Hranjec, *Bioorg. Med. Chem*., **19**, 6329 (2011),

The Ugi Four-Component Reaction: Application in the synthesis of bis-hydantoins

Ş. Gülten

Department of Chemistry, Faculty of Science, Çanakkale Onsekiz Mart University, 17020 Çanakkale, Turkey

Three new bis 1,3,5-trisubstituted hydantoins were synthesized by combining an Ugi four-component condensation reaction with a base induced cyclization. In the two-step sequence, first three new bis Ugi compounds were synthesized by the Ugi four-component condensation reaction, and then bis 1,3,5-trisubstituted hydantoins were obtained by intramolecular cyclization reaction.

INTRODUCTION

Multicomponent reactions (MCRs) are one-pot processes in which three or more reactants combine together simultaneously or in a stepwise domino fashion to form a new product which contains portions of all the components (Figure 1). MCRs provide a simple and powerful access to a large number of molecules from simple substrates with broad structural diversity and molecular complexity [1-3].
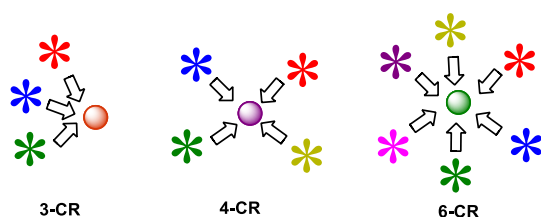
Figure 1. Schematic representation of a three-component reaction (3-CR), a four-component reaction (4-CR) and a six-component reaction (6-CR)

Not all MCRs follow the same strategy: the pathways can be either convergent or divergent (Figure 2). During convergent synthesis, separate reactants combine together in independent reactions to form intermediates, which subsequently react and combine together to form the final product [1, 4]. High atom economy, easy operation, lower energy consumption, higher overal yield, less solvent being used (or solvent-free), time, resource efficiency, waste reduction *via* removal of intermediate separations and contributing to a more green process are properties of MCRs [1, 3, 5].

Multicomponent reactions have been known for more than 170 years. The first reported multicomponent reaction was Strecker's synthesis of α-amino cyanides in 1850. Since then, numerous MCRs have been reported, such as the Hantzsch dihydropyridine synthesis (1881), the Biginelli reaction (1891), the Mannich reaction (1912), the Passerini reaction (1921), and the Ugi reaction (1959) (Figure 3) [6-8].
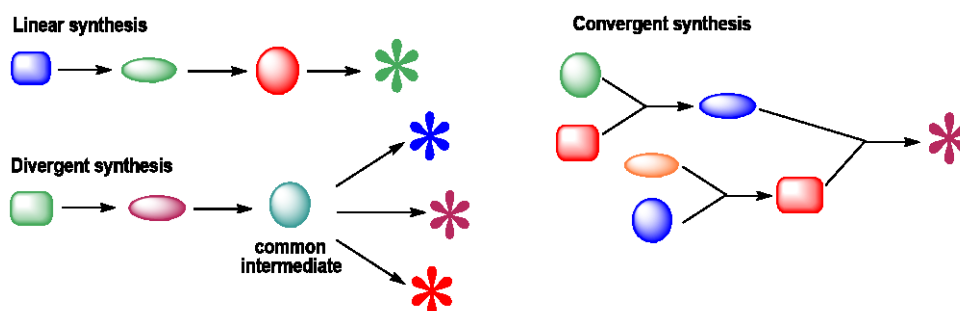
Figure 2. Schematic representation of linear, convergent and divergent synthesis

---
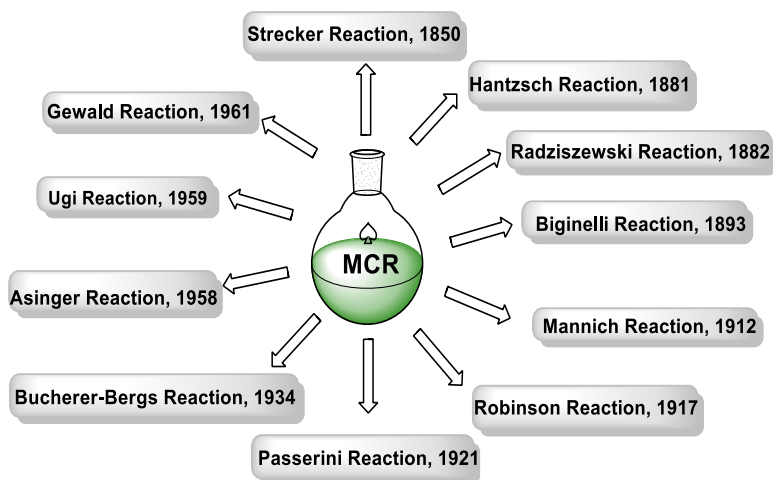
Figure 3. The brief history of multicomponent reactions
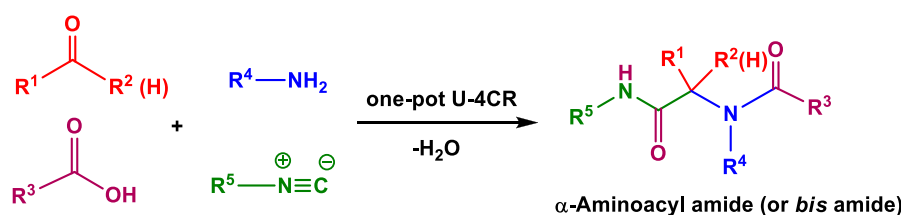
Scheme 1. The Ugi four-component reaction (U-4CR)
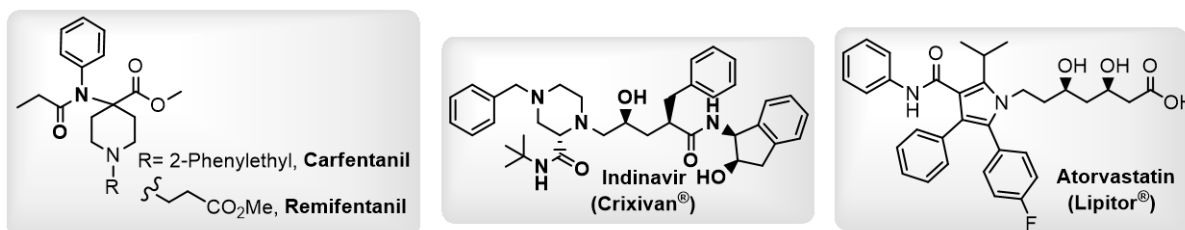
Scheme 2. Structures of carfentanil, remifentanil, crixivan and lipitor

The Ugi reaction is favoured in polar protic solvents such as methanol and, to some extent in water. The U-4CR is one of the most important MCRs to access peptide-like structures (Scheme 1) [9-16].

The synthesis of the potent analgesics carfentanil and remifentanil was reported using an U-4CR followed by methanolysis of the carfentanil amide and the remifentanil amide Ugi products (Scheme 2) [17]. The first synthesis of Merck HIV protease inhibitor Crixivan (Indinavir) by a conventional multistep sequence of procedures was ineffective and expensive. After the introduction of an U-4CR as a key step Crixivan could be prepared in fewer steps and in better yields (Scheme 2) [18]. In another example, Pfizer's Lipitor (Atorvastatin) belongs to a class of statins, lipid-lowering drugs for the prevention of events associated with cardiovascular disease. It was the best-selling pharmaceutical drug of all time worldwide until its patent expired in late 2011. Lipitor could be formed through U-4CR in an overall short and high-yield synthesis that performs better than the Paal–Knorr synthetic route [19].

Hydantoins (imidazolidine-2,4-diones) constitute a very old class of cyclic ureides of α-amino acids. Hydantoin was first isolated by the Nobel laureate, Adolf von Baeyer in 1861 [20, 21]. Over the last 150 years hydantoin-containing heterocyclic compounds have become increasingly important in the chemical and pharmaceutical industries. The hydantoin framework itself possesses no biological activity, but 5-substituted and 5,5-disubstituted derivatives have a wide range of therapeutic applications [21-25]. Hydantoin derivatives have been used as hypnotics, anticonvulsants, antiarrhythmics, antidiabetics, antimuscarinics, antiulcer, antiviral or antibacterial agents [21-25].

EXPERIMENTAL

All reagents and solvents were purchased from Fluka, Acros Organics, Riedel-de Haën and Merck

and were used without further purification. The melting points were measured on an Stuart SMP10 melting point apparatus and are uncorrected. The IR spectra were recorded on a One FT-IR ATR Perkin Elmer. The ^{1}H and ^{13}C NMR spectra were taken with a Jeol NMR 400 MHz spectrometer and the chemical shifts were recorded in ppm downfield with respect to tetramethylsilane (TMS) as an internal standard.

General procedure for the synthesis of bis Ugi products (1a-1c).

A solution of aromatic diamino compound (1.0 mmol) in MeOH (7 mL) was treated with benzaldehyde (2.0 mmol), a solution of cyclohexyl isocyanide (2.0 mmol) in MeOH (3 mL), and trichloro acetic acid (2.0 mmol) in the order given. The reaction mixture was stirred at room temperature for 24-28 hours, and then filtered. The precipitate was washed first with Et$_2$O and then with n-hexane to remove unreacted reagents or by-products and dried to give pure white solid Ugi adducts 1a-1c.

General procedure for the synthesis of bis 1,3,5-trisubstituted hydantoins (2a-2c).

A 1.0 M ethanolic solution of NaOEt (2.5 mmol) was slowly added to a solution of 1 (1.0 mmol) in EtOH (5 mL). The mixture was stirred for further 8-10 hours at room temperature and then filtered. The collected solid was washed with Et$_2$O (5 mL) and filtered to give almost pure 2a-2c.

Spectroscopic results

N,N'-(4,4'-(Ethane-1,2-diyl)bis(4,1-phenylene)) bis(2,2,2-trichloro-N-(2-(cyclohexylamino)-2-oxo-1-phenylethyl)acetamide) (1a): IR-ATR: 3268, 3063, 3034, 2927, 2854, 1690, 1649, 834, 739, 698 cm^{-1}; ^{1}H NMR (400MHz, CDCl$_3$): δ = 7.65 (2H, br s, 2NH), 7.3-7.16 (14H, m, CH$_{Ar}$), 7.1 (4H, d, J=8.2 Hz, CH$_{Ar}$), 5.97 (1H, s, PhCH), 5.23 (1H, d, J=7.8 Hz, PhCH), 3.79-3.77 (2H, m, 2CH cyclohexyl), 2.71 (4H, s, CH$_2$CH$_2$), 1.94-1.81 (4H, m, 2CH$_2$ cyclohexyl), 1.64-1.58 (4H, m, 2CH$_2$ cyclohexyl), 1.34-1.31 (4H, m, 2CH$_2$ cyclohexyl), 1.31-1.28 (8H, m, 4CH$_2$ cyclohexyl) ppm; ^{13}C NMR (100MHz, CDCl$_3$): δ = 167.43 (C$_q$), 161.01 (C$_q$), 141.71 (C$_q$), 136.28 (C$_q$), 133.47 (C$_q$), 132.24 (CH$_{Ar}$), 130.71 (CH$_{Ar}$), 129.00 (CH$_{Ar}$), 128.61 (CH$_{Ar}$), 128.23 (CH$_{Ar}$), 127.93 (CH$_{Ar}$), 93.15 (C$_q$), 70.11 (CH), 49.04 (CH), 37.48 (CH$_2$), 32.91 (CH$_2$), 32.88 (CH$_2$), 25.52 (CH$_2$), 24.94 (CH$_2$), 24.83 (CH$_2$) ppm.

N,N'-(4,4'-Oxybis(4,1-phenylene))bis(2,2,2-trichloro-N-(2-(cyclohexylamino)-2-oxo-1-phenyl ethyl)acetamide) (1b): IR-ATR: 3363, 3079, 3047, 2929, 2854, 1683, 1652, 1244, 1213, 833, 727 cm^{-1};

^{1}H NMR (400MHz, CDCl$_3$): δ = 7.84 (2H, br s, 2NH), 7.26-7.16 (14H, m, CH$_{Ar}$), 7.1 (4H, d, J=8.2 Hz, CH$_{Ar}$), 5.89 (1H, d, J=7.3 Hz, PhCH), 5.38 (1H, d, J=8.3 Hz, PhCH), 3.89-3.84 (2H, m, 2CH cyclohexyl), 2.2-1.86 (4H, m, 2CH$_2$ cyclohexyl), 1.70-1.54 (8H, m, 4CH$_2$ cyclohexyl), 1.42-0.91 (8H, m, 4CH$_2$ cyclohexyl) ppm; ^{13}C NMR (100MHz, CDCl$_3$): δ= 167.56 (C$_q$), 161.05 (C$_q$), 156.54 (C$_q$), 134.41 (C$_q$), 133.37 (C$_q$), 133.31 (CH$_{Ar}$), 130.81 (CH$_{Ar}$), 129.09 (CH$_{Ar}$), 128.66 (CH$_{Ar}$), 117.75 (CH$_{Ar}$), 93.12 (C$_q$), 69.66 (CH), 69.57 (CH), 49.11 (CH), 32.90 (CH$_2$), 32.86 (CH$_2$), 25.50 (CH$_2$), 24.95 (CH$_2$), 24.82 (CH$_2$) ppm.

N,N'-(4,4'-Sulfonylbis(4,1-phenylene))bis(2,2,2-trichloro-N-(2-(cyclohexylamino)-2-oxo-1-phenyl ethyl)acetamide) (1c): IR-ATR: 3263, 3088, 3041, 2929, 2854, 1677, 1646, 1496, 1240, 1223, 732, 699 cm^{-1}; ^{1}H NMR (400MHz, CDCl$_3$): δ = 7.66 (2H, d, J=7.3 Hz, 2NH), 7.62-7.35 (14H, m, CH$_{Ar}$), 7.2 (4H, d, J=8.2 Hz, CH$_{Ar}$), 6.01 (1H, s, PhCH), 5.4 (1H, d, J=7.8 Hz, PhCH), 3.79-3.68 (2H, m, 2CH cyclohexyl), 1.73-1.48 (12H, m, 6CH$_2$ cyclohexyl), 1.39-1.1 (8H, m, 4CH$_2$ cyclohexyl) ppm; ^{13}C NMR (100MHz, CDCl$_3$): δ= 168.8 (C$_q$), 159.23 (C$_q$), 148.56 (C$_q$), 137.42 (C$_q$), 133.27 (C$_q$), 131.98 (CH$_{Ar}$), 130.25 (CH$_{Ar}$), 129.83 (CH$_{Ar}$), 128.52 (CH$_{Ar}$), 122,90 (CH$_{Ar}$), 92.86 (C$_q$), 70.13 (CH), 50.11 (CH), 32.92 (CH$_2$), 32.83 (CH$_2$), 25.71 (CH$_2$), 25.63 (CH$_2$), 24.81 (CH$_2$) ppm.

1,1'-(4,4'-(Ethane-1,2-diyl)bis(4,1-phenylene)) bis(3-cyclohexyl-5-phenylimidazolidine-2,4-dione) (2a): IR-ATR: 2935, 2855, 1768, 1708 cm^{-1}; ^{1}H NMR (400MHz, CDCl$_3$): δ = 7.50-7.131 (14H, m, CH$_{Ar}$), 6.9 (4H, m, CH$_{Ar}$), 5.98 (2H, s, 2PhCH), 4.04-4.03 (2H, m, 2CH cyclohexyl), 2.75 (4H, s, CH$_2$CH$_2$), 2.35-2.14 (6H, m, 3CH$_2$ cyclohexyl), 1.82-1.57 (8H, m, 4CH$_2$ cyclohexyl), 1.36-1.23 (6H, m, 3CH$_2$ cyclohexyl) ppm; ^{13}C NMR (100MHz, CDCl$_3$): δ = 170.10 (C$_q$), 156.91 (C$_q$), 138.12 (C$_q$), 136.83 (C$_q$), 135.73 (C$_q$), 133.52 (CH$_{Ar}$), 129.54 (CH$_{Ar}$), 129.21 (CH$_{Ar}$), 127.85 (CH$_{Ar}$), 127.48 (CH$_{Ar}$), 73.08 (CH), 63.71 (CH), 37.46 (CH$_2$), 30.57 (CH$_2$), 25.71 (CH$_2$), 24.47 (CH$_2$) ppm.

1,1'-(4,4'-Oxybis(4,1-phenylene))bis(3-cyclo hexyl-5-phenylimidazolidine-2,4-dione)(2b): IR-ATR: 2926, 2854, 1773, 1704 cm^{-1}; ^{1}H NMR (400MHz, CDCl$_3$): δ = 7.99-7.80 (4H, m, CH$_{Ar}$), 7.42-6.99 (14H, m, CH$_{Ar}$), 5.85 (2H, s, 2PhCH), 3.80-3.75 (2H, m, 2CH cyclohexyl), 2.62-2.50 (4H, m, 2CH$_2$ cyclohexyl), 1.85-1.77 (8H, m, 4CH$_2$ cyclohexyl), 1.65-1.55 (4H, m, 2CH$_2$ cyclohexyl) ppm; ^{13}C NMR (100MHz, CDCl$_3$): δ = 170.82 (C$_q$), 157.92 (C$_q$), 150.01 (C$_q$), 136.89 (C$_q$), 132.25 (C$_q$),

129.83 (CH$_{Ar}$), 129.15 (CH$_{Ar}$), 127.85 (CH$_{Ar}$), 127.45 (CH$_{Ar}$), 121.33 (CH$_{Ar}$), 72.6 (CH), 62.86 (CH), 30.48 (CH$_2$), 24.82 (CH$_2$), 24.56 (CH$_2$) ppm.

1,1'-(4,4'-Sulfonylbis(4,1-phenylene))bis(3-cyclo hexyl-5-phenylimidazolidine-2,4-dione) (2c): IR-ATR: 2931, 2857, 1771, 1708 cm^{-1}; ^{1}H NMR (400MHz, CDCl$_3$): δ = 8.0-7.75 (8H, m, CH$_{Ar}$), 7.42-7.12 (10H, m, CH$_{Ar}$), 5.88 (2H, s, 2PhCH), 3.48-3.55 (2H, m, 2CH cyclohexyl), 2.62-2.50 (4H, m, 2CH$_2$ cyclohexyl), 1.81-1.75 (8H, m, 2CH$_2$ cyclohexyl), 1.60-1.55 (4H, m, 2CH$_2$ cyclohexyl), 1.21-1.15 (4H, m, 2CH$_2$ cyclohexyl) ppm; ^{13}C NMR (100MHz, CDCl$_3$): δ = 171.12 (C$_q$), 157.81 (C$_q$), 144.21 (C$_q$), 137.23 (C$_q$), 136.95 (C$_q$), 130.10 (CH$_{Ar}$), 129.99 (CH$_{Ar}$), 128.95 (CH$_{Ar}$), 127.86 (CH$_{Ar}$), 123.16 (CH$_{Ar}$), 72.8 (CH), 63.86 (CH), 30.43 (CH$_2$), 26.23 (CH$_2$), 24.52 (CH$_2$) ppm.

RESULTS AND DISCUSSION

Initially, bis Ugi products 1a-1c were synthesized in good yields by amine (4,4´-diaminobibenzyl, 4,4´-diaminodiphenyl ether and 4,4´-diaminodiphenyl sulfone), benzaldehyde, cyclohexyl isocyanide and trichloro acetic acid in MeOH at room temperature.

Upon treatment with NaOEt in EtOH at room temperature, Ugi adducts 1a-1c underwent a ring-closure reaction to give bis 1,3,5-trisubstituted hydantoins 2a-2c in good yields (Scheme 3).

The products were identified by FT-IR, ^{1}H NMR and ^{13}C NMR studies. In the IR spectra of 1a-1c, the amide NH and the CCl$_3$ absorptions were detected at 3368-3263 cm^{-1} and 834-699 cm^{-1}, respectively. The trichloroacetamide and the amide carbonyl groups gave peaks at 1690-1677 cm^{-1} and 1652-1646 cm^{-1}, respectively. In the ^{1}H NMR spectra of 1a-1c, the proton in the position α to the amido group was detected at δ = 5.23-6.01 ppm. Again, the IR spectra gave useful information about the structure of compounds 2a-2c. In fact, the absorptions due to the amide NH and to the CCl$_3$ group were not detected. Furthermore, a CO peak at 1773-1768 cm^{-1} was found in agreement with the presense of a cyclic urea moiety. The CO absorptions due to the γ-lactam and the amide moties were overlapped and unique peak at 1708-1704 cm^{-1} was observed. As expected, neither the NH proton signal in the ^{1}H NMR spectra nor the CCl$_3$ carbon signal in the ^{13}C NMR was detected.
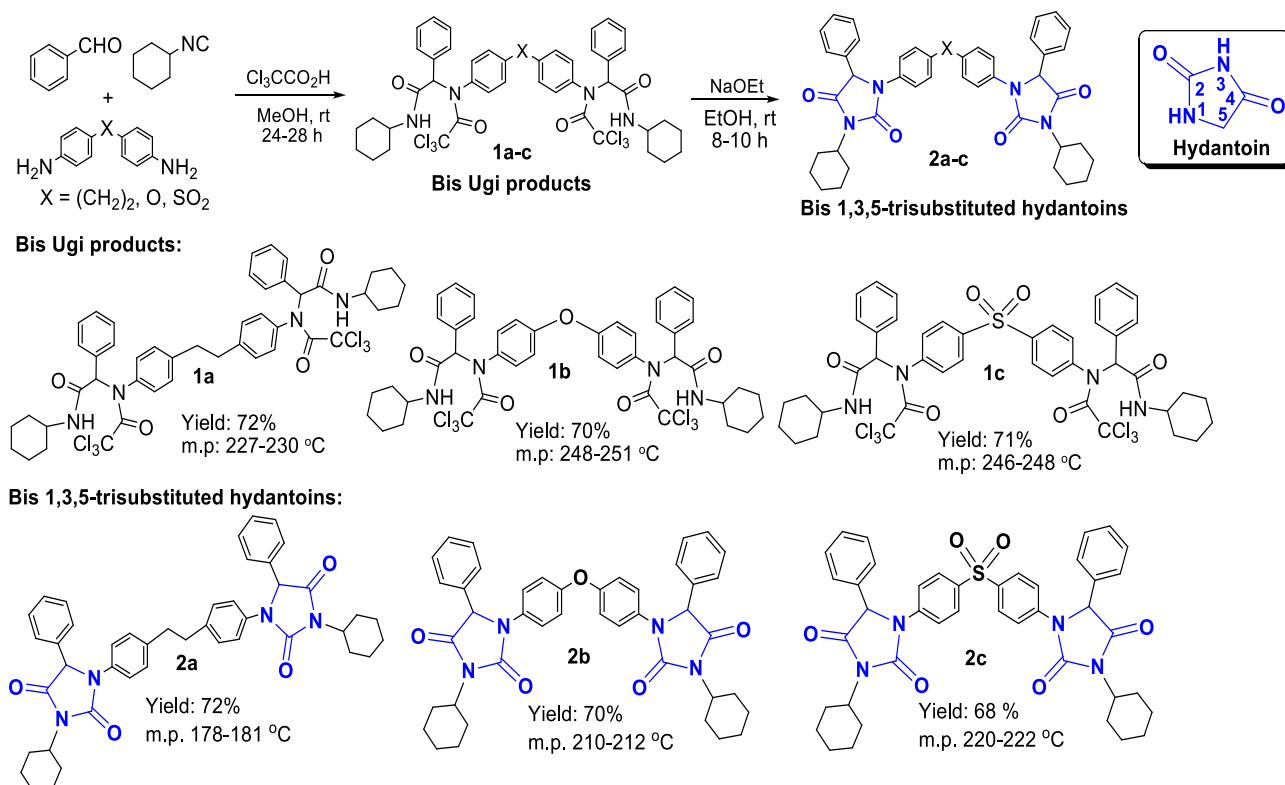
Scheme 3. Synthesis of bis Ugi products 1a-1c and bis 1,3,5-trisubstituted hydantoins 2a-2c

The bis Ugi products 1a-1c and 1,3,5-trisubstituted bis hydantoin 2a-2c were synthesized in good yields.

In the first step of U-4CR, the *in situ* imine (or iminium) formation was observed by the reaction of

the aldehyde and the amine. In the second step, protonation of the imine by the acid gave electrophilic iminium ion and nucleophilic acid anion. These intermediates reacted with the isocyanide in the third step (nucleophilic addition

reaction). The stable Ugi product was obtained after Mumm rearrangement (Scheme 4) [26, 27].
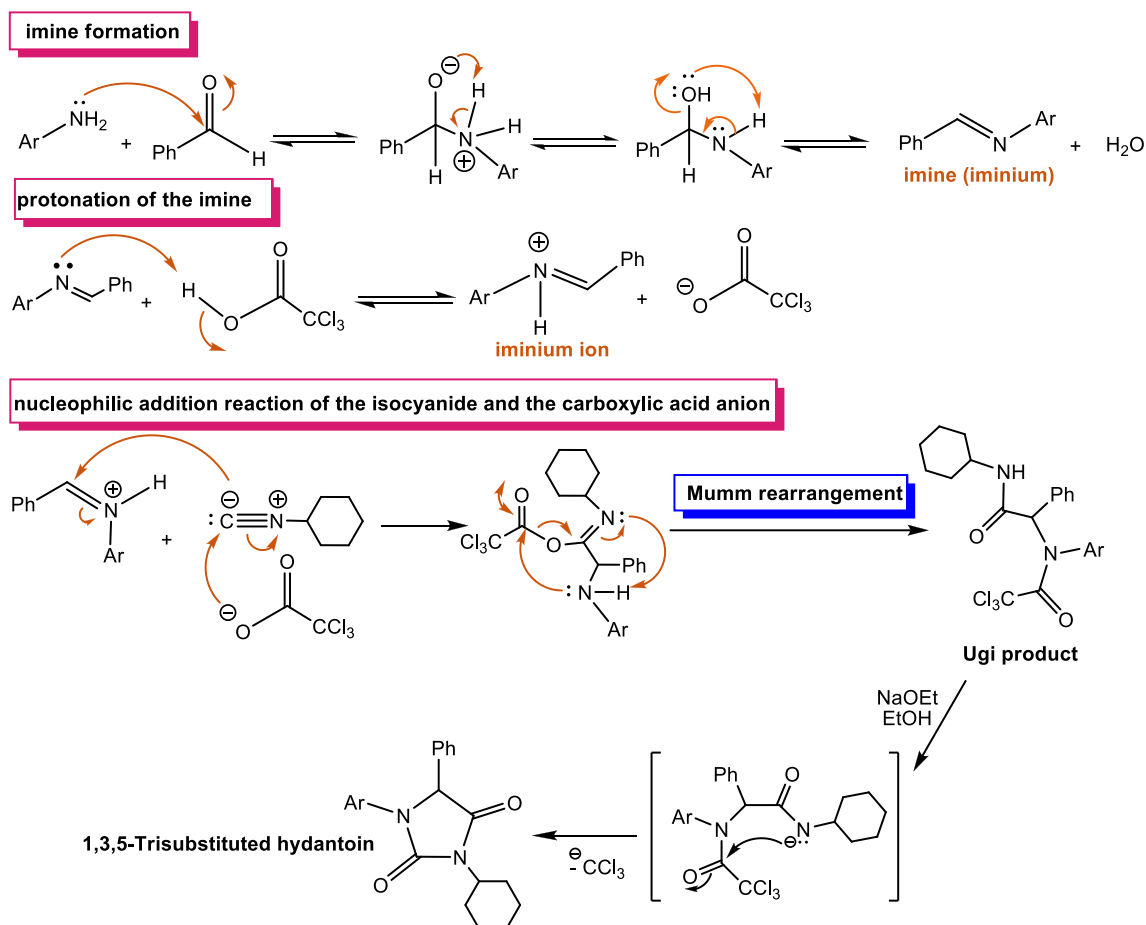
Scheme 4. Formation of bis Ugi products and bis 1,3,5-trisubstituted hydantoins

CONCLUSIONS

In this work we report the synthesis of new Ugi products by four-component Ugi condensation and the subsequent synthesis of hydantoins based on a ring closure reaction. This was achieved in a two-step sequence, using simple and commercially available starting materials.

REFERENCES

1. G. Bosica, R. Abdilla, *Catalysts*, **12**, 725 (2022).
2. A. Dömling, W. Wang, K. Wang, *Chem. Rev.,* **112**, 3083 (2012).
3. H. G. O. Avim, E. N. S. Júnior, B. A. D. Neto, *RSC Adv.,* **4**, 54282 (2014).
4. J. Shimokawa, *Tetrahedron Lett.,* **55**, 6156 (2014).
5. M. A. Fouad, H. Abdel-Hamid, M. S. Ayoup, *RSC Adv.*, **10**, 42644 (2020).
6. S. E. Hooshmand, W. Zhang, *Molecules,* **28**, 1642 (2023).
7. H. Malinakova, *Reports in Organic Chemistry*, **5**, 75 (2015).
8. A. Strecker, *Justus Liebigs Annalen der Chemie*, **75**, 27 (1850).
9. I. Ugi; R. Meyr, *Angew. Chem*., **70**, 702 (1958).

10. I. Ugi, R. Meyr, U. Fetzer, *Angew. Chem*., **71**, 386 (1959).
11. I. Ugi, K. Offermann, *Angew. Chem. Int. Ed. Engl.*, **2**, 624 (1963).
12. M. Veiderma, *Proc. Estonian Acad. Sci. Chem.,* **56**, 98 (2007).
13. I. Akritopoulou-Zanze, *Curr. Opin. Chem. Bio*., **12**, 324 (2018).
14. E. Ruijter, R. V. A. Orru, *Drug Discov. Today Technol.,* **10**, e15-e20 (2013).
15. C. G. Neochoritis, T. Zhao, A. Dömling, *Chem. Rev.,* **119**, 1970 (2019).
16. A. Dömling, *Chem.* Rev., **106**, 17 (2006).
17. S. Malaquin*,* M. Jida, J. C. Gesquiere, R. Deprez-Poulain, B. Deprez, G. Laconde, *Tetrahedron Lett.*, **51**, 2983 (2010).
18. K. Rossen, P. J. Pye, L. M. DiMichele, R.P. Volante, P. J. Reider, *Tetrahedron Lett.,* **39**, 6823 (1998).
19. T. Zarganes-Tzitzikas, C. G. Neochoritis, A. Dömling, *ACS Med. Chem. Lett*., **10**, 389 (2019).
20. A. Baeyer, *Justus Liebigs Ann. Chem*., **119**, 126 (1861).
21. X. del Corte, A. López-Francés, E. Martínez de Marigorta, F. Palacios, J. Vicario, *Molbank*, **2021**, M1218 (2021).
22. T. Marcelli, F. Olimpieri, A. Volonterio, *Org. Biomol. Chem.*, **9**, 5156 (2011).
23. J.M. Ignacio, S. Macho, S. Marcaccini, R. Pepino, T. Torroba, *Synlett,* **20**, 3051 (2005).
24. M. Meusel, M. Gütschow*, Org. Prep. Proced. Int*., **36**, 391 (2004).
25. C.A. López, G.G. Trigo, *Adv. Heterocycl. Chem*., **38**, 177 (1985).
26. Ş. Gülten, *J. Chem. Educ*., **97**, 3839 (2020).
27. Ş. Gülten*, The second Anatolian Conference on Synthetic Organic Chemistry (ACSOC- II)*, Aydın, Turkey, 4 (2016).

The synergistic effect between Golden root and *Cannabis Sativa* L. Determination of the antioxidant activity of the extracts

N.B. Vetskov[1], I.S. Hinkov[1], K.V. Petkova- Parlapanska[2*], E.D. Georgieva[2,3], G.D. Nikolova[2], Y. D. Karamalakova[2]

[1] University of Chemical Technology and Metallurgy, 8 Kliment Ohridski Blvd., Sofia 1756, Bulgaria
[2] Chemistry and Biochemistry Department, Medical Faculty, Trakia University, 11 Armeiska Str., 6000 Stara Zagora, Bulgaria
[3]Department of General and Clinical Pathology, Forensic Medicine, Deontology and Dermatovenerology, Medical Faculty, Trakia University, 11 Armeiska Str., 6000 Stara Zagora, Bulgaria

The study aimed to compare the chemical composition and *in vitro* antioxidant activity of an extract obtained from *Cannabis sativa* L and golden root (*Rhodiola rosea* L), which are both used as natural anxiolytics. The phytochemical profile (HPLC - DAD analysis), total polyphenol content (TPC), and antioxidant capacity (AOC) of the combination of *Rhodiola rosea* extract and *Cannabis sativa* oil were investigated to study their effects. To determine the DPPH radical-scavenging activity, an electron paramagnetic radical spectrometer (EPR-X-band) was used as a promising technique. The results indicated that the new extract derived from the combination of *Rhodiola rosea* and *Cannabis sativa* was richer in phenolic compounds and exhibited higher antioxidant activity. These findings provide valuable insights for potential *in vivo* studies that involve the simultaneous use of the two plants.

Keywords: *Cannabis sativa* L*, Rhodiola rosea* L*,* antioxidant activity, phenolic composition

INTRODUCTION

Synergy refers to the phenomenon where certain substances work together to produce a greater overall effect than the sum of their individual effects. This can often be observed when different herbal products interact with each other. Identifying and utilizing these interactions is crucial, as they can be harnessed to effectively treat a wide variety of diseases [1].

Cannabis sativa L (*C. sativa*) and *Rhodiola rosea* L (*R. rosea*) are popularly used as natural anxiolytics. The occurrence of *Rhodiola rosea* is not common in some regions and is mostly cultivated due to the accumulation of active compounds in it over several years. The golden root is found in Bulgaria, mostly on rocky places and mountain meadows up to 2600 m above sea level in Rila, Pirin, Western Rhodopes, Western and Central Stara Planina mountains. Traditionally, it has been used as a central nervous system stimulant. The pharmacological effects of *R. Rosea* are believed to be due to the presence of the glucosides rosavin, rosin and rosarin. However, there is a lack of sufficient data in the literature on the presence and amount of individual phenolic compounds in *Rhodiola rosea* L extracts, and their influence on the biological action of the extracts [4]. Over the years, the medicinal properties of

another anxiolytic C *sativa*, and the action of cannabidiol (CBD) in neurodegenerative diseases have been increasingly discussed [5]. There is evidence that the therapeutic benefits of the plant are based not only on cannabinoids, but also on other secondary metabolites such as terpenes and flavonoids. Different parts of the plant, such as leaves, flowers, and pollen, contain at least 26 flavonoids [6, 7]. However, to understand the contributions of each natural product to this "entourage effect", further research is needed [8].

Electron paramagnetic resonance (EPR), also known as electron spin resonance (ESR), spectroscopy has been utilized in natural product research since the 1960s. EPR experiments are designed to demonstrate specific reactivity with various radicals, providing information on intrinsic antioxidant potential with minimal environmental impact. Spectrophotometric assays using DPPH are routinely used for this purpose [9]. Although this method has its advantages, it also has a main drawback which is spectral interference. The solvent used and the presence of unwanted colored compounds in the sample can result in interference that affects the accuracy of results. However, the EPR method can avoid this interference and ensure that these factors do not influence the outcome of the analysis [10].

The present study aims to evaluate the combined effects of *Cannabis sativa* oil and *Rhodiola rosea*

* To whom all correspondence should be sent:
E-mail: kamelia.parlapanska@trakia-uni.bg

extract and compare the chemical composition of their mixture in terms of polyphenol composition and antioxidant activity. The total plyphenol content was determined using the Folin-Ciocalteu method, while individual phenolic compounds were determined using HPLC-DAD. The antioxidant activity was evaluated through DPPH, PBN, and TEMPOL assays using an Electron paramagnetic radical spectrometer (EPR-X-band).

EXPERIMENTAL

Plant material and extraction procedure

The extract of golden root (*Rhodiola rosea* L) was obtained by extracting 1 gram of golden root with 10 mL of 50 vol. % ethanol solution (solid to liquid ratio 1:10). The weight of the samples was measured by Sartorius analytic balance (precision 0.1 mg). The extraction process was performed once in a stirred round-bottom two-neck flask, thermostated in a silicon oil bath (operational temperature was controlled *via* immersed thermometer and a reflux condenser was mounted to avoid evaporation of the solvent, at stirring frequency of 800 min^{-1}). The flask was centered and immersed to the level of the solvent without contact with the bottom of the bath. For separating the solid from the liquid after the extraction Büchner funnel vacuum filtration was used.

Cannabis sativa oil was purchased from the pharmacy - DragonflyCBD™. *Cannabis* oil has a low THC percentage (0.3 %), so it is non-psychoactive. *Cannabis sativa* oil is usually obtained by steam distillation. Still, the only effective method to extract all valuable substances is supercritical extraction, using not only CO_2 but propane or butane, dimethyl ether, ethanol, or mixtures of these extractants. [11].

Sample preparation

Rhodiola rosea L extract (50 % EtOH) was mixed with *Cannabis sativa* oil in a 1:1 ratio.

Analysis of the extracts

TPC - total phenol content. The total phenol content (TPC) of the extracts was determined by the Folin - Ciocalteu method described by Singleton *et al*. with some modifications [12] using gallic acid as a standard for deriving the calibration line. Double - beam UV-VIS spectrophotometer (T 60, PG Instruments Ltd., Great Britain) was used to analyze the samples. Light absorption was measured at 765

nm. To avoid accidental errors, each analysis was repeated at least three times. The results are presented as g gallic acid equivalent (GAE) per mL. The results of the analyses performed in the present study are presented as mean ± RSD (n=2).

HPLC- DAD analysis

The method of high-performance liquid chromatography with a diode detector (HPLC-DAD) was used to determine 8 components: epicatechin gallate, catechin, rutin, quercetin, myricetin, kaempferol, gallic acid [13]. Analyses were performed with an Agilent 1100 HPLC system (Agilent 1100 HPLC, Agilent Technologies, CA, USA) equipped with a DAD detector (G1315B, Agilent Technologies, CA, USA) and operated by an HP Chemstation. The column used was Purospher star, Hiber RT 125 - 4; RP18 (Purospher star, Merck, Germany). The column temperature was 25 °C. Separation was performed using a linear gradient of 0.1 % TCA (A) and 100 % acetonitrile (B). The gradient started with 5 % B, 15 % B at 16.5 min, 33 % B at 22.5 min, 100 % B at 30.5 min, 5 % B at 35 min until the 40th to re-equilibrate. The flow rate was 1.6 mL/min. The injection volume for samples and standards was 30 μL. DAD acquisition was set in the 200 - 400 nm range. Identification of the main compounds was performed by comparing the retention times and UV spectra of the peaks obtained in both the sample and standard chromatograms.

EPR spectroscopy

DPPH radical scavenging activity. DPPH (1,1-diphenyl-2-picrylhydrazyl) radical-scavenging capacity of the tested extracts was determined by the method of Bernardo Dos Santos *et al*. [14], modified by Zheleva *et al*. [15]. To measure DPPH scavenging capacity, 98 % ethanolic DPPH solution (80 mM, stock) and test natural products (5 mM) were mixed and homogenized. After 1 minute of incubation in the dark, 0.20 μL of the mixture were transferred to non-heparinized capillary tubes (Micro- 221), which were placed as sample tubes in standard EPR quartz tubes. Generation of the system (DPPH- H/R) was initiated after 1 minute and the DPPH solution was used as an internal standard. DPPH radical scavenging ability was calculated relative to the equation:

Scavenged DPPH (%) = $[(I_O - I)/I_O]$ x 100%

where: I_O - the double-integrated intensity of the DPPH signal for the blank; I - the double-integrated DPPH signal intensity of the test sample.

In vitro indirect EPR study of alpha-phenyl-N-tetrabutylnitrone (PBN)

To measure the *in vitro* inhibitory ability, a PBN solution (5 mM, stock) dissolved in DMSO and 5 mM of the tested natural product was mixed and homogenized. After 30 minutes of incubation in the dark, 0.20 µL of the mixture were transferred to non heparinized capillary tubes. The PBN-generated adduct was a sextet. The amount of spin adducts formed between the PBN and the lipid radicals present was calculated after integrating the area under the EPR spectra recorded in the control sample and the samples containing the test product. The double - integrated PBN signal intensity of the test sample was calculated by:

Scavenged PBN (%) = $[(I_O - I)/I_O] \times 100\%$

Generation of the system was initiated after 30 minutes and PBN/DMSO solution was used as an internal standard at field center 3513 G, microwave power 2.05 mW, modulation amplitude 10.00 G, field width 200.00 G, 1 number of scans performed. The PBN inhibitory capacity of the test samples was calculated according to the given equation, where I_O is the double integrated intensity of the PBN/DMSO signal for the blank.

In vitro EPR estimation of TEMPOL (4-hydroxy-2,2,6,6-tetramethylpiperidine-1-oxyl) radical levels

Nitroxide radical solution with a starting concentration of 2 mM was added to the studied samples in a ratio of 1:5 and stirred on a vortex for 5 s at room temperature. An aliquot of the sample was taken in a microcapillary (volume 10 µL) and placed in the EPR cavity, after which the measurement started. For each measurement, a new amount of the reaction mixture (nitroxide/ sample) was taken, and the analysis was performed at different incubation times (1, 10, 30, 60, 90, and 120 min). The EPR data were calculated as a percentage of the control, 0.2 mM TEMPOL/DMSO [16].

Statistical analysis

EPR spectral processing was performed using Bruker Win-EPR and Simfonia software. Statistical analysis was performed with Statistica 8.0, Stasoft, Inc., one - way ANOVA, and Student - t - test to determine significant differences between data sets. Results were expressed as mean ± standard error (SE). A value of $p < 0.05$ was considered statistically. Kinetic data were expressed as the average of two independent measurements, which were processed using the computer programs Origin 6.1 and Microsoft Excel 2010.

RESULTS AND DISCUSSION

TPC - total phenol content

The results obtained for TPC are presented in Fig. 1. The analysis of the presented results shows that TPC (43.2 ± 1.38 mg GAE/mL) in the combined extract increased by about 30 %.
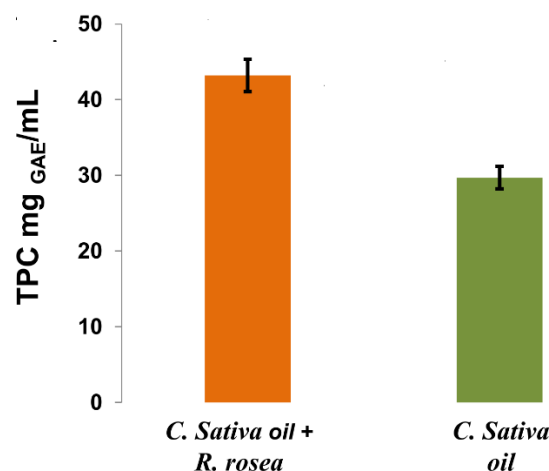

Fig. 1. Total phenol content (TPC) of combined extract (*C. sativa* and *R. rosea*) and *C. sativa* oil.

The *C. Sativa* and *R. rosea* combined extract contained a significantly higher amount of TPC than the extract of *C. Sativa* oil ($p < 0.05$). This finding highlights the potential benefits of using a combination of these two extracts in various applications. Although there is limited literature data on total phenolic compounds in *R. rosea* extracts, the results indicated that further investigation of the use of *R. rosea* in combination with other natural extracts is needed [17].

HPLC- DAD analysis

HPLC-DAD analysis revealed that the combined extract of the two plants had a significantly increased quercetin content (Table 1, Fig. 2). The concentration (µg/mL) is presented as mean ±RSD (n = 2) of each identified compound. This information is valuable in understanding the potential health benefits of these plants and their extracts. Quercetin has been shown to exhibit synergistic effects with cisplatin in human cancer cell lines. The significant antioxidant properties of *C. sativa* seed oil generally depended on the phenolic compounds present in the sample, which is in agreement with the data reported by other researchers [18]. The presence of a phenolic pattern and alkyl and hydroxyl groups on the phenolic ring (as seen in apigenin, quercetin, luteolin, catechin, epicatechin, and canflavin A and B) enhances the antioxidant capacity of the oils [19]. However, there is a possibility that CBD increases the antioxidant activity of terpenes and/or polyphenols through a

synergistic effect, as an increase in antioxidant activity in *C. sativa* extracts has been reported when cannabinoids are accompanied by a large amount of polyphenols [20]. Quercetin was found to be present in the hydroalcoholic extract of the four cultivars [21, 22]. It is interesting to note that samples with different concentrations of the main cannabinoid CBD exhibited similar radical scavenging activity. Therefore, it can be concluded that the antioxidant activity is a consequence of the presence of many different compounds, i.e. flavonoids and phenolic compounds. Thus, the authors explain that the antioxidant capacity may be the result of a synergistic effect between CBD and the phenolic types of metabolites that are present in these cannabis oils [23].

Table 1. Polyphenol content of *C. sativa* and *R. rosea* combined extract and *C. sativa* oil.

	Analyte	Concentration, µg/mL
Cannabis sativa	rutin	19.95
	quercetin	4.12
Cannabis sativa + Rhodiola rosea	rutin	19.82
	quercetin	7.21

From the results presented in Table 1 it is clear that two flavonols - rutin and quercetin - were identified using the validated liquid chromatography method. A higher content of quercetin (7.21 ± 0.13 µg/mL) was found in the combined extract compared to that in *C. sativa* oil (4.12 ± 0.17 µg/mL).

Investigation of the formation of stable radical structures in natural antioxidants by direct EPR spectroscopy

The radical scavenging activity of medicinal extracts is linked to their capacity to create stable radical structures. Direct EPR spectroscopy, in the extract of *C. sativa* and *R. rosea*, registered a stable EPR singlet signal (Fig. 3). The values of the

measured g factors were 2.0041 ± 0.0002 for the combined extract and 2.0042 ± 0.0002 for the extract obtained from *C. sativa* oil alone, respectively. The measured peak-to-peak distance was of the order of 9 G.

The extraction of these two plants together did not destroy the stable radical structure. Based on the data obtained, in the identification of the recorded stable free-radical form, we hypothesized that the stable structure is due to the high content of quercetin after our HPLC analysis [18].
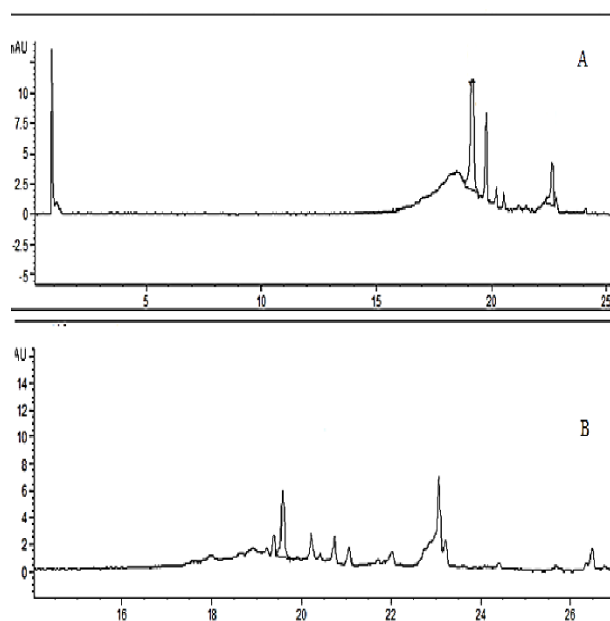

Fig. 2. HPLC chromatogram of the *Cannabis sativa* oil (A) and *C. sativa* and *R. rosea* combined extract (B)- chromatogram at 368 nm.

DPPH radical scavenging activity

The antioxidant properties were evaluated by determining the DPPH radical scavenging capacity in the extract of *R. rosea* and *C. sativa*. The results are presented in Fig. 4.
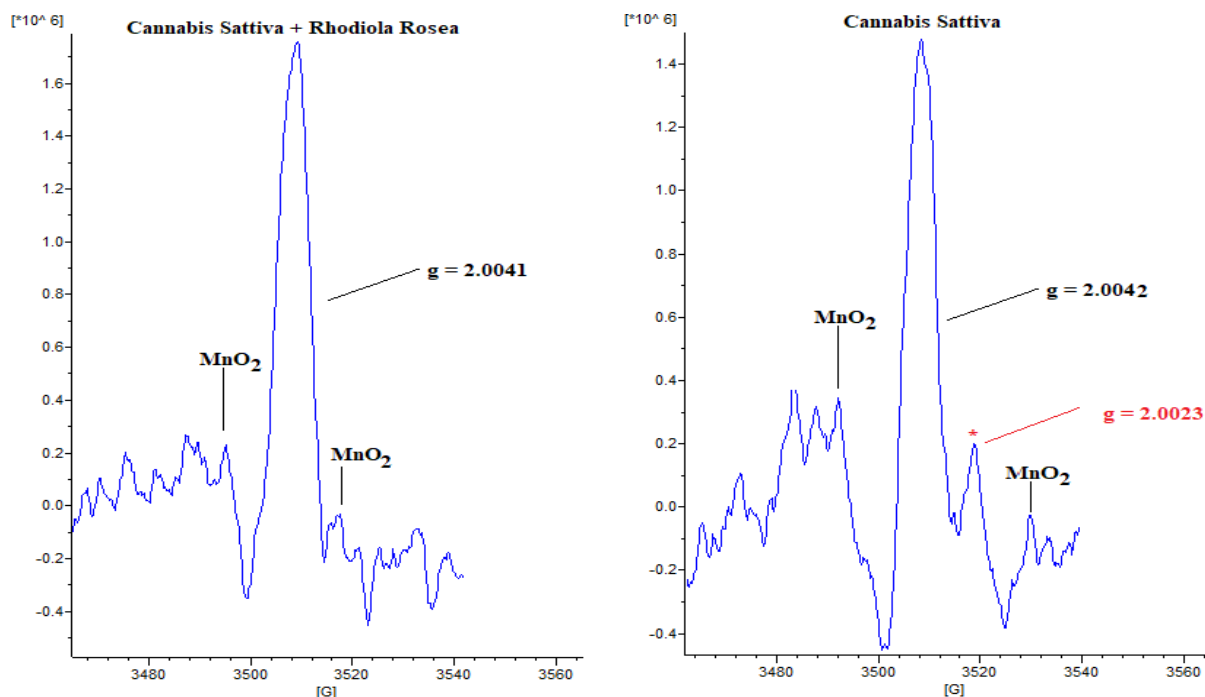
Fig. 3. Direct EPR spectra of the extract of *C. sativa* and *R. rosea* and spectra obtained from *C. sativa* oil. Values are the arithmetic mean of 3 consecutive measurements.
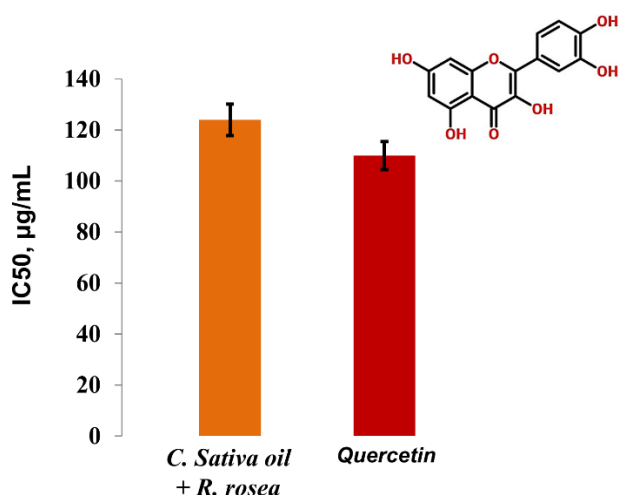
Fig. 4. DPPH radical scavenging capacity of *C. sativa* and *R. Rosea* combined extract. Pure quercetin was used as control

Based on the presented IC_{50} values in Fig. 4. ($IC_{50} = 120.17 \pm 1.87$ µg/mL), it was discovered that *C. sativa* and *R. rosea* combined extract exhibited high antioxidant activity comparable to pure quercetin. The results of the study found 87.3 % scavenged (p < 0.002) DPPH radicals at the concentration of the extract (2 %), compared to the control sample.

In vitro indirect EPR study of alpha-phenyl-N-tetrabutylnitrone (PBN)

Experiments involving the peroxyl (or hydroperoxyl) radical are of particular relevance to

the antioxidant capacity as they predominate in lipid oxidation in biological systems [19].

The results of the *in vitro* study of superoxide anion radicals reveal that the obtained extract inhibits 94.96 % of the generation of superoxide radicals ($O2^{\bullet-}$) within the first minute. Several studies have shown that both NO and $O2^{\bullet-}$ are involved in multiple pathophysiological processes and therefore it is important to establish the activity of the product against these radicals to be used for therapeutic purposes [21].

Fig. 5. Inhibition of peroxyl radical of the PBN-1- hydroxyethyl radical adducts.

Cytotoxic aldehydes produced as a result of lipid peroxidation can block macrophage action, inhibit protein synthesis, inactivate enzymes, cross-link proteins and lead to thrombin generation [24].

Therefore, lipid peroxidation plays a crucial role in inflammation, cancer and heart disease. From the obtained results, it can be concluded that the combined extract of *Cannabis sativa* oil and *Rhodiola rosea* 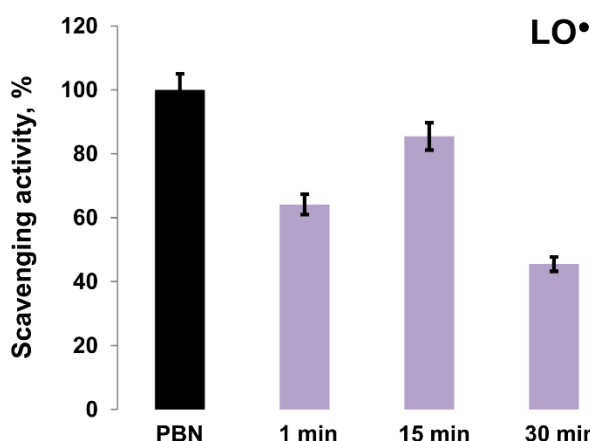inhibit lipid radicals (p < 0.003). Maximal inhibition is at 15 min, probably due to the interaction of phenolic compounds and PBN.

The antioxidant compounds in *C. sativa* and *R. rosea* combination scavenge the biggest radical amounts, 15 minutes after the start of experiment. Importantly, after this time, the antioxidant activity sharply decreases.

Importantly, after this time, the antioxidant activity sharply decreases. Quercetin is one of the most effective inhibitors of lipid peroxidation [25], and the increased amount of this flavonoid (found by HPLC-DAD analysis, Table 1) is due to lipid radical inhibition.
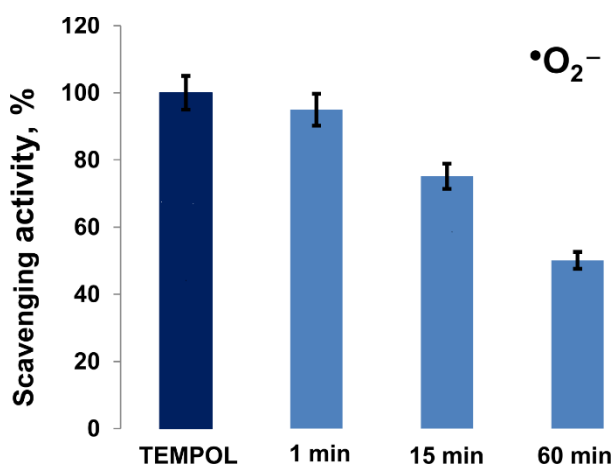
In vitro EPR estimation of TEMPOL radical levels

Fig. 6. Monitoring of ($\bullet O_2^-$) produced by catalase - mimic reaction.

CONCLUSIONS

The present study outlines the activity of the combined extract of *Cannabis sativa* seed oil and *Rhodiola rosea* extract in *in vitro* tests. As a byproduct of the electron transfer process, reactive oxygen species have shown their ubiquity in the cell in the form of various groups of oxygen radicals, including singlet oxygen ($^1O_2$); superoxide anion radical ($O_2\bullet^-$); hydroxyl radical ($\bullet OH$), hydrogen peroxide (H_2O_2), and their overproduction leads to the occurrence of oxidative stress. That is why it is important to determine the possibility of plant products - oils and extracts to inhibit these radicals. The phenolic composition of the secondary metabolites of *Cannabis sativa* and *Rhodiola rosea* shows a high antioxidant potential. EPR experiments - lipid peroxidation, superoxide anion ($\bullet O_2^-$) inhibition, hydroxyl radical -($\bullet OH$) and DPPH

radical scavenging were designed to show specific reactivity with different radicals, providing information on antioxidant potential. As EPR studies are taken as preliminary *in vivo*, our preliminary study demonstrates the best biomedical prospects for obtaining the extract as a future drug or source of new functional products - an important protection against various diseases related to oxidative stress.

Conflict of interest: The authors declare that they have no conflict of interest.

REFERENCES

1. R. Pezzani, B. Salehi, S. Vitalini, M. Iriti, F. A. Zuñiga, J. Sharifi-Rad, N. Martins, *Medicina*, **55**, 110 (2019).
2. M. Malík, P. Tlustoš, *Plants*, **12**, 1364 (2023).
3. M. N. Khanam, M. Anis, S. B. Javed, J. Mottaghipisheh, D. Csupor, *Agronomy*, **12**, 1178, (2022).
4. D. N. Olennikov, N. K. Chirikova, A. G. Vasilieva, I. A. Fedorov, *Antioxidants*, **9**, 526 (2020).
5. J. Moreira, M. Machado, M. Dias-Teixeira, R. Ferraz, C. Delerue-Matos, C. Grosso, *Acta Pharm. Sin. B.*, (2023).
6. Y. Liu, H. Y. Liu, S. H. Li, W. Ma, D. Wu, T. Li, R. Y. Gan, TrAC, *Trends Anal. Chem.*, **149**, 116554 (2022).
7. G. R. Gandhi, A. B. S. Vasconcelos, D. T. Wu, H. B. Li, P. J. Antony, H. Li, F. Geng, R. Q. Gurgel, N. Narain, R.Y. Gan, *Nutrients*, **12**, (2020).
8. S. Sofrás, M. F. Desimone, *Pharm. Des.*, **29**, 394, (2023).
9. W. Brand-Williams, Wendy, M. E. Cuvelier, C. Berset, *LWT*, **28**, 25, (1995).
10. A. J. Fielding, *J. Nat. Prod.*, **1**, 16 (2022).
11. A. Dobreva, *Phytologia Balcanica*, **28**, (2022).
12. J. M. Peñarrieta, J. A. Alvarado, B. Bergenståhl, B. Åkesson, *Rev. Boliv. Quím.*, **24**, 5 (2007).
13. V. Dimcheva, N. Kaloyanov, M. Karsheva, *Open Journal of Anal. Bioanal. Chem.*, **3**, 39 (2019).
14. D. H. S. Bernardo dos Santos, V. Silva, S. Bolzani, *J. Brazilian Chem. Soc.*, **20**, 1483 (2009).
15. A. Zheleva, R. Kumar, R. Sharma, Y. Karamalakova, V. Gadjeva, *Biotechnol. Biotechnol. Equip.*, **39**, (2009).
16. E. Georgieva, V. Atanasov, R. Kostandieva, V. Tsoneva, M. Mitev, G. Arabadzhiev, Y. Yovchev, Y.

Karamalakova, G. Nikolova, *Int. J. Mol. Sci.*, **24**, 5807 (2023).
17. M. Polumackanycz, P. Konieczynski, I. E. Orhan, N. Abaci, A. Viapiana, *Antioxidants*, **11**, 919 (2022).
18. A. Smeriglio, *Phytotherapy Research*, **30**, 1298 (2016).
19. A. Mohanan, *Food Chem.*, **266**, 524 (2018).
20. A. Nuutila, *Food Chemistry*, **4**, 485 (2003).
21. A. Hacke, *Analyst*, **144**, 4952 (2019).
22. V. di Giacomo, L. Recinella, *Antioxidants,* **10**, 44 (2021).
23. C. Cantele, Bertolino, *Antioxidants*, **9**, 1131 (2020).
24. B. Halliwell, *Methods in Enzymology*, **186**, 1 (1990).
25. W. Oh, *Food Chemistry*, **364**, 130394 (2021).

Thermodynamic models for solution behavior and solid-liquid equilibrium in acetate binary systems from low to very high concentration at 25°C

Ch. Christov*, Ts. Tsenov, S. Donchev

Department of Chemistry, Faculty of Natural Sciences, Shumen University "Konstantin Preslavski", 115, Universitetska Str., 9700 Shumen, Bulgaria

In this study we developed new thermodynamic models for solution behavior and solid-liquid equilibrium in eight acetate binary systems from low to very high concentration at 25°C: six systems of the type 1-1 ($X(CH_3COO)$-H_2O with X= (Li, Na, K, Rb, Cs, and Tl)) and two systems of the type 2-1 ($Y(CH_3COO)_2$-H_2O with Y= (Mg, and Ba)). Models were developed on the basis of Pitzer ion interactions approach. To parameterize models for binary systems we used all available experimental osmotic coefficients data (φ) for the whole concentration range of solutions. To develop models, we used different versions of the standard molality-based Pitzer approach. It was established that for all acetate systems under study application of extended approach with 4 parameters (β^0, β^1, β^2 and C^φ) and variation of α_1 and α_2 terms in fundamental Pitzer equations leads to the lowest values of standard model-experiment deviation. The predictions of new developed here models are in excellent agreement with experimental φ data, and with recommendations on the mean activity coefficients ($\gamma_\pm$) from low to very high concentration: up to 23.8 m in $K(CH_3COO)$-H_2O, up to 39.2 m in $Rb(CH_3COO)$-H_2O, and up to 52.2 m in $Cs(CH_3COO)$-H_2O. On the basis of evaluated binary parameters important thermodynamic characteristics (Deliquescence Relative Humidity DRH, thermodynamic solubility products K°_{sp}; standard molar Gibbs free energy of formation, $\Delta_f G^\circ_m$) for 7 acetate solids were determined at 25°C. The calculated DRH and $\Delta_f G^\circ_m$ values were compared with those reported in the literature. The models described in this study are of high importance, especially in development and improvement of technology for production and purification of acetate solutions and solid phases.

Keywords: Computer thermodynamic modeling; Pitzer approach; acetate binary systems; solid-liquid equilibrium

INTRODUCTION

Computer models that predict solution behavior and solid-liquid-gas equilibria close to experimental accuracy have wide applicability. They can simulate the complex changes that occur in nature and can replicate conditions that are difficult or expensive to duplicate in the laboratory. Such models can be powerful predictive and interpretive tools to study the geochemistry of natural waters and mineral deposits, solve environmental problems and optimize industrial processes. However, development of comprehensive models for natural systems, with their complexity and sensitivity, is a very difficult, time consuming and challenging task.

The specific interaction approach for describing electrolyte solutions to high concentration introduced by Pitzer [1, 2] represents a significant advance in physical chemistry that has facilitated the construction of accurate computer thermodynamic models. It was shown that this approach could be expanded to accurately calculate solubilities in complex brines, and to predict the behavior of natural and industrial fluids from very low to very high concentration at standard temperature of 25°C,

and in the temperature range from 0°C to 250°C [2-14]. In this study we developed new not concentration-restricted thermodynamic models for solution behavior and solid-liquid equilibrium in eight acetate binary systems from low to very high concentration at 25°C: six systems of the type 1-1 ($X(CH_3COO)$-H_2O with X= (Li, Na, K, Rb, Cs, and Tl)) and two systems of the type 2-1 ($Y(CH_3COO)_2$-H_2O with Y= (Mg, and Ba)). Models were developed on the basis of Pitzer ion interactions approach [1-14]. The previously developed by Pitzer and Mayorga [2] and by Kim and Frederick [3] Pitzer approach based thermodynamic models for acetate binary systems were tested by comparison with experimental osmotic coefficient data and with recommendations on activity coefficients ($\gamma_\pm$) in binary solutions. The models which give the best agreement with (φ)-, and ($\gamma_\pm$) data from low to high concentration, up to m(sat), were accepted as correct models which can be used for solubility calculations in binary acetate systems.

Acetate is an ingredient used in many products like cosmetics, cleaning supplies, textiles and photographic films.

---

* To whom all correspondence should be sent:
E-mail: *ch.christov@shu.bg*

Acetate has also historically been used as a coating on magnetic tapes used for early computer storage, and for the plastic sheets used with overhead projectors. The models described in this study are of high importance, especially in development and improvement of technology for production and purification of acetate solutions and solid phases.

METHODOLOGY

The models for acetate binary systems have been developed and tested on the basis of Pitzer's semi-empirical equations [1, 2]. Pitzer approach has found extensive use in modeling of the thermodynamic properties of aqueous electrolyte solutions. According to Pitzer theory, electrolytes are completely dissociated and in the solution there are only ions interacting with one another [1, 2]. Two kinds of interactions are observed: (i) specific Coulomb interaction between distant ions of different signs, and (ii) nonspecific short-range interaction between two and three ions. The first kind of interaction is described by an equation of the type of the Debye-Hueckel equations. Short-range interactions in a binary system (MX(aq)) are determined by Pitzer using the binary parameters of ionic interactions $(\beta^{(0)}, \beta^{(1)}), C^{\varphi}$. The Pitzer's equations are described and widely discussed in the literature [1-14]. Therefore, these equations are not given here. According to the basic Pitzer equations, at constant temperature and pressure, the solution model parameters to be evaluated for mixed ternary system are: 1) pure electrolyte $\beta^{(0)}$, $\beta^{(1)}$, and C^{φ} for each cation-anion pair; 2) mixing θ for each unlike cation-cation or anion-anion pair; 3) mixing ψ for each triple ion interaction where all ions are not of the same sign [4-14]. Pitzer and Mayorga [2] did not present analysis for any 2-2 (e.g. $MgSO_4$-H_2O) or higher {e.g. 3-2: $Al_2(SO_4)_3$-H_2O} electrolytes. Pitzer and Mayorga modified the original equations for the description of 2-2 binary solutions: parameter $\beta^{(2)}(M,X)$, and an associated α_2 term are added to the original expression. Pitzer presented these parameterizations, assuming that the form of the functions (i.e. 3 or 4 β and C^{φ} values, as well as the values of the α terms) vary with electrolyte type. For binary electrolyte solutions in which either the cationic or anionic species are univalent (e.g. NaCl, Na_2SO_4, or $MgCl_2$), the standard Pitzer approach uses 3 parameters (i.e. omits the $\beta^{(2)}$ term) and α_1 is equal to 2.0 ([1, 2, 4, 6]). For 2-2 type of electrolytes the model includes the $\beta^{(2)}$ parameter and α_1 equals to 1.4 and α_2 equals to 12 [13].

To describe the high-concentration solution behavior of systems showing a "smooth" maximum

on $\gamma\pm$ *vs.* m dependence, and to account for strong association reactions at high molality, Christov and co-authors [5-12, 14] used a very simple modeling technology: introducing into a model a fourth ion interaction parameter from the basic Pitzer theory $\{\beta^{(2)}\}$, and varying the values of α_1 and α_2 terms. According to previous studies of Christov [6-13] an approach with 4 ion interaction parameters ($\beta^{(0)}$, $\beta^{(1)}$, $\beta^{(2)}$, and C^{φ}), and varying α_1 and α_2 values can be used for solutions for which ion association occurs in the high molality region. This approach was used for binary electrolyte systems of different type: 1-1, 2-1, 3-1, 1-2 and 3-2 [5-12,14]. The resulting models reduce the sigma values of fit of experimental activity data, and extend the application range of models for binary systems to the highest molality, close or equal to molality of saturation {m(sat)}, and in case of data availability: up to supersaturation.

RESULTS AND DISCUSSION

In this study we developed new not concentration-restricted thermodynamic models at 25°C for solution behavior and solid-liquid equilibrium in all acetate binary systems, for which activity data are available: six systems of the type 1-1 (X(CH$_3$COO)-H$_2$O with X= (Li, Na, K, Rb, Cs, and Tl)) and two systems of the type 2-1 (Y(CH$_3$COO)$_2$-H$_2$O with Y= (Mg, and Ba). The new models are developed on the basis of Pitzer ion interactions approach. To parameterize models for acetate binary systems we used all available experimental osmotic coefficients data for whole concentration range of solutions, and up to saturation point. The models have been constructed using low molality data from Hamer and Wu [15] and Mikulin [17], and osmotic coefficients data-point at saturation from Mikulin [17]. The low molality osmotic coefficients data presented by Robinson and Stokes [16] are very close to the data given in [17]. To develop the models, we used different versions of standard molality-based Pitzer approach. It was established that for all acetate systems application of extended approach with 4 parameters ($\beta^{(0)}$, $\beta^{(1)}$, $\beta^{(2)}$ and C^{φ}) and variation of α_1 and α_2 terms in fundamental Pitzer equations leads to the lowest values of standard model-experiment e deviation. In Table 1 we compare single electrolyte parameters for the binary acetate systems (Li(CH$_3$COO)-H$_2$O, Na(CH$_3$COO)-H$_2$O, K(CH$_3$COO)-H$_2$O, Rb(CH$_3$COO)-H$_2$O, Cs(CH$_3$COO)-H$_2$O, Tl(CH$_3$COO)-H$_2$O, Mg(CH$_3$COO)$_2$-H$_2$O, and Ba(CH$_3$COO)$_2$-H$_2$O), evaluated within this study and given in the literature.

Table 1. Comparison of single electrolyte parameters for binary acetate systems (Li(CH₃COO) (aq), Na(CH₃COO) (aq), K(CH₃COO) (aq), Cs(CH₃COO) (aq), Rb(CH₃COO) (aq), Tl(CH₃COO) (aq)), Ba(CH₃COO)₂ (aq), Mg(CH₃COO)₂ (aq)), evaluated within this study and given in literature. m (max) = maximum molality (mol.kg⁻¹) of experimental activity data used in model parameterization and validation, σ = standard deviation of fit of osmotic coefficients, n = number of experimental data points

System	Ref. Model /This study	α_1	α_2	$\beta^{(0)}$	$\beta^{(1)}$	C^φ	$\beta^{(2)}$	σ	m (max)/	Activity data (φ) source
Li(CH₃COO) (aq)	K&F[a]	2	-	0.11215	0.20243	-0.00519	-	0.00117	4	[15]
	P&M[b]	2	-	0.1124	0.2483	-0.00525	-	0.001	4	[16]
	This study[c]	2	-1	0.110162	0.252672	-0.00598	0.00068	0.00039	9	[17] (n=24)
Na(CH₃COO) (aq)	K&F[a]	2	-	0.13723	0.34195	-0.00474	-	0.00096	3.5	[15]
	P&M[b]	2	-	0.1426	0.3237	-0,00629	-	0.001	3.5	[16]
	This study[c]	2	1	0.114574	0.173754	-0.00333	0.12613	0.00037	8	[17] (n=24)
K(CH₃COO) (aq)	K&F[a]	2	-	0.15283	0.35513	-0.00432	-	0.00087	3.5	[15]
	P&M[b]	2	-	0.1587	0.3251	-0,00660	-	0.001	3.5	[16]
	This study[c]	2	-1	0.156809	0.327685	-0.00727	0.00046	0.00259	25	[17] (n=41)
Rb(CH₃COO) (aq)	K&F[a]	2	-	0.16296	0.32918	-0.00561	-	0.00062	3.5	[15]
	P&M[b]	2	-	0.1622	0.3353	-0.00551	-	0.001	3.5	[16]
	This study[c]	2.62	0.02	-2.247348	0.264659	0.00215	2.47881	0.00161	40	[17] (n=48)
Cs(CH₃COO) (aq)	K&F[a]	2	-	0.17144	0.32896	-0.00793	-	0.00063	3.5	[15]
	P&M[b]	2	-	0.1628	0.3605	-0.00555	-	0.001	3.5	[16]
	This study[c]	-0.8	1	0.112181	0.000109	-0.00252	0.28736	0.00436	53	[17] (n=47)
Tl(CH₃COO) (aq)	K&F[a]	2	-	0.00878	-0.04105	-0.00153	-	0.00215	6	[15]
	P&M[b]	2	-	0.0082	0.0131	-0.00127	-	0.001	6	[16]
	This study[c]	2	1	0.026702	0.131112	-0.00326	-0.09122	0.00021	6	[17] (n=23)
Mg(CH₃COO)₂ (aq)	K&F[a]	2	-	0.22930	2.04167	-0.01460	-	0.00370	4	[16]
	This study[c]	2	1	0.111212	-0.27943	0.00080	0.71466	0.00251	6	[17] (n=21)
Ba(CH₃COO)₂ (aq)	K&F[a]	2	-	0.28725	2.87507	-0.04539	-	0.00663	3.5	[16]
	This study[c]	2	1	-0.013209	-1.44114	0.00519	1.63477	0.00200	5	[17] (n=18)

[a]Kim, Frederlck (1988) [3]; [b] Pitzer, Mayorga (1973) [2]; [c]Accepted model

On Fig. 1 we compare model calculated (lines) osmotic coefficients (φ) of Li(CH₃COO), Na(CH₃COO), K(CH₃COO), Rb(CH₃COO), Cs(CH₃COO), Tl(CH₃COO), Mg(CH₃COO)₂, and Ba(CH₃COO)₂ in binary solutions Li(CH₃COO)-H₂O, Na(CH₃COO)-H₂O, K(CH₃COO)-H₂O, Rb(CH₃COO)- H₂O, Cs(CH₃COO)-H₂O, Tl(CH₃COO)-H₂O, Mg(CH₃COO)₂-H₂O and Ba(CH₃COO)₂-H₂O against molality at T = 25ºC with recommendations in literature (symbols). The predictions of new developed here models are in excellent agreement with experimental osmotic coefficients data (φ) in

binary solutions from low to extremely high concentration (up to 23.8 m in K(CH$_3$COO)-H$_2$O, up to 39.2 m in Rb(CH$_3$COO)-H$_2$O, and up to 52.2 m in Cs(CH$_3$COO)-H$_2$O). As it is shown on Fig. 1 for acetate systems, the new models developed in this study are in pure agreement at high concentration with the standard approach 3-parameters low molality models of Pitzer and Mayorga [2] and of Kim and Frederick [3].
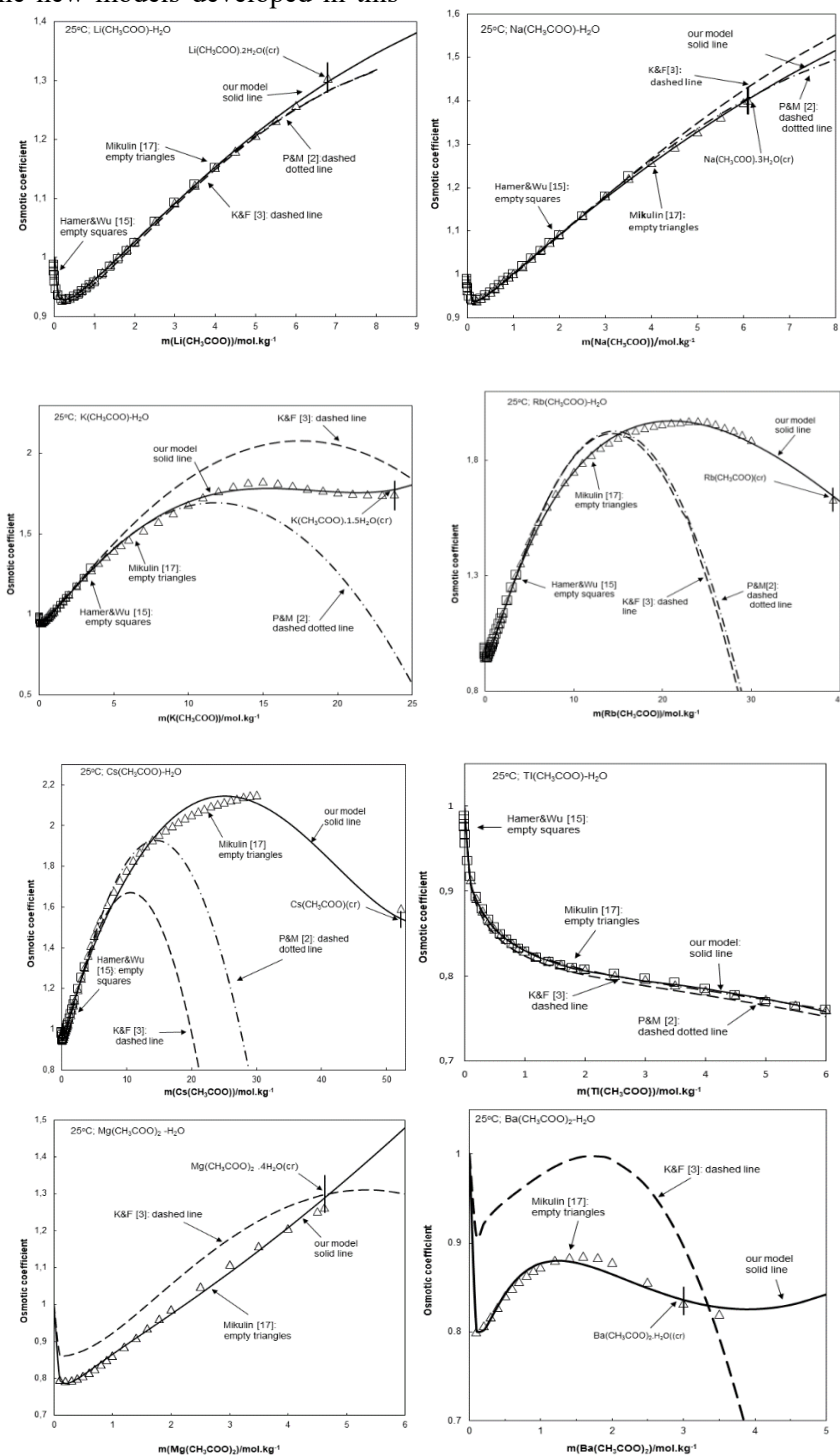
Fig. 1. Comparison of model calculated (lines) osmotic coefficients (φ) of Li(CH$_3$COO), Na(CH$_3$COO), K(CH$_3$COO), Rb(CH$_3$COO), Cs(CH$_3$COO), Tl(CH$_3$COO), Mg(CH$_3$COO)$_2$, and Ba(CH$_3$COO)$_2$ in binary solutions Li(CH$_3$COO)-H$_2$O, Na(CH$_3$COO)-H$_2$O, K(CH$_3$COO)-H$_2$O, Rb(CH$_3$COO)-H$_2$O, Cs(CH$_3$COO)-H$_2$O, Tl(CH$_3$COO)-H$_2$O, Mg(CH$_3$COO)$_2$-H$_2$O and Ba(CH$_3$COO)$_2$-H$_2$O against molality at T = 298.15 K with recommendations in literature (symbols). Heavy solid lines represent the predictions of the developed in this study and accepted models. Dashed lines, and dashed dotted lines represent the predictions of the reference models of Kim and Frederick [3], and of Pitzer and Mayorga [2], respectively. The experimental data are taken from Mikulin [17] (empty triangles), and Hammer and Wu [15] (empty squares). The vertical lines denote the molality of stable crystallization of solid acetate phases {from Mikulin [17]}.

Table 2. Comparison between model calculated and recommended values of the Deliquescence Relative Humidity [DRH (%) = a_w^s × 100; where a_w^s is activity of water at saturation], of the logarithm of the thermodynamic solubility product (K^o_{sp}), and standard molar Gibbs energy of formation, $\Delta_f G^o_m$, of acetate solid phases crystallizing from saturated binary solutions at T = 25°C; m^s= molality of saturation (mol.kg^{-1}).

Salt composition	m^s		$\ln K^o_{sp}$	DRH(%)		$\Delta_f G^o_m$ /(kJ.mol^{-1})		
	Exp[17]	Calc.	Calc.	Calc.	From [17]	Calc.^{a}	From [18]	From [17]
Li(CH$_3$COO).2H$_2$O(cr)	6.79	6.79	3.4669	72.81	72.70	-1128.28	-	- 1135.16
Na(CH$_3$COO).3H$_2$O(cr)	6.1	6.1	3.4977	73.46	73.5	-1333.93	-1328.6	- 1340.34
K(CH$_3$COO).1.5H$_2$O(cr)	23.8	23.8	7.7059	21.84	22.5	-989.17	-	- 997.26
Rb(CH$_3$COO)(cr)	39.2	39.2	11.9479	9.77	≈ 10	- 623.67	-	- 622.12
Cs(CH$_3$COO)(cr)	52.2	52.2	13.0764	5.48	≈ 5	-628.916	-	-
Mg(CH$_3$COO)$_2$.4H$_2$O(cr)	4.62	4.62	2.5138	72.47	72.9	-2135.71	-	- 2149.40
Ba(CH$_3$COO)$_2$.H$_2$O(cr)	3.0	3.0	0.6006	87.33	87.4	-1535.03	-	- 1546.82

$^a\Delta_f G^o_m$ values for solid phases are calculated using chemical potential values of solution components given in Wagman *et al.* [18].

On the basis of binary parameters evaluated in this study we determined water activity (a_w) and Deliquescence Relative Humidity (DRH (%)) of solid phases crystallizing from saturated binary solutions. According to Lach *et al.* [5] and Donchev *et al.* [14]:

DRH (%) = a_w (sat) × 100   (1)

where a_w (sat) is activity of water at saturation. The results of DRH calculations are given in Table 2. The DRH predictions of new and accepted models are in excellent agreement with the experimental data determined using isopiestic method, and given in [17]. According to model calculations, the solid-liquid phase change of Cs(CH$_3$COO)(cr) occurs at extremely low relative humidity of environment. As a next step, using the accepted new developed parameterizations, and experimentally determined molalities (m(sat)) of the saturated binary solutions [17] we calculated the logarithm of the thermodynamic solubility product (ln K°$_{sp}$) of acetate solid phases crystallizing from saturated binary solutions at 25°C. The calculation approach is the same as in [5-14]. Therefore, for Na(CH3COO.3H$_2$O)(s):

K°sp (Na(CH3COO.3H$_2$O)(s) = γ$_{(±)}$(sat)^2.m(sat)^2 a_w^5
          (2)

Then, the calculated K°sp values can be directly used to calculate standard chemical potential ($\Delta_f G^o_m$) of acetate solids [5]. K°sp *vs.* standard chemical potential:

RTln K°sp (Na(CH3COO.3H2O)(s)) = $\Delta_f G^o_m$ (Na(CH3COO.3H2O)(s) -$\Delta_f G^o_m$(Na$^+$) - $\Delta_f G^o_m$ (CH3COO$^-$) – 3$\Delta_f G^o_m$ (H$_2$O)   (3)

In Table 2 we compare model calculated and recommended values of the Deliquescence Relative Humidity (DRH), of the logarithm of the thermodynamic solubility product (ln K°$_{sp}$), and standard molar Gibbs energy of formation, $\Delta_f G^o_m$, of acetate solid phases crystallizing from saturated binary solutions at T = 25°C.

The calculated $\Delta_f G^o_m$ for Na(CH$_3$COO).3H$_2$O(cr) lies between the recommended values of Wagman *et al.* [18] and Mikulin [17]. For all other acetate solids $\Delta_f G^o_m$ values are given only in [17]. A good agreement is obtained for Rb(CH$_3$COO)(cr). The pure agreement for other acetate solids is mainly due to the different values for chemical potential values of solution components used in this study and in [17] (see Eq. (3)). Here we calculate $\Delta_f G^o_m$ values for solid acetate phases using chemical potential values of solution components given in Wagman *et al.* [18].

CONCLUSIONS

In this study we developed new not concentration restricted thermodynamic models for solution behavior and solid-liquid equilibrium in binary solutions Li(CH$_3$COO)-H$_2$O, Na(CH$_3$COO)-H$_2$O, K(CH$_3$COO)-H$_2$O, Rb(CH$_3$COO)-H$_2$O, Cs(CH$_3$COO)-H$_2$O, Tl(CH$_3$COO)-H$_2$O, Mg(CH$_3$COO)$_2$-H$_2$O and Ba(CH$_3$COO)$_2$-H$_2$O at T = 25°C. The new models were developed on the basis of Pitzer ion interactions approach. To develop the models, we

used different versions of standard molality-based Pitzer approach. The models which give the best agreement with (φ)-, and ($\gamma_\pm$) data from low to high concentration, up to m(sat), were accepted as correct models which can be used for solubility calculations in binary systems and determination of thermodynamic characteristics of acetate solid phases. It was established that for all acetate systems under study application of extended approach with 4 parameters ($\beta^{(0)}$, $\beta^{(1)}$, $\beta^{(2)}$ and C^φ) and variation of α_1 and α_2 terms in fundamental Pitzer equations leads to the lowest values of standard model-experiment deviation. The predictions of new developed here models are in excellent agreement with experimental osmotic coefficients data (φ) in binary solutions from low to extremely high concentration (up to 52.2 m in Cs(CH$_3$COO)-H$_2$O). On the basis of evaluated binary parameters important thermodynamic characteristics (Deliquescence Relative Humidity DRH, thermodynamic solubility products K°_{sp}; standard molar Gibbs free energy of formation, $\Delta_f G^\circ_m$) for 7 acetate solids were determined at 25°C. The calculated DRH and $\Delta_f G^\circ_m$ values are compared with those reported in the literature.

REFERENCES

1. K. Pitzer, *J. Phys. Chem.*, **77**, 268 (1973)
2. K. Pitzer, G. Mayorga, *J. Phys. Chem.*, **77** (19), 2300 (1973).
3. H.-T. Kim, W. Frederlck, *J . Chem. Eng. Data,* **33** (2), (1988).
4. J. H. Park, C. Christov, A. Ivanov, M. Molina, *Geophys. Res. Lett.,* **36,** LO2802 (2009).
5. A. Lach, L. André, S. Guignot, C. Christov, P. Henocq, A. Lassin, *J . Chem. Eng. Data*, **63**(3),787 (2018).
6. C. Christov*, J. Chem. Thermodyn.*, **27** (11), 1267 (1995).
7. C. Christov, *CALPHAD*, **22**, 449 (1998).
8. C. Christov, *J. Chem. Thermodyn.,* **31**(1), 71(1999).
9. C. Christov, *J. Chem. Thermodyn.,* **32**(3), 285 (2000).
10. C. Christov, *CALPHAD,* **25**(1), 11 (2001).
11. C. Christov, *CALPHAD*, **26**(1), 85 (2002).
12. C. Christov, *CALPHAD*, **26**(3), 341 (2002).
13. C. Christov, T Ojkova, D Mihov, *J. Chem. Thermodyn.,* **30**(1), 73 (1998).
14. S. Donchev, T. Tsenov, C. Christov, *Biorisk,* **17**, 389 (2022).
15. W.J. Hamer, Y-C. Wu, *J. Phys. Chem. Ref. Data*, **1**, 1047 (1972).
16. R. Robinson, R. Stokes R. (1965) *Electrolyte Solutions*, 2nd edn. revised; Butterworths, London, 1965.
17. G. Mikulin, *Voprosy Fizicheskoi Khimii Electrolytov*, Khimiya, St. Petersburg, 1968, p. 417.
18. D. Wagman, W. Evans, V. Parker, R. Schumm, I. Halow, S. Bayler, K. Churney, R. Nutall, *J. Phys. Chem. Ref. Data* 11 (Suppl. 2) (1982).

Composition and antioxidant potential of essential oil of *Geranium macrorrhizum* L. from different regions of Bulgaria

M. T. Tzanova[*], N. Hr. Grozeva, M. A. Gerdzhikova, M. Hr. Todorova

Faculty of Agriculture, Trakia University, Studentski grad Str., 6000 Stara Zagora, Bulgaria

The common geranium (*Geranium macrorrhizum* L.) is the economically most important species of the genus *Geranium*, and is highly valued for its fragrance and medicinal properties. Object of the present study is the essential oil (EO) prepared by hydro-distillation of aerial parts and rhizomes of common geranium from four floristic regions of the country. Its quality was determined by GC-MS analysis. The antioxidant potential of *G. macrorrhizum* was evaluated by the DPPH method. Forty-two compounds were identified. In the EOs from the aerial parts, the compound in the most quantity was the sesquiterpene germacrone (from 51.41 to 62.58 %). In the EOs from the rhizomes, this compound was only 5.80-8.94%. The most common ingredient of the rhizome EO was another sesquiterpene: cis-β-elemenone in a quantity from 45.20 to 50.64%. Other nine compounds were present only in the rhizome samples, among which the sesquiterpene globulol was found in good quantities: 15.71 – 15.90%. Monoterpenes like α-terpinene and phellandrene, and sesquiterpenes like eudesm-11-en-4α,6α-diol and eudesm-7(11)-en-4-ol acetate were detected only in some EOs from the aerial parts. The radical scavenging potentials of the EOs were from 33.15 to 41.79 µmol TE/100 µg EO, the rhizome samples showing weaker antioxidant potential compared to the aerial parts. Pearson correlation coefficients between the main ingredients of the EOs from the aerial parts and the radical scavenging potential pointed to the strongest impact of germacrene A on the antioxidant value. The large differences in the results are due to the different agro-ecological conditions under which the plants were grown.

Key words: Essential oil; *Geranium macrorrhizum* L.; Germacrone; Radical scavenging potential; Sesquiterpenes

INTRODUCTION

Common geranium *(Geranium macrorrhizum)* is a perennial plant of the *Geraniaceae* family. Natural habitats of the species are the mountains and semi-mountain regions in the country from 300 to 2500 m above sea level [1]. According to Yankulov [2] and Stoeva [3], common geranium is particularly widespread in the Rhodopes, the Rila and the Balkan Mountains. It is cold hardy and drought tolerant, likes semi-shaded areas and is not demanding of the soil. *G. macrorrhizum* is widely used as an ornamental plant, and finds application in many Bulgarian rituals and customs. The common geranium is also a nectariferous plant. Its extracts possess a wide range of antimicrobial, antiviral, hypotensive, antispasmodic, sedative, astringent, cardiotonic, antioxidant and antiatheromatous properties [4-6]. The phyto-therapeutic effect of geranium drug is also associated with its tannin content. The highest tannin content in the aboveground mass was found in the budding phase, and in roots - in autumn [7]. In Bulgarian traditional medicine, this species is used to treat skin diseases, as a disinfectant bath and a poultice of the affected area; it is also used to relieve pruritus, itching and skin lesions [8], and as a remedy for malignant diseases of the hematopoietic organs [3]. In the folk veterinary medicine of Italy, this species has found application in the treatment of diarrhea [9].

Essential oils of *Geraniaceae* species act as inhibitors of α-amylase, α-glucosidase and pancreatic lipase [10], and can be used to treat diabetes [11]. Common geranium is the economically most important species of the genus *Geranium*, highly valued for its fragrance and medicinal properties, and the plant is mainly used for the production of essential oil [3]. Bulgarian geranium oil is well known on the international market and is highly valued. Until recently, our country was one of the few in the world that produced it. The main constituent of the essential oil is germacrone (50-65 %), as well as terpinene, pinene, cymol, caryophyllene, borneol, murulene, elemenone, geraniol and others [12, 13].

The present study aimed to evaluate the quality and the antioxidant potential of the essential oil from aerial parts and rhizomes of common geranium from different regions of the country.

MATERIALS AND METHODS

Plant material and sample preparation

The plant material, object of the present study, were the aerial parts and rhizome of *G. macrorrhizum* collected from four floristic regions

* To whom all correspondence should be sent:
E-mail: *tzanova_m@yahoo.com*

of Bulgaria, grown as an ornamental plant (Table 1). Aerial parts were collected during the full flowering period (May – June 2022), and the rhizome – in the autumn of the same year. From each population, 4 batches were collected, and 200 g average sample of population was prepared. Each sample was extracted by hydro-distillation for 4 hours with a Clevenger-type apparatus according to the European Pharmacopoeia 7th edition [14]. The organic layer obtained on top of the aqueous distillate was separated. After drying with anhydrous sodium sulfate (Na_2SO_4) the essential oil (EO) was kept in sealed airtight glass vials at 4 °C until used.

GC analysis

The EO samples were analyzed on an Agilent 7890A gas chromatograph (Agilent Technologies, CA, USA) with FID and Agilent 5975 Inert MS quadrupole detection with electron capture ionization (70 eV). The chromatographic conditions were: DB-5 MS column CA, USA (5 % phenyl methyl siloxane 30 m × 0.32 mm i.d., film thickness 0.25 μm), carrier gas helium (0.8 ml/min), 1 μl injection volume, split mode 100:1, injector and FID temperature of 250 °C, 2 s scan time, and m/z=40-450 scanning range of MS detector. The start column temperature was 65 °C and at the end of the 34 min single run it was set at 230 °C with a rate of 1 °C/min. Before injecting, the EO sample was diluted with methanol in a ratio of 1:20 (v/v).

The EO components were identified by comparing the registered mass spectra with those of the NIST 08 database (National Institute of Standardization and Technology, Gaithersburg, MD, USA) or by comparison of their mass spectra and retention indices with those reported in literature [16, 17].

DPPH test

The method described by Mileva *et al.* [18] was applied to measure the radical scavenging potential of the EO samples. In brief, to 2 mL of 100 M solution of DPPH in ethanol, 20 μL of 100 mg/mL ethanolic solution of EO sample was added. Two parallel samples of each extract were analyzed. Absorption at 517 nm was measured on a Thermo Scientific Evolution 300 spectrophotometer after 30 min. Since the composition of the extracts is complex, the results for their radical scavenging capacity were compared with Trolox and calculated by regression analysis from the linear dependence between concentration of Trolox and absorption at 517 nm. The results were expressed as μmol Trolox equivalent (TE) in 100 μg EO and as inhibition of DPPH in percentage (I, %) calculated by the formula:

$$I (\%) = [(Abs_0 - Abs_{sample})/(Abs_0)]*100$$

Table 1. *G. macrorrhizum* populations from different regions of Bulgaria and EO yield

Sample ID	Sample	Location, latitude	Elevation, m a.s.l.	Soil type*	EO quantitative yield, % w/w
A1	Aerial parts	Thracian Plain, green areas around Trakia University, town of Stara Zagora 42.4006 N, 25.5711 E	303	Anthrosols	0.035 ± 0.020
A2	Aerial parts	The Rhodopes (Eastern), town of Ivaylovgrad 41.5272 N, 26.1328 E	180	Anthrosols	0.061 ±0.008
A3	Aerial parts	The Balkan Range (Central), town of Kazanlak 42.6349 N, 25.3884 E	425	Fluvisols	0.042±0.002
A4	Aerial parts	Sredna Gora (Eastern), Pryaporets village, 42.4632 N, 25.5379 E	618	Anthrosols	0.062±0.004
A5	Aerial parts	The Balkan Range (Western), town of Varshets 43.2044 N, 23.2937 E	395	Chernozem	0.012±0.006
R1	Rhizomes Sept. 2022	Thracian Plain, green areas around, Trakia University, Stara Zagora 42.4006 N, 25.5711 E	303	Anthrosols	0.007±0.002
R2	Rhizomes Oct. 2022	Thracian Plain, green areas around Trakia University, Stara Zagora 42.4006 N, 25.5711 E	303	Anthrosols	0.008±0.002

*according to FAO 2001 [15]

IC$_{50}$ was defined as the quantity of substance necessary to decrease the initial DPPH by 50%.

Data were obtained from the plotted graph of scavenging activity of each sample. Lower IC$_{50}$ value means higher antiradical activity. Each experiment was carried out in triplicate and data were presented as a mean of the three values. Pearson's correlation was evaluated.

RESULTS AND DISCUSSION

The quantitative yields of the essential oil obtained from the aerial parts of *G. macrorrhizum* varied from 0.012% (A5) to 0.06% (A4 and A2) (Table 1). There was a six-fold difference between the lowest and the highest value. Similar biases in EO yields among different populations were estimated by other researchers [19, 20]. The quantities of the essential oil obtained from the rhizomes were much lower (0.007% and 0.008%). The differences between the EOs extracted from aerial parts and rhizomes were not only as regards the yield values. There were deviations also in the quality of the EOs.

The chemical compositions of the EOs obtained as described in Materials and Methods section are presented in Table 2.

From the results obtained in the present study, the main components in the EO samples from the aerial parts of the collected plants were the sesquiterpene germacrone (from 51.41% to 62.58%); in the EOs from the rhizomes, this compound was only 5.80-8.94%. Ivanov [21] carried out the first studies on the composition of geranium oil from Bulgarian populations. The author found that the oil mainly contained sesquiterpene hydrocarbons. The liquid part of geranium oil consists of about 10% terpene compounds and about 20% sesquiterpene hydrocarbons. The most significant achievement in geranium oil research was the solution of the question of the structure of germacrone, the crystalline component of the oil. Its structure was confirmed by the synthesis of the hydrocarbon germacrone, which is identical to the hydrocarbon produced by complete hydrogenation of germacrone.

The hydrogen monoterpene limonene was quantified between 0.17% and 0.78% in four of five EOs extracted from the aerial parts. In the group of oxygenated monoterpenes linalool dominates in contents from 0.11 and 0.35%. This compound was not found in the rhizome samples. The most abundant oxygenated sesquiterpene was the germacrene, which is identified in three isomers: germacrene A, germacrene B and germacrene D. Germacrene D was in the lowest amounts and ranged between 0.6 and 2.13%. Values of germacrene D more than 30% are toxic. In the present study, the highest concentrations were found for germacrene B between 2.7 and 6.77% (Table 2). The β-eudesmol is another toxic compound, which is more than 40% in the EO sample [22]. In the tested samples this compound was found in EOs extracted from aerial parts and rhizomes in the range from 0.78 to 3.00%. Monoterpenes like α-terpinene and phellandrene, and sesquiterpenes like eudesm-11-en-4α,6α-diol and eudesm-7(11)-en-4-ol acetate were found only in some EOs from the aerial parts (Table 2).

Navarro-Rocha *et al.* [20] studied the biological activities of *G. macrorrhizum* and identified β-elemenone (30.53%), thymol (18.52%) and germacrone (15.54%) as main ingredients of the EOs obtained from wild populations, and linalool (26.45%) and linalyl acetate (25.11%) as major components of the EOs from cultivated populations. A similar composition has been reported for collected wild individuals of this species in Hungary [23]. The essential oil of common geranium grown as an ornamental plant was dominated by linalool (26.45%) and linalyl acetate (25.11%). Ameline *et al.* [24] reported that the major components of the EO from common geranium were germacrone and β-elemene. So, the Bulgarian populations of common geranium are distinguished by a high content of germacrone - a substance with anticancer activities [25, 26].

Table 2. Chemical composition of EO from the tested *G. macrorrhizum* populations, %

Peak No	RT*	RI**	Name	A1	A2	A3	A4	A5	R1	R2
1	12.16	1002	α-Phellandrene	nd***	nd	nd	0.68	nd	nd	nd
2	12.51	1011	α-Terpinene	nd	nd	nd	0.12	nd	nd	nd
3	12.75	1018	p-Cymene	0.20	0.13	0.51	0.66	0.82	nd	nd
4	12.90	1022	Limonene	0.78	0.34	0.17	0.72	nd	nd	nd
5	13.47	1041	trans-β-Ocimene	0.11	0.15	0.10	0.3	nd	nd	nd
6	13.84	1058	γ-Terpinene	0.10	0.12	0.08	0.74	nd	nd	nd
7	14.70	1083	Terpinolene	0.18	0.10	0.09	0.88	nd	nd	nd

8	15.16	1090	Linalool	0.65	0.24	0.46	0.11	0.35	nd	nd
9	16.73	1141	trans-Verbenol	nd	nd	nd	nd	nd	0.11	0.45
10	17.32	1206	Verbenone	nd	nd	nd	nd	nd	0.57	1.29
11	17.57	1217	trans-Carveol	0.48	0.18	0.14	0.13	0.12	0.51	0.67
12	17.60	1220	2,3-dimethyl-Benzofuran	nd	nd	nd	4.72	nd	nd	nd
13	18.06	1228	cis-p-Mentha-1(7),8-dien-2-ol	0.50	0.22	0.13	0.50	0.22	nd	0.23
14	18.76	1256	Canrenone	nd	nd	nd	nd	nd	0.27	0.39
15	22.04	1340	trans-Carveyl acetate	0.81	0.94	1.12	0.35	0.16	0.48	0.87
16	23.12	1371	Isoledene	nd	nd	nd	nd	nd	0.30	0.48
17	23.46	1390	β-Elemene	0.25	0.36	0.49	0.32	0.34	nd	nd
18	23.89	1403	Italicene	0.20	0.47	0.25	0.46	0.10	nd	nd
19	24.23	1414	α-Gurjunene	nd	nd	nd	nd	nd	0.39	0.57
20	24.48	1421	γ-Elemene	0.40	0.58	0.95	0.83	0.51	nd	nd
21	24.94	1440	cis-β-Famesene	nd	nd	nd	nd	nd	0.72	1.24
22	25.69	1452	ar-Curcumene	1.08	6.35	0.3	5.89	0.80	nd	nd
23	25.71	1473	γ-Muurolene	nd	nd	nd	nd	nd	1.23	2.56
24	25.77	1477	γ-Curcumene	0.80	2.75	0.15	1.24	0.50	nd	nd
25	26.00	1482	trans-β-Guaiene	nd	nd	nd	nd	nd	7.88	9.91
26	27.34	1495	Germacrene D	2.13	1.20	0.60	0.92	0.21	1.19	0.33
27	27.72	1514	Germacrene A	3.03	4.96	4.55	3.85	2.54	0.65	0.53
28	28.61	1555	Germacrene B	3.36	2.70	5.59	2.76	6.77	0.71	1.44
29	28.66	1570	Globulol	nd	nd	nd	nd	nd	15.90	15.71
30	29.21	1580	Germacrene D-4-ol	1.34	1.83	1.52	1.68	0.91	0.31	1.38
31	29.37	1588	Viridiflorol	1.02	1.95	2.24	1.45	0.50	1.13	1.74
32	29.83	1601	cis-β-Elemenone	1.43	1.73	4.10	0.91	0.75	50.64	45.20
33	29.94	1610	5-epi-7-epi-α-Eudesmol	3.63	4.42	8.92	1.72	6.20	1.37	1.42
34	30.01	1622	10-epi-y-Eudesmol	1.43	2.96	5.81	6.07	0.84	1.26	1.14
35	30.15	1633	γ-Eudesmol	5.24	2.35	1.22	2.55	3.80	1.09	0.98
36	30.36	1647	β-Eudesmol	3.00	1.38	1.97	2.18	1.60	0.78	2.11
37	30.49	1654	α-Eudesmol	1.36	0.33	1.89	2.11	1.44	0.84	0.73
38	30.65	1666	7-epi-α-Eudesmol	2.72	3.34	2.20	2.80	4.03	0.63	1.15
39	31.01	1695	Germacrone	62.58	56.78	53.32	51.41	61.70	8.94	5.80
40	32.14	1751	(2E,6E)-Farnesol	0.31	0.26	0.55	0.17	0.92	1.16	0.82
41	33.40	1810	Eudesm-11-en-4α,6α-diol	nd	nd	nd	nd	1.40	nd	nd
42	33.85	1843	Eudesm-7(11)-en-4-ol, acetate	nd	nd	nd	nd	1.65	nd	nd

*retention time; **relative index; ***not detected.

Table 3. Radical scavenging potential of EO from *G. macrorrhizum*

ID	R1	R2	A1	A2	A3	A4	A5
IC$_{50}$, mg/ml EO	0.237	0.236	0.205	0.192	0.196	0.208	0.217
µmolTE/100 µg EO	33.30	33.15	38.91	41.79	40.88	38.30	36.64

The EO extracted from the rhizomes of *G. macrorrhizum* were rich in the oxygenated sesquiterpenes cis-β-elemenone (from 45.2 to 50.64 %), and globulol (from 15.71 to 15.90%). The second one was not identified in the EOs from the aerial mass. Other eight compounds were present only in the rhizomes samples: trans-β-guaiene (7.88-9.91%); γ-muurolene (1.23-2.55%); cis-β-famesene (0.72-1.24%); verbenone (0.57-1.29%); α-gurjunene (0.39-0.57%)**;** canenone (0.27-0.39%); isoledene (0.30-0.48%); trans-verbenol (0.11-0.45%).

The antioxidant activity was evaluated as radical scavenging potential of the EOs extracted from the aerial parts and rhizomes of *G. macrorrhizum* plants collected from different populations, and the results for the EO from the aerial parts were from 36.64 (A5) to 41.79 (A2) μmol TE/100 μg EO, which is equal to IC_{50}, *ca*. 0.20 mg/ml EO. The results for the rhizomes were on average 33 μmol TE/100 μg EO, which is equal to IC_{50}, *ca*. 0.24 mg/mlEO (Table 3). So, the rhizome samples showed a weaker antioxidant potential compared to the aerial parts. The differences in the antioxidant potentials of the EOs from aerial parts and rhizomes are due to their different chemical composition.

Zeljković *et al.* [28] calculated the IC_{50} values for the essential oil extracted from aerial parts from *Geranium kikianum, which* ranged *ca*. 70 mg/mL using the DPPH method. The samples tested by the authors were also rich in germacrone. The mean content of this cyclic ketone was 45.6%. Compared to the results obtained in the present study, the EOs from *G. macrorrhizum* showed much stronger radical scavenging potential than EO from *G. kikianum.*

The calculation of the Pearson correlation coefficients between the main ingredients of the EOs from the aerial parts and the radical scavenging potential showed the strongest impact of germacrene A (0.923) on the radical scavenging activity. The coefficient of correlation between this parameter and germacrone was 0.391. The research on the impact of the ingredients on the antioxidant activities of the EO from Bulgarian geranium could lead to interesting results, Moreover, the plant shows promising anticancer activities.

CONCLUSION

In the EOs from the aerial parts of *G. macrorrhizum*, the compound in the most quantity was the sesquiterpene germacrone (from 51.41 to 62.58 %). In the EOs from the rhizomes, this compound was only 5.80-8.94%. The most common ingredient of the rhizome EO was another sesquiterpene: cis-β-elemenone in quantity from 45.20 to 50.64%. Other nine compounds were present only in the rhizome samples, among which the sesquiterpene globulol was found in good quantities: 15.71 – 15.90%. Monoterpenes like α-terpinene and phellandrene, and sesquiterpenes like eudesm-11-en-4α,6α-diol and eudesm-7(11)-en-4-ol acetate were determined only in some EOs from the aerial parts. The radical scavenging potentials of the EOs were from 33.15 to 41.79 μmol TE/100 μg EO, the rhizomes samples showing a weaker antioxidant potential compared to the aerial parts. The calculation of the Pearson correlation coefficients between the main ingredients of the EOs from the aerial parts and the radical scavenging potential showed the strongest impact of germacrene A (0.923) on the antioxidant value. The large differences in the results are due to the different agro-ecological conditions under which the plants were grown.

REFERENCES

1. B. Assyov, A. Petrova, in: Conspectus of the Bulgarian Vascular Flora. Distribution Maps and Floristic Elements, B. Asǎov, A. Petrova (eds.) Bulgarian Biodiversity Foundation, Sofia, 2012, p. 192, (in Bulgarian).
2. J. Yankulov, Main aromatic plants, 19 modern cultivation technologies. Hermes, Plovdiv, 2000. P. 178.
3. T. Stoeva, in: Geranium and Pelargonium, M. Lis-Balchin (ed.), Taylor & Francis, London, 2002, p. 30.
4. G. Miliauskas, T. Beek, P. Venskutonis, *Food Chem.,* **85**, 231 (2004).
5. S. Ivancheva, M. Nikolova, R. Tsvetkova, in: Phytochemistry: Advances in Research. Research Signpost, F. Imperato (ed.), Trivandrum, India, 2006, p. 87.
6. N. Radulovic, M. Dekic, Z. Stojanovic-Radic, *Med. Chem. Res.* **21(5)**, 601 (2012).
7. E. Genova, S. Ivancheva, *Phytol. Balanica,* **1**, 93 (1995).
8. D. Jordanov, P. Nikolov, A. Boichinov, Phytotherapy, Medicina Publishers, Sofia, 1973, p. 201 (in Bulgarian).
9. P. Gastaldo, G. Barberis, F. Fossati, *ATTI.* **35**, 125 (1978).
10. M Govindappa, *J. Diabetes Metab.*, **6**, 7 (2015).
11. J. Riyaphan, D. C. Pham, M. K. Leong, C. F. Weng, *Biomolecules*, **11**, 1877 (2021).
12. I. Ognyanov, PhD Thesis, Sofia Univ., 1958.
13. E. Tsankova, PhD Thesis, BAS, Sofia, 1977.

14. European Pharmacopoeia 7th edn., Council of Europe, Strasbourg, 2010.
15. FAO, Lecture notes on the major soils of the world. World Soil Resources Reports, 94. Rome: Food and Agriculture Organization of the United Nations, 2001, p. 334.
16. E. Kováts, *Helv. Chim. Acta*, **41 (7)**, 1915 (1958).
17. R. P. Adams, Identification of essential oil components by gas chromatography/ mass spectrometry, 4th edn., Allured Publ., Carol Stream, I, USA 2007.
18. M. M. Mileva, V. K. Kusovski, D. S. Krastev, A. M. Dobreva, A. S. Galabov, *Int. J. Curr. Microbiol. Appl. Sci.,* **3(7)** 11 (2014).
19. S. Ć. Zeljković, S. Siljak-Yakovlev, K. Tan, M. Maksimović, *Plant Syst. Evol.,* **306**, 18 (2020).
20. J. Navarro-Rocha, A. F. Barrero, J. Burillo, A. S. Olmeda, A. González-Coloma, *Ind. Crops Prod.* **116**, 41 (2018).
21. D. Ivanov, *Chemistry: Bulg. J. Sci. Educ.,* **21(2),** (2012) (in Bulgarian).
22. J. Buckle, in: Clinical Aromatherapy, 3rd edn., Elsevier, Churchill Livingstone, St. Louis (MO) 2015.
23. N. S. Radulović, M. S. Dekić, Z. Z. Stojanović-Radić, S. K. Zoranić, *Chem. Biodivers.,* **7(11)**, 2783 (2010).
24. A. Ameline, J. Dorland, P. Y. Werrie, A. Couty, M. L. Fauconnier, M. Lateur, G. Doury, *J. Pest. Sci.,* **96(4)**, (2023).
25. S. Soodvilai, P. Meetam, L. Siangjong, R. Chokchaisiri, A. Suksamrarn, S. Soodvilai, *Biol. Pharm. Bull.*, **43(11),** 1693 (2020).
26. L. Wu, L. Wang, X. Tian, J. Zhang, H. Feng, *BMC Complement. Med. Ther.,* **20**, 21 (2020).
27. N. S. Devi, R. K. I. Singh, *Ann. Phytomedicine*, **10(2),** 157 (2021).
28. S. C. Zeljković, K. Tan, S. Siljak-Yakovlev, M. Maksimović, *Nat. Prod. Commun.,* **12(2),** 273 (2017).

Recent progress in electrochemical detection of amaranth in food samples: A brief review

T. M. Dodevska*, D. T. Hadzhiev, I. G. Shterev

Department of Organic Chemistry and Inorganic Chemistry, University of Food Technologies, 26, Maritsa Blvd., Plovdiv 4002, Bulgaria

Amaranth (E 123, AM) is a red synthetic azo dye authorized as a food additive in the EU. In contrast to natural colorants, AM has significant advantages such as low production cost, excellent water solubility, and high stability. AM is used to enhance the natural color, to decrease the loss of color due to processing treatments, and to provide color to colorless ultra-processed foods, making food more attractive to the consumers. AM is widely used in food industry to improve the appearance and color of different types of food and beverages, including confectionery products, jelly, candies, jams, dairy products, ice creams, sausages, wines, syrups and soft drinks. Many of these food products are manufactured directly for, and marketed directly to, children. The high amount of AM in food products can cause adverse health effects such as dizziness, allergies, and respiratory problems. Moreover, long-term studies indicated that the potential adverse effects induced by AM include genotoxicity and cytotoxicity. Therefore, the development of a precise and easy-to-handle alternative for a quick and efficient quantitative detection of AM in food products is necessary for consumer safety. Modern electroanalytical techniques have the advantages of excellent sensitivity and selectivity, instrumental simplicity and portability, providing reliable alternatives to the conventional analytical methods. In this brief review, we have summarized recent trends in the electrochemical sensor systems applied for the analysis of AM in food samples, critically evaluated the performance metrics of these sensors: sensitivity, linear range, limit of detection and stability. Finally, the current challenges and future prospects are outlined.

Keywords: electrochemical sensors; electroanalysis; azo dyes; food colorants; food analysis; food safety

INTRODUCTION

Color is one of the most important sensory attributes of food that plays an essential role in food appearance and acceptability. Color perception is the major visual factor related to product quality that influences the customer selection. Therefore, coloring agents that have been obtained by chemical synthesis, are routinely added to various food products to impart desirable sensory characteristics [1]. Synthetic colorants, especially azo-dyes, have been widely used in food industry due to their excellent water solubility, high coloring ability, good color uniformity, high chemical and photolytic stability, low microbiological contamination and low production cost [2]. However, most azo dyes have potential risks to human health because they contain azo group (-N=N-) and aromatic structures. The toxic effects of azo dyes are induced by their degradation products. Under reductive conditions, the azo groups can be cleaved leading to aromatic amines, which exhibit carcinogenic and mutagenic properties [3].

Amaranth (AM) is a widely used synthetic azo dye, normally supplied as sodium, potassium or calcium salt. AM is soluble in water (70 g/L at 25 ºC), slightly soluble in ethanol (up to 4 g/L), but insoluble in vegetable oils. The powders or granules are of a red-brown shade; in liquid form it has a bluish-red color [4].

Based on the Food and Agriculture Organization (FAO) and World Health Organization (WHO) recommendations, acceptable daily intake of AM is between 0 and 0.5 mg/kg [5]. Recently, pediatric studies have demonstrated the relationship of AM consumption with hyperactivity and irritability in children [4]. At higher levels AM is toxic as it can cause a number of adverse health effects such as genotoxicity, cytostaticity, and cytotoxicity. Zhang and Yadi [6] performed mechanistic and conformational studies on the interaction of AM with human serum albumin (HSA). The binding of AM to HSA induced the conformational change of HSA which represents the disturbance in hydrogen bonding networks [6]. Moreover, according to the results obtained by Basu and Kumar in 2015 AM was expected to be able to induce unfolding and loss of a large part of the helical stability of hemoglobin, which significantly affects the secondary structural changes in human hemoglobin [7].

---

* To whom all correspondence should be sent:
E-mail: *dodevska@mail.bg*

Literature survey reveals several conventional analytical methods for determination of AM in foods and beverages including spectrophotometry [8], high performance liquid chromatography (HPLC) [9], liquid chromatography/mass spectrometry (LC-MS/MS) [10], or capillary electrophoresis [11]. However, most of these methods require specific and relatively expensive equipment, advanced technical expertise, and need of complicated, time-consuming pretreatment procedures. Therefore, it is important to develop new, straightforward, precise and easy-to-handle alternative for quick and efficient quantitative detection of AM in food products for controlling food quality and ensuring the consumers health safety. Due to high sensitivity, simplicity, and rapid sample preparation procedures with high level of automation, electrochemical techniques are the best candidates for the on-site detection of azo dyes, including AM.

In this review, we mainly introduce the research progress of electrochemical sensors in the detection of AM and its application in actual food sample detection. Because the electrode is the core part of the entire sensor device, we summarized the development process of the electrode for quantitative AM detection, and described the modification method and materials. The following part of this article will provide a brief overview on how advances in electroanalytical technology have contributed towards developing sensor devices for AM quantitative detection in food and beverage products.

STATE-OF-THE-ART IN ELECTROCHEMICAL SENSORS FOR THE ANALYSIS OF AMARANTH

It is well known that the performance of electrochemical sensors highly depends on the type of electrode materials used. The best approach to date in order to achieve high stability, sensitivity, and selectivity of sensors during electroanalysis is electrode surface modification. After modification, the electrode shows special surface effect, size effect, and catalytic activity. These specific properties enhance the electrical conductivity of the working electrode, accelerate the electron transfer in the interface, and reduce the redox overpotential of AM. In order to promote the electrochemical reaction and improve the electrode efficiency, modification of the working electrodes using inorganic nanomaterials (graphene, graphene oxide, carbon nanotubes, metal nanoparticles, metal oxide nanoparticles, quantum dots), conductive polymers, ionic liquids, and metal organic frameworks has been extensively investigated.

Graphene (GR) is a two-dimensional sheet of hexagonally arranged carbon atoms with sp^2-hybridization. The combination of attributes such as extremely large surface area and electrical conductivity, high mechanical strength, and low cost makes GR an ideal platform for the anchoring of metal nanoparticles for electrochemical sensing applications [12]. The electrochemical detection and degradation processes of AM using gold electrodes modified with GR/TiO$_2$-Ag composite was investigated by Stefan-van Staden *et al.* [3]. Graphene nanosheets (GRS) prepared by ultrasonic exfoliation of graphite powder in N-methyl-2-pyrrolidone (NMP), were dispersed into N,N-dimethylformamide (DMF) and then used to modify the surface of GCE [2]. The modification of GRS obviously enhances the surface roughness of GCE and provides larger response area and higher accumulation ability for AM. As a result, the catalytic activity for AM is improved effectively on the surface of GRS and the oxidation signals enhance significantly. Based on the remarkable signal enhancement effects of NMP-exfoliated graphene, a sensitive and rapid electrochemical method has been developed for the determination of AM. The linear range is from 2.5 to 125 nM, and the detection limit is extremely low (LOD = 0.75 nM). The sensing platform was used in different drink samples (Fanta, Mirinda), and the results were found to be consistent with the values obtained by HPLC.

A new stable and interference-free voltammetric sensor for highly selective determination of AM in soft drinks was constructed [13]. Surface functionalization of GR with poly(sodium 4-styrenesulfonate) (PSS), a water-soluble polymer used as emulsifying agent, not only improves GR nanosheets dispersibility, but also allows them to be further decorated with other nanomaterials, including metal nanoparticles. Palladium nanoparticles (PdNPs), in particular, are attractive for sensing applications due to their excellent catalytic activity towards AM oxidation. In the development of electrochemical sensors Pd has been mainly used as nano-sized particles for surface modification of various electrode materials. This approach reduces the cost of catalysts, improves their electrocatalytic performance since it provides extremely high surface area and decreases the poisoning effect caused by the adsorption of intermediates and reaction products [14]. The proposed sensor platform PSS-GR-Pd/GCE was employed for measurement of AM in Fanta drink using the standard addition method with satisfying results. According to the presented results, the

proposed method has definite precision and accuracy.

As an oxidation derivative of GR, graphene oxide (GRO) is rich in oxygen-containing groups and has been demonstrated to have good catalytic activities, particularly for the oxidation of AM. Through further functionalization, the electrochemical activity of GRO could be further improved and agglomerating of GRO in aqueous solution could be effectively prevented. An electrochemical sensor was fabricated by modifying nanoporous gold (NPG)-coated glassy carbon electrode (NPG/GCE) with functionalized graphene oxide /chitosan/ionic liquid nanocomposites (fGRO/CS/IL) [15]. As a result of the synergistic effect of NPG and fGRO/CS/IL, the resulting electrode (fGRO/CS/IL/NPG/GCE) showed the highest current response signal of AM due to ultrahigh surface area, electronic conductivity, as well as the improvement of the surface structure. For practical applications, the electrode was validated for the determination of AM in three types of drinks (Fanta Drink, Mirinda Drink and Minute Maid) with satisfactory results.

Reduced graphene oxide (rGRO) is the functionalized product of GRO which has enormous advantages such as better conductivity than that of GRO because of reinstated sp^2-carbon network. A new SnO$_2$/rGRO nanocomposite has been engineered to be utilized as chemically modified sensor for the low-level quantification of AM in soft drinks and water samples [16]. The combinations of rGRO improved the properties of SnO$_2$ nanoparticles and effectively reduced the degree of restacking of graphene nanosheets, as well as increased the active adsorption sites of rGRO. The developed sensor SnO$_2$/rGRO/Nafion/GCE showed excellent anti-interference behavior which highlights the selectivity profile of the sensor for targeted analysis. The effectiveness of SnO$_2$/rGRO/Nafion/GCE was investigated for AM analysis in Sprite, 7-Up, and Sting. The proposed method exhibited acceptable recovery values in the real matrix that proves its reliability to be utilized as a sensitive sensor for AM monitoring at commercial level in different soft drinks.

Researchers have used various types of ionic liquids (ILs) in electrode fabrication with the intention of developing novel electrochemical sensor platforms or as unique electrocatalytic substances, as they possess sophisticated conductivity, low volatility and high chemical stability [12]. Due to wide electrochemical windows and high electrical conductivity, ILs were suggested for modification of electrochemical sensors in voltammetric analysis. Sheikhshoaie *et al.* 2017 reported coupling of ILs and nanomaterials for fabrication of a highly sensitive sensor for AM [17]. RuO$_2$ nano-road, synthesized by sol-gel method, was used for modification of carbon paste electrode in the presence of 1,3-dipropylimidazolium bromide as a conductive binder. The developed electrode CPE/RuO$_2$/NR/DPIBr showed high performance ability for quantification of AM at nanomolar levels. A linear calibration was achieved in range of 0.008–550 μM (LOD = 3 nM). This device was successfully applied for the detection and analysis of AM in soft drinks, orange and apple juices. CPE/RuO$_2$/NR/DPIBr exhibited advantages including improved electrocatalytic ability and good stability. Authors reported a relative standard deviation (RSD) of 2.2% of the electrode signal when CPE/RuO$_2$/NR/DPIBr was stored for 35 days in laboratory that confirms stability of the novel sensor for analysis of AM.

The electrochemical field has witnessed the enormous use of screen-printed carbon electrodes (SPCEs) mainly because of their unique properties compared to other conventional electrodes, including wide potential window, standard background current, reproducibility and high repeatability, commercial availability, cost-effectiveness, ability to connect to portable devices, need for low power, linear output, and possibility of miniaturization. It is therefore considered a potential tool for on-site applications. Sensor systems for AM were developed using screen-printing technique [18-22]. rGRO-methionine [18], double-stranded copper(I) helicate and SWCNTs [19], Pd/GRO nanocomposite [20], Ni–Mo-MOF [21], and V$_2$O$_5$-nanoplates [22] were employed as electrode modifying materials. Tajik *et al.* have fabricated metal–organic framework (MOF) – modified screen printed electrode for sensitive and rapid detection of AM [21]. Conductive metal–organic frameworks (MOFs) are a class of porous materials consisting of organic nodes connected by organic linkers. These attractive materials have many advantages, such as adjustable structure, extraordinarily high surface areas, simple synthesis protocol, and catalytic capacity, making them helpful in effective coating materials for electrocatalytic electrodes that are used in sensing applications. Additionally, the high porosity of MOFs makes them easy to encapsulate metal nanoparticles (MNPs) within their porous channels/cavities, resulting in the formation of MNPs/MOF composites that show high conductivity, excellent sensing and catalytic applications because of synergistic interactions between components [23]. The proposed novel Ni–

Mo-MOF-modifed screen printed electrode (Ni–Mo-MOF/SPCE) was applied for quantitative detection of AM in real samples [21]. According to the proposed protocol, appropriate recoveries were found to detect the AM in fruit juices and tap water. Authors stated that the hybrid bimetallic MOF possesses increased stability and improved catalytic properties for the electrooxidation of AM.

Table 1 summarizes the electrochemical sensors applicable to the quantitative analysis of AM in foods and beverages.

Table 1. Comparison of the analytical parameters of electrochemical sensors for the determination of AM in foods and beverages

Modified electrode	Method	Linear range	LOD (nM)	Analytical application	Ref.
GS/GCE	DPV	2.5–125 nM	0.75	soft drink	2
Au/GTA	LSV	0.3–100 μM	100	–	3
PSS-GR-Pd/GCE	DPV	0.1–9 μM	7	Fanta	13
fGRO/CS/IL/NPG/GCE	SWV	8–1200 nM	23	Fanta, Mirinda, Minute Maid	15
SnO$_2$/rGRO/Nafion/GCE	DPV	1–800 nM 1–60 μM	0.68 2.7	Sprite, 7-Up, Sting, river water	16
CPE/RuO$_2$/NR/DPIBr	SWV	0.008–550 μM	3	soft drink, orange and apple juices	17
rGRO-methionine/SPCE	DPV	1–10 μM 10–100 μM	57	SPY red wine cooler, Sprite	18
H-SWCNT/SPCE	SWV	0.057–1.4 μM	30	synthetic orange juice, soft drink	19
Pd/GRO/SPE	DPV	0.08–360 μM	30	orange and apple juices, tap water	20
Ni–Mo-MOF/SPCE	DPV	0.15–500 μM	50	orange and apple juices, tap water	21
V$_2$O$_5$- NPs/SPE	DPV	0.1–270 μM	40	apple juice, tap water	22
AC-Co$_3$O$_4$-CPE	DPV	0.1–215 μM	10	grape soda, lemon soda	24
N-rGRO/GCE	DPV	0.1–600 μM	30	orange and apple juices, tap water	25
PLA-ERGO/GCE	DPV	0.75–75 μM	250	soft drink	26
1-M-3-BIBR/CuO/SWCNTs/CPE	SWV	0.004–750 μM	1	fruit juices; sausage	27

Poly(L-arginine)–electrochemically reduced graphene modified glassy carbon electrode (PLA–ERGO/GCE) was fabricated by cyclic voltammetry method and the electrochemical behavior of AM and carmine on this electrode was studied [26]. The experimental results indicated that the oxidation peaks of carmine and AM were separated at 121 mV in phosphate buffer solution at pH=2.5. The linear range for the simultaneous determination of carmine and AM were 7.5×10^{-7}–7.5×10^{-5} M and the detection limits were 7×10^{-8} M for carmine and 2.5×10^{-7} M for AM, respectively. The method has been applied to the simultaneous determination of carmine and AM in commercial soft drink with satisfactory results.

Karimi-Maleh *et al.* [27] designed a highly sensitive electrochemical sensor for the simultaneous detection of AM and nitrite in foodstuffs, based on carbon paste electrode modified with 1-methyl-3-butylimidazolium bromide and CuO decorated single-wall carbon nanotubes (1-M-3-BIBr/CuO/SWCNTs/CPE). Synergistic effect between CuO/SWCNTs and 1-M-3-BIBr helps in increasing the ability of proposed sensor for nanomolar determination of AM in food samples. Also, 1-M-3-BIBr/CuO/SWCNTs/CPE resolved the overlapping signal of AM and nitrite for simultaneous analysis of these compounds in food samples. The square-wave voltammograms of AM and nitrite showed two well-separated signals corresponding to the oxidation of AM and nitrite that is sufficient for simultaneous determination of amaranth and nitrite at a surface of 1-M-3-BIBr/CuO/SWCNTs/CPE. The developed electrode achieved dynamic ranges 0.004–750 μM for AM and 1.0–10000 μM for nitrite. The detection LODs of AM and nitrite were 1.0 nM and 0.5 μM, respectively. The same electrode was successfully

applied to the analysis of AM and nitrite in foodstuffs (fruit juice and sausage) by standard addition method.

Based on above discussion, we can conclude that the electrochemical determination of AM is a reliable, simple and cheap method, but further improvement is needed in terms of anti-interference ability, reproducibility, and long-term stability. Therefore, future research on electrochemical detection of AM could be based on these aspects.

CONCLUSION, REMARKS AND OUTLOOK

This paper summarizes recent electrochemical sensors designed to detect AM in foodstuffs. Despite the drastic advancements, some challenges are yet to be tackled in order to commercialize electrochemical sensing technologies and apply to food quality control. Addressing the below-mentioned issues is necessary for the application of electrochemical sensors, particularly for AM analysis. Factors including accuracy and affordability should be seriously considered with novel strategies to overcome the limitations in these aspects.

- Considering the high matrix complexity of food/beverage samples, effective approaches should be developed to suppress the non-specific adsorption of interfering species on the electrode surface. Biofouling is a persistent problem that results in a loss of catalytic activity and negatively affects electrochemical sensor's performance in real samples.

- Development of low-cost fabrication methods for mass production of sensor devices while maintaining the accuracy and precision achieved within a laboratory environment. Additionally, the preparation process should be improved by adopting standardized and controllable manufacturing process ensuring the repeatability between sensor devices.

- Fabrication of inexpensive and durable portable electrochemical sensors.

- Integrated smartphone-based electrochemical sensors are important to accomplish the practical application and commercialization of electrochemical sensors for food safety analysis.

REFERENCES

1. M. G. Corradini, Synthetic Food Colors, in: Encyclopedia of Food Chemistry, L. Melton, F. Shahidi, P. Varelis (eds.), Academic Press, 2019, p. 291.
2. W. Huang, M. Zhang, W. Hu, *Ionics*, **23**, 241 (2017).
3. F. Pogacean, M.-C. Rosu, M. Coros, L. Magerusan, M. Moldovan, C. Sarosi, A.-S. Porav, R.-I. Stefan-van Staden, S. Pruneanu, *J. Electrochem. Soc.*, **165(8)**, B3054 (2018).
4. K. Rovina, S. Siddiquee, S. Shaarani, *Trends Food Sci. Technol.,* **65**, 68 (2017).
5. J. Zhang, M. Wang, C. Shentu, W. Wang, Z. Chen, *Food Chem.*, **160**, 11 (2014).
6. G. Zhang, M. Yadi, *Food Chem.*, **136**, 442 (2013).
7. A. Basu, G. S. Kumar, *J. Hazard. Mater.,* **289**, 204 (2015).
8. Y. Ni, Y. Wang, S. Kokot, *Talanta*, **78(2)**, 432 (2009).
9. H. Wu, J. B. Guo, L. M. Du, H. Tian, C. X. Hao, Z. F. Wang, J. Y. Wang, *Food Chem.,* **141(1)**, 182 (2013).
10. C. F. Tsai, C. H. Kuo, D. Y. C. Shih, *J. Food Drug Anal.*, **23**, 453 (2015).
11. A. P. Patsovskii, N. V. Rudometova, Y. S. Kamentsev, *J. Anal. Chem.*, **59 (2)**, 150 (2004).
12. T. Dodevska, D. Hadzhiev, I. Shterev, *ADMET and DMPK*, **11(2)**, 135 (2023).
13. Y. Gao, L. Wang, Y. Zhang, L. Zou, G. Li, B. Ye, *Talanta,* **168**, 146 (2017).
14. T. Dodevska, I. Shterev, *Monatsh. Chem.*, **151**, 495 (2020).
15. Q. Zhang, W. Cheng, D. Wu, Y. Yang, X. Feng, C. Gao, L. Meng, X. Shen, Y. Zhang, X. Tang, *Food Chem.,* **367**, 130727 (2022).
16. J. A. Buledi, A. R. Solangi, A. Hyder, N. H. Khand, S. A. Memon, A. Mallah, N. Mahar, E. N. Dragoi, P. Show, M. Behzadpour, H. Karimi-Maleh, *Food Chem. Toxicol.*, **165**, 113177 (2022).
17. M. Sheikhshoaie, H. Karimi-Maleh, I. Sheikhshoaie, M. Ranjbar, *J. Mol. Liq.*, **229**, 489 (2017).
18. C. Akkapinyo, K. Subannajui, Y. Poo-arporn, R. P. Poo-arporn, *Molecules*, **26**, 2312 (2021).
19. N. Nuñez-Dallos, M. A. Macías, O. García-Beltrán, J. A. Calderón, E. Nagles, J. Hurtado, *J. Electroanal. Chem.,* **822**, 95 (2018).
20. S. Tajik, H. Beitollahi, H. W. Jang, M. Shokouhimehr, *RSC Adv.*, **11**, 278 (2021).
21. S. Tajik, Y. Orooji, F. Karimi, Z. Ghazanfari, H. Beitollahi, M. Shokouhimehr, R. S. Varma, H. W. Jang, *J. Food Meas. Charact.*, **15**, 4617 (2021).
22. R. Zaimbashi, A. Mostafavi, T. Shamspur, *J. Electrochem. Sci. Eng.,* **12(6)**, 1153 (2022).
23. N. Kajal, V. Singh, R. Gupta, S. Gautam, *Environ. Res.*, **204**, 112320 (2022).
24. S. Z. Mohammadi, Y.-M. Baghelani, F. Mousazadeh, S. Rahimi, M. Mohammad-Hassani, *J. Electrochem. Sci. Eng.,* **12(6)**, 1165 (2022).
25. H. Moradpour, H. Beitollahi, F. G. Nejad, A. Di Bartolomeo, *Materials*, **15**, 3011 (2022).
26. Q. Q. Hu, H. Gao, Y. M. Wang, W. Ma, D. M. Sun, *J. Anal. Chem.,* **73(8)**, 817 (2018).
27. M. Bijad, H. Karimi-Maleh, M. Farsi, S.-A. Shahidi, *Food Anal. Methods,* **10**, 3773 (2017)

Stability of phycocyanin extracted from *Arthrospira platensis* under different conditions

G. Gavrailov[1], V. Y. Andonova[1], A. Ts. Gerasimova[2], G. D. Gentscheva[3], N. Petkova[4], Kr. T. Nikolova[5]*

[1]Department of Pharmaceutical Technologies, Medical University of Varna, Faculty of Pharmacy, 84 Tzar Osvoboditel Blvd., 9002 Varna, Bulgaria

[2] Department of Chemistry, Medical University of Varna, Faculty of Pharmacy, 84 Tzar Osvoboditel Blvd., 9002 Varna, Bulgaria

[3]Department of Chemistry and Biochemistry, Medical University of Pleven, Faculty of Pharmacy,1 Saint Kliment Ohridski Str., 5800 Pleven, Bulgaria

[4]Department of Organic Chemistry and Inorganic Chemistry, University of Food Technologies, Technological Faculty, 26 Maritza Blvd., 4002 Plovdiv, Bulgaria

[5]Department of Physics and Biophysics, Medical University of Varna, Faculty of Pharmacy, 84 Tzar Osvoboditel Blvd., 9002 Varna, Bulgaria

Phycocyanin is a pigment-protein complex widely used in the cosmetic, pharmaceutical, and food industries. A green method was used to extract phycocyanin from *Spirulina* (*Arthrospira platensis*) with the best yield and purity at an ultrasonic frequency of 40 kHz, extraction time of 1 hour, and temperature of 40ºC. The present study aimed to observe phycocyanin's thermal and chemical stability over 1 h. Model buffered solutions of phycocyanin with pH 4.8, 5.8, 6.0, and 7.4 were tested at temperatures 50ºC, 60ºC, and 70ºC. Phycocyanin quantification was performed every 10 minutes. The results showed a first-order kinetic model. For all temperatures, phycocyanin remained stable at pH=4.8 and pH=5.8. At a temperature of 70ºC, its concentration significantly decreased. A strong correlation between the color parameters of the solutions and their concentrations was found. Based on the results, the phycocyanin half-life $t_{50\%}$ in the model systems used was determined.

Keywords: stability of phycocyanin, green extraction methods, *Arthrospira platensis*

INTRODUCTION

Natural pigments from plants, algae, and animals are a desirable alternative to dyes in the pharmaceutical, cosmetic, and food industries. Their application in these industries aims to provide healthier lifestyles to consumers [1]. The phycobiliproteins contained in the cyanobacterium *Arthrospira platensis* and other green algae are divided into four spectroscopic classes by their absorption in the visible range of the spectrum: phycoerythrocyanins, phycoerythrin, phycocyanins, and allophycocyanins [2]. They are natural blue dyes for chewing gums, dairy products, jellies [3], and lipsticks. They are also biomarkers in medicine because of the high relative fluorescence intensity [4]. Phycocyanin is found in *Arthrospira platensis* in the highest concentrations, reaching up to 20% of the dry mass, with a relative molecular weight between 20 and 50 kD [5], containing a protein and a non-protein component [6]. It can be included in medicinal preparations to alleviate and treat condi-

tions associated with inflammation, weakened immunity, or tumor cell development due to oxidative stress [7]. The valuable properties of this pigment lead to its frequent use as an additive in pharmaceutical, cosmetic, and food products. It is water-soluble and can be easily extracted from *Arthrospira platensis* as a protein-pigment complex. The main problem with this pigment is its protein nature. Like all proteins, phycocyanin is sensitive to certain temperatures and pH levels. The presence of a chromophore in its structure also makes it photosensitive [8].

A number of authors indicate that phycocyanin is insoluble in acidic environments with pH levels below 3.0 and highly soluble in neutral environments with pH levels around 7.0 [9]. It is unstable in the pH range of 4 to 4.5, located near the isoelectric point of the indicated protein (at pH = 3.4) [10]. Due to the reduced electrostatic repulsion around that point, aggregation and precipitation are enhanced.

---

* To whom all correspondence should be sent:
E-mail: *kr.nikolova@abv.bg*

A team of scientists from the Central Food Science and Technology Research Institute, Mysore, India, investigated the stability of phycocyanin at pH ranging from 2.5 to 13 using different buffers at both room temperature (25±2°C) and low temperature (9±1°C). Temperature stability was investigated at 10, 30, 45, and 55°C by incubating the samples in a water bath while maintaining the appropriate temperature. Stability studies at different pH levels over a period of 4 weeks showed that phycocyanin was stable in the pH range 5-7.5 at ambient temperature (25±2°C) and low temperature (9±1°C). The effect of temperature on the stability of phycocyanin shows that it is precarious at 45°C and above [11].

These studies show that phycocyanin is unstable at the acidic pH of the stomach, and enteric-coated dosage forms need to be prepared to increase drug release and its bioavailability.

The present study aimed to investigate the effects of different temperatures and pH levels on the chemical stability of phycocyanin with respect to its potential inclusion in oral dosage forms and nutritional supplements.

MATERIALS AND METHODS

Materials

The present study used *Arthrospira platensis* grown in a bioreactor in Bulgaria's Varvara region to extract phycocyanin. All chemicals and reagents (acetic acid and its sodium acetate salt, hydroxymethylaminomethane hydrochloride, hydroxymethylaminomethane, and sodium chloride) required for the preparation of the buffers were purchased from Merck, Germany.

To increase the purity and yield of phycocyanin without the need for further purification, ultrasonic extraction was performed. 2 g of *Arthrospira platensis* was weighed into 50 mL test tubes with caps, and the extraction was carried out in distilled water (1:25 w/v) using a VWR ultrasonic bath (Malaysia) at 45 kHz, power 30W (UAE 45 kHz). The extracts were filtered through a paper filter and then prepared for analysis.

Preparation of buffer solutions

The thermal stability of phycocyanin was tested by preparing buffer solutions of different acidity and of the indicated substance (1 mg/mL). Acetate buffers with pH levels of 4 - 7 were prepared from weak acetic acid and sodium acetate salt. Buffer systems with pH levels of 4.8, 5.8, and 6.0 were prepared. The buffer solution with physiological pH level of 7.4 was prepared by using hydroxymethylaminomethane hydrochloride

(0.2313 g), hydroxymethylaminomethane (0.0282 g), and sodium chloride (0.7540 g) for volume 100 mL. Acetic acid and sodium acetate salt concentrations are 0.1 mol/L. The mixing ratio of salt to acid is as follows: pH=4.8 (1:1); pH=5.8 (10:1); pH=6.0 (15.5:1).

Spectrophotometric evaluation of phycocyanin content

The phycocyanin content of the solutions was determined spectrophotometrically (Thermo Science, USA) according to the formulas:

$$Cphycocyanin \left(\frac{mg}{mL}\right) = \frac{A_{620nm} - 0.474.A_{652nm}}{5.34}, \quad (1)$$

$$Alophycocyanin \left(\frac{mg}{mL}\right) = \frac{A_{652} - 0.208 * A_{620}}{5.09} \quad (2)$$

A_{620nm} is the optical density of the sample at the wavelength characterizing the absorption maximum of phycocyanin, and A_{652nm} is the optical density of the sample characterized as the absorption length for phycoerythrin.

The concentration of phycocyanin was determined as the sum of the values from formulas (1) and (2) [12, 13].

Determination of phycocyanin degradation kinetics

The degradation kinetics of phycocyanin were studied under "stress" conditions at 50°C, 60°C, and 70°C and pH levels of 4.8, 5.8, 6.0, and 7.4. After spectrophotometric determination of the initial concentration of phycocyanin in the respective buffer solution (pH 4.8, 5.8, 6.0, and 7.4) at 25°C, 6 equal parts of it were placed in closed flasks which were tempered in a water bath (50°C, 60°C and 70°C) for 1 hour. The chemical degradation of phycocyanin in the buffer solutions was studied spectrophotometrically by reading the absorbance at the indicated wavelengths in formulas (1) and (2) every 10 minutes at the respective temperatures for an hour.

Determination of degradation rate constant

That constant can be determined from the integral form of the following differential equation describing a first-order reaction:

$$\frac{dC}{C} = -k. dt, \quad (3)$$

where: C is phycocyanin concentration (mg/mL); k is the constant of degradation rate (min^{-1}); t is time (min).

The half-life of phycocyanin under various conditions was determined from equation (4) [14, 15].

$$t_{1/2} = ln (2)/k \quad (4)$$

The relative concentration (C_R, %) of phycocyanin at each combination of external factors (pH, temperature, and time) was determined. C_R is the remaining phycocyanin concentration as a percentage of its initial concentration in the respective buffer.

$$C_R, \% = \frac{c}{c_0} \times 100 \qquad (5)$$

Colorimetric measurements

Using VISIONlite ColorCalc software, the color parameters of the samples were determined using a spectrophotometer (Thermo Fisher, USA). The samples were in a buffer solution of concentration 0.01 mg/ mL .

Statistical analysis

All results were obtained by three parallel analyses. Table 1 showя the mean results ± the standard deviation of the measurement using Excel and Anova.

RESULTS AND DISCUSSION

Phycocyanin degradation kinetics and determination of degradation rate constant

The pH levels of the solvents used are one of the most important factors related to the stability of phycocyanin. In the present study, the stability of the substance in acetate buffer was determined by spectroscopy in the visible range, and the optimal pH range for its stability was found.

The relative protein concentration was determined for each of the three temperatures at four different pH levels for 60 min. The results are presented in Figure 1.

After applying linear regression models using the Origin Pro 2015 software product, phycocyanin degradation was found to be of first-order. All coefficients of determination are above 0.87. The half-life and rate constant results at different temperatures and pH levels were calculated

according to correlations (3) and (4) and are presented in Table 1.
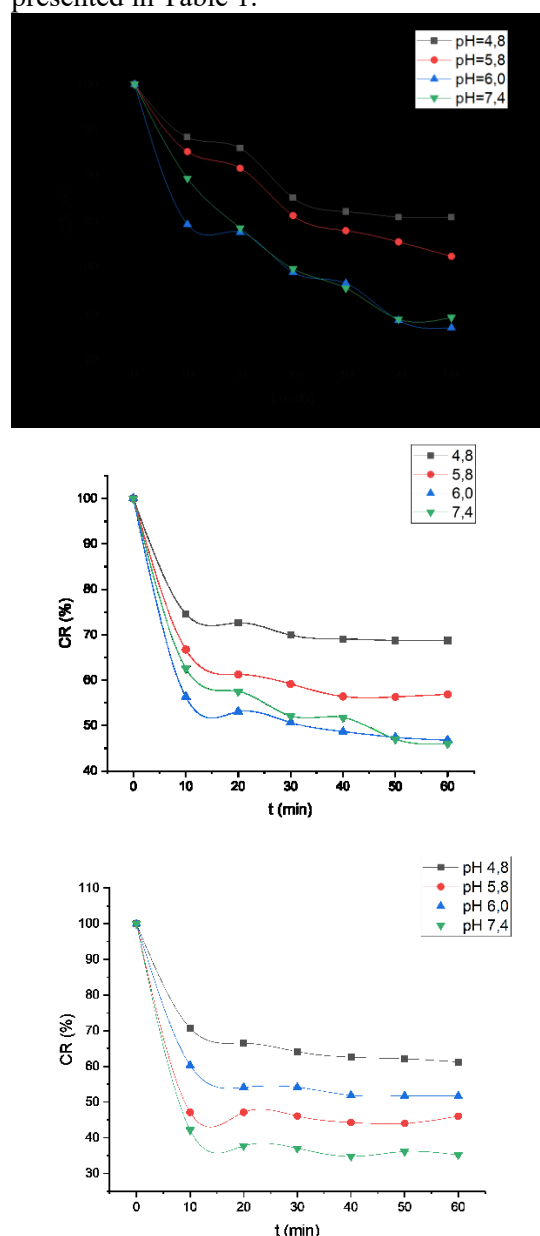
Figure 1. Effect of pH on the stability of phycocyanin in acetate buffer at A: 50°C, B: 60°C, C: 70°C.

Table 1. Degradation rate and half-life values of phycocyanin at 50 °C, 60 °C, 70 °C and pH 4.8, 5.8, 6.0, 7.4.

T,^{0}C	pH=4.8		pH=5.8		pH=6.0		pH=7.4	
	$k \pm SD$, min^{-1}	$\tau_{1/2} \pm SD$, min	$k \pm SD$, min^{-1}	$\tau_{1/2} \pm SD$, min	$k \pm SD$, min^{-1}	$\tau_{1/2} \pm SD$, min	$k \pm SD$, min^{-1}	$\tau_{1/2} \pm SD$, min
50	0.0029 ± 3.10^{-4}	239.02 ± 3.2	0.00583 ± 4.10^{-4}	119.51 ± 2.7	0.004 ± 2.2.10^{-4}	173.2 ± 5	0.0059 ± 1.10^{-4}	117.48 ± 4.4
60	0.0083 ± 7.10^{-4}	83.51 ± 4.7	0.0123 ± 2.10^{-4}	55.90 ± 1.9	0.0165± 7,9.10^{-4}	42.01 ± 2.3	0.0160 ± 2.10^{-4}	43.32 ± 2.1
70	0.0101 ± 10.10^{-4}	68.63 ± 1.4	0.0182 ± 9.10^{-4}	38.09 ± 3.2	0.0235± 8.10^{-4}	46.83 ± 2.3	0.0235 ± 5.10^{-4}	29.5 ± 1.9

The degradation of phycocyanin at 50°C is very slow. Its half-life at 50°C and pH 4.8 is 239.02 min. At 60°C, the degradation rate increases dramatically, and the half-life decreases up to 3 times for different pH levels. With the increase in temperature, the half-life decreases. According to the data in Table 1, the half-life of phycocyanin is most extended at 50°C and pH 4.8 – 239.02 min and shortest at 70°C and pH 7.4 – 29.5 min. Other authors have reported similar results. Chaiklahan *et al.* stated that at pH 5.0, 6.0, 7.0, and temperature 51°C, the half-lives were 62 min, 167 min, and 108 min, respectively [3]. Our results at pH 6.0 and 7.4 are close to those shown, but at pH 4.8, they are about 4 times higher. That might have happened because:

✓ In the above study the information was obtained using citrate-phosphate buffer, whereas in the present study acetate buffer was used;

✓ the stability of phycocyanin depends very much on the strain of *Spirulina* from which it is extracted [16].

At 70°C, protein denaturation is accelerated. A similar result was reported in [17, 16]. Accordingly, phycocyanin was more stable at pH levels of 5.0 to 6.0 since the hexameric form of phycocyanin predominates in this pH range [18]. Significantly longer half-lives in the present study were found at a temperature of 70°C relative to other sources. At the indicated temperature and pH 4.8, 6.0, and 7.0, the half-life was 68.6 min, 46.8 min, and 29.5 min, respectively. Carle and Schweiggert, 2016 at the same temperature and pH of 5.0, 6.0, and 7.0, indicated half-lives of 7.5 min, 14.5 min, and 6.0 min, respectively [19].

The following can be concluded from the study of temperature-dependent phycocyanin degradation.

✔At 50°C, degradation occurs slowly, and the relative amount of undegraded phycocyanin decreases in an average of 30 minutes at different pH levels from 10% to 13% relative to the original quantity.

✔At 60°C, the relative amount of undegraded phycocyanin decreases in 30 minutes at different pH levels from 40% to 50% relative to the original quantity.

✔At 70°C, the reduction is 40% to 70% from the original quantity under the abovementioned conditions.

In addition to temperature, protein denaturation depends on the pH of the environment. Phycocyanin was most stable at a pH of 5.0-6.0 and a temperature of 50°C (the decrease in relative concentration in 60 minutes was from 13% to 19%), and at a temperature

of 60°C (the decrease in the relative amount of undegraded phycocyanin in 60 minutes was from 30% to 60%). The protein is unstable at pH 7.4 and temperatures of 60°C and 70°C. Therefore, pH values significantly control phycocyanin's aggregation and dissociation processes to monomers, trimers, hexamers, and oligomers. The hexameric structure of the protein is known to be protected from denaturation.

Table 2. Estimated values of k and $t_{1/2}$ at 25°C and 37°C.

t = 25 °C	pH = 4.8	pH = 5.8	pH = 6.0	pH = 7.4
k	0.0012	0.0005	0.0004	0.0009
$\tau_{1/2}$, min	599.54	1275.90	1907.47	788.79
t = 37 °C	pH = 4.8	pH = 5.8	pH = 6.0	pH = 7.4
k	0.0027	0.001343	0.001312	0.0024
$\tau_{1/2}$, min	260.25	516.0	528.46	290.10

Colorimetric measurements

A linear regression dependence was demonstrated with correlation coefficients above 0.9 between luminosity and relative phycocyanin concentration. Figure 2 shows 3D graphs of luminosity's dependence on pH and time for the three temperatures [20]. The latter better explains the stability at pH 4.8 and 6.0 at 50°C and 60°C. A similar fact was reported by Adams *et al.*, who found that at pH 6.0, the trimeric form is about 23% of the protein, and the remainder is hexameric [21]. At pH 6.0, 50°C, and 70°C, phycocyanin is more stable than at pH 5.8. But at 60°C, it is more stable at pH 5.8 compared to pH 6.0. This fact is also confirmed by Antelo *et al.* [9]. Several other authors confirm our study's findings [3, 22]. The stability of phycocyanin is due to the hexameric structure resulting from linking the monomers into a ring trimer [23]. The monomers consist of two polypeptides: alpha (α) – linked to one phycocyanobilin, and beta (β) – related to two phycocyanobilins [23]. At pH levels around 2, the protein does not dissolve even after homogenization. The fact is explained by the cyclic conformation and folding of the chromophore [24, 25]. At pH 3.0, phycocyanin precipitates and denatures. At pH 4.0, the solution with the indicated protein is turbid.

The degradation of phycocyanin under different factors is associated with the loss of color of the solutions. Color is one of the primary sensory characteristics that consumers evaluate when choosing food and food supplements. To assess the color degradation, transmission and absorption spectra measurements were made, and color parameters such as lightness (L), color coordinates (a), and (b) were determined in the CIELab small color difference colorimetric system.
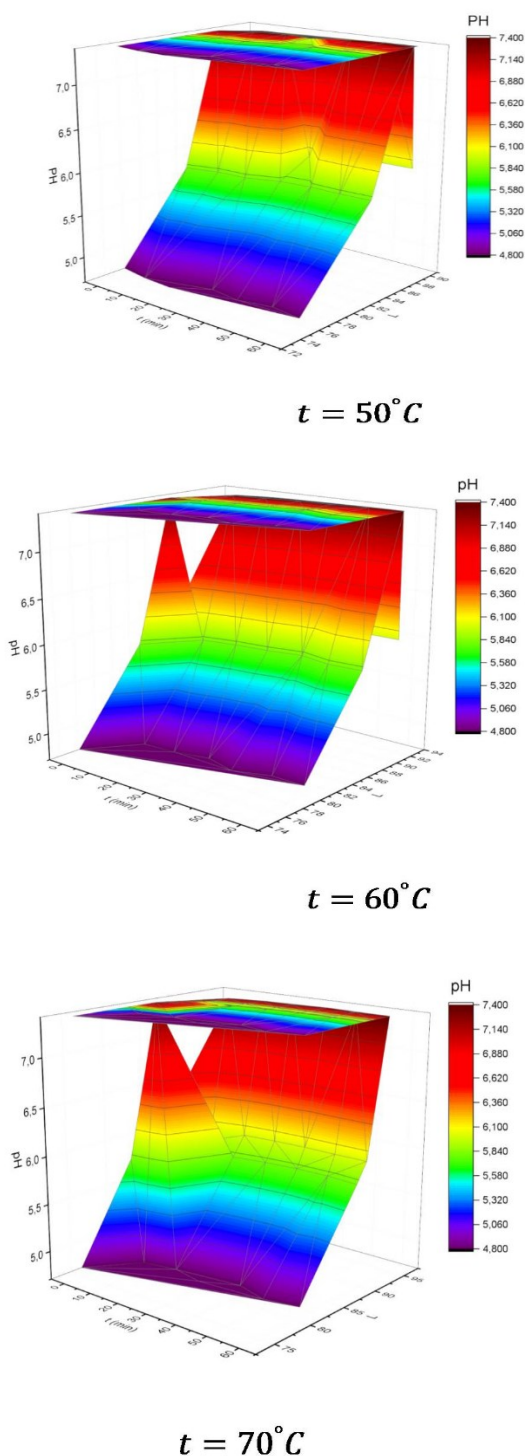

$t = 50°C$

$t = 60°C$

$t = 70°C$

Figure. 2. Dependence of luminosity of phycocyanin solutions on pH and time at different temperatures.

A linear regression relationship with correlation coefficients above 0.9 between lightness and relative phycocyanin concentration is demonstrated. Figure 2 shows 3D plots of the dependence of luminosity on pH and time for each of the three temperatures. The temperature-increasing degradation of phycocyanin appears after 40 minutes as decreasing color density at pH 6.0 and 7.4.

CONCLUSION

The optimal conditions for incorporating phycocyanin into food products and food additives under which it remains stable are in the temperature range from room temperature up to about 50°C and at pH 4.5 to 5.5. There is a linear correlation between luminosity and relative concentration of phycocyanin.

REFERENCES

1. E. N. Dewi, R. AyuKurniasih, and L. Purnamayanti, *Philippine Journal of Science*, **147** (2), 201 (2018).
2. J. Abalde, L. Betancourt, E. Torres, A. Cid, C. Barwell, *sp. IO9201, Plant Sci*., **136**, 109 (1998).
3. R. Chaiklahan, N. Chirasuwan, B. Bunnag, *Process Biochem*, **47**, 659 (2012).
4. S.T. Silveira, J.F.M. Burkert, J.A.V. Costa, et al., *Bioresour. Technol*., **98**, 1629 (2007).
5. H. M. Patel, R. P. Rastogi, U. Trivedi, D. Madamwar, *Algal Research*, **32**, 372 (2018).
6. B. Fernández-Rojas, J. Hernández-Juárez, J. Pedraza-Chaverri, *Journal of Functional Foods*, **11**, 375 (2014).
7. J.P. Kehrer, L. O. Klotz, *Crit. Rev. Toxicol*., **45**, 765 (2015).
8. M. Wan, H. Zhao, J. Guo, L. Yan, D. Zhang, W. Bai, Y. Li, *Algal Research*, **58**, 102391 (2021).
9. F. S. Antelo, J. A. V. Costa, S. J. Kalil, *Biochem. Eng. J.* **41** (1), 43 (2008).
10. L. Y. Zhang, Z. Abbaspourrad, *Food Hydrocolloids*, **119**, 106852 (2021).
11. R. Sarada, M. G. Pillai, G. A. Ravishankar, *Process Biochemistry*, **34**, 795 (1999).
12. A. Bennett, L. Bogorad, *J. Cell Biol*., **58**, 419 (1973).
13. A. Patel, S. Mishra, R. Pawar, P. K. Ghosh, *Protein Exp. Purif*., **40**, 248 (2005).
14. A. Patel, R. Pawar, S. Mishra, S. Sonawane, P.K. Ghosh, *Indian J. Biochem. Biophys*., **41**, 254 (2004).
15. N. Koca, F. Karadeniz, H. S. Burdurlu, *Food Chem*., **100**, 609 (2006).

16. H.-L. Wu, G. H. Wang, W. Z. Xiang, et al., Int. *J. Food Prop*., **19,** 2349 (2016).
17. L. Bocker, S. Ortmann, J. Surber, *Food Sci. Emerg. Technol*., **52**, 116. e121 (2019).
18. D. P. Jaeschke, I. R. Teixeira, L. Damasceno, F. Marczak, G. D. Mercali*, Food Research International*, **143**, 110314 (2021).
19. R. Carle, R. M. Schweiggert, (eds.), Food Color. Duxford, UK, Woodhead Publishing, 2016.
20. O. H. W. Kao, M. R. Edwards, D. S. Berns*, Biochem J*., **147**, 63 (1975).
21. S. M. Adams, O. H. W. Kao, D. S. *Berns, Plant. Physiol.,* **64**, 525 (1979).
1. H.-L. Wu, G.-H. Wang, W.-Z. Xiang, et al., *Int. J. Food Prop*., **19**, 2349 e2362 (2016).
22. B. Yuan, Z. Li, H. Shan, B. Dashnyam, X. Xu, D. J. McClements, B. Zhang, M.Tan, Z. Wang, C. Cao, *Curr. Res. Food Sci*., **5**, 2329 (2022).
23. M. F. Falkeborg, M. C. Roda-Serrat, K. L. Burnæs, et al*., Food Chem*. **239**, 771 e780 (2018).
24. M. Debreczeny, Z. Gombos, V. Csizmadia, et al*., Biochem. Biophys. Res. Commun.,* **159**, 1227 e1232 (1989).

The effects of NaCl, KCl, CaCl$_2$ and MgCl$_2$ on the germination and seedling growth of *Oryza sativa* L. seeds

G. N. Desheva[*], S. A. Tosheva, E. K. Valchinova, A. D. Pencheva

Agricultural Academy, Institute of Plant Genetic Resources, 2 Druzhba Str., 4122 Sadovo, Bulgaria

The effect of increasing concentrations (50, 100, 150, 200, 250, 300 mM) of chloride salts (NaCl, KCl, CaCl$_2$ and MgCl$_2$) on the seed germination and seedling characteristics in the early growing stage was investigated during the period 2021-2022. The seeds of five introduced varieties grown on alluvial-meadow soil type in the territory of the town Plovdiv, Bulgaria were used. The trials were performed in two replicates of 25 seeds for each variant. Germination of seeds was performed between rolls of filter paper with 20 ml of the respective solutions tested. Different chloride salts and their concentrations caused different effects on the studied germination and seedling characteristics. Rice seeds showed a higher germination rate under salinity stress caused by NaCl and KCl than under stress caused by CaCl$_2$ and MgCl$_2$. Increasing the salt concentration extended the mean germination time for all four salts. The highest value of the relative injury coefficient was recorded when rice seeds were treated with MgCl$_2$ at salt concentrations of 150, 200, 250 and 300 mM, as well as when treated with CaCl$_2$ at a concentration of 300 mM. The seedling height reduction varied widely from 14.10% (at 50 mM NaCl) to 100% (at 250 mM and 300 mM MgCl$_2$, 300 mM CaCl$_2$). In general, the application of increasing concentrations of NaCl and KCl salts from 50 mM to 300 mM caused an osmotic stress on rice seeds, while CaCl$_2$ at 300 mM and MgCl$_2$ at 250-300 mM solutions caused a toxicity effect.

Keywords: rice, chloride salts, seed germination, tolerance

INTRODUCTION

Salinization is one of the major abiotic environmental factors globally limiting plant growth and development [1, 2]. The main causes of salinization are rising groundwater levels with high salt sontent, poor quality of drainage irrigation systems, excessive use of fertilizers, high temperatures coupled with increased evaporation as a result of changing climate [3, 4]. Although it is difficult to determine the exact value, the area of salinized soils is increasing, and this phenomenon is particularly intense in irrigated lands. It is estimated that about 20% of irrigated areas producing one-third of the world's food is affected by salinization [5, 6]. Salinization, on the one hand, causes osmotic stress (a decrease in external water potential) that compromises the plant's ability to take up water and, on the other hand, leads to ionic imbalance, also called ionic stress [7, 8]. Harmful effects of high saltinization can be detected throughout the life cycle from inhibition or delay of seed germination to plant death [9].

In general, saline soils consist of different water-soluble salts and exchangeable Na+ with different effects on seed germination. Different crops show specific germination patterns in saline environments [10, 11].

Rice is a soil salinity-sensitive crop and its sensitivity is variable at different stages of growth and development. It is strongest during germination and up to full rooting of plants [12]. Flowering is the other very sensitive stage of crop development. Salinization during pollination and fertilization leads to sterility [13].

The objective of this study was to determine the effect of different concentrations of chloride salts (NaCl, KCl, CaCl$_2$ and MgCl$_2$) on seed germination and growth parameters of rice.

MATERIALS AND METHODS

The effect of six levels (50, 100, 150, 200, 250, 300 mM) of salinization with chloride salts (NaCl, KCl, CaCl$_2$, and MgCl$_2$) on seed germination and early seedling growth parameters in 5 introduced rice cultivars were investigated in 2021 and 2022. Seeds were collected from a comparative variety of trials established in the region of Plovdiv, Bulgaria on alluvial-meadow soil type. Two replicates of 25 seeds were set for each experimental variant. Germination was carried out in a growth chamber between rolls of filter paper with 20 ml of the respective test solutions at a temperature of 25 ± 1°C, for 14 days. Seeds were counted as germinated when the germ has reached at least 2 mm.

---

* To whom all correspondence should be sent:
E-mail: *gergana_desheva@abv.bg*

The number of germinated seeds was registered every day until a consistent number was achieved. The following characteristics were calculated: germination (G, %), germination index (GI), mean germination time (MGT, day) and relative injury rate (RIR). GI and MGT were calculated according to Al-Mudaris [14], while RIR according to Li [15]. On the fourteenth day of the experiment, ten seedlings were randomly selected from each treatment with the chloride salts, for measurement of length of the shoot (ShL, cm) and root (RL, cm). Seed vigor index (VI) was calculated using the equation of Abdul-Baki and Anderson [16]. Seedling height reduction (%) was established according to Islam & Karim [17], while Salt Tolerance (ST) - according to Mujeeb-ur-Rahman *et al.* [18]. Mean data from the two-year experiment were analyzed by using ANOVA and Duncan's multiple range test and SPSS22.0 software was used for statistical data processing.

RESULTS AND DISCUSSION

Salinity influences the seed germination *via* osmotic stress, specific ionic effects and oxidative stress, which is reflected in a decrease in germination rate and an elongated germination time [19]. The *Oryza sativa* seeds responded differently at specific chloride salts concentrations, as shown in Table 1. Maximum germination (between 98.20% and 99.80%) occurred in the non-saline treated seeds (control). Rice seeds showed a higher germination rate under salinity stress caused by NaCl and KCl than under stress caused by CaCl$_2$ and MgCl$_2$. The lowest germination was recorded in seeds treated with 250 mM CaCl$_2$ (16.40%), while at high salinity levels of 300 mM CaCl$_2$, no germinated seeds were recorded. On the other hand, at medium salinity levels in the range of 150 - 200 MgCl$_2$ on the 14th day of seed setting for germination, abnormally germinated seeds characterized by poorly developed shoots and absence of any root system were observed in all tested cultivars, while at high MgCl$_2$ concentrations (250 - 300 mM MgCl$_2$) all seeds were dead (Table 1). Therefore, NaCl and KCl at 50 - 300 mM solutions, CaCl$_2$ at 50 - 250 mM solutions and MgCl$_2$ at 50 - 200 mM solutions caused osmotic stress on rice seeds, while CaCl$_2$ at 300 mM and MgCl$_2$ at 250 - 300 mM solutions caused a toxicity effect.

According to Stefanello *et al.* [20], the accumulation of high salt concentrations in cells can deactivate enzymes, inhibit protein synthesis, and prevent seed germination. Barichello *et al.* [21]

stated that excess salts cause cytotoxicity and dehydration of cells, which reduces metabolic activity and synthesis of new tissues in the seeds due to low water availability. On the other hand, Liu *et al.* [22] demonstrated in their study that salinity suppresses rice seed germination by reducing the bioactive gibberellin GA content as a result of increasing the inactivation of bioactive GAs. Furthermore, deficiency of bioactive GA inhibited seed germination by reducing α-amylase activity through down-regulation of α-amylase gene expression. Many authors [6, 22-27] also confirmed that NaCl treatment significantly inhibited seed germination and noted a wide variation in germination and growth parameters among studied rice varieties due to different levels of salt applications. Kalhori *et al.* [6] while investigating the effect of four different salts on seed germination and morphological characteristics of *Oryza sativa* L. also found that NaCl, KCl, MgCl$_2$ and MgSO$_4$ had a negative effect on seed germination. They found that among the four salts, NaCl provided better germination even at the highest salinity level of 250 mM. On the other hand, rice seeds under KCl and MgCl$_2$ germinated less at the highest salinity level, suggesting that the cultivar studied has low tolerance to high salinity levels of these salts.

Salinity had a significant increasing effect on the germination time to a defined level. Increasing the salt concentration extended the mean germination time for all four salts. The highest mean germination time was recorded from seeds treated with 300 mM NaCl (9.63 days), following with 300 mM KCl (8.71 days). Differences from the control variants were statistically proven at p≤0.05. In the experiments with CaCl$_2$ and MgCl$_2$, the most significant differences to the controls were found at 200 mM CaCl$_2$ and at 100 mM MgCl$_2$ (Table 1). Momayezi *et al.* [28] also reported on prolongation of mean germination time in treatments with over 5 dSm[1] NaCl. Kalhori *et al.* [6] noted that the increase in mean germination time is more pronounced at higher salinity levels of NaCl, KCl, MgCl$_2$ and MgSO$_4$. Higher GI values were recorded for the controls and at the lowest concentration of the four salts, indicating a higher percentage and degree of seed germination in the batch studied. As the salt concentrations increased, the GI values significantly decreased, with the lowest value recorded for the CaCl$_2$ variant at a concentration of 250 mM. At the highest concentration, the GI varied in very close values when salting with NaCl and KCl solutions (251.40 and 249.40, respectively) (Table 1).

Table 1. Effect of different chloride salts and their concentrations on germination (G, %), mean germination time (MGT, day) and germination index (GI) of *Oryza sativa* seeds.

Germination (G, %)				
Salinity	NaCl	KCl	CaCl$_2$	MgCl$_2$
0 mM	99.80cA	99.20cA	98.20dA	98.80bA
50 mM	98.80cB	98.80cB	94.60dA	98.40bB
100 mM	98.40cB	98.20cB	93.00dA	97.40bB
150 mM	95.50cC	97.20cC	87.60dB	0.00aA
200 mM	85.70cC	91.40cC	69.40cB	0.00aA
250 mM	71.50bB	72.20bB	16.40bA	0.00aA
300 mM	38.50aB	35.60aB	0.00aA	0.00aA
Mean	84.03	84.66	65.60	42.09
Mean germination time (MGT, day)				
Salinity	NaCl	KCl	CaCl$_2$	MgCl$_2$
0 mM	2.76aB	2.49aAB	2.06bA	2.07bA
50 mM	3.54abB	3.08aAB	2.77bcA	2.97cAB
100 mM	4.18bcB	4.02bAB	3.45cA	3.71dAB
150 mM	4.76cB	4.66bB	4.35dB	0.00aA
200 mM	6.31dB	5.70cB	5.53fB	0.00aA
250 mM	8.02eB	6.75dB	0.00aA	0.00aA
300 mM	9.63fC	8.71eB	0.00aA	0.00aA
Mean	5.60	5.06	2.76	1.25
Germination index (GI)				
Salinity	NaCl	KCl	CaCl$_2$	MgCl$_2$
0 mM	2.76aB	2.49aAB	2.06bA	2.07bA
50 mM	3.54abB	3.08aAB	2.77bcA	2.97cAB
100 mM	4.18bcB	4.02bAB	3.45cA	3.71dAB
150 mM	4.76cB	4.66bB	4.35dB	0.00aA
200 mM	6.31dB	5.70cB	5.53fB	0.00aA
250 mM	8.02eB	6.75dB	0.00aA	0.00aA
300 mM	9.63fC	8.71eB	0.00aA	0.00aA
Mean	5.60	5.06	2.76	1.25

Means within a column that have different lowercase letters (a-f) are significantly different from each other (Duncan's multiple range test, P≤0.05). Means within a row that have different uppercase letters (A-C) are significantly different from each other (Duncan's multiple range test, P≤0.05).

Table 2. Effect of different chloride salts and their concentrations on the Relative Injury Rate of *Oryza sativa* seeds.

Relative Injury Rate (RIR)						
Salinity	50 mM	100 mM	150 mM	200 mM	250 mM	300 mM
NaCl	0.010 a	0.014a	0.043a	0.142a	0.285a	0.615a
KCl	0.006a	0.012a	0.022a	0.080a	0.272a	0.642a
CaCl$_2$	0.038b	0.054b	0.109b	0.296b	0.834b	1.000b
MgCl$_2$	0.004a	0.014a	1.000c	1.000c	1.000b	1.000b
Mean	0.015	0.024	0.294	0.380	0.598	0.814

Means within a column that have different lowercase letters (a-c) are significantly different from each other (Duncan's multiple range test, P≤0.05).

Decreases in germination index with increasing NaCl salinity levels in rice were also confirmed by Pradheeban *et al*. [23] and Ologundudu *et al*. [29].

The relative injury rates for each salt type with respective salinity levels are presented in Table 2. The highest values of the relative injury coefficients were recorded when rice seeds were treated with MgCl$_2$ at concentrations of 150 - 300 mM salt, as well as when treated with CaCl$_2$ at a concentration of 300 mM. Our results are consistent with those obtained by Kalhori *et al.* [6] who observed the serious injure at 200 mM salt concentration of MgCl$_2$ treatments. At the low concentrations of 50 - 100 mM the greatest damage was found when seeds were treated with a CaCl$_2$ solution. NaCl and KCl salts

caused a lower relative degree of damage compared to the other two salts.

The four types of salts had different effect on the growth on *Oryza sativa* seedlings. Shoot, root and total length of rice seedlings decreased with the increase in the salt concentrations in all variants of salinity stress. $CaCl_2$ and $MgCl_2$ salts induced significantly greater negative effect on these variables when compared to NaCl and KCl (Table 3). At the lowest concentration of 50 mM of the studied salts, the greatest ShHR was observed for the $CaCl_2$ variant (36.92%) and in terms of RHR - for the $MgCl_2$ variant (51.50%), but the differences in values compared to the $CaCl_2$ variant were not statistically significant. At the highest concentration of 300 mM the NaCl and KCl salts caused a suppressive effect expressed by a reduction in shoot and root height between 89.90% and 95.25% for shoot and 95.68 - 96.59 % for root, respectively. $CaCl_2$ and $MgCl_2$ salts had a toxic effect on shoot and root growing. On an average, over the whole experiment, the inhibitory effects of the different chloride salts and their concentrations were higher on the root than on the shoot. Kumari *et al.* [30] in his experiment found that under different salt stress (0 - 2.5%) created by a salt mixture of NaCl, $CaCl_2$, and Na_2SO_4 in a 7:2:1 ratio, the rice root growth was more affected than the shoot growth.

The seedling height reduction widely varied from 14.10% (at 50 mM NaCl) to 100% (at 250 mM and 300 mM $MgCl_2$, 300 mM $CaCl_2$) (Table 5). Our findings are in agreement with the results obtained by Kalhori *et al.* [6], who noted that the rice seedling height is less affected by NaCl treatment at 50-250 mM salinity levels as least reduction percentages were recorded at all NaCl concentrations. Reduction of shoot/root lengths with increasing salinity in rice was also reported by other workers [23, 26, 27, 31-34].

Vigor index represents the germination capacity and growing tendency of the seedling. The vigor of *Oryza sativa* seeds was significantly different when treated by four salinities at different concentrations (Table 4). The vigor indices were significantly reduced as salinity increased. In NaCl and KCl salinity, stress indices were higher than in $CaCl_2$ and $MgCl_2$ salinity stress. The highest vigor indices were recorded in 50 mM NaCl and 50 mM KCl, followed by 100 mM NaCl and 100 mM KCl. This result indicated that the capacity of germination and growing tendency of rice seed was higher when germinated in 50-100 mM NaCl and KCl. Diaguna *et al.* [33] stated that the differences in vigor index and germination percentage at salinity of 2000, 4000 and 6000 ppm of NaCl are due to osmotic stress from salinity which inhibits rice germination. The results obtained by Yousof [35] also indicated that $CaCl_2$ salinity levels (9 dS/m) delayed germination, seed and seedling vigor characters compared with normal salinity (0.3 dS/m).

Table 3. Effect of different chloride salts and their concentrations on the shoot, root and seedling height reductions of *Oryza sativa* L. seeds.

Shoot Height Reduction (ShHR, %)						
Salinity	50 mM	100 mM	150 mM	200 mM	250 mM	300 mM
NaCl	15.17a	38.90b	67.62ab	82.02a	88.09a	95.25b
KCl	19.19a	38.82a	59.71a	80.58a	87.12a	89.99a
CaCl₂	36.92b	61.83b	73.59b	84.93a	98.64b	100.00c
MgCl₂	21.58a	61.01b	72.44b	84.90a	100.00b	100.00c
Mean	23.22	50.14	68.34	83.11	93.43	96.31
Root Height Reduction (RHR, %)						
Salinity	50 mM	100 mM	150 mM	200 mM	250 mM	300 mM
NaCl	12.34a	26.34a	52.76a	72.07a	87.11a	95.68a
KCl	13.65a	28.96a	59.79b	84.29b	93.01b	96.59a
CaCl₂	49.11b	80.97b	92.72c	96.22c	99.78c	100.00b
MgCl₂	51.50b	90.48c	100.00d	100.00d	100.00c	100.00b
Mean	31.65	56.69	76.32	88.15	94.98	98.07
Seedling Height Reduction (SHR, %)						
Salinity	50 mM	100 mM	150 mM	200 mM	250 mM	300 mM
NaCl	14.10a	31.50a	58.80a	76.20a	87.50a	95.00a
KCl	16.30a	33.10a	60.60a	83.20b	90.70b	94.10a
CaCl₂	44.00b	73.00b	84.90b	91.60c	99.40c	100.00b
MgCl₂	38.10b	77.00b	87.60b	93.20c	100.00c	100.00b
Mean	28.13	53.65	72.98	86.05	94.40	97.28

Means within a column that have different lowercase letters (a-d) are significantly different from each other (Duncan HSD test, P≤0.05).

Table 4. Effect of different chloride salts and their concentrations on the vigor index of *Oryza sativa* L. seedser

Vigor index (VI)				
Salinity	NaCl	KCl	CaCl₂	MgCl₂
0 mM	1786.59fB	1698.91fB	1220.57eA	1249.54dA
50 mM	1514.06eB	1406.98eB	647.49dA	764.11cA
100 mM	1200.13dB	1121.36dB	305.844cA	274.34bA
150 mM	681.99cC	645.04cC	157.15bB	70.03aA
200 mM	364.32bC	263.55bB	69.51aA	31.84aA
250 mM	161.60aC	112.40abB	7.18aA	0.00aA
300 mM	39.73aB	37.61aB	0.00aA	0.00aA
Mean	821.20	755.12	343.96	341.41

Means within a column that have different lowercase letters (a-f) are significantly different from each other (Duncan's multiple range test, P≤0.05). Means within a row that have different uppercase letters (A-C) are significantly different from each other (Duncan's multiple range test, P≤0.05).

Table 5. The mean salt tolerance indices of rice at germination and early seedling stage

Germination salt tolerance index							
Salinity	50 mM	100 mM	150 mM	200 mM	250 mM	300 mM	Mean
NaCl	99.00b	98.59b	94.88c	86.61c	71.54b	38.50b	81.5212
KCl	99.60b	99.00b	97.99c	92.15c	72.78b	35.94b	82.9115
CaCl₂	96.23a	94.60a	89.06b	70.45b	16.56a	0.00a	61.1497
MgCl₂	99.59b	98.76b	0.00a	0.00a	0.00a	0.00a	33.0575
Mean	98.60	97.74	70.48	62.30	40.22	18.61	64.6600
Seedling salt tolerance index							
Salinity	50 mM	100 mM	150 mM	200 mM	250 mM	300 mM	Mean
NaCl	86.27b	68.66b	41.33b	24.28c	12.82c	5.08b	39.74
KCl	83.72b	66.92b	39.44b	16.93b	9.13b	5.86b	37.00
CaCl₂	55.96a	27.10a	15.02a	8.40a	0.59a	0.00a	17.84
MgCl₂	61.97a	22.91a	12.43a	6.81a	0.00a	0.00a	17.35
Mean	71.98	46.40	27.05	14.10	5.63	2.74	27.98

Means within a column that have different lowercase letters (a-c) are significantly different from each other (Duncan's multiple range test, P≤0.05).

Analysis of the results in Table 5 showed that at different chloride salts and doses the salt tolerance indices significantly varied. At salinity levels in the range of 50 - 150 mM solutions, rice seeds showed very high germination tolerance toward all salts tested, ranging between 89.06% and 99.59%, except for the treatment with 150 mM MgCl₂ where seeds were sensitive to salinity. At 200 - 250 mM solutions, the tolerance of the *Oryza sativa* seeds varied from very high to high for treatment with 200 - 250 mM NaCl, 200 - 250 mM KCl and 200 mM CaCl₂.

Medium tolerance to germination was established at 300 mM NaCl and 300 mM KCl. Very low germination salt tolerance was recorded in the variant with 250 mM CaCl₂. Rice seeds were sensitive to germination in 200 - 300 mM solutions of MgCl₂ and 300 mM CaCl₂. Seedling tolerance indices varied from 86.27% to 0%. At the lowest concentration of 50 mM NaCl and 50 mM KCl rice seeds had very high tolerance of seedling growth. High seedling tolerance indices were recorded in the variants with 50 mM MgCl₂, 100 mM KCl, 100 mM

NaCl. At average salinity doses (150 - 200 mM), the tolerance was between medium for 150 mM NaCl to very low for treatments with 150 mM CaCl₂ and MgCl₂, 200 mM solutions of KCl, CaCl₂ and MgCl₂. In the variants with high concentrations (250 - 300 mM) rice seeds showed very low tolerance of seedling growth in all chloride salts, except for the treatments with 250 mM MgCl₂ and 300 mM CaCl₂ and MgCl₂, where it was sensitive.

CONCLUSIONS

The response of rice seeds to salt stress varied depending on the type and the concentration of salt.

The application of increasing concentrations of NaCl and KCl salts from 50 mM to 300 mM caused osmotic stress on rice seeds, resulting in decreased germination and germination index values, extended mean germination time, increased relative injury rate and reduced seedling height.

At concentrations in the range of 250 - 300 mM of MgCl₂ and 300 mM of CaCl₂, rice seeds did not germinate because of the toxic effect of the salts.

The inhibitory effect of the different chloride salts and of their concentrations was more pronounced on the root than on the shoot.

REFERENCES

1. I. Stavi, N. Thevs, S. Priori, *Front. Environ. Sci.*, **9**, 712831 (2021).
2. Ch. Zhao, H. Zhang, Ch. Song, Jian-Kang Zhu, S. Shabala, *The Innov. J.*, **1**(1), 1 (2020).
3. V. Karolinoerita, W. A. Yusuf, *J. Sumberdaya Lahan*, **14**(2), 91 (2020).
4. A. Hassani, A. Azapagic, N. Shokri, *Nat. Commun.*, **12**, 6663 (2021) https://doi.org/10.1038/s41467-021-26907-3
5. P. Shrivastava, R. Kumar, *Saudi J. Biol. Sci.,* **22**, 123 (2015).
6. N. Kalhori, T. Ying, R. Nulit, M. Sahebi, R. Abiri, N. Atabaki, *Int. J. Adv. Res. Botany*, **4**(1), 29 (2018).
7. R. Machado, R. Serralheiro, *Hortic.*, **30**(2), 30 (2017).
8. A. Radanielson, O. Angeles, T. Li, A. Ismail, D. Gaydon, *Field Crops Res*., **220**, 46 (2018).
9. M. Hasanuzzaman, M. Fujita, *J. Molec. Sci.*, **23**(9), 4810 (2022) https://doi.org/10.3390/ijms23094810.
10. S. Shiade, B. Boeld, *Acta Agric. Scand.- B Soil Plant Sci.,* **70**(60), 485 (2020).
11. N. Tarchoun, W. Saadaoui, N. Mezghani, O. Pavli, H. Falleh, S. Petropoulos, *Plants,* **11**(6), 800 (2022). https ://doi.org/10.3390/plants11060800.
12. L. I. Rodríguez Coca, M. T.García González, Z. Gil Unday, J. Jiménez Hernández, M. Rodríguez Jáuregui, Y. Fernández Cancio, *Sustainability*, **15**, 1804 (2023). https://doi.org/10.3390/su15031804.
13. W. Irakoze, H. Prodjinoto, S. Nijimbere, G. Rufyikiri, S. Lutts, *Agronomy*, **10**(6), 864 (2020). https://doi.org/10.3390/agronomy10060864.
14. M. A. Al-Mudaris, *Der Tropenlandwirt, Beitrage zur tropischen Landwirtschaft und Veterinarmedizin*, **99**, 147 (1998).
15. Y. Li, *Pakistan J. Biolog. Sci*., **11**(9), 1268 (2008).
16. A. A. Abdul-Baki, J. D. Anderson, *Crop Sci.*, **13**, 630 (1973), http://dx.doi.org/10.2135/ cropsci1973.0011183X001300060013x.
17. M. Islam, M. Karim, *The Agriculturists*, **8**(2), 57 (2010).
18. U. Mujeeb-ur-Rahman, A. Soomro, M. Zahoor-ul-Haq, Sh. Gul, *World J. Agric. Sci.,* **4**(3), 398 (2008).
19. C. Uçarlı, in: Abiotic Stress in Plants. Intechopen, 2021, doi: 10.5772/intechopen.93647.
20. R. Stefanello, B. Viana, P. Goergen, L. Neves, U. Nunes, *Braz. J. Biol.*, **80**(2), 285 (2020). https://doi.org/10.1590/1519-6984.192140.
21. H. A. Barichello, R. Stefanello, G. G. Bastiani, L. A. S. Neves, *Hoehnea*, **48**, e1202020 (2021). https://doi.org/10.1590/2236-8906-120/2020.
22. L. Liu, W. Xia, H. Li, H. Zeng, B. Wei, S. Han, C. Yin, *Front. Plant Sci.*, **9**, 275 (2018). doi: 10.3389/fpls.2018.00275.
23. L. Pradheeban, N. Nissanka, L. Suriyagoda, *Tropical Agric. Res.,* **25**(3), 358 (2014). doi:10.4038/tar.v25i3.8045.
24. C. Zheng, Z. Zhang, G. Zhou, X. Xie, *Shandong Agric. Sci.*, **50**, 38 (2018).
25. M. Anshori, B. Purwoko, I. Dewi, W. Suwarno, S. Ardie, *IOP Conf. Series: Earth and Environ. Sci.*, **484** (2020) 012001IOP Publishing, doi:10.1088/1755-1315/484/1/012001.
26. M. S. Jahan, M. S. Hossain, U. Chakma, *Bull. Inst. Trop. Agr., Kyushu Univ.*, **44**, 17 (2021).
27. R. Zhang, S. Hussain, Y. Wang, Y. Liu, Q. Li, Y. Chen, H. Wei, P. Gao, Q. Dai, *Agronomy*, **11**, 1569 (2021). https://doi.org/10.3390/ agronomy1108156.
28. M. R. Momayezi, A. R. Zaharah, M. M. Hanafi, I. Mohd Razi, *Pertanika J. Trop. Agric. Sci.*, **32**(2), 247 (2009).
29. A. F. Ologundudu, A. A. Adelusi, R. O. Akinwale, *Not. Sci. Biol.,* **6**(2), 237 (2014).
30. R. Kumari, P. Kumar, V. K. Sharma, H. Kumar, *J. Cell Tissue Res.,* **16**(3), 5901 (2016).
31. S. M. E. Mokhtar, A. Samb, A. O. Moufid, A. O. M. S. Boukhary, T. K. O. Djeh, *Int. J. Agri. Crop Sci.*, **8**(3), 346 (2015).
32. C. Vibhuti, K. Shahi, S. S. Bargali, Bargali, *Indian J. Agric. Sci.*, **85**(1), 102 (2015).
33. R. Diaguna, F. Ch. Suwarno, M. S. Suwarno, *Int. J. Applied Sci. Tech.,* **7**(3), 69 (2017).
34. B. Ijaz, C. Sudiro, R. Jabir, F. L. Schiavo, M. Z. Hyder, T. Yasmin, *Int. J. Agric. Biol*., **21**(3), 667 (2019).
35. F. I. Yousof, *J. Plant Production*, *Mansoura Univ.*, **4**(4), 523 (2013). doi: 10.21608/JPP.2013.72394.

Mineral composition of chickpea grain (*Cicer arietinum* L.) depending on the fertilization with liquid organic fertilizers

M. Gerdzhikova[*], T. Zhelyazkova

Trakia University, Faculty of Agriculture, Student campus, 6000 Stara Zagora, Bulgaria

The objective of the study is to establish the effect of the liquid organic fertilizers Naturamin Plus and Amalgerol Essence on the mineral composition of chickpea grain (*Cicer arietinum* L.). The experiment was conducted in the period 2019-2021 in the region of Central South Bulgaria. Fertilizers were tested in two phases of development of the chickpea: growth phase (4th leaf) and beginning of flowering. The results obtained about the mineral composition were processed with ANOVA. The application of liquid organic fertilizers in chickpea has a proven positive effect on the N content in the grain. The highest content was found after treatment with Amalgerol Essence at a dose of 3.0 l/ha at the beginning of the flowering phase. The liquid organic fertilizers Naturamin Plus and Amalgerol Essence do not significantly change neither the content of the other macroelements (P, K, Ca, Mg) nor the content of the trace elements Fe, Cu and Mn in chickpea grain. Treatment of chickpea with Naturamin Plus and Amalgerol Essence at the beginning of the flowering phase results in reduced Zn content in the grain. During fertilization with Naturamin Plus and Amalgerol Essence a tendency to increase the Ca:P ratio in both phases of application was observed. The fertilizers had a more pronounced effect on the Ca:Mg ratio when applied at the beginning of the flowering phase.

Key words: chickpea, liquid organic fertilizers, nitrogen content, mineral composition, Ca:P ratio, Ca:Mg ratio

INTRODUCTION

Chickpea is the third-largest grain bean culture in the world beans production. Traditionally it is grown in Asia, Europe, Africa and Australia as a source of cheap protein for human nutrition [1]. It not only contributes to solving the protein problem in feeding people, but also supplies essential vitamins and minerals [2]. About 100 g of chickpea grains can meet the daily dietary needs of Fe and Zn and 200 g can meet the needs of Mg. Chickpea consumption has a beneficial effect on some diseases such as CVD, type 2 diabetes, digestive diseases and some cancers and is an alternative for the prevention of chronic degenerative diseases [3−5].

Chickpea can be used as a high-energy and high-protein food in animal diets to assist milk, meat and/or egg production [6]. Chickpea grain is a good source of protein in feeding broiler chickens and at the same time it has a beneficial effect on the dietary value of chicken meat and the expected enhancing effect on consumer health [7]. Mineral substances are responsible for the functioning of important enzyme systems in the human, animal and plant organism [8]. The most common mineral in the human and animal body is Ca – structural component of bones and teeth, important for the normal flow of many vital functions. Ca deficiency results in rickets, slow growth in animal development and osteoporosis, rickets and other human diseases [9-11]. Phosphorus is often discussed in connection with Ca, as the two minerals function together in bone formation [10]. Ruminants can tolerate large variations in the Ca:P ratio in feed, but ratios under 1:1 and over 7:1 lead to reduced growth and development [12, 13]. Magnesium is involved in the composition of bones, the construction and activation of important enzymes, the transmission of nerve impulses and the normal function of muscles. When there is a lack of Mg, Grass tetany is observed in ruminants [10]. Favorable quantitative relations between macro- and trace elements in feed increase their availability to animals.

Plants are the main natural source of mineral substances for humans and animals [8]. Legumes are richer in minerals than cereals [14, 15]. The low uptake efficiency by plants of some trace elements introduced through soil fertilization can be overcome by alternative methods such as foliar fertilization during vegetation [16, 17]. A number of authors reported that the application of organic fertilizers during vegetation affects the chemical composition by increasing the content of protein (N), fat, fibers and mineral substances in chickpea seeds [18-25]. According to Ansari *et al.* [26], liquid biofertilizers increased chickpea productivity but did not affect the N (protein) content of the grain. The lack of influence of various complex suspension fertilizers on the content of N (protein)

---

* To whom all correspondence should be sent:
E-mail: *mariya.gerdzhikova@trakia-uni.bg*

was reported by Milev *et al.* [27] in soybean and Ilieva and Vasileva [28] in pea.

Rathod *et al.* [29] found that soil application of NPK along with foliar application of Zn and B increased the uptake of trace elements (Fe, Cu, Mn, Zn and B) in chickpea grain. Hidoto *et al.* [16] reported that foliar application of Zn increased the Zn content of chickpea grain by up to 22% compared to its soil application and pre-sowing seed treatment. Kobraee [30] observed an increased concentration of Zn and Mn in chickpea seeds and synergistic effects between these elements during their foliar application. An increased content of Zn and Fe in the chickpea grain after foliar application of mineral, chelated and nanoforms of Zn and Fe before flowering was also reported by Dhaliwal *et al.* [31] and Pal *et al.* [32].

The objective of this study was to determine the effect of liquid organic fertilizers Naturamin Plus and Amalgerol Essence on the mineral composition of chickpea grain. Some quantitative relations between macroelements in the grain were also established.

MATERIAL AND METHODS

Materials

The study was conducted in the period 2019-2021 in the region of Central South Bulgaria. The field experiment was conducted by the block method in 4 replications, size of the experimental area 10 m^2, under non-irrigated conditions, with a predecessor common wheat. The soil type was Haplic Vertisol, containing medium available humus, neutral to low alkaline reaction, low in available nitrogen and phosphorus and high in available potassium [33]. Meteorological conditions during the study period were characterized as relatively favorable [33]. Vegetation rainfall totals during the study years were above the multiyear average, but unevenly distributed. Average air temperatures for the chickpea vegetation period did not significantly differ from perennial averages.

The tested fertilizers had the following composition: Naturamin Plus (NP) – total 400 g/l amino acids, free amino acids – 200 g/l, N – 75 g/l, Fe – 12 g/l, Mn – 7.5 g/l, B – 1.3 g/l, Cu – 1.2 g/l, Mo – 0,5 g/l, Zinc (Zn) – 2.5 g/l; Amalgerol Essence (AE) – free amino acids, organic N (3%) and organic K (3%), plant herb extracts, seaweed extract, plant hormones, antioxidants, total organic carbon 22.7%. The fertilizers are certified according to European Council Regulation (EC) No 834/2007 for use in organic production.

The treatment was carried out in two phases of chickpea development: growth phase (4th leaf) and beginning of flowering with NP at doses of 1.5; 2.5 and 3.5 l/ha and AE at doses of 1.0; 2.0 and 3.0 l/ha.

Determination of mineral composition

The nitrogen content (N) was determined by the method of Kjeldahl (BDS – EN ISO 5983); phosphorus (P) – by colorimetry, measured at 470 nm on a SPEKOL 11 spectrophotometer; potassium (K); calcium (Ca), magnesium (Mg), manganese (Mn), iron (Fe), copper (Cu) and zinc (Zn) with Perkin Elmer AANALYST-800 atomic absorption spectrometer [38].

Statistical analysis

The results for the mineral composition were statistically processed with ANOVA LSD test for statistical significance of the differences, using MS Excel software – 2010.

RESULTS AND DISCUSSION

Fertilization with the liquid organic fertilizers NP and AE in 2019 (Table 1) increased the N content in the chickpea grain in both phases of application compared to the control variant.

The positive influence of fertilization is more pronounced at the beginning of the flowering phase, the highest values of N being recorded when treated with NP 3.5 l/ha and AE 1.0 l/ha. In 2021, again higher N content was observed at the beginning of the flowering phase - 38.74 g/kg when applying NP 3.5 l/ha and 39.38 g/kg when applying AE 3.0 l/ha.

On average for the study period, the higher N content in the grain due to NP fertilization at the 4th leaf phase was not statistically proven. In this phase, differences with the control were statistically proven only with AE at a dose of 1.0 l/ha (P<0.05). The positive influence of fertilization was more pronounced at the beginning of the flowering phase on average for the experimental period, and the differences from the control were statistically well proven when applying AE at doses of 1.0 and 3.0 l/ha (P<0.001) and NP 3.5 l/ha (P<0.01).

Of the macronutrients P, K, Ca and Mg included in this study (Table 2), potassium had the highest content in the chickpea grain. The established values for P content were higher than those for Ca and Mg. These results coincide with those obtained by Jukanti *et al.* [3] and Thavarajah and Thavarajah [15].

Table 1. Nitrogen content of chickpea grain, g/kg DM, n=39

Variant/Dose, l/ha	Years		Average	
	2019	2021	g/kg	%
Control (untreated)	35.58	38.06	36.82 ± 1.24	100.00
Growth phase (4th leaf)				
NP 1.5	36.49	37.69	37.09 ± 0.60ab	100.74
NP 2.5	36.93	37.52	37.22 ± 0.30ab	101.10
NP 3.5	36.49	36.69	36.59 ± 0.10a	99.37
AE 1.0	36.86	38.60	37.73 ± 0.87*bc	102.47
AE 2.0	37.09	37.46	37.28 ± 0.19ab	101.24
AE 3.0	36.99	37.14	37.06 ± 0.08ab	100.66
Average	36.81	37.52	37.16	
Beginning of flowering				
NP 1.5	36.84	37.32	37.08 ± 0.24ab	100.70
NP 2.5	36.28	38.62	37.45 ± 1.17b	101.71
NP 3.5	37.61	38.74	38.18 ± 0.56**bc	103.68
AE 1.0	37.60	38.93	38.27 ± 0.66***c	103.93
AE 2.0	37.23	36.82	37.02 ± 0.21ab	100.55
AE 3.0	37.32	39.38	38.35 ± 1.03***c	104.16
Average	37.15	38.30	37.72	

Different letters indicate statistically significant differences among variants at P<0.05; *, **, *** – statistically significant differences between the variants and control at P<0.05, 0.01 and 0.001, respectively.

Table 2. Content of P, K, Ca and Mg of chickpea grain average for the period 2019-2021, g/kg DM, n=39

Variant/Dose, l/ha	P	K	Ca	Mg
Control (untreated)	3.70 ± 0.50	7.21 ± 0.37	2.11 ± 0.66	1.15 ± 0.11
Growth phase (4th leaf)				
NP 1.5	3.70 ± 0.70ab	7.25 ± 0.68ab	2.13 ± 0.73a	1.16 ± 0.17bc
NP 2.5	3.60 ± 0.50a	7.12 ± 0.61a	1.95 ± 0.68a	1.08 ± 0.07b
NP 3.5	3.70 ± 0.30ab	7.42 ± 0.29ab	2.00 ± 0.74a	1.14 ± 0.02bc
AE 1.0	4.05 ± 0.45ab	7.42 ± 0.21ab	2.00 ± 0.62a	1.05 ± 0.08*ab
AE 2.0	4.00 ± 0.70ab	7.18 ± 0.49ab	2.04 ± 0.68a	1.10 ± 0.13bc
AE 3.0	3.90 ± 0.40ab	7.29 ± 0.21ab	1.98 ± 0.69a	1.18 ± 0.05bc
Average	3.83	7.28	2.02	1.12
Beginning of flowering				
NP 1.5	3.80 ± 0.20ab	7.36 ± 0.10ab	2.02 ± 0.64a	0.96 ± 0.07**a
NP 2.5	4.05 ± 0.35ab	7.60 ± 0.27b	2.08 ± 0.68a	1.07 ± 0.08b
NP 3.5	4.15 ± 0.35b	7.67 ± 0.15*b	2.13 ± 0.70a	1.20 ± 0.11c
AE 1.0	3.70 ± 0.50ab	7.40 ± 0.10ab	2.01 ± 0.77a	1.07 ± 0.03b
AE 2.0	3.70 ± 0.20ab	7.21 ± 0.23ab	2.02 ± 0.68a	1.11 ± 0.02bc
AE 3.0	3.90 ± 0.40ab	7.07 ± 0.32a	1.95 ± 0.63a	1.11 ± 0.02bc
Average	3.88	7.38	2.03	1.09

Different letters indicate statistically significant differences between variants at P<0.05; *, ** – statistically significant differences between the variants and control at P<0.05 and 0.01, respectively.

Treatment with the organic fertilizer NP 3.5 l/ha at the beginning of the flowering stage increased provenly (P<0.05) the K content compared to the control by 6.5% and had the strongest positive effect on P, Ca and Mg content in the grain (by 12.2%, 0.9%, and 3.6%, respectively), but the differences from the control were not statistically proven. On average for the study period the lowest P, K and Ca content in the growth phase was reported for treatment with NP 2.5 l/ha, and at the phase beginning of flowering

with AE, but the differences with the non-treated control were not proven.

A reduction in Mg content in the chickpea grain was reported in the growth phase after treatment with AE 1,0 l/ha (P<0.05) and at the beginning of the flowering phase for the variant fertilized with NP 1.5 l/ha (P<0.01).

For the trace elements studied in this research (Table 3), it is evident that fertilization with the organic fertilizers NP and AE has no significant effect on Fe, Cu and Mn content in chickpea grain.

Table 3. Content of Fe, Cu, Zn and Mn in chickpea grain average for the period 2019-2021, mg/kg DM, n=39

Variant/Dose, l/ha	Fe	Cu	Zn	Mn
Control (untreated)	58.97 ± 3.89	8.26 ± 1.59	29.90 ± 0.63	27.60 ± 8.22
Growth phase (4th leaf)				
NP 1.5	62.61 ± 2.81[b]	8.51 ± 1.20	29.25 ± 0.80[bc]	26.30 ± 8.46
NP 2.5	58.69 ± 2.40[ab]	8.58 ± 2.20	29.71 ± 0.72[c]	25.85 ± 8.44
NP 3.5	60.10 ± 6.35[ab]	8.39 ± 1.04	30.00 ± 0.97[c]	26.40 ± 7.47
AE 1.0	56.11 ± 5.47[a]	8.23 ± 1.53	28.82 ± 0.08[*b]	26.59 ± 7.02
AE 2.0	58.83 ± 6.97[ab]	8.22 ± 1.17	29.46 ± 0.19[c]	27.06 ± 6.73
AE 3.0	61.58 ± 4.05[b]	8.22 ± 1.47	29.01 ± 0.86[*bc]	27.40 ± 7.77
Average	59.65	8.36	29.37	26.60
Beginning of flowering				
NP 1.5	59.58 ± 5.64[ab]	8.53 ± 2.45	27.80 ± 0.02[***ab]	26.12 ± 7.87
NP 2.5	60.30 ± 2.21[ab]	8.48 ± 2.22	27.90 ± 0.24[***ab]	27.46 ± 7.30
NP 3.5	57.62 ± 5.25[ab]	8.20 ± 1.71	29.47 ± 0.66[c]	29.00 ± 7.70
AE 1.0	58.45 ± 2.82[ab]	7.87 ± 1.20	28.54 ± 1.22[**ab]	27.43 ± 6.71
AE 2.0	58.81 ± 3.90[ab]	7.93 ± 1.69	28.60 ± 0.97[**b]	27.16 ± 8.07
AE 3.0	59.91 ± 0.48[ab]	8.26 ± 2.15	27.74 ± 0.88[***a]	27.37 ± 7.42
Average	59.11	8.21	28.34	27.42

Different letters indicate statistically significant differences among variants at P<0.05; *, **, *** – statistically significant differences between the variants and control at P<0.05, 0.01 and 0.001, respectively.

Table 4. Influence of treatment with leaf fertilizers on the Ca:P ratio and Ca:Mg ratio average for the period 2019-2021

Variant/ Dose, l/ha	Growth phase (4th leaf)		Beginning of flowering	
	Ca:P	Ca:Mg	Ca:P	Ca:Mg
Control	1:1.76	1.83:1	1:1.76	1.83:1
NP 1.5	1:1.74	1.83:1	1:1.88	2.07:1
NP 2.5	1:1.84	1.81:1	1:1.95	1.95:1
NP 3.5	1:1.85	1.75:1	1:1.95	1.78:1
AE 1.0	1:2.02	1.91:1	1:1.84	1.88:1
AE 2.0	1:1.97	1.85:1	1:1.83	1.82:1
AE 3.0	1:1.97	1.69:1	1:2.00	1.75:1
Average	1:1.90	1.81:1	1:1.91	1.87:1

Higher content of the trace elements Fe, Cu and Zn was reported when fertilizing with NP at phase 4th leaf but no differences with the non-treated control were proven. Liquid organic fertilizer AE applied in phase 4th leaf resulted in reduction of Zn content by 3.0% – 3.6% compared to the control but the differences have a low degree of reliability (P<0.05). At the beginning of flowering phase treatment of chickpea with liquid organic fertilizers provenly reduced Zn content in the grain (P<0.001). The lowest Zn content was reported in treatment with AE 3.0 l/ha – 7.2% lower than the unfertilized control. The average values of Fe and Cu content (59.35 and 8.28 mg/kg, respectively), obtained in this study, are similar to the ones established by Jukanti *et al.* [3] and Thavarajah and Thavarajah [15]. The established Zn content is lower and that of Mn is higher than the ones reported by Jukanti *et al.* [3] and Thavarajah and Thavarajah [15].

Optimum Ca:P ratio in feed for ruminants is 2:1 (typical of green forages), although that ratio can vary a lot [10]. Ciepiela and Godlewska [34] found an increase of the ratios Ca:P and Ca:Mg in the vegetative application of organic biofertilizers in crops of grass species. According to Wolski *et al.* [35] foliar treatment with biostimulants reduced the Ca:P ratio in the biomass of three types of grass mixtures.

On average for the period of the present study, the Ca:P ratio in chickpea grain increased compared to the control variant (Table 4) as a result of the application of both foliar fertilizers. An increase is observed in the two treatment phases.

The average value is 1:1.90 (with variation from 1:1.74 to 1:2.02) and is close to that of Todorov *et al.* [36], who established a ratio of 1:2.1, unlike Iqbal *et al.* [37], who report a ratio Ca:P = 1:1.27 and

Thavarajah and Thavarajah [15], who report a ratio Ca:P = 1:2.55.

From data by Todorov *et al.* [36], the Ca:Mg ratio in chickpea grain is 2:1. The Ca:Mg ratio established in this study in chickpea grain is 1.84:1 on average, varying from 1.69:1 to 2.07:1. Higher, but not proven values of the Ca:Mg ratio (1.87:1 on average) were detected when chickpea was treated with the liquid fertilizers NP and AE at the beginning of the flowering phase.

CONCLUSIONS

Application of the liquid organic fertilizers Naturamin Plus and Amalgerol Essence to chickpeas has a proven positive effect on the N content in the grain. The highest content was found in treatment at the beginning of the flowering phase with Amalgerol Essence at a dose of 3.0 l/ha. The use of the liquid organic fertilizers Naturamin Plus and Amalgerol Essence does not significantly change the content of the other macroelements (P, K, Ca, Mg).

Liquid organic fertilizers Naturamin Plus and Amalgerol Essence do not affect the Fe, Cu and Mn content in chickpea grain. Treatment of chickpeas at the beginning of the flowering phase with Naturamin Plus and Amalgerol Essence results in a decrease of Zn content in the grain.

When fertilizing chickpeas with the liquid organic fertilizers Naturamin Plus and Amalgerol Essence, a tendency to increase the Ca:P ratio in the grain was observed in both phases of application. Fertilizers have a stronger effect on the Ca:Mg ratio when applied at the beginning of the flowering phase.

REFERENCES

1. M. Zia-Ul-Haq, S. Iqbal, S. Ahmad, M. Imran, A. Niaz, M. I. Bhanger, *Pakistan Food Chemistry*, **105**(4), 1357 (2007).
2. A. M. Ghribi, I. M. Gafsi, C. Blecker, S. Danthine, H. Attia, S. Besbes, *Journal of Food Engineering,* **165**, 179 (2015).
3. A. K. Jukanti, P. M. Gaur, C. L. Gowda, R. N. Chibbar, *British Journal of Nutrition*, **108**(S1), 11 (2012).
4. J. M. Faridy, C. M. Stephanie, M. O. Gabriela, J. M. Cristian. *Plant Foods Hum. Nutr.*, **75**(2), 142 (2020).
5. J. Wang, Y. Li, A. Li, R. H. Liu, X. Gao, D. Li, Z. Xue, *Food Research International*, **150**, 110790 (2021).
6. V. A. Bampidis, V. Christodoulou, *Animal Feed Science and Technology*, **168**(1-2), 1 (2011).
7. A. Danek-Majewska, M. Kwiecień, A. Winiarska-Mieczan, M. Haliniarz, A. Bielak, *Animals*, **11**(12), 3367 (2021).
8. K. O. Soetan, C. O Olaiya, O. E. Oyewole, *African Journal of Food Science*, **4**(5), 200 (2010).
9. J. Hejazi, A. Davoodi, M. Khosravi, M. Sedaghat, V. Abedi, S. Hosseinverdi, E. Ehrampoush, R. Homayounfa, L. Shojaie, *Biomedical Research and Therapy*, **7**(4), 3709 (2020).
10. National Academies of Sciences, Engineering, and Medicine. Nutrient requirements of beef cattle. National Academy Press. Washington, D.C., 2016, p. 494.
11. M. Vlok, A. M. E. Snoddy, N. Ramesh, B. J. Wheeler, V. G. Standen, B. T. Arriaza, *American Journal of Human Biology*, **35**(2), 1 (2023).
12. E. Alfaro, M. W. Neathery, W. J. Miller, C. T. Crowe, R. P. Gentry, A. S. Fielding, D. G. Pugh, D. M. Blackmon, *Journal of Dairy Science*, **71**(5), 1295 (1988).
13. R. E. Ricketts, J. R. Campbell, D. E. Weinman, M. E. Tumbleson, *Journal of Dairy Science,* **53**(7), 898 (1970).
14. S. Akibode, M. Maredia, Global and regional trends in production, trade and consumption of food legume crops, (No. 1099-2016-89132), (2011).
15. D. Thavarajah, P. Thavarajah, *Food Research International*, **49**(1), 99 (2012).
16. L. Hidoto, W. Worku, H. Mohammed, T. Bunyamin, *Journal of Soil Science and Plant Nutrition*, **17**(1), 112 (2017).
17. K. Siavashi, R. Soleimani, *Iranian Journal of Soil and Water Research*, **18**, 42 (2004).
18. A. S. Abdalla, M. E Abdelgani, A. G. Osman, *Pakistan Journal of Nutrition*, **12**(1), 1 (2013).
19. B. Nandan, B. S. Jamwal, B. C. Sharma, K. Anil, G. Vikas, *International Journal of Basic and Applied Agricultural Research*, **12**(2), 184 (2014).
20. R. S. Oliveira, P. Carvalho, G. Marques, L. Ferreira, M. Nunes, I. Rocha, H. Freitas, *Journal of the Science of Food and Agriculture*, **97**(13), 4379 (2017).
21. A. Pasqualone, C. Summo, D. De Angelis, G. Cucci, D. Caranfa, G. Lacolla, *Plants*, **10**(7), 1441 (2021).
22. M. F. Seleiman, M. S. Abdelaal, *Egyptian Journal of Agronomy*, **40***(1)*, 105 (2018).
23. M. Uddin, S. Hussain, M. Khan, M. Akhtar, N. Hashmi, M. Idrees, T. A. Dar, *Turkish Journal of Agriculture and Forestry*, **38**(1), 47 (2014)
24. P. Shinde, R. Hunje, *Legume Research - An International Journal*, **42**(6), 818 (2019).
25. M. S. Venkatesh, P. S. Basu, *Journal of Food Legumes*, **24**(2), 110 (2011).
26. M. F. Ansari, D. R. Tipre, S. R. Dave, *Biocatalysis and Agricultural Biotechnology*, **4**(1), 17 (2015)
27. G. Milev, M. Nankova, R.Todorova, *Scientific Works Papers, 3(2),* 165 (2014).
28. A. Ilieva, V. Vasileva, *Banat's Journal of Biotechnology*, **4**(7), 74 (2013).

29. S. Rathod, S. Channakeshava, B. Basavaraja, K. S. Shashidhara, *Journal of Pharmacognosy and Phytochemistry*, **9**(4), 3356 (2020).
30. S. Kobraee, *Journal of Applied Biology and Biotechnology*, **7**(3), 20 (2019).
31. S. S. Dhaliwal, V. Sharma, A. K. Shukla, V. Verma, S. K. Behera, P. Singh, S. Alotaibi, A. Gaber, A. Hossain, *Agronomy*, **11**(12), 2436 (2021).
32. V. Pal, G. Singh, S. S. Dhaliwal, *Journal of Plant Nutrition*, **42**(15), 1789 (2019).
33. T. Zhelyazkova, M. Gerdzhikova, S. Atanasova, *Scientific Papers. Series A. Agronomy*, **65**(1), 625 (2022).
34. G. A. Ciepiela, A. Godlewska. *Fresenius Environmental Bulletin*, **26**(4), 2779 (2017).
35. K. Wolski, M. Biernacik, S. Świerszcz, M. Talar-Krasa, O. Leshchenko, *Journal of Elementology*, **24**(1), 385 (2019).
36. N. Todorov, I. Krachunov, D. Dzhuvinov, A. Aleksandrov, Guide for Animal Nutrition. Matkom, Sofia, 2007, p. 399.
37. A. Iqbal, I. A. Khalil, N. Ateeq, M. S. Khan, *Food Chemistry*, **97**(2), 331 (2006).
38. AOAC international. Official methods of analysis of AOAC (18th edn., rev. 2), Association of Official Analytical Chemists Intern, Gaithersburg, MD, USA, 2007.

Mineral composition of tef (*Eragrostis tef* (Zucc.) Trotter) – a new fodder crop in Bulgaria

A. Cholakova[*], T. Zhelyazkova, M. Gerdzhikova, P. Veleva

Trakia University, Faculty of Agriculture, Students' campus, Stara Zagora 6000, Bulgaria

The effect of the sowing rate and nitrogen fertilization on the mineral composition of the tef biomass (*Eragrostis tef* (Zucc.) Trotter) was studied in 2021 – 2022 in the region of Central South Bulgaria. Three sowing rates – 10, 15 and 20 kg ha^{-1}, and four levels of nitrogen fertilization – 0, 30, 60 and 90 kg ha^{-1} were studied in two development phases (milk and dough maturity). Nitrogen content was higher in the milk maturity phase. The highest nitrogen content was found at fertilization with 90 kg ha^{-1} of nitrogen at a sowing rate of 15 kg ha^{-1} in both harvesting phases. The increase of nitrogen and sowing rates had no significant effect on Mg content, but there was a negative tendency in P, K and Ca content. A strong positive correlation was found between the N and Mg contents, a good positive correlation – between the Ca and Mg contents; between the N and P and Ca contents and between the P and Mg contents. Climatic factors had the strongest effect on the content of macroelements in the tef biomass. Nitrogen fertilization had a strong effect on N content, while the harvesting phases and the sowing rate influenced the K content. No regular influence of the tested sowing rates, nitrogen fertilizing rates and harvesting phases on the Ca:P and Ca:Mg ratios was found.

Key words: *Eragrostis tef* (Zucc.) Trotter, mineral composition, nitrogen rate, sowing rate, phase of harvesting

INTRODUCTION

Tef (*Eragrostis tef* (Zucc.) Trotter) is an annual cereal plant. Its grain is an important ingredient in the diet of the population in Ethiopia, Eritrea, South Africa and is used to produce traditional foods and beverages [1]. Due to the many dietary benefits and tolerance to extreme environmental conditions, this cereal crop is promising for cultivation and forage [2-4].

In the last decade, the demand for crops adaptive to the stress of climatic changes to provide biomass and grain in a short period under adverse environmental conditions has increased [5, 6]. The biological characteristics of the crop permit its use in compressing crop rotations - it can be successfully sown as a second crop on non-irrigated areas. Tef has a high drought tolerance. In the literature, it is presented as a crop that can replace or supplement some of the fodder crops - alfalfa, corn, sorghum, barley and wheat in the absence of sufficient moisture supply [7-9]. In comparison with other cereals, tef is less infested by diseases and pests [4, 9, 10].

The use of tef as a "healthy food" is due to the unique taste of the gluten-free grain and its biochemical composition [11]. The amylase content (20-26%) in the grain is comparable to other cereals [1] while the fiber is in higher percentage - 9.8% for tef [3].

The valuable biological qualities and the favourable chemical composition rank tef as an important crop for solving not only the food needs of the population, but also as a fodder crop. Studies on the mineral composition of tef biomass worldwide are quite scarce, especially for its cultivation as bulk forage. In recent years, some authors have reported the potential of the crop to produce silage and hay harvested in different phenological phases and studied the chemical and mineral composition of the tef biomass [4, 12]. The quality of tef forage is highly dependent on nitrogen fertilization, the maturity phase at harvest and the number of swaths [13, 14]. Currently, there is limited information on the nutritional value of the biomass and its potential for use as ruminant feed. According to literature, the content of crude protein in the tef biomass sources ranges from 8.5 to 21.5% [2, 4, 8, 14-17], the fiber content varies from 53 to 73% [2, 8] depending on the maturity phase. According to some authors, tef hay has the potential to replace corn silage in cattle rations and become a major forage source in the nutrition of bulls and dairy heifers [12, 16]. The maturity phase at harvest is one of the major factors affecting forage quality and digestibility [4, 16-18].

The objective of this study is to determine the influence of the sowing rate and nitrogen fertilization on the mineral composition and the

---

* To whom all correspondence should be sent:
E-mail: *aneta.cholakova@trakia-uni.bg*

quantitative ratios between the macroelements in two phases of harvesting the tef biomass grown for fodder under the conditions of Central South Bulgaria.

MATERIALS AND METHODS

The research was conducted in the period 2021-2022 in the area of the village of Tulovo, Stara Zagora county, located in the region of Central South Bulgaria. The field experiment was conducted with a white variety of tef of the Dutch company "Millets place". The experiment was based on the method of fractional plots and size of the harvest plot was 10 m^2, under non-irrigated conditions, after predecessor wheat. The soils in the area are alluvial, slightly to moderately enriched with humus (1.6% - 2.6%), with a slightly acidic to neutral reaction, slightly stocked with nitrogen (31.0 – 35.0 kg ha^{-1}) and phosphorus (8.0 – 27.0 ppm) and slightly to well stocked with potassium (93.0-136.0 ppm). The influence of sowing rate and nitrogen fertilization on the mineral composition of tef (*Eragrostis tef* (Zucc.) Trotter) biomass in two development phases (milk and dough maturity) were tested.

The studied factors and their levels were as follows: factor A: sowing rate, kg ha^{-1} (A1 – 10; A2 – 15; A3 – 20); factor B: nitrogen fertilization rates, kg ha^{-1} (B1 – 0; B2 – 30; B3 – 60; B4 – 90). Variant 1 (A1B1) was adopted as a control – harvested at the milk maturity phase, with a sowing rate of 10 kg ha^{-1} without nitrogen fertilization. With the main tillage, background fertilization with 50 kg ha^{-1} P_2O_5 was made. Fertilization with nitrogen in the specified rates (factor B) was made immediately before sowing.

Plant materials and processing

Aerial parts of tef were harvested at a height of 6 cm from the base of the stem in two phases of development – milk and dough maturity. Average plant samples in 3 replicates were collected from each variant. Plant samples were pre-processed - cleaning from contaminants, drying in a dryer at 60°C and grinded in a mechanical grinder (final powder size less than 400 μm). The samples were stored in dark and cool rooms at 16 - 18 °C prior to the analysis. The prepared samples were analyzed in the Chemical laboratory at the Faculty of Agriculture, Trakia University, Bulgaria.

Determination of mineral composition

The nitrogen content (N) was determined by the method of Kjeldahl (BDS – EN ISO 5983); phosphorus (P) – by colorimetry, measured at 470 nm on a SPEKOL 11 spectrophotometer; potassium (K); calcium (Ca), magnesium (Mg) with Perkin Elmer AANALYST-800 atomic absorption spectrometer [22].

Statistical analysis

The investigated parameters were measured in three replicates and the average results are presented as experimental results ± standard deviation (SD). To establish the influence of sowing rate, nitrogen fertilization rate and development phases on the mineral composition statistical procedures were applied by an ANOVA LSD test for statistical significance of the differences. After significant results were obtained by the ANOVA test, Tukey's HSD test was applied to all pairwise differences between means. The significant differences were tested and p values < 0.05 were considered statistically significant. To establish correlation dependencies and factor analysis, the software package for statistical data processing MS Excel software - 2010 was used.

RESULTS AND DISCUSSION

Nitrogen content for all three tested sowing rates was higher in the milk maturity phase (Table 1). Examining the results obtained on nitrogen content in the dry matter (DM) of tef biomass, an increase in its content was observed with an increase in nitrogen fertilization rates from 0 to 90 kg ha^{-1} in both analyzed phases, as established by some authors [4, 19]. The highest values were obtained by fertilizing with 90 kg ha^{-1} N and sowing rate of 15 kg ha^{-1}– 17.32 g kg^{-1} (milk maturity phase) and 16.72 g kg^{-1} (dough maturity phase).

In the milk maturity phase, the higher nitrogen content in the tef biomass compared to the control when using a nitrogen fertilization rate of 90 kg ha^{-1} was statistically very well proven at sowing rates of 10 and 15 kg ha^{-1} (P<0.001) and was not demonstrated at the highest sowing rate. At fertilization rate of 60 kg ha^{-1}, the differences in content were proven at all three sowing rates (P<0.05, P<0.01). For fertilization rate of 30 kg ha^{-1}, differences were proven only at a sowing rate of 15 kg ha^{-1} (P<0.05). In the dough maturity phase, the higher nitrogen content in the tef biomass compared to the control when using nitrogen fertilization rate of 90 kg ha^{-1} was statistically proven at sowing rates of 10 and 15 kg ha^{-1} (P<0.05, P<0.001). At a fertilization rate of 60 kg ha^{-1}, the differences in content were proven at the low sowing rate (P<0.01). For a fertilization rate of 30 kg ha^{-1}, no differences were statistically proven at all three sowing rates.

Table 1. Content of N, P, K, Ca and Mg in the tef biomass for 2021/2022 period, g kg⁻¹ DM

Variant	N	P	K	Ca	Mg
Milk maturity phase					
1 A_1B_1 (control)	13.71±2.0	2.70±0.33	7.60±0.54	3.66±0.16	1.42±0.19
2 A_1B_2	14.79±1.6[ba]	2.60±0.13[a]	7.60± 0.31[bc]	3.11±0.28[ab**]	1.38±0.20
3 A_1B_3	15.52±1.8[b*]	2.60±0.20[a]	7.49±0.42[b]	2.96±0.25[a***]	1.49±0.21
4 A_1B_4	16.74±3.8[cba***]	2.65±0.23[a]	6.61±0.23[a***]	3.19±0.32[ab**]	1.49±0.19
5 A_2B_1	14.11±2.3[a]	2.60±0.20[a]	6.70±0.39[a***]	3.03±0.09[ab***]	1.27±0.14
6 A_2B_2	15.27±1.6[ab*]	2.50±0.13[a]	7.01±0.07[a*]	2.87±0.37[a***]	1.34±0.13
7 A_2B_3	16.28±2.1[c**]	2.80±0.53[ab]	7.09±0.29[ab*]	3.00±0.19[a***]	1.37±0.20
8 A_2B_4	17.32±1.4[c***]	2.85±0.43[ab]	6.84±0.33[a**]	2.84±0.17[a***]	1.47±0.16
9 A_3B_1	13.57±2.5[a*]	2.65±0.03[a]	7.65±0.25[bc]	2.75±0.38[a***]	1.45±0.30
10 A_3B_2	14.16±2.7[a]	2.65±0.03[a]	7.02±0.20[*]	2.86±0.48[a***]	1.47±0.33
11 A_3B_3	15.91±2.3[b**]	2.55±0.03[a]	7.34±0.18[ab]	2.96±0.35[a***]	1.45±0.25
12 A_3B_4	15.03±3.1[b]	2.50±0.07[a]	6.91±0.15[a**]	2.82±0.24[a***]	1.58±0.27
Dough maturity phase					
13 A_1B_1	14.26±2.7[a]	3.20±0.47[b*]	8.40±0.18[c**]	2.68±0.28[a***]	1.34±0.22
14 A_1B_2	14.87±2.8[b]	2.70±0.40[ab]	8.25±0.17[c**]	3.55±0.11[b]	1.35±0.17
15 A_1B_3	16.05±2.0[cb**]	2.70±0.33[ab]	7.86±0.13[bc]	3.01±0.18[ab***]	1.32±0.16
16 A_1B_4	15.31±3.2[bc *]	3.00±0.07[b]	8.09±0.00[c*]	3.04±0.30[ab***]	1.36±0.23
17 A_2B_1	13.26±2.4[a]	2.60±0.27[a]	7.75±0.17[bc]	3.19±0.04[ab**]	1.40±0.14
18 A_2B_2	14.03±1.8[a]	2.75±0.37[ab]	8.04±0.28[c]	3.23±0.21[ab*]	1.48±0.17
19 A_2B_3	15.11±2.0[ba]	3.10±0.00[b]	7.26±0.48[ab]	2.78±0.07[a***]	1.47±0.11
20 A_2B_4	16.72±1.4[c***]	2.70±0.07[ab]	7.90±0.43[bc]	3.22±0.12 [ab*]	1.52±0.11
21 A_3B_1	13.86±2.8[a]	2.75±0.17[ab]	7.74±0.44 bc	3.33±0.03[ab]	1.55±0.04
22 A_3B_2	14.02±2.7[a]	2.65±0.23[a]	7.15±0.03 ab	3.48±0.03[ab]	1.47±0.19
23 A_3B_3	14.15±2.8[a]	2.65±0.23[a]	7.32±0.12 ab	2.89±0.35[a***]	1.37±0.17
24 A_3B_4	15.21±2.8[b]	2.45±0.03[a]	7.21±0.18 ab	2.87±0.10[a***]	1.38±0.15
LSD, P < 0.05	1.50	0.44	0.47	0.33	15.76
LSD, P < 0.01	2.01	0.58	0.62	0.44	20.96
LSD, P < 0.001	2.63	0.76	0.82	0.58	24.67

The data are presented as mean ± SD; *, **, *** – Statistically significant differences between variants and control at P<0.05; 0.01 and 0.001, respectively; a,b,c – Different letters indicate statistically significant differences between variants at P<0.05.

The content of phosphorus in the above-ground biomass of tef was 2.70 g kg⁻¹ DM in the control variant. A comparison between the harvesting phases shows that its content is higher in the dough maturity phase. The variation of the values depending on the sowing rates is within small limits. The highest values weere recorded at a sowing rate of 15 kg ha⁻¹ in the first phase and at a sowing rate of 10 kg ha⁻¹ in the second phase on average for the experimental period. Nitrogen fertilization with increasing rates did not lead to increased phosphorus content in tef biomass. The highest values were most often observed in the unfertilized variants. On average for the period of the experiment, higher phosphorus content in the tef biomass was statistically proven in the non-fertilized variant at a

sowing rate of 10 kg ha⁻¹ in the dough maturity phase, compared to the control, but with a low level of reliability (P<0.05). A lower phosphorus content was not statistically proven either in the milk phase or in the dough phase.

Compared to the macronutrients phosphorus, calcium and magnesium, potassium is in the largest amount. Compared by phases, potassium content is higher in the dough maturity phase. Fertilization with increasing nitrogen rates from 0 to 90 kg ha⁻¹ did not increase the potassium content in the tef biomass. The lowest potassium content on average for the study period was found in the milk maturity phase, in the variant fertilized with 90 kg ha⁻¹ N at a sowing rate of 10 kg ha⁻¹ (6.61 g kg⁻¹ DM) and in the non-fertilized variant at a sowing rate of 15 kg ha⁻¹

(6.70 g kg^{-1} DM). These lower values of potassium content in the above-ground biomass of tef were statistically very well proven (P<0.001). The lower values of potassium in the same phase at sowing rates of 15 and 20 kg ha^{-1} and the highest nitrogen fertilization rates were also well proven (P<0.01). The highest average potassium content was found in the dough maturity phase, at asowing rate of 10 kg ha^{-1}, in the non-fertilized variant and those fertilized with 30 and 90 kg ha^{-1} N (8.40, 8.25 and 8.09 g kg^{-1} DM, respectively). The higher values compared to the control variant were well proven statistically (P<0.01 and P<0.05).

The highest value of the Ca content depending on the sowing rates, was recorded at a sowing rate of 10 kg ha^{-1} in the milk maturity phase. No strict regularity was observed, according to which fertilization with increasing nitrogen rates leads to an increased content of calcium in the biomass of tef. The highest value (3.66 g kg^{-1} DM) was found for the control variant. For the experimental period, compared to the control, the lower content of calcium in the biomass of tef was statistically very well proven for all variants in the milk maturity phase, regardless of sowing rate (P < 0.001, P < 0.01). This also applies to the dough maturity phase in the variants fertilized with 60 and 90 kg ha^{-1} N (P < 0.001, P < 0.05).

The content of Mg in the biomass of tef varied in a narrow range – from 1.27 to 1.58 g kg^{-1} DM. When applying nitrogen fertilization with increasing doses from 0 to 90 kg ha^{-1} a slight increase in the magnesium content of tef biomass was observed. The highest value (1.58 g kg^{-1} DM) was in the variant fertilized with 90 kg ha^{-1} N, and the lowest (1.27 g kg^{-1} DM) - in the non-fertilized variant in the milk maturity phase. Compared to the control variant, no differences in magnesium content were statistically proven.

Vinyard *et al.* [4] and Ream *et al.* [12] found a decrease in crude protein content in the tef biomass when harvested in early-heading stages of maturity compared to late-heading stages of maturity. For the other macroelements, the changes were within narrow limits.

Significant positive correlations were established between the nitrogen content and the content of magnesium, phosphorus and calcium in the tef biomass, and negative - to the potassium content (Table 2). Well-proven positive correlation dependences were established between the calcium content and the magnesium content; between the phosphorus content and the magnesium and calcium content and negative between the potassium content and magnesium content. Authors [21] reported a highly significant correlation between Mg and Ca (r = 0.9272) in wheat, indicating a similar pattern for the effect of fertilization in tef.

Table 2. Correlation (r) dependences between the contents of macroelements .

	N	P	K	Ca	Mg
N	1	0.572**	-0.443**	0.555**	0.855**
P		1	-0.056	0.349**	0.575**
K			1	-0.135	-0.406**
Ca				1	0.686**
Mg					1

** – Statistical significance at P < 0.01

Factor analysis shows that the year conditions had the strongest and very well proven (P<0.001) effect on N, P, Ca and Mg content in the tef biomass (Table 3), while the K content was most influenced by the harvesting phase. Nitrogen fertilization rate had a strong effect on the N content (P<0.001). Sowing rate influenced the K content (P<0.01). Harvesting phase influenced the P content, while the Mg content was influenced by the year*sowing rate and year*phase (P<0.05).

Table 3. Influence of factors on the mineral composition of the tef biomass, %

Factors	N	P	K	Ca	Mg
Year	83.01***	41.88***	19.84***	41.54***	81.63***
Nitrogen rate	7.57***	1.33	5.58	6.10	0.83
Sowing rate	1.16	3.77	11.55**	2.94	0.88
Phase of maturity	0.55	3.38*	24.80***	1.68	0.08
Year*nitrogen rate	0.47	10.86	1.77	1.07	0.28
Year*sowing rate	1.94	0.99	1.68	1.23	2.39*
Year*phase	0.13	0.00	1.69	4.32	2.00*
Other factors	5.17	37.79	33.09	41.12	11.91

*, **, *** – Statistical significance at P<0.05; 0.01 and 0.001, respectively

Table 4. Ca:P ratio and Ca:Mg ratio of the tef biomass for the 2021/2022 period

Variant	Ca:P	Ca:Mg	Variant	Ca:P	Ca:Mg
Milk maturity phase			Dough maturity phase		
1 A_1B_1 (control)	1.4:1	2.6:1	13 A_1B_1	0.8:1	2.0:1
2 A_1B_2	1.2:1	2.2:1	14 A_1B_2	1.3:1	2.6:1
3 A_1B_3	1.1:1	2.0:1	15 A_1B_3	1.1:1	2.3:1
4 A_1B_4	1.2:1	2.1:1	16 A_1B_4	1.0:1	2.2:1
5 A_2B_1	1.2:1	2.4:1	17 A_2B_1	1.2:1	2.3:1
6 A_2B_2	1.1:1	2.1:1	18 A_2B_2	1.2:1	2.2:1
7 A_2B_3	1.1:1	2.2:1	19 A_2B_3	0.9:1	1.9:1
8 A_2B_4	1.0:1	1.9:1	20 A_2B_4	1.2:1	2.1:1
9 A_3B_1	1.0:1	1.9:1	21 A_3B_1	1.2:1	2.1:1
10 A_3B_2	1.1:1	1.9:1	22 A_3B_2	1.3:1	2.4:1
11 A_3B_3	1.2:1	2.0:1	23 A_3B_3	1.1:1	2.1:1
12 A_3B_4	1.1:1	1.8:1	24 A_3B_4	1.2:1	2.1:1

In the present study, the Ca:P ratio varied from 0.8:1 to 1.4:1 and the Ca:Mg ratio varied from 1.8:1 to 2.6:1 in the tef biomass (Table 4). The average values of these ratios during the two harvesting phases were equal. No regular influence of the studied sowing rates and nitrogen fertilizer rates on the Ca:P and Ca:Mg ratios was found.

Fujihara *et al.* [19] found high Ca:P ratio values (over 6:1, even over 12:1) in wheat straw and green-pea straw, while in wild grass, this ratio was below 6:1. Optimum Ca:P ratio in green feed for ruminants is 2:1, although that ratio can vary a lot [20]. In the present experiment, balanced ratios were found between Ca:P and Ca:Mg.

CONCLUSION

Nitrogen fertilization has a positive effect on the nitrogen content in the tef biomass. Nitrogen content is higher in the milk maturity phase. The highest nitrogen content was found at fertilization with 90 kg ha^{-1} of nitrogen at a sowing rate of 15 kg ha^{-1} in both harvesting phases.

With an increase in the sowing rate and nitrogen fertilization, a decrease in phosphorus, potassium and calcium content was observed. The use of different sowing rates and nitrogen fertilization doses does not significantly change the magnesium content of the tef biomass.

A strong positive correlation (r = 0.855) was found between the N and Mg contents, a good positive correlation – between the Ca and Mg contents (r = 0.686); between the N and P and Ca contents (r = 0.572; 0.555) and between the P and Mg contents (r = 0.575).

Climatic factors have the strongest effect on the content of macroelements in the tef biomass.

Nitrogen fertilization has a strong effect on N content, while the harvesting phase and the sowing rate influence the K content.

No regular influence of the tested sowing rates, nitrogen fertilizer rates and harvesting phases on the Ca:P and Ca:Mg ratios was found.

REFERENCES

1. G. Bultosa, Encyclopedia of food grains, **2**, 209 (2016).
2. S. Norberg, J. Roseberg, A. Charlton, C. Shock, Extension Service, Oregon State University, 2008.
3. Y. Gebru, B. Sbhatu, K. Kim, *Journal of Food Quality*, **1-6**, (2020).
4. J. R. Vinyard, J. B. Hall, J. E. Sprinkle, G. E. Chibisa, *Journal of Animal Science*, **96(8)**, 3420 (2018).
5. Z. Tadele, *Planta*, **250**, 677 (2019).
6. G. Cannarozzi, Z. Tadele, in: M. A. Chapman (ed.), Cham: Springer International Publishing, 2022, p. 27.
7. K. Twidwell, A. Boe, P. Casper, *SDSU Extension Extra Archives*, 278 (2002).
8. D. Miller, in: Proceedings of the 2009 California Alfalfa & Forage Symposium and Western Seed Conference, Reno, NV, USA, 2009.
9. R. Barretto, R. M. Buenavista, J. L. Rivera, S. Wang, P. V. Prasad, K. Siliveru, *International Journal of Food Science and Technology*, **56(7)**, 3125 (2021).
10. S. Ketema, Institute of Agricultural Research, Addis Abeba, Ethiopia, 1993.
11. D. Ivanova, *New Knowledge Journal of Science*, **7(2)**, 209 (2018).
12. N. Ream, A. Stevens, B. Hall, E. Chibisa, *Applied Animal Science*, **36**(5), 600 (2020).
13. Y. Nakata, S. Idota, M. Tobisa, Y. Ishii, *Agricultural Sciences*, **9**, 129 (2018).
14. M. Laca, Doctoral dissertation, Utah State University, 2021.
15. L. Sang-Hoon, L. Dong-Gi, L. Ki-Won, *Research Journal of Biotechnology*, **10**, 4 (2015).

16. A. Saylor, Doctoral dissertation, Kansas State University, 2017.
17. I. Kakabouki, A. Tzanidaki, A. Folina, I. Roussis, E. Tsiplakou, P. Papastylianou, D. Bilalis, *Agronomy Research,* **18**(2), 422 (2020).
18. E. Billman, I. Souza, R. Smith, K. Soder, N. Warren, A. Brito, *Crop, Forage & Turfgrass Management*, **8**(1) (2022).
19. T. Fujihara, C. Hosoda, T. Matsui, *Journal of Animal Sciences*, **8**(2), 179 (1995).
20. National Academies of Sciences, Engineering, and Medicine. Nutrient requirements of beef cattle, National Academy Press. Washington, D.C., 2016, p. 494.
21. X. Zhu, H. Zhang, L. Yan, *Journal of Plant Nutrition*, **34**(9), 1321 (2011).
22. AOAC international, Official methods of analysis of AOAC (18th edn., rev. 2), Association of Official Analytical Chemists Intern., Gaithersburg, MD, USA, 2007.

A complete ^{1}H and ^{13}C NMR data assignment for two substituted fluorenylspirohydantoins

M. Marinov[1], D. Stoitsov[2*], M. Frenkeva[2], P. Marinova[3], P. Penchev[2], N. Stoyanov[4]

[1] *Faculty of Plant Protection and Agroecology, Department of Chemistry and Phytopharmacy, Agricultural University – Plovdiv, Bulgaria*

[2] *Faculty of Chemistry, Department of Analytical Chemistry and Computer Chemistry, University of Plovdiv "Paisii Hilendarski", Plovdiv, Bulgaria*

[3] *Faculty of Chemistry, Department of Inorganic Chemistry with Methodology of Chemistry Education, University of Plovdiv "Paisii Hilendarski", Plovdiv, Bulgaria*

[4] *Department of Chemical, Food and Biotechnologies, "Angel Kanchev" University of Ruse, Razgrad Branch, Bulgaria*

This work presents the spectral characterization of 1',3'-bis(hydroxymethyl)-2'*H*,5'*H*-spiro[fluorene-9,4'-imidazolidine]-2',5'-dione and 2-bromo-2'*H*,5'*H*-spiro[fluorene-9,4'-imidazolidine]-2',5'-dione. The structures of the substituted fluorenylspirohydantoins were verified by ^{1}H NMR and ^{13}C NMR spectroscopy. In addition, 2D NMR spectra, including ^{1}H-^{1}H COSY, HMQC, HMBC and ^{1}H-^{1}H NOESY sequences, were used for a complete assignment of the ^{1}H and ^{13}C chemical shifts for each compound.

Keywords: 1',3'-bis(hydroxymethyl)-2'*H*,5'*H*-spiro[fluorene-9,4'-imidazolidine]-2',5'-dione, 2-bromo-2'*H*,5'*H*-spiro[fluorene-9,4'-imidazolidine]-2',5'-dione, NMR.

INTRODUCTION

Hydantoins usually serve as a base for synthesis of numerous biologically active derivatives [1]. Such examples are the fluorenylspirohydantoins where the hydantoin ring shares a carbon (C-5(9'), i.e. spiro-carbon) with the fluorene substituent (**1** and **2**). The compounds from this class possess antitumor and antibacterial activity [2-6] which explains their use as constituents in various pharmaceutical products. Also, they were found to coordinate metal ions which led up to the synthesis of some biologically active copper (II), nickel (II), platinum (II) and ruthenium (III) complexes [7-11]. It should be mentioned that the fluorenylspirohydantoins can act as aldose reductase inhibitors [12-14]. In addition, the fluorene-containing compounds find application in the manufacturing of organic light emitting diodes (OLED) [15].

The aim of this work was the structure verification of two substituted fluorenylspirohydantoins (**1** and **2**) by means of one- and two-dimensional NMR techniques, including ^{1}H-^{1}H COSY, HMQC, HMBC and ^{1}H-^{1}H NOESY sequences. 2D NMR spectra were proved to be useful for the verification of large and complex organic structures showing the correlations (spin couplings) between nuclei of the same or different kind in a given molecule [16, 17].Thus, valuable information can be extracted from the different types of 2D NMR spectra about the neighborhood and bonding of nuclei in complex structures, as it was reported in [16]. For example, the ^{1}H-^{1}H COSY spectrum shows mainly the spin couplings between vicinal hydrogens separated by three bonds (^{3}J$_{HH}$). Both HMQC (Heteronuclear Multiple Quantum Coherence) and HSQC (Heteronuclear Single Quantum Coherence) spectra provide information about the ^{1}J$_{CH}$ couplings between ^{13}C nuclei and protons attached to the corresponding carbons. Although HSQC ensures better ^{13}C resolution along the v$_1$-axis, it is used much less often, compared to HMQC, due to the following disadvantages [18-20]. Firstly, the HSQC experiment requires more than twice as many pulses as the basic HMQC sequence. Secondly, HSQC is more sensitive to variations in the inhomogeneity of the applied magnetic field and RF pulse to the sample and is more susceptible to artifacts than HMQC. Therefore, it is accepted that HMQC is more robust to experimental imperfections and changes than HSQC. As a result, it could be assumed that the single bond ^{1}H-^{13}C couplings in a given structural fragment that is present in similar complex organic structures can be detected with higher reproducibility when HMQC is used instead of HSQC.

On the other hand, the HMBC (Heteronuclear Multiple- Bond Coherence) spectrum reveals the spin couplings between ^{1}H and ^{13}C nuclei separated by two or more chemical bonds. Finally, the ^{1}H-^{1}H NOESY (Nuclear Overhauser Effect Spectroscopy)

spectrum shows the homonuclear correlations between protons spatially located from each other at a distance <5 Å [16]. All of this kind of various and valuable information, provided by the 2D NMR spectra, was used to fully assign the ^{1}H and ^{13}C NMR chemical shifts for 1',3'-bis(hydroxymethyl)-2'*H*,5'*H*-spiro[fluorene-9,4'-imidazolidine]-2',5'-dione (**1**) and 2-bromo-2'*H*,5'*H*-spiro[fluorene-9,4'-imidazolidine]-2',5'-dione (**2**).
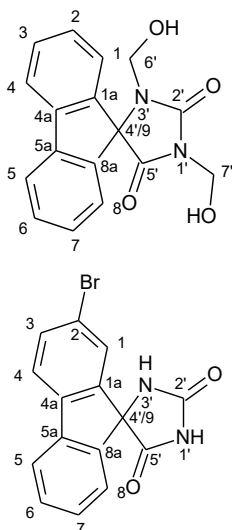
Fig. 1. Studied compounds **1**(top) and **2**(bottom)

EXPERIMENTAL

Instrumentation

Digital apparatus (SMP10) and Koffler apparatus were used for measuring the melting points of the synthesized compounds. The UV-Vis spectra were measured on a Perkin-Elmer Lambda 9 UV/Vis/NIR spectrophotometer from 200 nm to 1000 nm. The IR spectra were registered in KBr pellets on a VERTEX 70 FT-IR (Bruker Optics) spectrometer from 4000 cm^{-1} to 400 cm^{-1} at a resolution of 4 cm^{-1} with 9 scans. The Raman spectra (the stirred crystals placed in aluminium disc) were measured on RAM II (Bruker Optics) with a focused laser beam of 50 mW power of a Nd:YAG laser (1064 nm) from 4000 cm^{-1} to 51 cm^{-1} at a resolution of 2 cm^{-1} with 25 scans. The Attenuated Total Reflection FTIR (ATR) spectra were recorded with a VERTEX 70 FT-IR spectrometer (Bruker Optics). The ATR accessory is MIRacle™ with a one-reflection ZnSe element (PIKE Technology) and the stirred crystals were pressed by an anvil to the reflection element; the spectra are from 4000 cm^{-1} to 600 cm^{-1} at a resolution of 2 cm^{-1} with 16 scans.

^{1}H, ^{13}C and 2D NMR spectra of 1',3'-bis(hydroxymethyl)-2'*H*,5'*H*-spiro[fluorene-9,4'-imidazolidine]-2',5'-dione and 2-bromo-2'*H*,5'*H*-spiro[fluorene-9,4'-imidazolidine]-2',5'-dione were

recorded on a Bruker Avance II + 600MHz NMR spectrometer operating at 600.130MHz (^{1}H) and 150.903MHz (^{13}C), using TMS as internal standard and DMSO-d6 as solvent. The temperature was kept at 293.0 K for all NMR experiments. Chemical shifts are expressed in ppm and coupling constants (J) in Hertz. 1D and 2D NMR spectra were recorded using the standard Bruker pulse programs.

Materials

Puriss p.a. grade reagents purchased from Merck and Sigma-Aldrich were used in this study

Synthesis of 1',3'-bis(hydroxymethyl)-2'H,5'H-spiro[fluorene-9,4'-imidazolidine]-2',5'-dione

1',3'-Bis(hydroxymethyl)-2'*H*,5'*H*-spiro[fluorene-9,4'-imidazolidine]-2',5'-dione was obtained in crystal-like form by refluxing a mixture of (9'-fluorene)-spiro-5-hydantoin (5 g, 0.02 mol) and formalin (37%, 35 cm^3) for 6 hours. The product was filtered off and subsequently recrystallized from ethyl acetate/petroleum ether. The achieved yield was 4.60 g (82%). Melting point = 181–182°C; R$_f$= 0.65 (used mobile phases in a given volume ratio - ethyl acetate: petroleum ether = 1:2).

Synthesis of 2-bromo-2'H,5'H-spiro[fluorene-9,4'-imidazolidine]-2',5'-dione

2.55 cm^3 (8 g, 0.05 mol) of Br$_2$ in 25 cm^3 of glacial CH$_3$COOH was added dropwise to an aqueous suspension of (9'-fluorene)-spiro-5-hydantoin (5 g, 0.02 mol) in a hot glacial CH$_3$COOH (250 cm^3) and 2 g FeCl$_3$. The resulting mixture was stirred for 2.5 hours, heated once at 90-91 ^{o}C for 18 hours, then heated again at 100 ^{o}C for another 9 hours and diluted with water. The obtained crystals were filtered off and recrystallized from ethanol. The achieved yield was 4.60 g (70%). Melting point = 352-353 °C, R$_f$= 0.63 (used mobile phases in a given volume ratio - chloroform: methanol = 9:1). A modification of the procedure of Pan and Fletcher [2] was used to synthesize the compound 2-bromo-2'*H*,5'*H*-spiro[fluorene-9,4'-imidazolidine]-2',5'-dione. Thin layer chromatography, performed on Kieselgel 60 F$_{254}$, 0.2 mm Merck plates, was applied to determine the purity of both compounds.

UV-Vis and IR spectral data for 1',3'-bis(hydroxymethyl)-2'H,5'H-spiro[fluorene-9,4'-imidazolidine]-2',5'-dione

UV-Vis (DMSO): λ$_{max}$ = 273 nm.

IR (KBr, cm^{-1}): 3377 (υ(CO-H)), 3331 (υ(CO-H)), 3063 (υ(C-H), arom.), 3010 (υ(C-H), arom.), 2948 (υ$_{as}$(CH$_2$)), 2925 (υ$_{as}$(CH$_2$)), 2900 (υ$_s$(CH$_2$)), 2853 (υ$_s$(CH$_2$)), 1770 (υ(C=O)), 1704 (υ(C=O)),

1585, 1465, 1450, 1435, 1370, 1344, 1333, 1290, 1244, 1214, 1179, 1164, 1081($\upsilon(CH_2$-OH)), 1066, 1042, 1032 ($\upsilon(CH_2$-OH)), 1000, 952, 924, 873, 868, 789, 775, 738, 722, 651, 627, 602, 544, 515, 494, 461, 418.

Raman spectral bands, ν_{max} (cm^{-1}): 3086 (υ(C-H), arom.), 3071 (υ(C-H), arom.), 3043 (υ(C-H), arom.), 2949 ($\upsilon_{as}(CH_2)$), 1769 (υ(C=O)), 1606, 1585, 1488, 1357, 1299, 1242, 1215, 1184, 1159, 1151, 1106, 1080 ($\upsilon(CH_2$-OH)), 1023 ($\upsilon(CH_2$-OH)), 1001, 872, 790, 753, 689, 621, 603, 548, 515, 423.

ATR spectral bands, ν_{max} (cm^{-1}): 3372 (υ(CO-H)), 3319 (υ(CO-H)), 3063 (υ(C-H), arom.), 3011 (υ(C-H), arom.), 2948 ($\upsilon_{as}(CH_2)$), 1768 (υ(C=O)), 1699 (υ(C=O)), 1584, 1464, 1450, 1424, 1368, 1343, 1332, 1289, 1243, 1213, 1179, 1164, 1108, 1078 ($\upsilon(CH_2$-OH)), 1065, 1041, 1030 ($\upsilon(CH_2$-OH)), 1000, 951, 924, 873, 868, 788, 774, 736, 649, 620.

UV-Vis and IR spectral data for 2-bromo-2'H,5'H-spiro[fluorene-9,4'-imidazolidine]-2',5'-dione

UV-Vis (DMSO): λ_{max} = 282 nm, 255 nm.

IR (KBr, cm^{-1}): 3349 (υ(N-H)), 3194 (υ(N-H)), 3069 (υ(C-H), arom.), 2975 ($\upsilon_{as}(CH_2)$), 2753, 1782 (υ(C=O)), 1756 (υ(C=O)), 1717 (υ(C=O)), 1607, 1483, 1467, 1449, 1398, 1294, 1242, 1204, 1179, 1156, 1130, 1113, 1086, 1052, 1023, 982, 953, 884, 826, 793, 782, 750, 734, 723, 693, 661, 655, 638, 564, 527, 510, 476, 447, 428.

Raman spectral bands, ν_{max} (cm^{-1}): 3071 (υ(C-H), arom.), 3050 (υ(C-H), arom.), 1763 (υ(C=O)), 1606, 1576, 1484, 1349, 1295, 1265, 1230, 1202, 1157, 1128, 1114, 1063, 1029, 989, 941, 762, 730, 692, 644, 529, 441.

ATR spectral bands, ν_{max} (cm^{-1}): 3354 (υ(N-H)), 3185 (υ(N-H)), 3073 (υ(C-H), arom.), 2716, 2369, 1951, 1779 (υ(C=O)), 1713 (υ(C=O)), 1606, 1576, 1507, 1484, 1466, 1449, 1395, 1293, 1264, 1235, 1202, 1179, 1156, 1129, 1113, 1087, 1062, 1015, 988, 953, 868, 823, 759, 742, 732, 718, 692, 654, 638.

Discussion of structure verification of **1** presented in Table 1

The ^{13}C NMR spectrum of 1',3'-bis(hydroxymethyl)-2'*H*,5'*H*-spiro[fluorene-9,4'-imidazolidine]-2',5'-dione (**1**) showed 11 signals – 6 pairs of atoms were magnetically equivalent (Table 1). The two signals with the highest chemical shifts

in ^{13}C NMR spectrum, δ_C 155.34 ppm and δ_C 171.10 ppm, were assigned to the carbonyl carbons, C$^{2'}$=O and C$^{5'}$=O, respectively. The signal at δ_C 73.71 ppm was for the spiro-carbon, C-4'/9. The DEPT 135 spectrum showed two negative signals at δ_C 63,83 ppm and 61.89 ppm confirming the presence of methylene groups in the structure. The HMQC spectrum showed correlations between the corresponding pairs of signals, (δ_H 4.40 ppm – δ_C 63.83 ppm) and (δ_H 4.91 ppm- δ_C 61.89 ppm). Additionally, two HMBC correlations were found for each of the signals at δ_H 4.40 ppm (with δ_C 73.71 ppm and δ_C 155.34 ppm) and δ_H 4.91 ppm (with δ_C 155.34 ppm and δ_C 171.10 ppm). The protons in the C$^{6'}$H$_2$ group are separated by three bonds only from the spiro-carbon, C-4'/9 (δ_C 73.71 ppm), compared to the protons in the C$^{7'}$H$_2$ group which are located at three bonds away from each of the two carbonyl carbons. Consequently, the signals at δ_H 4.40 ppm and δ_C 63.83 ppm were assigned to the protons and carbon in the C$^{6'}$H$_2$ group, respectively, while the signals at δ_H 4.91 ppm and δ_C 61.89 ppm were for the protons and carbon in the C$^{7'}$H$_2$ group. The COSY spectrum showed the following correlations, (δ_H 4.40 ppm - δ_H 5.77 ppm) and (δ_H 4.91 ppm - δ_H 6.57 ppm). Also, two HMBC correlations were found, (δ_H 5.77 ppm – δ_C 63.83 ppm) and (δ_H 6,57 ppm - δ_C 61.89 ppm). The lack of HMQC correlations for the signals at δ_H 5.77 ppm and δ_H 6.57 ppm showed that the protons of the hydroxyl groups are bonded to atoms that are different from C. Therefore, the signal with the chemical shift δ_H 5.77 ppm was assigned to the proton in the hydroxyl group which is bonded to the methylene group, C$^{6'}$H$_2$. Analogously, the signal with the chemical shift δ_H 6.57 ppm was assigned to the proton in the other hydroxyl group which is bonded to the methylene group, C$^{7'}$H$_2$.

The strong HMBC correlation, (δ_H 7.37 ppm - δ_C 73.71 ppm), showed the 3-bond coupling of H-1/8 with the spiro-carbon, C-4'/9. It is less likely to find HMBC correlations of H-2/7, H-3/6 or H-4/5 with C-4'/9, because these protons are separated from the spiro-carbon by more than three bonds. In addition, there is a COSY correlation, (δ_H 7.37 ppm - δ_H 7.35 ppm), showing the coupling of H-1/8 with H-2/7. Due to the fact that only the meta (vicinal) coupling ($^3J_{CH}$) in benzene rings is usually resolved, it is possible to assign the quaternary carbons, C-1a/8a and C-4a/5a [21, p. 27].

Table 1. ^{1}H and ^{13}C NMR spectral data and ^{1}H–^{1}H COSY and HMBC correlations for **1)** [600.130 MHz (^{1}H) and 150.903 MHz (^{13}C)][a].

Atom	δ (^{13}C), ppm	DEPT	δ (^{1}H), ppm	Multiplicity (J, Hz)	^{1}H-^{1}H COSY [b]	HMBC[b]
2' (C=O)	155.34	C				
5' (C=O)	171.10	C				
6'	63.83	CH$_2$	4.40	d (6.7)	OH (C-6')	2'. 4'/9
7'	61.89	CH$_2$	4.91	d (7.0)	OH (C-7')	2'. 5'
4'/9	73.71	C				
1/8	124.27	CH	7.37[c]	m	2	3. 4a . 4'/9
1a/8a	140.68	C				
2/7	128.15	CH	7.35[c]	m	1.3. 4[e]	1[e], 1a, 3[d], 4
3/6	130.08	CH	7.51	td (7.4; 1.4)	2, 4	1, 2[d], 4[e], 4a
4/5	120.86	CH	7.93	d (7.6)	2[e], 3	1[e], 2, 1a
4a/5a	141,15	C				
OH (C-7')			6,57	t (7,1)	7'	7'
OH (C-6')			5,77	t (6,8)	6'	6'

[a] In DMSO-d$_6$ solution. All these assignments were in agreement with COSY, HMQC and HMBC spectra.

[b] For brevity these correlations are given only in one of the benzene rings.

[c] Data from HMQC.

[d] These correlations are weak.

[e] These correlations are extremely weak.

In this case, there are two strong HMBC correlations, (δ$_H$ 7.37 ppm - δ$_C$ 141.15 ppm) and (δ$_H$ 7.35 ppm - δ$_C$ 140.68 ppm), indicating the coupling of the protons, H-1/8 and H-2/7, with the quaternary carbons, C-4a/5a and C-1a/8a.

It must be mentioned that the DEPT 135 spectrum didn't show any peaks at δ$_C$ 140.68 ppm and δ$_C$ 141.15 ppm supporting the hypothesis that the corresponding chemical shifts can be assigned to C-1a/8a and C-4a/5a. On the other hand, the multiplet structure of the signals at δ$_H$ 7.51 ppm (triplet of doublets) and δ$_H$ 7.93 (doublet) in addition to the following strong HMBC correlations, (δ$_H$ 7.51 ppm – δ$_C$ 141.15 ppm) and (δ$_H$ 7.93 ppm - δ$_C$ 140.68 ppm), showed that the signals with the chemical shifts δ$_H$ 7.51 ppm and δ$_H$ 7.93 were for H-3/6 and H-4/5, respectively. In addition, the COSY spectrum showed two strong correlations of H-3/6 (δ$_H$ 7.51 ppm) with both H-2/7 (δ$_H$ 7.35 ppm) and H-4/5 (δ$_H$ 7.93 ppm) as well as one weak correlation between H-2/7 and H-4/5.

Discussion of structure verification of 2 presented in Table 2

The ^{13}C NMR spectrum of 2-bromo-2'*H*,5'*H*-spiro[fluorene-9,4'-imidazolidine]-2',5'-dione **(2)** showed 15 signals corresponding to the number of

carbons in the compound (Table 2). Analogously to the previous structure, the signals at δ$_C$ 72.16 ppm, δ$_C$ 157.52 ppm and δ$_C$ 173.56 ppm were assigned to the spiro- and carbonyl carbons, C-4'/9, C^2=O and C^5=O, respectively. The ^{1}H NMR spectrum showed two singlet peaks at δ$_H$ 8.61 ppm and δ$_H$ 11.31 ppm corresponding to the protons in the NH groups. In comparison with the proton in the N^{3}H group, the proton in the N^{1}H group is located closer to the carbonyl group, C^5=O, thus, it would be more strongly deshielded by the magnetic anisotropic effect of the two carbonyl groups [21, page 58]. Therefore, the singlet with the highest chemical shift (δ$_H$ 11.31 ppm) can be assumed to correspond to the proton in the N^{1}H group. Based on the following HMBC correlations, (δ$_H$ 8.61 ppm - δ$_C$ 72.16 ppm; δ$_H$ 8.61 ppm - δ$_C$ 157.52 ppm; δ$_H$ 8.61 ppm - δ$_C$ 173.56 ppm), the signal with the chemical shift δ$_H$ 8.61 ppm was assigned to the proton in the N^{3}H group, separated by two bonds only from the spiro-carbon, C-4'/9 (δ$_C$ 72.16 ppm), compared to the proton in the N^{1}H group. On the other hand, no HMBC and COSY correlations were found for the singlet at δ$_H$ 11,31 ppm, assigned to the proton in the N^{1}H group. A possible reason could be the participation of the proton in the N^{1}H group in an intermolecular or intramolecular proton exchange

[22, p. 104]. As can be seen from Fig. 10, the widened shape of the singlet at δ_H 11.31 ppm indicates that the proton in the N^{1}H group could participate in an intermediate exchange [22, pp. 99-101].

The HMBC spectrum showed one strong and one weak correlation, (δ_H 7.48 ppm – δ_C 72.16 ppm) and (δ_H 7.75 ppm - δ_C 72.16 ppm), respectively. While there were not any COSY correlations for the singlet at δ_H 7.75 ppm, one weak COSY correlation was found between the doublet at δ_H 7.48 ppm and the triplet at δ_H 7.40 ppm. Additionally, the following HMBC correlations were found – (δ_H 7.75 ppm – δ_C 121.08 ppm), (δ_H 7.75 ppm – δ_C 132.76 ppm), (δ_H 7.75 ppm – δ_C 140.00 ppm), (δ_H 7.48 ppm – δ_C 130.00 ppm) and (δ_H 7.48 ppm – δ_C 139.52 ppm). It should be mentioned that the DEPT 135 spectrum didn't show any peaks at the chemical shifts (δ_C) 121.08 ppm, 139.52 ppm, 140.00 ppm, 142.85 ppm and 145.12 ppm. As it was mentioned previously, only the meta (vicinal) coupling ($^3J_{CH}$) is usually resolved in the benzene rings [21, page 27]. Thus, the signals at δ_H 7.48 ppm and δ_H 7.75 ppm were assigned to the protons, H-8 and H-1, separated by three bonds only from the spiro-carbon, C-4'/9 (δ_C

72.16 ppm), while the peaks at δ_C 130.00 ppm, δ_C 132.76 ppm, δ_C 139.52 ppm and δ_C 140.00 ppm were assigned correspondingly to C-6, C-3, C-5a and C-4a. Meanwhile, the triplet at δ_H 7.40 ppm was assigned to H-7, as one additional HMBC correlation was found, (δ_H 7.40 ppm - δ_C 142.85 ppm), showing the coupling of H-7 with C-8a.

The HMQC spectrum showed that the carbon, C-3, is bonded to the proton, H-3, with the chemical shift δ_H 7,70 ppm. In this case, only one COSY correlation, (δ_H 7.70 ppm - δ_H 7.88 ppm), was found for H-3. Also, one of the HMBC correlations of H-3 is with C-4a, (δ_H 7.70 ppm - δ_C 140.00 ppm). Two HMBC correlations were found, (δ_H 7.88 ppm – δ_C 139.52 ppm) and (δ_H 7.88 ppm – δ_C 145.12 ppm), showing the 3-bond coupling between H-4 and the quaternary carbons, C-5a and C-1a. In addition, there was one NOESY correlation between H-3 and H-4, (δ_H 7.70 ppm - δ_H 7.88 ppm) (Fig. 16), supporting the hypothesis that the bromine is bonded to the carbon, C-2, with the chemical shift (δ_C) 121.08 ppm. Another weak COSY correlation of H-7 (δ_H 7.40 ppm) with H-6 (δ_H 7.50 ppm) was found as there was a strong HMBC correlation between H-7 and C-5 (δ_C 121.05 ppm).

Table 2. ^{1}H and ^{13}C NMR spectral data and ^{1}H–^{1}H COSY and HMBC correlations for **2)** [600.130 MHz (^{1}H) and 150.903 MHz (^{13}C)][a]

Atom	δ (^{13}C), ppm	DEPT	δ (^{1}H), ppm	Multiplicity (J, Hz)	^{1}H-^{1}H COSY	HMBC
3' (NH)			8,61	s		2', 5', 4'/9
2' (C=O)	157,52	C				
1' (NH)			11,31	s		
5' (C=O)	173,56	C				
4'/9	72,16	C				
1	126,83	CH	7,75	s		2, 3, 4a, 4'/9[b]
1a	145,12	C				
2	121,08	C				
3	132,76	CH	7,70	dd (8,2; 1,2)	4	1, 2, 4a
4	122,63	CH	7,88	d(8,1)	3	1a, 2 , 3[b], 5a
4a	140,00	C				
5	121,05	CH	7,92	d (7,5)	6	4a, 8a, 7
5a	139,52	C				
6	130,00	CH	7,50	d(7,5)	5, 7[b]	5a, 8
7	128,81	CH	7,40	t(7,4)	6[b], 8[b]	5, 8a
8	123,54	CH	7,48	d(7,5)	7[b]	5a, 6, 4'/9
8a	142,85	C				

[a] In DMSO-d$_6$ solution. All these assignments were in agreement with COSY, HMQC and HMBC spectra.
[b] These correlations are weak.

Moreover, the COSY spectrum showed a strong correlation of H-6 (δ_H 7.50 ppm) with H-5 (δ_H 7.92 ppm) while three strong HMBC correlations of H-5 with C-7 (δ_C 128.81 ppm), C-4a (δ_C 140.00 ppm) and C-8a (δ_C 142.85 ppm) were additionally found.

CONCLUSION

This work highlighted the importance of the 2D NMR spectroscopy in the structure verification of organic compounds. The thorough analysis of the ^{1}H-^{1}H COSY, HMQC, HMBC and ^{1}H-^{1}H NOESY spectra ensured the accurate and complete assignment of the ^{1}H and ^{13}C NMR chemical shifts for the two substituted fluorenylspirohydantoins - 1',3'-bis(hydroxymethyl)-2'*H*,5'*H*-spiro[fluorene-9,4'-imidazolidine]-2',5'-dione and 2-bromo-2'*H*,5'*H*-spiro[fluorene-9,4'-imidazolidine]-2',5'-dione.

REFERENCES

1. E. Kleinpeter, *Struct. Chem.*, **8**, 161 (1997).
2. H. L. Pan, T. L. Fletcher, *J. Med. Chem.*, **10**, 957 (1967).
3. S. Samanta, A. Pain, M. Ghosh, S. Dutta, U. Sanyal, *Exp. Oncol.*, **27**, 279 (2005).
4. P. Marinova, M. Marinov, M. Kazakova, Y. Feodorova, A. Slavchev, D. Blazheva, D. Georgiev, P. Penchev, V. Sarafian, N. Stoyanov, *Acta Chim. Slov.,* **63,** 26 (2016).
5. P. Marinova, M. Marinov, Y. Feodorova, M. Kazakova, D. Georgiev, E. Trendafilova, P. Penchev, V. Sarafian, N. Stoyanov, *Proceedings*, **52**, 33 (2013).
6. P. Marinova, M. Marinov, M. Kazakova, Y. Feodorova, D. Blazheva, A. Slavchev, H. Sbirkova-Dimitrova, V. Sarafian, N.Stoyanov, *Russian Journal of General Chemistry*, **91**, 939 (2021).
7. P. Marinova, M. Marinov, M. Kazakova, Y. Feodorova, D. Blazheva, A. Slavchev, D. Georgiev, I. Nikolova, H. Sbirkova-Dimitrova, V. Sarafian, N.

Stoyanov, *Russian Journal of Inorganic Chemistry*, **66**, 1925 (2021).
8. A. Ahmedova, G. Pavlović, M. Marinov, P. Marinova, G. Momekov, K. Paradowska, S. Yordanova, S. Stoyanov, N. Vassilev, N. Stoyanov, *Inorganica Chimica Acta*, **528**, 120605 (2021).
9. P. Marinova, M. Marinov, D. Georgiev, M. Becheva, P. Penchev, N. Stoyanov, *Rev. Roum. Chim*, **64**, 595, (2019).
10. A. Ahmedova, P. Marinova, K. Paradowska, M. Marinov, M. Mitewa, *J. Mol. Struct.*, **892**, 13, (2008).
11. P. Marinova, M. Marinov, M. Kazakova, Y. Feodorova, P. Penchev, V. Sarafian, N. Stoyanov, *Biotechnol. Biotec. Eq.,* **28**, 316 (2014).
12. B. M. York, *US Patent* No 4,438,272 (1984).
13. P. Bovy, A. Lenaers, M. Callaert, N. Herickx, C. Gillet, J. Roba, J. M. Dethy, B. Callaert-Deveen, M. Janssens, *Eur. J. Med. Chem.*, **23**, 165 (1988).
14. P. Bovy, R. C. Gillet, A. Lenaers, P. Niebes, J. Roba, G. Lambelin, *US Patent* No 4, 853,401 (1989).
15. K. R. J. Thomas, J. T. Lin, C. M. Tsai, H. C. Lin, *Tetrahedron*, **62**, 3517 (2006).
16. M. Elyashberg, *TrAC Trends in Analytical Chemistry*, **69**, 88 (2015).
17. P. Penchev, N. Stoyanov, M. Marinov, *Spectrochimica Acta Part A: Molecular and Biomolecular Spectroscopy*, **78**, 559 (2011).
18. J. Lambert, E. Mazzola, Nuclear Magnetic Resonance Spectroscopy: Introduction to Principles, Applications, and Experimental Methods, Pearson Education Inc., Upper Saddle River, New Jersey 07458, USA, 2004, p. 258.
19. W. Reynolds, D. Burns, *Annual Reports on NMR Spectroscopy*, **76**, 1 (2012).
20. P. Mandal, A. Majumdar, *Concepts in Magnetic Resonance Part A*, **20A**, 1 (2004).
21. E. Breitmaier, Structure Elucidation by NMR in Organic Chemistry: A Practical Guide, John Wiley & Sons Ltd, Chichester, U.K., 2002.
22. S. Spasov, L. Kamenov, Nuclear magnetic resonance in organic chemistry, Science and Art Ltd, Sofia, Bulgaria, 1971 (in Bulgarian).

Investigation of the electret properties of PDLA/PEC porous composite films

A. P. Viraneva*, M. G. Marudova, A. V. Grigorov, T. A. Yovcheva

University of Plovdiv "Paisii Hilendarski", Department of Physics, 24 Tzar Asen Str., 4000 Plovdiv, Bulgaria

Received November 3, 2023; Revised: April 11, 2024

In the present paper the influence of both time and low pressure on the surface potential decay of porous composite films of poly(D-lactic acid) and poly(ε-caprolactone) was investigated. The samples were charged in a corona discharge by means of a corona triode system under room conditions. Positive or negative voltage was applied to the corona electrode and voltage of the same polarity as that of the corona electrode was applied to the grid. After charging, the initial surface potential was measured using the method of the vibrating electrode with compensation. Two groups of tests were performed. In the first group, after charging, the electrets were placed into a vacuum chamber where the pressure was reduced step by step in the range from 1000 mbar to 0.1 mbar. At each step the samples were stored for 1 minute. After that the electrets were removed from the vacuum chamber, their surface potential was measured again and the normalized surface potential was calculated. The influence of low pressure was analyzed by the equation that describes processes of desorption from the electret's surface. In the second group, after charging, the electret surface potential was measured by the time of storage. The possible surface potential decay mechanisms responsible for the electret's behavior were discussed. It was established that the surface potential decay depends on both corona polarity and type of films. It was shown that the samples charged in a positive corona are more stable than those charged in a negative corona.

Keywords: corona discharge, porous composite films

INTRODUCTION

Over the last two decades, biodegradable polymers, such as poly(lactic acid) PLA, poly(glycolic acid) PGA and poly(ε-caprolactone) PEC, belonging to the family of poly(a-hydroxyesters), have emerged as a class of biomaterials of growing interest for application in surgery, drug delivery, tissue engineering, food industry, etc. [1, 2]. Polymer blending of two different kinds of biopolymers in different ratios has been demonstrated to improve the film properties, when compared to pure films [3, 4]. Different modification methods such as corona discharge treatment and lyophilizing [5-7] can further improve biocompatibility and assist in the creation of stable porous structures. In order to obtain stable electrets for different applications the influence of different factors as time of storage, temperature, humidity, low pressure, etc., on the charge decay has been studied [8]. In this paper the influence of time of storage and low pressure on the surface potential decay of porous composite films PDLA/PEC was investigated.

MATERIALS AND METHODS

Sample preparation

In the present paper two biodegradable polymers were used. Poly(D-lactic acid) (PDLA) was purchased from Sigma-Aldrich and poly(ε-caprolactone) (PEC) from Lactel Absorbable Polymers (USA). Both polymers were dissolved in 1,4 dioxane at 10 % w/v and the resulting solutions were used for the creation of a mixture at the desired mass ratio of 50/50. Additionally, two further films of pure PDLA and PEC with the same polymer concentrations were also created. All solutions were placed in Petri dishes in a freezer at -16 °C until completely frozen. After that the frozen solution was placed in a lyophilizer for 3 days and dried until the solvent evaporates. The obtained films were kept for 24 hours in a desiccator at room temperature and relative humidity.

Corona charging and surface potential measurement

Samples with 30 mm diameter were cut from the composite films. The charging of the samples in a corona discharge was carried out by means of a conventional corona triode system consisting of a corona electrode (needle), a grounded plate electrode and a grid placed between them. The samples were charged under room conditions for 1 minute. Positive or negative 5 kV voltage was applied to the corona electrode. Voltages of 1 kV of the same polarity as that of the corona electrode were applied to the grid. The electrets surface potential of the charged samples was measured by the vibrating electrode method with compensation and the estimated error was less than 5%. The

normalized surface potentials V/V_0 were calculated, as the value V_0 is the initial surface potential measured about 1 minute just after charging the electrets.

Low-pressure measurement

After charging to the initial surface potential V_0, the samples were placed into a vacuum chamber, consisting of isolated bases and a jar bell, at low pressure. The pressures created in the vacuum chamber were 0.1 mbar, 1 mbar, 5 mbar, 10 mbar, 20 mbar, 40 mbar, 66 mbar, 120 mbar, 250 mbar, 500 mbar, 750 mbar and 1000 mbar. The pressure in the vacuum chamber was reduced step by step in the range from 1000 mbar to 0.1 mbar. At each step the samples were kept at the respective constant pressure for 1 minute. After that the electrets were removed from the vacuum chamber, the surface potential V was measured again and the normalized surface potential V/V_0 was calculated.

Differential scanning calorimetry (DSC)

A method of differential scanning calorimetry was applied for determining the phase state of the samples. The measurements were carried out with DSC 204F1 Phoenix (Netzsch Gerätebau GmbH, Germany) which was calibrated with an indium standard (T_m=156.6 ºC, ΔH_m=28.5 J/g). About 5 mg of the films were placed and sealed in an aluminium pan. An identical empty pan was used as a reference. The measurements were performed in argon atmosphere in the temperature range from 20 °C to 250 °C at a heating rate of 10 °C/min. The DSC thermograms were analysed by Netzsch Proteus – Thermal Analysis software.

The degrees of crystallinity for PEC (χ_{PEC}) and PDLA (χ_{PDLA}) compounds in the films were calculated based on the equation:

$$\chi_{PEC/PDLA} = \frac{\Delta H_m(PEC/PDLA)}{\Delta H_m^0(PEC/PDLA) \cdot \omega_{PEC/PDLA}} \cdot 100 \quad (1)$$

where $\Delta H_m(PEC/PDLA)$ is the specific melting enthalpy [J.g^{-1}] of the PEC or PDLA; ΔH_m^0 is the melting enthalpy of 100 % crystalline polymer ($\Delta H_m^0 = 139.3$ J.g^{-1} for PEC [9]) and $\Delta H_m^0 = 106.0$ J.g^{-1} for PDLA [10], and $\omega_{PEC/PDLA}$ is the mass fraction of PEC/PDLA, respectively.

The total crystallinity was calculated according to equation (2):

$$\chi = \omega_{PEC}\chi_{PEC} + \omega_{PDLA}\chi_{PDLA} \quad (2)$$

RESULTS AND DISCUSSION

According to the experimentally obtained thermograms, the melting transitions of the two components in the mixed films take place at temperatures of 67 °C and 155 °C, which are the melting temperatures of the pure substances. This observation indicated that PEC and PDLA were not miscible at molecular level. Similar results were reported by other authors [11].

The degrees of crystallinity of PEC and PDLA, and the total degree of crystallinity of the composite films are presented in Figure 1.

Based on the findings presented in Figure 1, it is evident that introducing PDLA into PEC leads to an augmentation in crystallinity. Likewise, the incorporation of PEC into PDLA has a similar, albeit more pronounced, impact on elevating crystallinity. Consequently, one could speculate that the introduction of inhomogeneities and the existence of two phases within the mixtures result in a nucleation effect and contribute to the heightened degree of crystallinity. The total crystallinity of the films decreases when the content of PDLA increases.
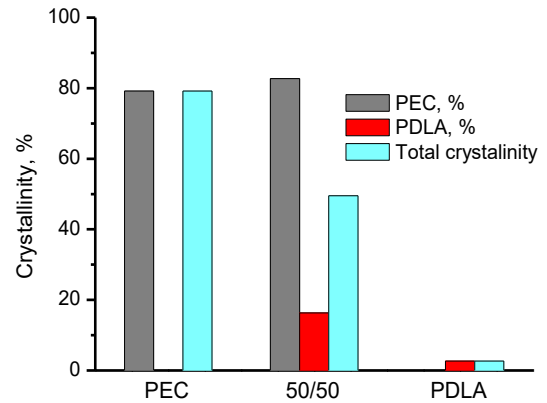
Figure 1. Degrees of crystallinity of PDLA/PEC films.

Time storage influence on the electrets surface potential decay

The normalized surface potential (dependence) on the storage time for positively and negatively charged PDLA, 50/50 and PEC electrets was studied for 6 hours. The surface potential was measured once every 5 minutes for the first 30 minutes, during which the charge was rapidly decaying. After this period, the surface potential was measured more rarely, with the steady-state values of the normalized surface potential (6 hours) stabilizing for all investigated electrets. The steady-state values of the surface potential for PDLA, 50/50 and PEC electrets are presented in Figure 2.
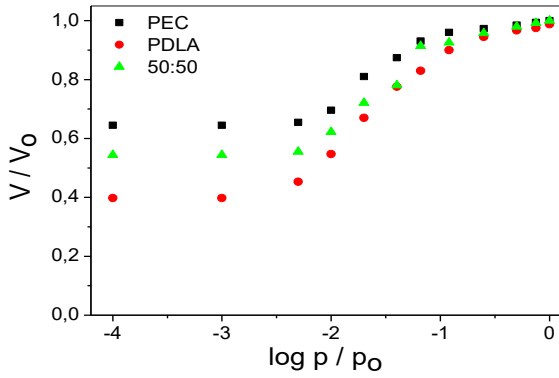
Figure 2. The steady-state values of the normalized surface potential at a time of 6 hours for all investigated electrets.

The obtained experimental results demonstrate the following features:

✓ The steady state values of the normalized surface potential for the samples charged in a positive corona are higher than those for the samples charged in a negative corona for all investigated samples. This was observed earlier in [12].

✓ The steady state values of the normalized surface potential are highest for the PEC electrets irrespective of the corona polarity.

This is probably due to the different degrees of crystallinity, determined by DSC method (see Figure 1).

Low-pressure influence on the electrets surface potential decay

The dependences of the normalized surface potential V/V_0 on the low pressure for positively and negatively charged PDLA, 50/50 and PEC films were investigated. The dependences are presented in Figures 3 and 4.
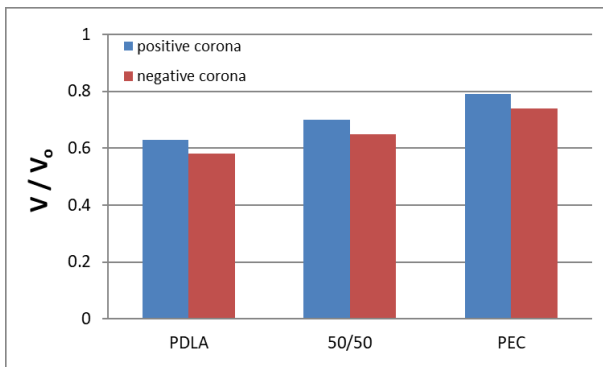
Figure 3. The normalized surface potential dependences on the normalized pressure for positively charged porous composite electrets.

In Figures 3 and 4 the symbol p_0 marks the atmospheric pressure and p is the pressure created in the vacuum chamber. Each point in the figures is a mean value of 5 samples. The calculated standard deviation was 5 % better than the mean value with confidence level 95 %.
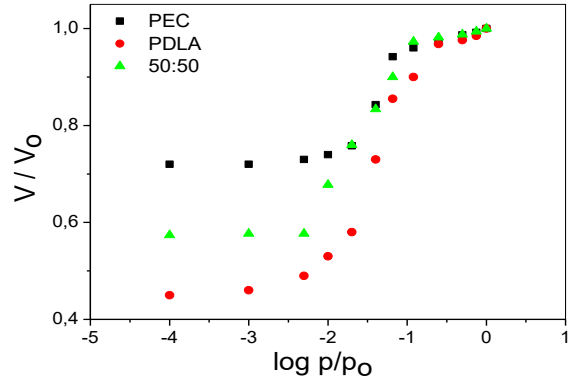
Figure 4. The normalized surface potential dependences on the normalized pressure for negatively charged porous composite electrets.

Table 1. The steady-state values of the normalized surface potential at a pressure of 0.1 mbar for all investigated electrets.

Samples	V/V_0	
	Positive corona	Negative corona
PDLA	0.45	0.4
50/50	0.57	0.54
PEC	0.72	0.65

The results presented in Figures 3 and 4 and Table 1 show that:

✓ Each curve consists of three parts. Similar behavior has also been observed in [13].

✓ The steady-state values of the normalized surface potential at a pressure of 0.1 mbar for the samples charged in a positive corona are higher than those for the samples charged in a negative corona independently of the sample type.

✓ The steady-state values of the normalized surface potential at a pressure of 0.1 mbar are highest for PEC samples independently of the corona polarity. We assume that this is due to the different structures of the polymers, which leads to the formation of different localized surface states that capture charges.

Table 2. Values of the parameters *a*, *b*, *c* and *d* obtained by fitting data to the equation 3.

Samples	Positive corona				Negative corona			
	a	*b*	*c*	*d*	*a*	*b*	*c*	*d*
PDLA	0.46± 0.02	0.53± 0.02	-1.42± 0.02	0.45± 0.02	0.39± 0.01	0.59± 0.01	-1.62± 0.01	0.61± 0.01
50/50	0.57± 0.02	0.43± 0.02	-1.60± 0.02	0.51± 0.02	0.54± 0.02	0.45± 0.02	-1.53± 0.02	0.51± 0.02
PEC	0.73± 0.01	0.26± 0.01	-1.38± 0.01	0.27± 0.01	0.64± 0.01	0.35± 0.01	-1.62± 0.01	0.45± 0.01

The results presented in Figures 3 and 4 were analyzed by the equation that describes the processes of desorption from the electrets surface accompanied with surface diffusion. This equation was earlier described in [14].

$$\theta = a + \frac{1}{2}b\left(1 + erf\left(\frac{x-c}{\sqrt{2}d}\right)\right) \tag{3}$$

where $\theta = V/V_0$ is the normalized surface potential, $x = \log(p/p_0)$ and *a*, *b*, *c* and *d* are parameters. The parameter values for all investigated samples were obtained by fitting and they are presented in Table 2.

If one knows the initial surface potential value of different porous composite electrets, the data obtained for the parameters could be used to determine the pressure range in which the potential sharp decay is occurring. This has a practical benefit because of the fact that these composite films can be used under conditions of reduced pressures.

CONCLUSION

In this study the influence of different factors on the surface potential decay of porous composite films PDLA/PEC was investigated. It was established that the steady-state values of the normalized surface potential for PEC electrets are the highest compared to other investigated samples. This may be due to the highest value of the degree of crystallinity determined by the DSC method. It was also established that the low-pressure curves consist of three parts and these curves were analyzed by the equation that describes the processes of desorption from the electrets surface accompanied with surface diffusion. The results show that the obtained porous composite films PDLA/PEC possess excellent electret properties.

REFERENCES

1. V. Guarino, F. Causa, P. Taddei, M. di Foggia, G. Ciapetti, D. Martini, C. Fagnano, N. Baldini, L. Ambrosio, *Biomaterials,* **29**, 3662 (2008).
2. W. Li, M. Guo, J. Zeng, X. Yue, X. Zhang, *Material Express*, **13**, 852 (2023).
3. B. Zhu, T. Bai, P. Wang, Y. Wang, C. Liu, C. Shen, *International Journal of Biological Macromolecules,* **153**, 1272 (2020).
4. J. Yeh, J. Yeh, C. Wu, C. Tsou, W. Chai, J. Chow, C. Huang, K. Chen, C. Wu, *Polymer-Plastics Technology and Engineering,* **48**, 571 (2009).
5. N. Hongsriphan, J. Nualyung, N. Yaothaisong, P. Patanathabutr, *IOP Conference Series: Material Science and Engineering*, **1280**, 1 (2023).
6. M. Hoque, C. McDonagh, B. Tiwari, J. Kerry, S. Pathania, *Applied Science*, **12**, 1346 (2022).
7. K. Nakagawa, S. Surassmo, S. Min, M. Choi, *Journal of Food Engineering*, **102**(2), 177 (2011).
8. A. Viraneva, I. Vlaeva, T. Yovcheva, *Bulg. Chem. Commun.*, **54**, (B2): 82 (2022).
9. W. Chin-San, *Polymer Degradation Stability*, **80**(1), 127 (2003).
10. D. Hutmacher, M. Hürzeler, H. Schliephake, *International Journal of Oral Maxillofacial Implants*, 11, 667 (1996).
11. D. Priselac, S. Poljaček, T. Tomašegović, M. Leskovac, *Polymers*, **14**(9), 1792 (2022).
12. A. Viraneva, I. Bodurov, A. Grigorov, T. Yovcheva, T. Vasileva, V. Bivolarski, I. Iliev, *Bulg. Chem. Commun.*, **52**(A), 165 (2020).
13. T. Yovcheva, A. Viraneva, M. Galikhanov, *Journal of Physics: Conference Series*, **558**, 1 (2014).
14. A. Viraneva, T. Yovcheva, E. Pisanova, E. Gencheva, G. Mekishev, *AIP Conference Proceedings*, **1203**, 382 (2010).

In silico methods for predicting physico-chemical properties and biological activity of newly synthesized esters of Bexarotene

I. R. Iliev[*], S. F. Georgieva

Department of Pharmaceutical Chemistry, Faculty of Pharmacy, Medical University of Varna

The synthetic retinoid analogue Bexarotene (Targretin®, Ligand Pharmaceuticals Inc.) belongs to a group of compounds called rexinoids. They possess a specific affinity for the retinoid X receptor. The latter plays a role in the regulation of cell growth and differentiation through their ability to regulate transcription. Bexarotene is approved for the treatment of cutaneous T-cell lymphoma (CTCL), both as an oral and dermal dosage form. A total of 4 new Bexarotene esters were synthesized and an *in silico* analysis was performed using the OECD QSAR Toolbox, Molinspiration, PreADME/Tox and SwissADME software. The QSAR Toolbox results show that Bexarotene esters possess high metabolic activity with metabolites similar to those of Bexarotene. Alsom a hydrolysis process is observed making the esters act as prodrugs. According to Lipinski's rule of 5 all four Bexarotene derivatives give 1 violation and therefore have drug-like properties. The Molinspiration and SwissADME software showed affinity of the newly synthesized molecules for nuclear receptors which partly rejects the prodrug theory. After evaluating the pharmacokinetic profile of the esters, it was observed that the molecules present promising intestinal absorption, distribution, metabolism, excretion and toxicity (ADME/T) characteristics. Even though the *in silico* analysis gave promising results, further investigation is needed.

Keywords: pharmacokinetics, bioactivity, esters, prodrugs

INTRODUCTION

Cancer remains a pressing global health concern, accounting for a substantial burden of mortality and morbidity worldwide. According to the World Health Organization, it is estimated that the incidence of cancer will rise to 28.4 million cases by 2040, representing a significant 47% increase from 2020 [1, 2]. In the fight against cancer, the development of novel therapeutic agents and the exploration of their physico-chemical properties and biological activities are crucial for advancing treatment strategies. Bexarotene (Bex), presented in Figure 1, a retinoid X receptor-selective agonist, has exhibited promising potential in the realm of cancer therapy [3].
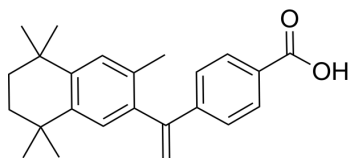
Figure 1. Structure of Bexarotene

The present study focuses on the *in silico* methods employed for predicting the physico-chemical properties and biological activities of newly synthesized esters of Bex. Leveraging computational tools and models, this research aims to streamline the process of identifying and characterizing potential drug candidates with enhanced efficacy and reduced adverse effects. Through the application of advanced computational techniques including quantitative structure-activity relationship (QSAR) analysis, and molecular dynamics simulations, a comprehensive understanding of the molecular interactions and pharmacological profiles of the synthesized esters can be achieved.

The integration of *in silico* approaches offers a holistic perspective on the physico-chemical and pharmacological aspects of the newly synthesized esters of Bex, providing valuable insights for potential applications and further research in cancer therapy. This article explores the use of *in silico* methods to predict the physico-chemical properties and biological activity of these synthesized Bex esters, drawing inspiration from the well-established drug Bex which has shown promise in cancer treatment [4] and potential in addressing central nervous system (CNS) diseases such as Parkinson's, Alzheimer's, and schizophrenia [5].

MATERIALS AND METHODS

For metabolic activation, we employed OECD QSAR Toolbox simulators, including '*In vivo* rat metabolism', 'Rat liver S9 metabolism', and 'Skin metabolism', predicting how the compounds transform in various contexts [6].

---

* To whom all correspondence should be sent:
E-mail: *i__iliev@abv.bg*

To evaluate toxicity, 'DNA binding by OASIS' and 'Protein binding by OASIS' profilers were used [6].

Molinspiration software (https://molinspiration.com/index.html) [7] calculated crucial molecular properties and predicted bioactivity against drug targets. PreADME/T software (https://preadmet.qsarhub.com/adme/) [8] assessed pharmacokinetic parameters and SwissADME software (https://www.swissadme.ch/) [9] aided in target prediction and understanding potential biological interactions.

The *in silico* analysis provided insights into the esters' properties, enhancing our understanding of their drug potential.

RESULTS AND DISCUSSION

We synthesized four novel Bex esters (E1, E2, E3, and E4) using methanol, ethanol, propanol, and butanol, respectively, following a classical esterification scheme by employing oxalyl chloride as a key reagent. Choosing primary alcohols—methanol, ethanol, propanol, and butanol—for Bex ester synthesis was driven by their enhanced reactivity and availability. This deliberate selection serves a dual purpose: to ensure controlled esterification and to systematically assess the process before exploring higher molecular mass alcohols. Our step-wise approach aligns with a commitment to methodical experimentation, laying a foundation for potential future studies involving larger alcohols.

The synthesized esters were characterized through various analytical techniques, including thin-layer chromatography (TLC), infrared spectroscopy (IR), and high-performance liquid chromatography (HPLC).

TLC analysis revealed distinct Rf values for Bex and the synthesized esters (0.75, 0.55, 0.64, 0.66, and 0.72) using a mobile phase of hexane:ethyl acetate (1:1). The analysis was carried out on UV-plates DC-Fertigfolien ALUGRAM SIL G/UV254 with a layer thickness of 0.20 mm impregnated with fluorescent indicator UV254. Detection was performed with UV light on a Nahita UV lamp.

Infrared spectra were taken in the range 4000-500 cm^{-1} on a Nicolet iS10 FT-IR spectrometer. The IR spectra displayed a notable shift in the peak associated with bexarotene, moving from 1673 cm^{-1} to 1717 cm^{-1}, indicative of the formation of the ester functional group.

Furthermore, HPLC was employed for a detailed characterization, utilizing a Thermo Scientific High Performance Liquid Chromatography (HPLC) apparatus model Spectra SYSTEM HPLC with manual injector, UV-VIS detector model Spectra SYSTEM UV2000 and fluorescence detector model Spectra SYSTEM FL3000. A Synergi 4u Hydro – RP 80A (250 × 4.00 mm) column protected with a Synergi 4u Hydro – RP 80A (250 × 4.00 mm) precolumn was used for the analysis. System control, data acquisition and analysis were performed using ChromQuest chromatographic data software, version 4.2.34. The following conditions were used: mobile phase composed of 60:40 methanol:acetonitrile ratio, flow rate set at 1.3 ml/min, UV detection at 260 nm, chromatographic column temperature of 40 °C, manual injector temperature of 25 °C, and sample volume for analysis set at 20.0 μl. The analysis was performed in isocratic mode, maintaining these conditions throughout a total duration of 15 minutes. The retention times for Bex and the esters were recorded as 5.052, 3.482, 3.752, 4.12, and 4.572 minutes, respectively.

OECD QSAR Toolbox

Our study delved into the metabolic potential of Bex and newly synthesized esters. These esters were created to broaden our investigation and understand their metabolic characteristics compared to the parent compound. Utilizing QSAR models, we examined their metabolic activation, physicochemical properties and factors influencing biological activity. Our research emphasized on assessing not only the parent compound but also the potential for altered biological activity through active metabolites and interactions with DNA and proteins, key considerations for evaluating safety.

Additionally, a mathematical model helped us analyze Bex's metabolic behavior and its physicochemical attributes. The results indicated that neither Bex nor its esters exhibited *in silico* binding to DNA or proteins, suggesting no mutagenic or genotoxic risks. The esters share an identical safety profile with Bex.

In vivo rat metabolism simulator

The study investigated Bex's metabolic activity using the *In vivo* rat metabolism simulator, identifying physicochemical properties influencing its biological activity. Results showed overlapping metabolites between Bex and its esters, due to hydrolysis, suggesting prodrug potential for the esters after oral administration.

These findings are detailed in Tables 1 to 5, presented in the appendix, showcasing metabolites for Bex and esters E1, E2, E3, and E4. Diverse ester metabolites, particularly in larger esters, were observed before hydrolysis, along with alcohol

metabolites, raising concerns about their pharmacological and toxicological effects.

The extensive range of possible metabolites raises concerns about their pharmacological and toxicological effects, emphasizing the need for additional studies to comprehensively assess the biological activity of these metabolites.

We characterized the newly obtained Bex derivatives, focusing on their potential to form active metabolites and interact with DNA and proteins. Both Bex and its esters exhibit the ability to form metabolites that can bind to DNA and proteins, raising concerns about genotoxicity and cellular disruption.

Bex yields 11 metabolites, with none binding to DNA but four binding to proteins. Conversely, the methyl ester (E1) produces 32 metabolites, with five binding to DNA and 15 to proteins. The ethyl ester (E2) generates 28 metabolites, including six binding to DNA and 14 to proteins. The propyl ester (E3) results in 32 metabolites, with four binding to DNA and 15 to proteins. Notably, the butyl ester (E4) is the most metabolically active, with 49 metabolites, seven binding to DNA, and 22 to proteins.

These interactions involve S_N2 reactions for DNA binding and mechanisms like Schiff base formation, nucleophilic addition, and S_N2 reactions for protein binding. For detailed information on binding abilities, refer to Tables 6 and 7, presented in the appendix. Ester E4 stands out as the most metabolically active, producing the highest number of metabolites binding to both DNA and proteins.

Rat liver S9 metabolism simulator

Investigating metabolism using the liver S9 fraction is essential due to its potential to create unique metabolites not seen in *in vivo* liver simulations. Tables 8 to 12, included in the appendix, show metabolites from liver S9 metabolism simulations of Bex and its esters (E1, E2, E3, and E4). Bex generates five metabolites, while esters produce more, with E1 yielding 12, and E2, E3, and E4 each producing 14 metabolites. This suggests that Bex esters might function as prodrugs since they hydrolyze into Bex and precursor alcohols, as seen in Tables 8 to 12, detailed in the appendix.

The study also assessed the potential for DNA and protein binding of metabolites generated in the liver S9 metabolism simulator for Bex and its esters (E1, E2, E3, and E4), as detailed in Table 13, attached in the appendix.

The analysis revealed that both Bex and its esters can form metabolites binding to proteins but not to DNA. This protein binding could potentially disrupt

cellular functions or indirectly lead to damage. Notably, none of the metabolites from the rat liver S9 metabolism simulation of Bex and its esters exhibited binding to DNA. Bex produced five metabolites, with three unable to bind to DNA, while two could bind to proteins through nucleophilic addition.

In the case of the E1 ester, eight metabolites did not bind to proteins, while the remaining four exhibited binding through nucleophilic addition. Regarding E2, E3, and E4 esters, nine metabolites showed no binding to proteins, one could bind through Schiff base formation, and four could bind through nucleophilic addition. Importantly, E2, E3, and E4 esters displayed the highest metabolic activity, resulting in more metabolites capable of binding to proteins.

Skin metabolism simulator

Bex is primarily used as a 1% gel for treating Cutaneous T-Cell Lymphoma (CTCL), making it essential to investigate the potential skin metabolism of newly synthesized Bex analogues.

The analysis assessed skin metabolism of Bex and its esters (E1, E2, E3, and E4), as detailed in Table 14, presented within the appendix.

Results indicate that during skin metabolism simulations, Bex generates one metabolite, while its esters each produce four metabolites, with a common metabolite (number 1) across all. Additionally, a hydrolysis process releases Bex (metabolite number 4) and the ester synthesis alcohol. This supports the potential use of Bex esters as prodrugs, aligning with QSAR Toolbox findings.

The study also assessed the potential for DNA and protein binding of metabolites generated in the skin metabolism simulator for Bex and its esters.

Results suggest that both Bex and its esters produce metabolites lacking the ability to bind to DNA or proteins due to their structural properties.

Molinspiration Cheminformatics software

Ideal drug molecules must adhere to Lipinski's rule, which defines specific physicochemical properties for oral bioavailability. Using Molinspiration software, Bex and its esters were evaluated, and they all violated only one rule as seen in Table 15, found in the appendix. This suggests good pharmacokinetic properties and oral bioavailability.

Drug-likeness involves complex molecular properties that impact a molecule's behavior in the body. Using Molinspiration software, it's evident that Bex is highly biologically active, as seen in Table 16 in the appendix. While the esters also

exhibit activity against receptors and enzymes, they may not strictly qualify as prodrugs. However, their activity could enhance the drug's effectiveness. Administering Bex as an ester prodrug at lower doses and less frequently may improve patient compliance.

PreADME/Tox software

Predicting the pharmacokinetic and toxicological profile of molecules is essential in drug development, saving time, cost, and unnecessary animal testing. The results of the *in silico* analysis assessed the absorption, distribution, metabolism, excretion, and toxicity of newly synthesized molecules and is presented in Table 17, included in the appendix.

When considering absorption and distribution, the compounds demonstrated remarkable intestinal absorption, an essential factor in oral drug administration, and an average cellular permeability increasing with molecular mass. Additionally, they exhibited a strong affinity for plasma proteins, which plays a critical role in drug distribution within the body. Among these compounds, Bex esters, unlike Bex, exhibited promising degree of absorption through the blood-brain barrier, hinting at their potential utility in the treatment of central nervous system (CNS) diseases such as Alzheimer's and Parkinson's and schizophrenia.

Regarding metabolism, all compounds were found to inhibit CYP2C9, and only Bex didn't inhibit CYP3A4. This suggests potential drug interactions and emphasizes caution when co-administering these compounds with others metabolized by the same enzymes.

In the context of excretion, the compounds exhibited low permeability in MDCK cell permeability assays, indicating prolonged renal excretion.

Turning to toxicity, the analysis raised concerns about mutagenicity, as all tested compounds displayed mutagenic effects, necessitating further *in vitro* and *in vivo* investigations to meticulously weigh the therapeutic advantages against potential risks. Encouragingly, only E1 exhibited carcinogenic activity in rat models, indicating a significant level of safety for compounds E2, E3, and E4. Moreover, the risk of cardiotoxicity, as indicated by inhibition of the hERG gene, was moderate for the assessed compounds.

In sum, the *in silico* evaluation provided a comprehensive ADME/T profile for the newly synthesized esters. Of particular note were the promising characteristics exhibited by E2, E3, and E4, rendering them potential candidates for CNS antineoplastic treatments.

SwissADME Target Prediction

In the target prediction analysis using SwissADME software for Bex and its newly synthesized esters, it was observed that esterification of Bex substantially reduces the probability of binding to RAR or RXR receptors, with this reduction becoming more pronounced as the ester size increases. This observation aligns with the data presented in Table 18 in the appendix. SwissTargetPrediction reaffirms the findings obtained from Molinspiration software.

Additionally, the analysis reveals a wide range of G-protein coupled receptors and enzymes that Bex and its esters can potentially interact with, supporting the results presented in Table 16 in the appendix. These interactions highlight the diverse pharmacological potential of these compounds in various biological systems. The compounds E1, E2, E4, and Bex exhibit interactions with various enzymes and receptors, hinting at potential central nervous system (CNS) effects. These include receptors associated with circadian rhythm regulation (Melatonin Receptor 1A and 1B), cognitive functions (Neuronal Acetylcholine Receptor Protein Alpha-7 Subunit), mood regulation (Serotonin 5a Receptor), stress responses and attention (Alpha-2b Adrenergic Receptor), Alzheimer's disease (Gamma-Secretase), sleep disorders (Adenosine A3 Receptor), synaptic plasticity and neurological disorders, such as schizophrenia (Metabotropic Glutamate Receptor 1), inhibitory signaling (Glycine Transporter 1), pain modulation (Mu Opioid Receptor), and wakefulness (Histamine H3 Receptor).

While these interactions suggest potential CNS effects, empirical studies are needed to validate these predictions. Understanding the precise mechanisms of action and clinical utility in CNS-related disorders requires further research and experimental validation.

CONCLUSION

In conclusion, our research harnessed the power of advanced metabolism simulator models to delve deep into the pharmacokinetic and toxicological aspects of newly synthesized Bex esters. Through a comprehensive analysis employing the *in vivo* rat metabolism simulator, liver S9 metabolism simulator, and skin metabolism simulator, we gained critical insights into how these compounds undergo transformations within the body.

The outcomes of our simulations underscore the promising potential of Bex esters as prodrugs, with

hydrolysis leading to the release of Bex and precursor alcohols. Particularly striking was the observation that the esters produced a greater number of metabolites compared to Bex alone, emphasizing their versatility in metabolic pathways.

Our research underscores the indispensable role of metabolism simulator models in the drug development process, offering invaluable insights that could shape the future of innovative therapies. While our study represents significant progress, the journey from synthesis to clinical application remains dynamic and full of potential, promising advancements in medical care.

Moreover, our study shed light on the pharmacokinetic properties of these esters, revealing their excellent intestinal absorption rates. Of special note are compounds E2, E3, and E4, which exhibited promising profiles for potential CNS antineoplastic applications.

However, it is crucial to acknowledge the concerns raised about mutagenicity, underlining the necessity for further *in vitro* and *in vivo* investigations to comprehensively evaluate the therapeutic benefits and associated risks.

The SwissTargetPrediction analysis expanded our horizons, revealing a decreasing likelihood of binding to RAR or RXR receptors with increasing ester size, a phenomenon confirmed by the Molinspiration software. Furthermore, the wide array of interactions observed with G-protein coupled receptors and enzymes hints at the diverse biological activities these esters might exhibit.

Notably, the tantalizing potential of these compounds in CNS applications adds an intriguing dimension to their therapeutic prospects. While further studies are imperative to validate these CNS effects, our findings provide a solid foundation for future investigations into the utilization of these esters in treating CNS disorders, such as Parkinson's, Alzheimer's, and schizophrenia.

In summary, our research findings collectively contribute to the characterization of these esters and their potential as promising drug candidates, not only in the realm of oncology but also in the exciting domain of CNS therapeutics. To unlock their full therapeutic potential in various medical applications, further studies, encompassing both *in vitro* and *in vivo* investigations, are warranted.

REFERENCES

1. M. Georgieva, D. Tzankova, E. Mateev, B. Angelov, M. Kondeva-Burdina, G. Momekov, V. Tzankova, A. Zlatkov, *Anti-cancer Agents Medicinal Chemistry*, **23 (**3), 346 (2023). doi: 10.2174/1871520622666220701114306.

2. International Agency for Research on Cancer. Global Cancer Statistics 2020: GLOBOCAN Estimates of Incidence and Mortality Worldwide for 36 Cancers in 185 Countries. CA: *A Cancer Journal for Clinicians*, 2020.

3. F. Cayrol, M. V. Revuelta, M. Debernardi, A. Paulazo, J. M. Phillip, N. Zamponi, H. Sterle, M. C. Díaz Flaqué, C. Magro, R. Marullo, E. Mulvey, J. Ruan, G. A. Cremaschi, L. Cerchietti. *Mol Cancer Ther.* **21** (9), 1485 (2022) https://doi.org/10.1158/1535-7163.MCT-22-0093.

4. P. Collins, C. Jones, S. Choudhury, L. Damelin. Tracing the Journey of Bexarotene from Drug Discovery to the Clinic: An Historical Perspective. *International Journal of Molecular Sciences*. **20 (**9), 2159 (2019) doi:10.3390/ijms20092159.

5. Y. Liu, P. Wang, G. Jin, P. Shi, Y. Zhao, J. Guo, Y. Yin, Q. Shao, P. Li, P. Yang. *Ageing Research Reviews*, **90**, page (2023), 102021, ISSN 1568-1637, https://doi.org/10.1016/j.arr.2023.102021.

6. U.S. Environmental Protection Agency. (2021). QSAR Toolbox. https://www.epa.gov/chemical-research/qsar-toolbox

7. Molinspiration Cheminformatic. (n.d.). Molinspiration Property Calculation. https://www.molinspiration.com/

8. PreADME/T. (n.d.). PreADME/T. https://preadmet.qsarhub.com/

9. A. Daina, O. Michielin, V. Zoete. SwissADME: A free web tool to evaluate pharmacokinetics, drug-likeness and medicinal chemistry friendliness of small molecules. *Scientific Reports*, **7 (**1) 42717 (2017). doi:10.1038/srep42717 http://www.swissadme.ch/index.php

APPENDIX

Table 1. Numbers and structure of predicted metabolites of Bex obtained after *in vivo* rat metabolism simulator.

1	2	3	4
5	6	7	8
9	10	11	

Table 2. Numbers and structure of predicted metabolites of compound E1 obtained after *in vivo* rat metabolism simulator.
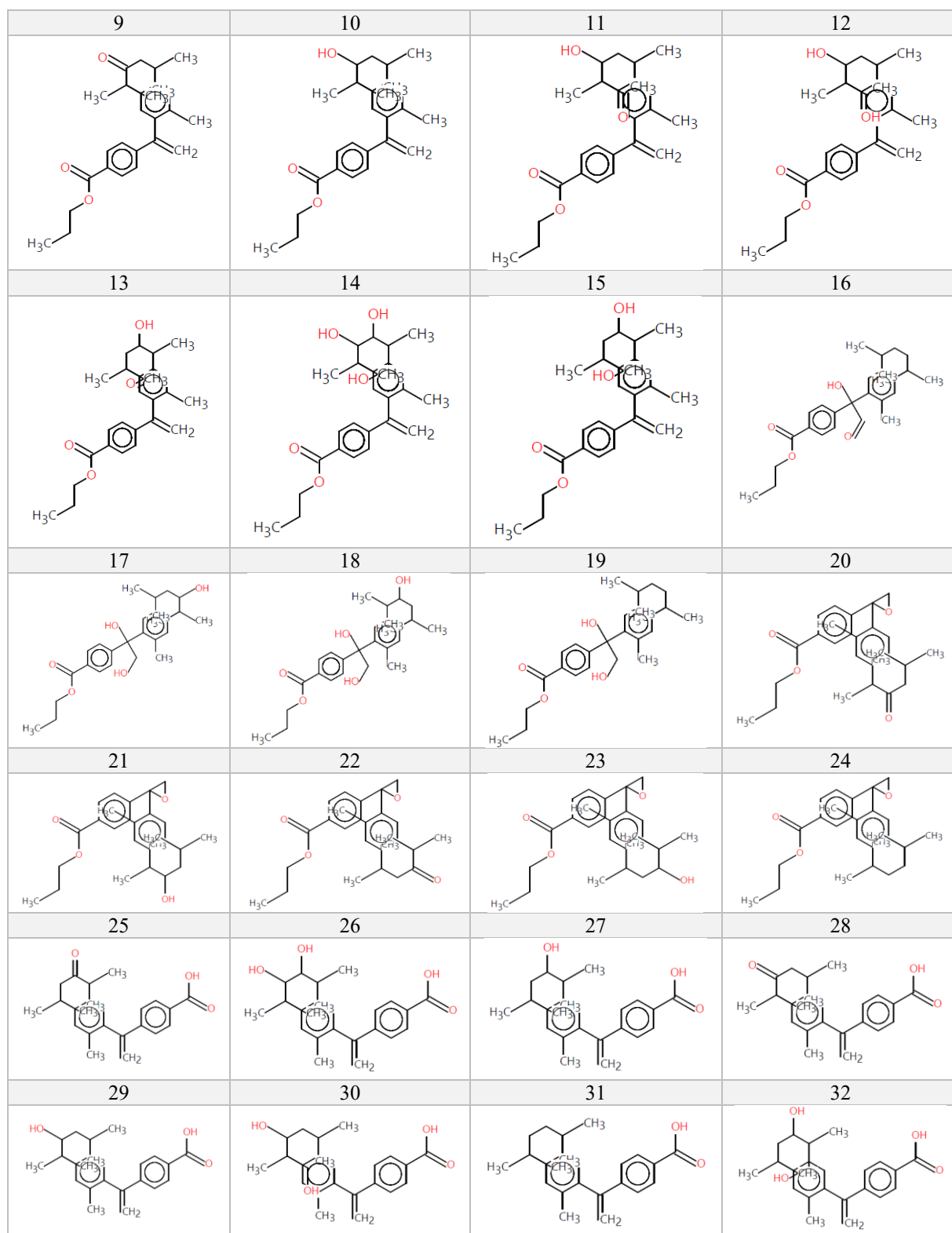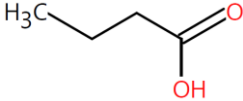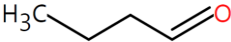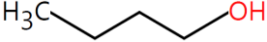
1	2	3	4
5	6	7	8
9	10	11	12

13	14	15	16
17	**18**	**19**	**20**
21	**22**	**23**	**24**
25	**26**	**27**	**28**
29	**30**	**31**	**32**
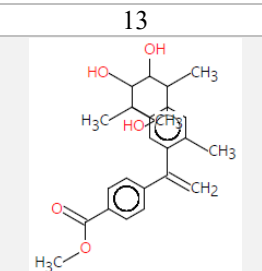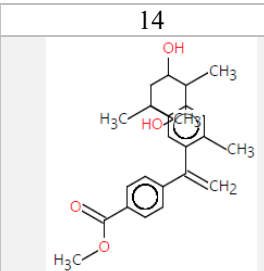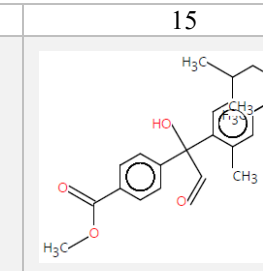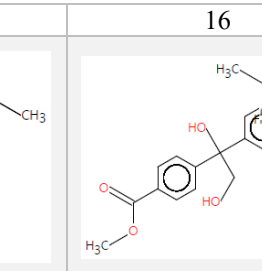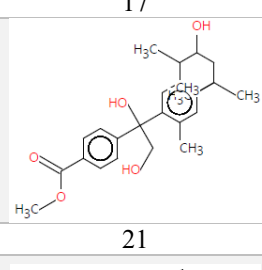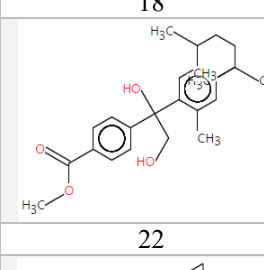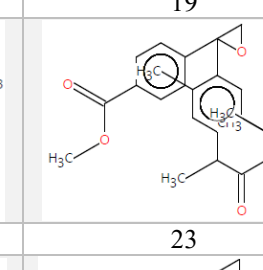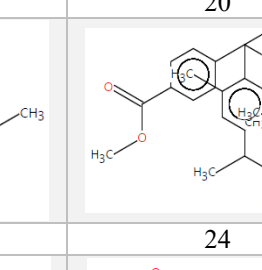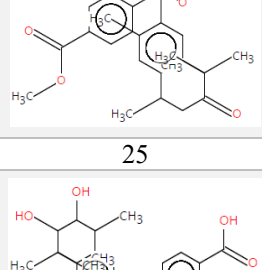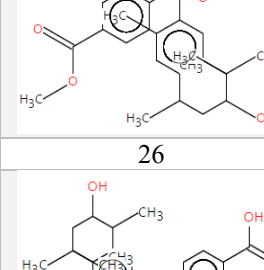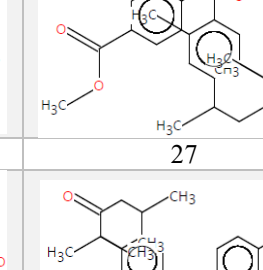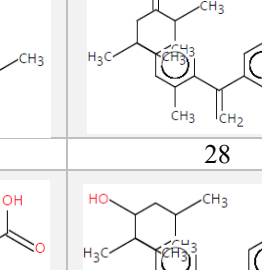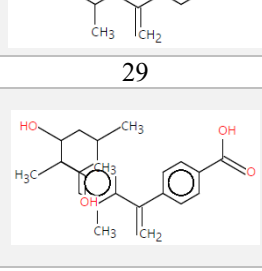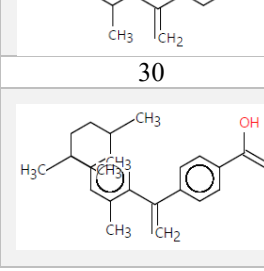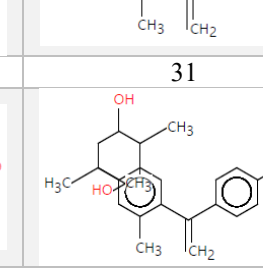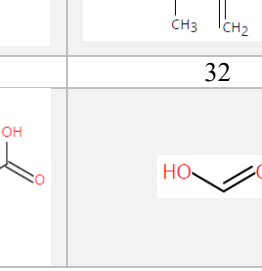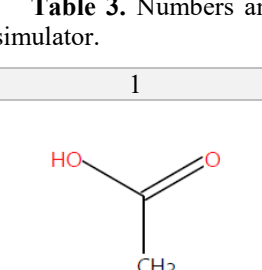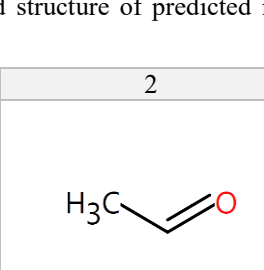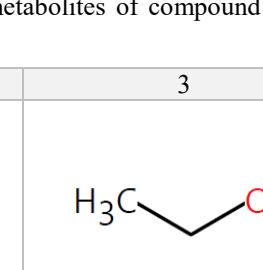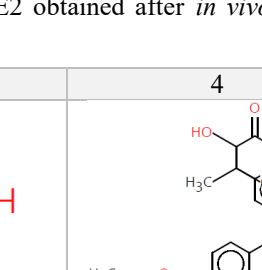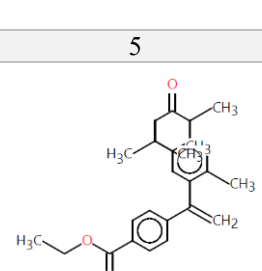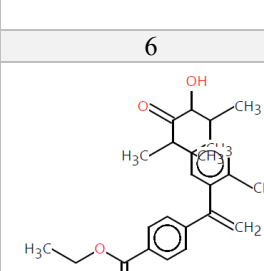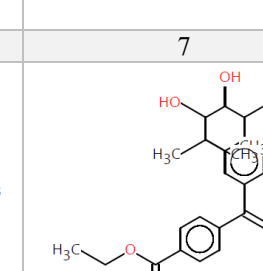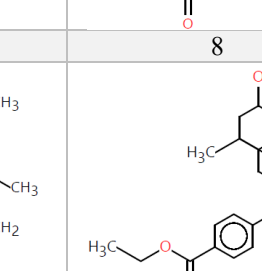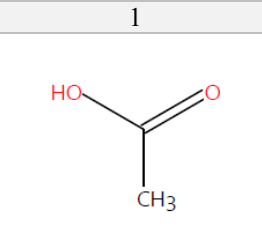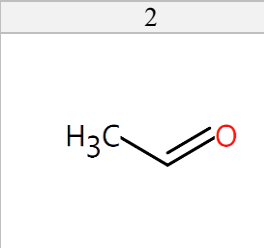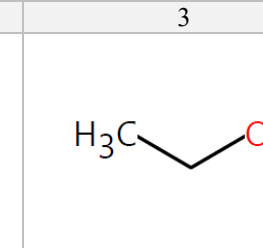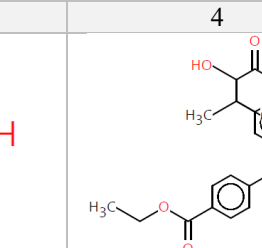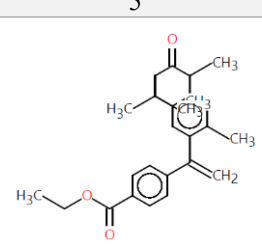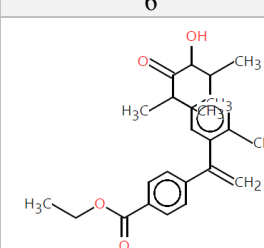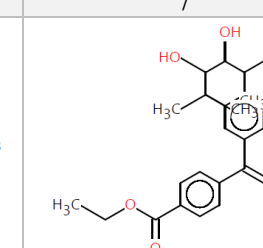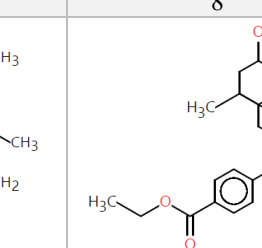
Table 3. Numbers and structure of predicted metabolites of compound E2 obtained after *in vivo* rat metabolism simulator.
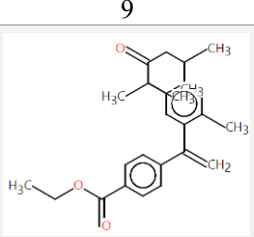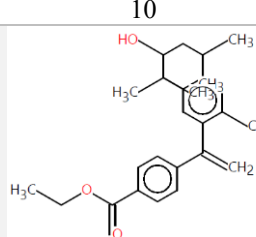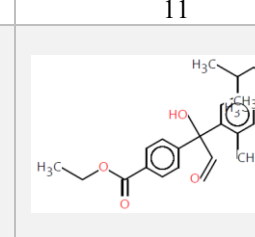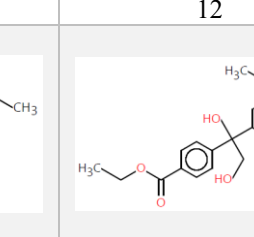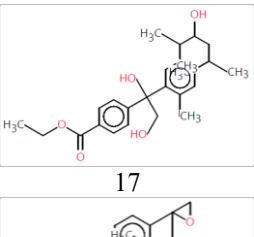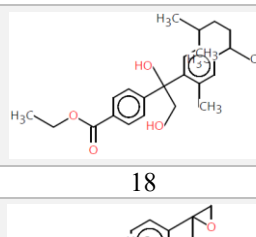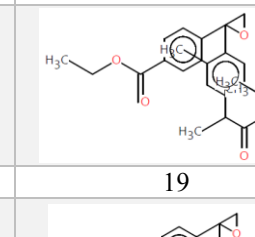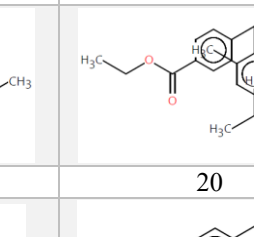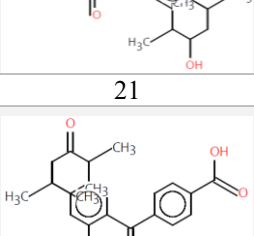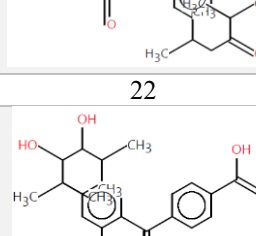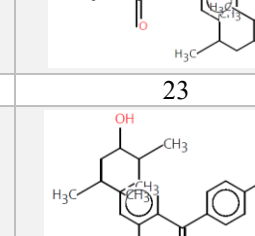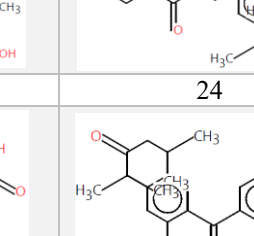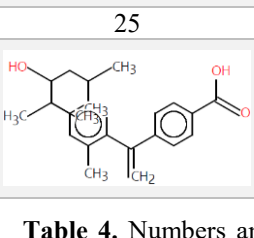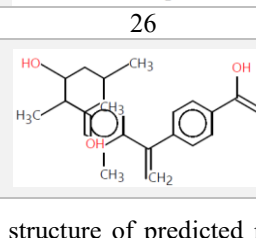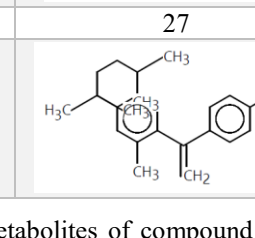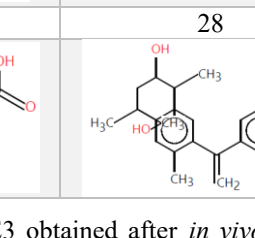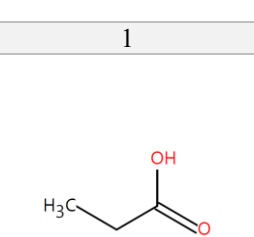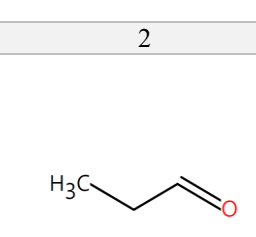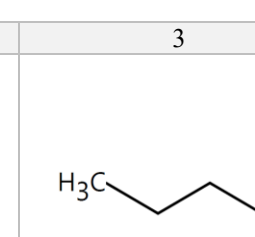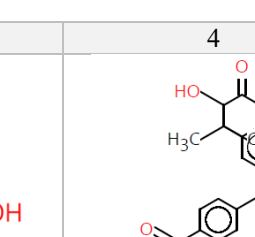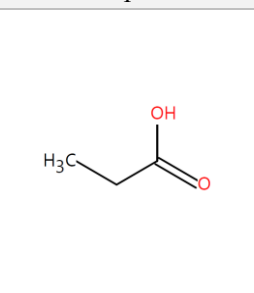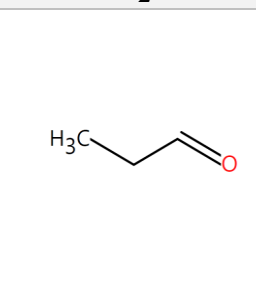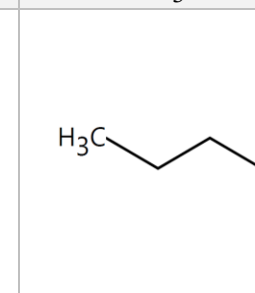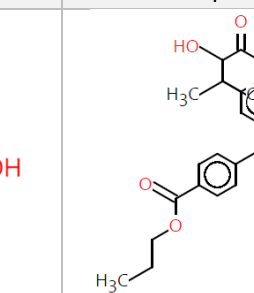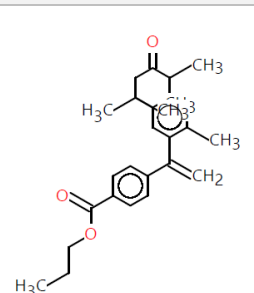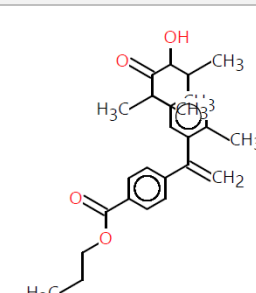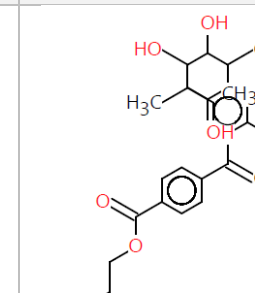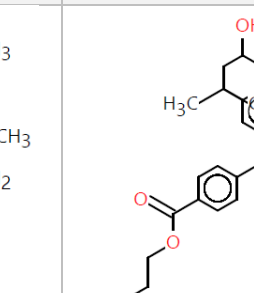
1	2	3	4
5	**6**	**7**	**8**

9	10	11	12

13	14	15	16

17	18	19	20

21	22	23	24

25	26	27	28

Table 4. Numbers and structure of predicted metabolites of compound E3 obtained after *in vivo* rat metabolism simulator.

1	2	3	4

5	6	7	8

9	10	11	12
13	**14**	**15**	**16**
17	**18**	**19**	**20**
21	**22**	**23**	**24**
25	**26**	**27**	**28**
29	**30**	**31**	**32**

85
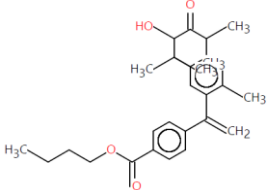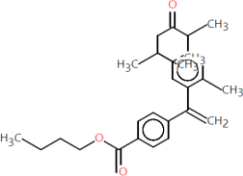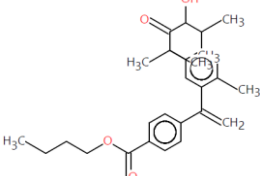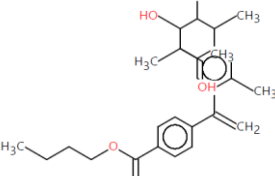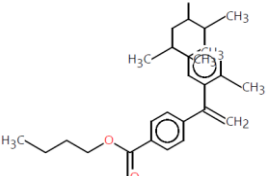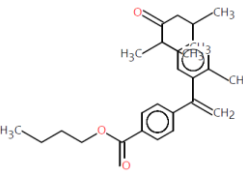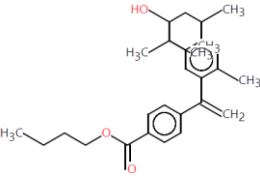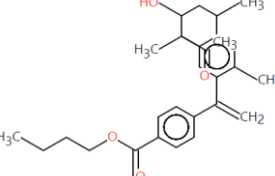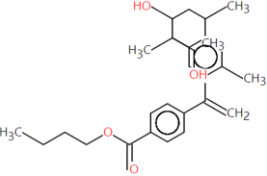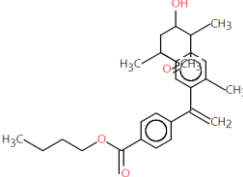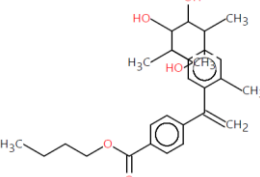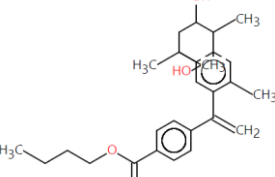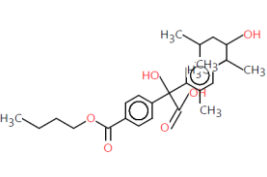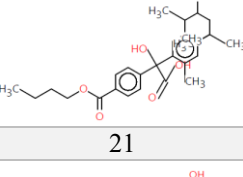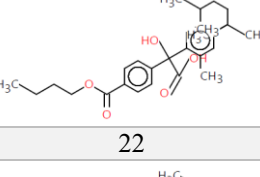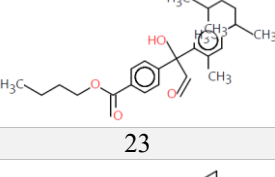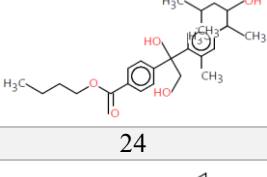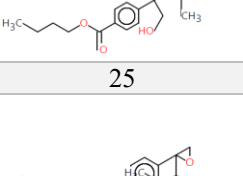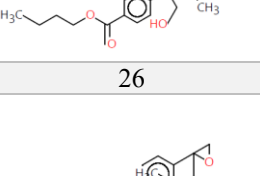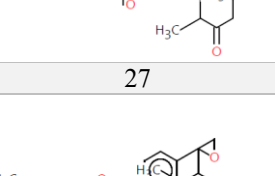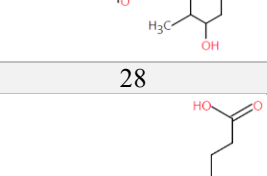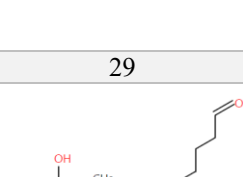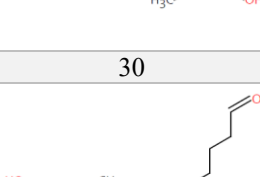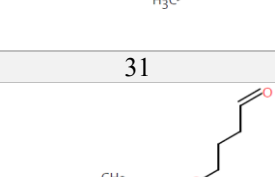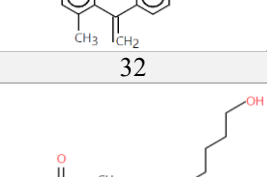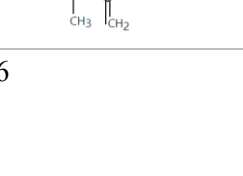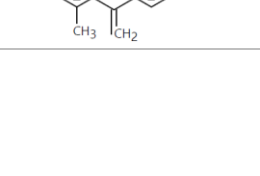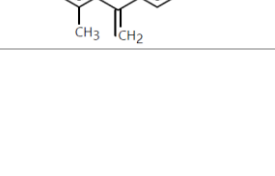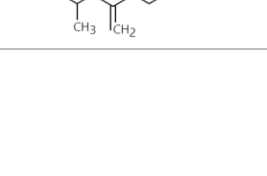
Table 5. Numbers and structure of predicted metabolites of compound E4 obtained after *in vivo* rat metabolism simulator.

1	2	3	4
5	**6**	**7**	**8**
9	**10**	**11**	**12**
13	**14**	**15**	**16**
17	**18**	**19**	**20**
21	**22**	**23**	**24**
25	**26**	**27**	**28**
29	**30**	**31**	**32**

33	34	35	36
37	**38**	**39**	**40**
41	**42**	**43**	**44**
45	**46**	**47**	**48**
49			

Table 6. Binding of Bex and Bex esters metabolites to DNA.

DNA binding	Structural alert	No alert found	Epoxides, Aziridines, Thiiranes and Oxetanes
	Mechanistil alert	-	*Alkylation, direct acting epoxides and related*
	Mechanistic domain	-	S_N^2
Metabolite №	*Bex*	1-11	-
	E1	1-18, 24-32	19-23
	E2	1-14, 21-28	15-20
	E3	1-19, 25-32	20-24
	E4	1-22, 28-46, 49	23-27, 47, 48

Table 7. Binding of Bex and Bex esters metabolites to proteins.

Protein binding	Structural alert	No alert found	Aldehydes	Ketones	Epoxides, Aziridines and Sulfuranes
	Mechanistic alert	-	*Schiff base formation with carbonyl compounds*	*Addition to carbon-hetero double bond*	*Ring opening S_N^2 reaction*
	Mechanistic domain	-	*Schiff base formation*	*Nucleophilic addition*	S_N^2
Me	*Bex*	2-4, 6, 8, 10, 11	7, 9	1, 5	-

E1	2, 6, 7, 9, 11, 13, 14, 16-18, 25, 26, 28-32	1, 10, 12, 15	3-5, 8, 19, 21, 24, 27	19-23
E2	1, 3, 7, 8, 10, 12-14, 22, 23, 25-28	2, 11	4-6, 9, 15, 18, 21, 24	15-20
E3	1, 3, 7, 8, 10, 12, 14, 15, 17-19, 26, 27, 29-32	2, 11, 13, 16	4-6, 9, 20, 22, 25, 28	20-24
E4	1, 3, 7, 8, 10, 12, 14-18, 20-22, 28, 33, 34, 36, 37, 39, 40, 42-46, 49	2, 11, 13, 19, 29-31	4-6, 9, 23, 25, 32, 35, 38, 41	23-27, 47, 48

Table 8. Numbers and structure of predicted metabolites of Bex obtained after rat liver S9 metabolism simulator.
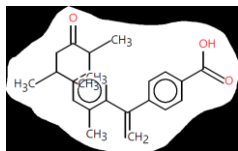
Table 9. Numbers and structure of predicted metabolites of compound E1 obtained after rat liver S9 metabolism simulator.
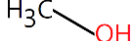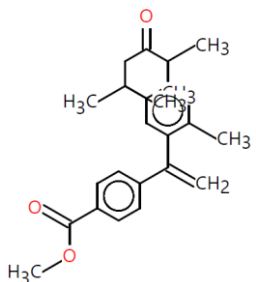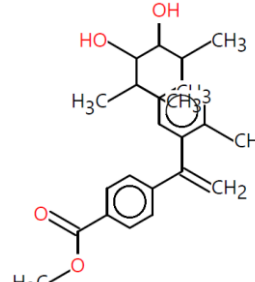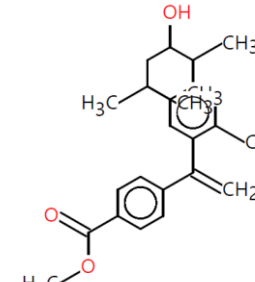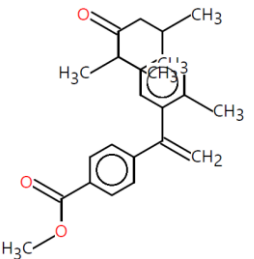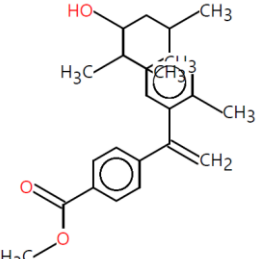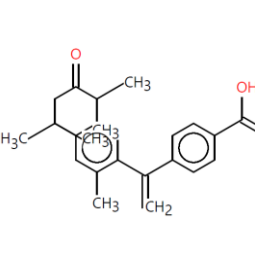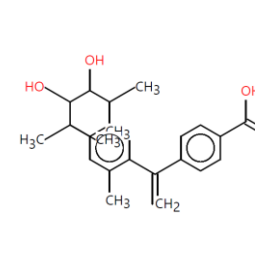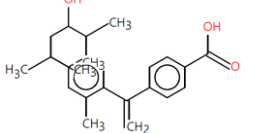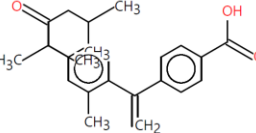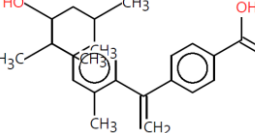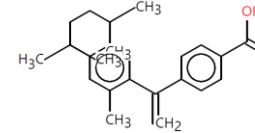
Table 10. Numbers and structure of predicted metabolites of compound E2 obtained after rat liver S9 metabolism simulator.
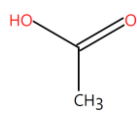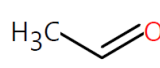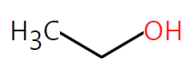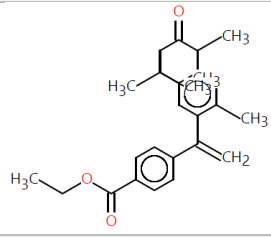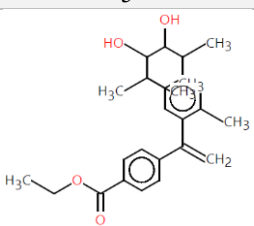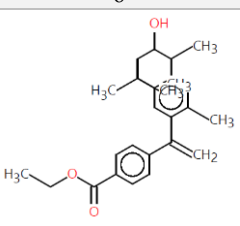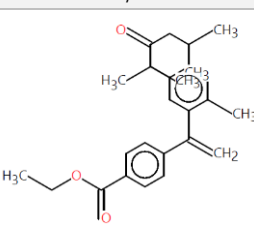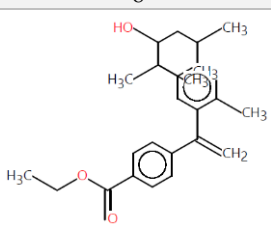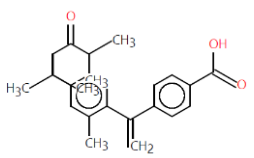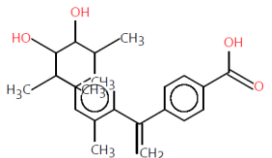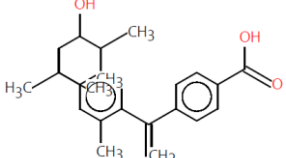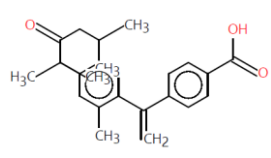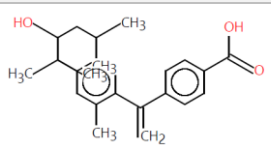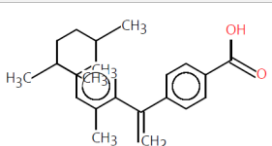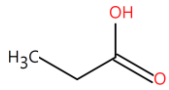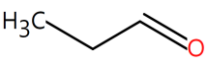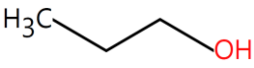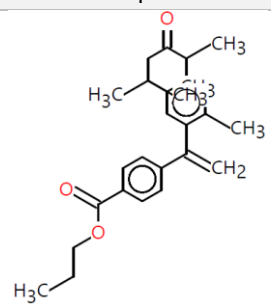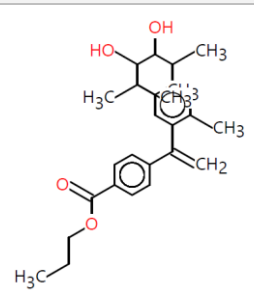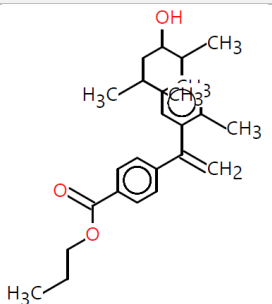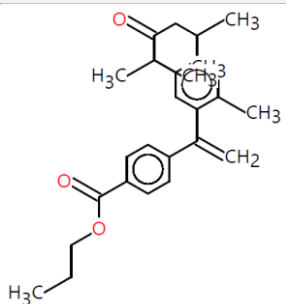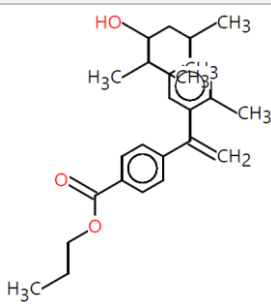
1	2	3	4
5	**6**	**7**	**8**
9	**10**	**11**	**12**
13		**14**	

Table 11. Numbers and structure of predicted metabolites of compound E3 obtained after rat liver S9 metabolism simulator.

1	2	3	4
5	**6**	**7**	**8**

9	10	11	12

13	14

Table 12. Numbers and structure of predicted metabolites of compound E4 obtained after rat liver S9 metabolism simulator.

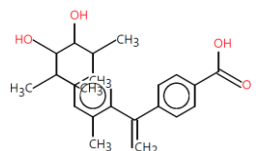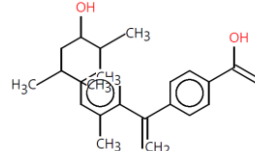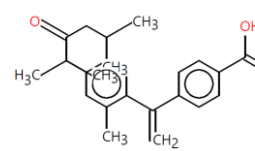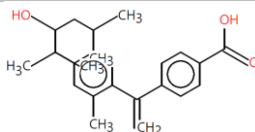| 1	2	3	4

5	6	7	8

9	10	11	12

13	14
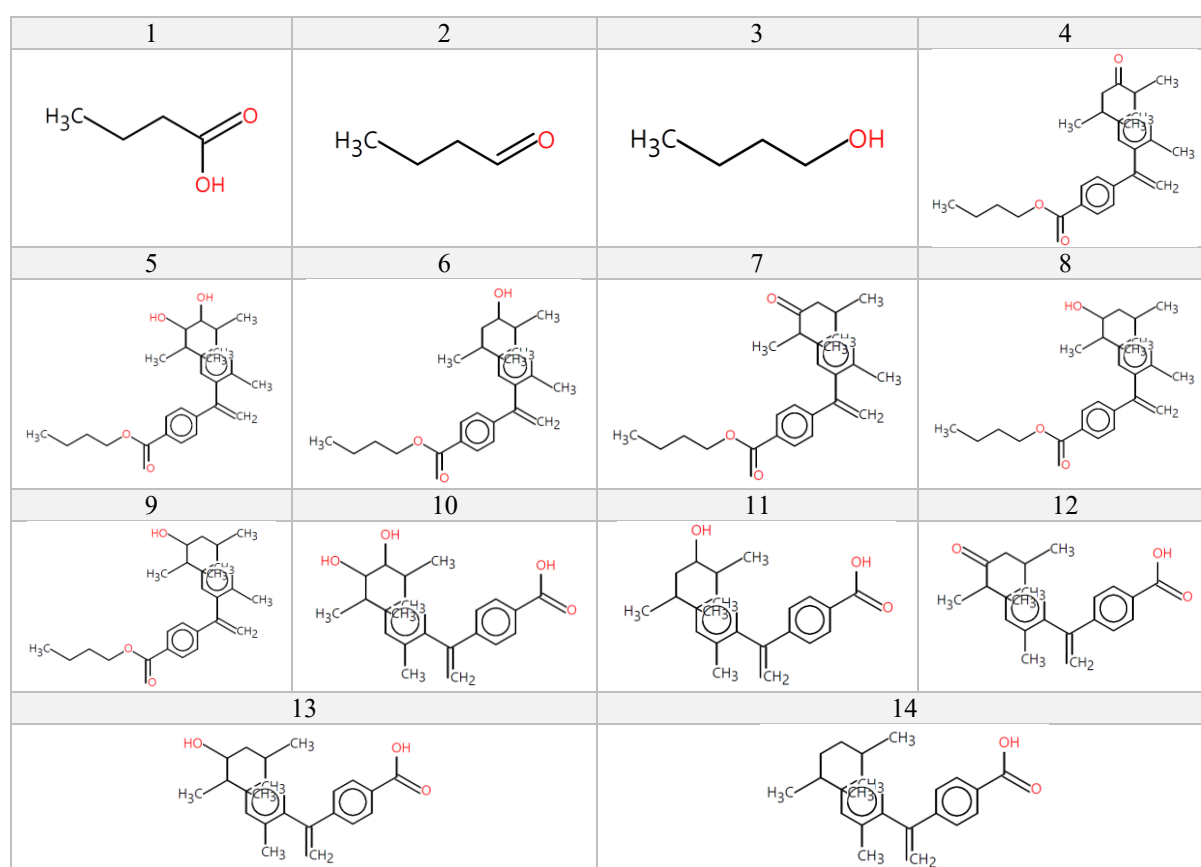
Table 13. Binding of Bex and Bex esters metabolites to DNA and proteins.

	Structural alert	No alert found		Structural alert	No alert found	Aldehydes	Ketones
DNA binding	Mechanistic domain	-	Protein binding	Mechanistic domain	-	Schiff base formation with carbonyl compounds	Addition to carbon-hetero double bonds
	Mechanistic domain	-		Mechanistic domain	-	Schiff base formation	Nuclephilic addition
Metabolite	Bex	1-5	Metabolite	Bex	2, 3, 5	-	1, 4
	E1	1-12		E1	1, 3, 4, 6, 8, 9, 11, 12	-	2, 5, 7, 10
	E2	1-14		E2	1, 3, 5, 6, 8, 10, 11, 13, 14	2	4, 7, 9, 12

| | E3 | 1-14 | | E3 | 1, 3, 5, 6, 8, 10, 11, 13, 14 | 2 | 4, 7, 9, 12 |
| | E4 | 1-14 | | E4 | 1, 3, 5, 6, 8, 10, 11, 13, 14 | 2 | 4, 7, 9, 12 |

Table 14. Numbers and structure of predicted metabolites of Bex and its esters E1, E2, E3 and E4 obtained after skin metabolism simulator.

Table 15. Pharmacokinetic parameters of Bex and newly synthesized Bex esters obtained using Molinspiration software.

Property	Bex	E1	E2	E3	E4
miLogP	6.81	7.07	7.44	7.95	8.41
TPSA	37.30	26.30	26.30	26.30	26.30
Molecular mass	348.49	362.51	376.54	390.57	404.59
Number of H⁻ acceptors	2	2	2	2	2
Number of H⁺ donors	1	0	0	0	0
Number of violations	1	1	1	1	1
Number of rotatable bonds	3	4	5	6	7
Molecular volume	348.76	366.29	383.09	399.89	416.69

Table 16. Bioactivity results of Bex and newly synthesized Bex esters obtained using Molinspiration software.

Property	Bex	E1	E2	E3	E4
GPCR ligand	0.47	0.32	0.28	0.30	0.33
Ion channel modulator	0.14	0,04	0.06	0.05	0.07
Kinase inhibitor	0.01	-0.06	-0.11	-0.09	-0.07
Nuclear receptor lignad	0.92	0.71	0.70	0.68	0.68
Protease inhibitor	0.02	-0.10	-0.13	-0.11	-0.07
Enzyme inhibitor	0.39	0.24	0.20	0.23	0.25

Table 17. Pharmacokinetic and toxicological parameters of Bex and newly synthesized Bex esters using PredADME/T software.

	ADME/T parameters	Bex	E1	E2	E3	E4
A	HIA	97.93	100	100	100	100
	Caco-2	22.220	27.559	42.081	43.436	44.676
	Skin permeability	-0.7892	-0.7898	-0.7696	-0.7324	-0.7089
D	PPB	100	100	100	100	100
	BBB	1.8619	9.2775	11.216	13.846	15.833
M	CYP3A4 inhibitor	-	Inhibitor	Inhibitor	Inhibitor	Inhibitor
	CYP3A4 substrate	Substrate	Substrate	Substrate	Substrate	Substrate
	CYP2C19 inhibitor	-	-	-	-	-
	CYP2C9 inhibitor	Inhibitor	Inhibitor	Inhibitor	Inhibitor	Inhibitor
	CYP2D6 inhibitor	-	-	-	-	-
	CYP2D6 substrate	-	-	-	-	-
E	MDCK	0.077539*	0.073390*	0.065640*	0.098970*	0.092798*
T	Ames test	+	+	+	+	+
	Carcinogenicity in rats	-	+	-	-	-
	Carcinogenicity in mice	-	-	-	-	-
	hERG Inhibition	Medium	Medium	Medium	Medium	Medium

Human intestinal absorption (HIA): Low absorption 0.00 – 20.00 %; Moderate absorption 20.00 – 70.00 %; Excellent absorption 70.00 – 100.00 %;

Caco-2 cell permeability: High permeability > 70.0 nm/sec; Medium permeability 4.0 - 70.0 nm/sec; Low permeability < 4.0 nm/sec;

Skin permeability: values vary from -3.00 to 6.00;

Plasma Protein Binding (PPB): Strong connection > 90.0%; Weak connection < 90.0

Blood Brain Barrier (BBB): High CNS absorption > 2.00; Intermediate CNS absorption 0.10 ÷ 2.00; Low CNS absorption < 0.10

MDCK: Low permeability < 25.0 nm/sec; Medium permeability 25.0 ÷ 500.0 nm/sec; high permeability > 500.0 nm/sec

Ames test: Positive: mutagenic; Negative: non-mutagenic.

Carcinogenicity: Positive: carcinogenic; Negative: non-carcinogenic.

Table 18. Swiss Target Prediction and predicted probability of binding of Bex and its newly synthesized esters.

Target	Probability, %				
	Bex	E1	E2	E3	E4
Retinoid X receptor beta	100	18.52	15.67	11.32	11.45
Retinoic acid receptor gamma	100	14.53	13.21	11.32	11.45
Retinoid X receptor gamma	100	12.93	13.21	11.32	11.45
Retinoic acid receptor beta	100	14.53	13.21	11.32	11.45
Retinoic acid receptor alpha	100	14.53	13.21	11.32	11.45
Retinoid X receptor alpha	100	12.93	13.21	11.32	11.45

Cytochrome P450 26B1	100	18.52	17.31	12.20	10.62
Cytochrome P450 26A1	11.75	0.00	11.57	0.00	10.62
Nuclear receptor ROR-gamma	10.93	11.33	11.57	0.00	10.62
Prostanoid EP4 receptor	10.93	0.00	0.00	0.00	0.00
Prostanoid EP1 receptor	10.93	0.00	0.00	0.00	0.00
Steroid 5-alpha-reductase 2	10.93	0.00	0.00	0.00	0.00
Peroxisome proliferator-activated receptor alpha	10.93	0.00	0.00	0.00	0.00
Peroxisome proliferator-activated receptor gamma	10.93	0.00	0.00	0.00	0.00
Peroxisome proliferator-activated receptor delta	10.93	0.00	0.00	0.00	0.00
Hepatocyte nuclear factor 4-alpha	10.93	11.33	11.57	0.00	10.62
Arachidonate 5-lipoxygenase	10.93	0.00	0.00	0.00	0.00
Free fatty acid receptor 1	10.93	0.00	0.00	0.00	0.00
Monocarboxylate transporter 1 (by homology)	10.93	0.00	0.00	0.00	0.00
Acyl-CoA desaturase	10.93	0.00	0.00	0.00	0.00
Leukotriene B4 receptor 1	10.93	0.00	0.00	0.00	0.00
G protein-coupled receptor 44	10.93	0.00	0.00	0.00	0.00
Solute carrier family 22 member 12	10.93	0.00	0.00	0.00	0.00
11-beta-hydroxysteroid dehydrogenase 1	10.93	11.33	11.57	0.00	10.62
Prostanoid DP receptor	10.93	0.00	0.00	0.00	0.00
T-cell protein-tyrosine phosphatase	10.93	0.00	0.00	0.00	0.00
p53-binding protein Mdm-2	10.93	0.00	0.00	0.00	0.00
Prostaglandin E synthase 2	10.93	0.00	0.00	0.00	10.62
Transient receptor potential cation channel subfamily M member 8	10.93	0.00	0.00	0.00	0.00
Alpha-2b adrenergic receptor	10.93	0.00	0.00	0.00	0.00
Adenosine A3 receptor	10.93	0.00	0.00	0.00	0.00
Gamma-secretase	10.93	0.00	0.00	0.00	0.00
Thromboxane-A synthase	10.93	0.00	0.00	0.00	0.00
Epoxide hydratase	10.93	11.33	11.57	0.00	0.00
Tyrosine-protein kinase receptor FLT3	0.00	11.33	0.00	0.00	0.00
Vasopressin V2 receptor	0.00	11.33	11.57	0.00	10.62
Cytochrome P450 11B1	0.00	11.33	11.57	0.00	0.00
Cytochrome P450 11B2	0.00	11.33	11.57	0.00	0.00
Cytochrome P450 19A1	0.00	11.33	0.00	0.00	0.00
Cytochrome P450 17A1 (by homology)	0.00	11.33	11.57	0.00	0.00
Metabotropic glutamate receptor 1	0.00	11.33	0.00	0.00	0.00
Glycine transporter 1 (by homology)	0.00	11.33	0.00	0.00	0.00
Histamine H3 receptor	0.00	11.33	11.57	0.00	0.00
P2X purinoceptor 7	0.00	11.33	11.57	0.00	0.00
Voltage-gated calcium channel alpha2/delta subunit 1	0.00	11.33	0.00	0.00	0.00
Melatonin receptor 1A	0.00	11.33	0.00	0.00	10.62
Melatonin receptor 1B	0.00	11.33	0.00	0.00	10.62
Glutaminyl-peptide cyclotransferase	0.00	11.33	0.00	0.00	0.00
Nuclear factor NF-kappa-B p65 subunit	0.00	11.33	11.57	0.00	0.00
Carbonic anhydrase II	0.00	11.33	0.00	0.00	0.00

Carbonic anhydrase VII	0.00	11.33	0.00	0.00	0.00
Carbonic anhydrase XII	0.00	11.33	0.00	0.00	0.00
Carbonic anhydrase XIV	0.00	11.33	0.00	0.00	0.00
Carbonic anhydrase IX	0.00	11.33	0.00	0.00	0.00
Metabotropic glutamate receptor 5 (by homology)	0.00	0.00	11.57	0.00	10.62
C-X-C chemokine receptor type 3	0.00	0.00	11.57	0.00	10.62
Phosphodiesterase 10A	0.00	0.00	11.57	0.00	10.62
Vasopressin V1a receptor	0.00	0.00	11.57	0.00	10.62
Protein farnesyltransferase	0.00	0.00	11.57	0.00	0.00
Geranylgeranyl transferase type I	0.00	0.00	11.57	0.00	0.00
Plasma retinol-binding protein	0.00	0.00	11.57	0.00	0.00
Mu opioid receptor	0.00	0.00	11.57	0.00	0.00
Neuronal acetylcholine receptor protein alpha-7 subunit	0.00	0.00	11.57	0.00	0.00
5-lipoxygenase activating protein	0.00	0.00	11.57	0.00	10.62
Adenosine A2a receptor	0.00	0.00	11.57	0.00	0.00
Dual specificity protein phosphatase 3	0.00	0.00	11.57	0.00	0.00
Tankyrase-1	0.00	0.00	11.57	0.00	0.00
Proteinase-activated receptor 1	0.00	0.00	0.00	0.00	10.62
C-C chemokine receptor type 1	0.00	0.00	0.00	0.00	10.62
Serotonin 5a (5-HT5a) receptor	0.00	0.00	0.00	0.00	10.62
Type-1 angiotensin II receptor (by homology)	0.00	0.00	0.00	0.00	10.62
Phosphodiesterase 7A	0.00	0.00	0.00	0.00	10.62

Biosensing L-DOPA with laccase-based enzyme electrodes: a comparative study

M. E. Shukri[1], N. Dimcheva[1,2*]

[1]*Laboratory on Biosensors, Centre of Technologies, University of Plovdiv "Paisii Hilendarski", 21 „Kostaki Peev" Str., Plovdiv, Bulgaria*
[2]*Faculty of Chemistry, Department of. Physical Chemistry, 24, "Tsar Assen" Str., Plovdiv 4000, Bulgaria*

The focus of the present work is to develop and optimize an electrochemical laccase-based biosensor for the determination of 3,4-dihydroxyphenyl-alanine, also known as L-DOPA. The biosensor was assembled on a conventional glassy carbon electrode, the surface of which was covered with laccase enzyme retained under a thin Nafion™ membrane. The enzymes used for this purpose were isolated and purified from the white-rot basidiomycetes (*Trametes sp.*) *Trametes pubescens* and *Trametes versicolor*. Although biochemically similar, the two enzymes demonstrated some differences in their affinity not only using 3,4-dihydroxyphenyl-L-alanine as enzyme substrate, but also when catecholamines such as dopamine and L-epinephrine were used. A range of electrochemical techniques were used for the study, such as cyclic voltammetry, chronoamperometry, and electrochemical impedance spectroscopy. Experiments were performed using buffers with different pH and applying various substrate concentrations. Activity and sensitivity of the two alternative laccase – based biosensors were compared by means of chronoamperometry. The biosensor produced on the basis of *Trametes pubescens* laccase, operating in citrate buffer with pH 4 proved to be more suitable than the one based on laccase purified from *Trametes versicolor* for biosensing L-DOPA.

Keywords: Laccase from basidiomycetes, electrochemical biosensor, L-DOPA.

INTRODUCTION

Due to its ability to prevent Parkinson's disease which is characterized by lack of dopamine in nerve cells, L-DOPA has gathered considerable attention. L-DOPA can be oxidized in cells by the enzyme tyrosinase, which reaction is responsible for the formation of the skin pigment melanin [1]. Reactive oxygen species (ROS) include hydroxyl radical (HO•), superoxide anion (O_2•-), and hydrogen peroxide (H_2O_2) can be produced during these reactions. L-DOPA is also a dopamine precursor, which may undergo enzyme-catalysed decarboxylation to form the neurotransmitter [2].

Laccases (EC 1.10.3.2, p-diphenol: dioxygen oxidoreductases) are multi-copper glycoproteins that are widely found in nature [3]. Through a reaction mechanism catalyzed by radicals, they oxidize a variety of aromatic and non-aromatic compounds *via* molecular oxygen [4]. Laccases show catalytic activity toward ortho- and para-diphenol groups, including mono-, di-, and poly-phenols, aminophenols, methoxyphenols, aromatic amines and ascorbate [5]. This class of multicopper oxidases can oxidize a variety of substrates by using oxygen as an electron acceptor. Neither reactive oxygen species (ROS), which are dangerous, nor partially reduced O_2 species are released by multicopper

oxidases (MCOs), which catalyse enzymatic conversion of O_2 directly to H_2O *via* a 4-electron mechanism [6].

Laccases belong to a rare class of metalloproteins that are capable of exchanging electrons with the underlying electrode surface and thus to reduce electrocatalytically oxygen to water [7, 8]. These enzymes have been detected in a variety of organisms, such as bacteria, fungi, plants, and insects. Most common laccase producers are the wood rotting basidiomycetes, e.g. *Trametes versicolor, Trametes pubescens, Trametes hirsute, Trametes ochracea, Trametes villosa, Trametes gallica, Cerena maxima, Coriolposis polyzona, Lentinus tigrinus, Pleurotus eryngii*, etc. [9, 10].

A number of analytical methods have been used for the determination of L-DOPA, such as high-performance liquid chromatography [11], electrochemiluminescence [12], spectrophotometry [13], flow injection analysis, capillary zone electrophoresis [14], and fluorescence methods [15]. Despite the high sensitivity offered by these methods, a number of drawbacks have been noted, including complexity of the equipment, need for highly-trained personnel, lengthy testing times, and high costs of analysis. In contrast to these approaches, electrochemical techniques have

---

* To whom all correspondence should be sent:
E-mail: *ninadd@uni-plovdiv.bg*

attracted increasing interest because of their ease of use, affordability, high sensitivity, and quick response time [16].

Biosensing L-DOPA is usually implemented by means of tyrosinase-based enzyme electrodes [17], operating within a large potential window, where undesired electrochemical transformations may take place as well. On the other side, there is only a limited number of reports on biosensing L-DOPA by means of a laccase-based enzyme electrode.

Thus, the purpose of the present work is to compare the catalytic performance of two laccase enzymes, purified from Basidiomycetes of *Trametes sp.* during the catalytic oxidation of L-DOPA, assayed electrochemically with the aim to select the best performing enzyme to be used in the construction of a biosensing system capable of discriminating between catecholamines and L-DOPA.

EXPERIMENTAL

Laccase (E.C. 1.10.3.2) enzymes from *Trametes versicolor* (Fluka) and *Trametes pubescens* (a generous gift from Prof. Dr. Roland Ludwig, Department of Food Science and Technology, BOKU–University of Natural Resources and Life Science) were with homogeneous specific activity of 23 U mg^{-1} and 46 U mg^{-1}, respectively. One unit of enzyme is defined as the oxidation of 1.0 μmol of ABTS per min at pH 4 and 30 °C. Laccases were used as solutions in 0.05 M sodium-citrate buffer, pH = 4, with concentrations of 50 mg/mL and 20 mg/mL, respectively.

The enzyme electrodes were prepared on the basis of commercial glassy carbon electrodes (2 mm diameter, Metrohm, Utrecht, The Netherlands). Prior to modification, the electrodes were cleaned by ultrasonication in ultrapure water for two minutes, after which they were polished with 0.05 μm alumina slurry on a polishing cloth (Kulzer, Hanau, Germany), water-rinsed and cleaned by ultrasonication in ultrapure water again.

Enzyme immobilization was implemented as follows: 2 μl of enzyme solution (20 mg/ml *Trametes pubescens* laccase or 50 mg/ml *Trametes versicolor* laccase) were drop-cast on the electrode surface. Then, a 4 μl drop of 0.2% Nafion 117 was applied. The surface was allowed to dry at room temperature.

After measurements, the enzyme electrodes were rinsed with bidistilled water and refrigerated at 4°C when not in use. The regeneration of the working enzyme electrodes can be done after the mechanical removal of the enzyme-polymer layer *via* polishing procedure and following the above steps.

All electrochemical experiments were performed in a conventional three-electrode cell with working volume of 10 mL, connected to a computer-controlled electrochemical workstation, Autolab PGSTAT 302 N (Metrohm-Autolab, Utrecht, The Netherlands) equipped with NOVA 2.1.6 software. Unmodified or modified glassy carbon electrode was used as working, Ag|AgCl, sat. KCl (Metrohm, Utrecht, The Netherlands)—as a reference—and a platinum foil as an auxiliary electrode. If not otherwise specified, all reported potentials were referred to Ag|AgCl, sat. KCl electrode.

Cyclic voltammetry was run at a scan rate of 5 mV.s^{-1}. Chronoamperometric detection was tested at three different potentials (-0.1 V, -0.2 V and -0.3 V). The chronoamperometric detection was carried out with a rotating disc electrode at a rotation speed of 500 rpm .

Volt-ampere curves were obtained by adding aliquots of L-DOPA with a concentration of 10 mM to 10 ml of citrate buffer (pH 4 and pH 4.5) in the following order - 3×20 μl, 3×50 μl, 3×100 μl, 3×200 μl, 3×500 μl, 3×1000 μl.

Electrochemical impedance spectroscopy (EIS) was performed in a conventional 3-electrode setup, in 0.1M KCl containing 5 mM of $K_4[Fe(CN)_6]/K_3[Fe(CN)_6]$ as redox probe over the range of frequencies from 100 kHz to 1 Hz.

RESULTS AND DISCUSSION

Enzyme immobilization on the electrode surface is of key importance when aiming at a long-lasting stability of the resulting bioelectrode. For this purpose, laccase was retained on the electrode surface under a semi-permeable membrane of ionomer Nafion, possessing negatively-charged groups. To examine the specific properties of the electrode-electrolyte interface of the studied system, electrochemical impedance spectroscopy (EIS) – a non-destructive alternating current technique, was applied.

Complex plane plots of the impedance for unmodified glassy carbon electrode and for the same electrode covered with polymer layer entrapping either of the two laccases are depicted in Fig. 1. Nyquist plot for the bare glassy carbon electrode consists of a semi-circle region characteristic for the charge-transfer resistance over the high frequencies range, followed by a very short linear region tilted at *ca.* 45° typical for Warburg impedance (indicative for diffusion control over the redox process) arising over the low-frequencies range. The EIS-spectra of glassy carbon electrodes bearing immobilized laccases are extremely similar to the one of the bare glassy carbon. The only difference is that the radii of

the semi-circle regions of the two enzyme-bearing electrodes are larger than the one observed in the EIS spectrum of bare glassy carbon electrode. This finding is associated with an increased charge transfer resistance, indicative for partly hampered penetration of the redox probe that is most probably a result from the increased thickness of the enzyme-confining polymer layer.
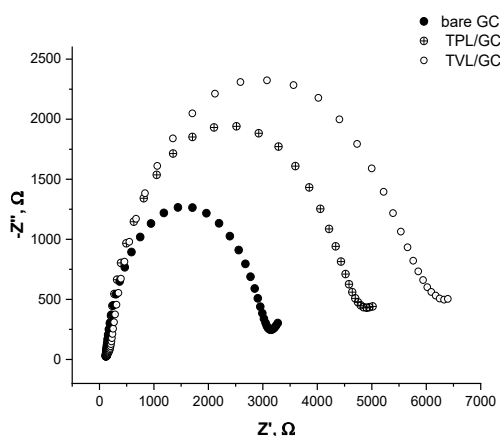
Fig. 1. Impedance spectra of: (●) bare glassy carbon electrode (GCE); (⊕) *Trametes pubescens* laccase immobilized on GCE; (o) *Trametes versicolor* laccase immobilized on GCE.

Further, the electrochemical activity of the two types of laccase-based enzyme electrodes was studied by cyclic voltammetry (CV). Comparison of the CVs of the enzyme electrode recorded in the absence and the presence of oxygen (Fig. 2) reveals laccase-catalyzed electrochemical reduction of dissolved oxygen. On the CVs recorded with a low scan rate in deaerated buffer (Fig. 2, black line) no peaks are detectable on both forward and reverse scans. On the other hand, the CV recorded in aerated buffer solution (Fig. 2, red line), shows a clearly expressed reductive wave starting below 0.1 V, which is due to the electrochemical reduction of dissolved oxygen catalyzed by the immobilized enzyme. As it was underlined in the Introduction, laccase is one of the few oxidoreductases capable of exchanging electrons with underlying electrode surfaces without the need for additional electron shuttles (mediators), with the efficiency of the electrical communication controlled by both the enzyme orientation and the distance between its active site and the electrode surface. It is hypothesized that the negatively charged Nafion membrane formed during the immobilization process electrostatically repulses the negatively charged laccase active site, this way orienting the enzyme in a conformation favorable for electron exchange with the underlying electrode surface,

which becomes obvious in the presence of molecular oxygen. Therefore, the voltammetric studies revealed its ability for performing bio-electrocatalytic oxygen reduction to water thus confirming that the chosen way of enzyme immobilization yields an enzyme electrode with electrocatalytically active enzyme.

The preliminary experiments have shown that in the presence of substituted phenols, the current of the oxygen reduction increases proportionally to the concentration of the added substance, which phenomenon is also known as mediated electron transfer (MET). In this respect, the electrode response of both types of laccase-based biosensors was studied at constant potentials over the range from -0.1 to -0.3 V *vs.* Ag|AgCl, sat. KCl upon addition of aliquots of 3,4-dihydroxy phenylalanine stock solutions to the working medium. The resulting dependencies of the electrode response on substrate concentration were found to follow Michaelis type kinetics, with the slopes of the linear parts of the plots being dependent on both the potential at which the bioelectrode was poised, and pH of the operating medium (Fig. 3). For both laccase-based electrodes, higher electrode sensitivities were detected at pH = 4.0, and therefore all further studies were performed at this pH.
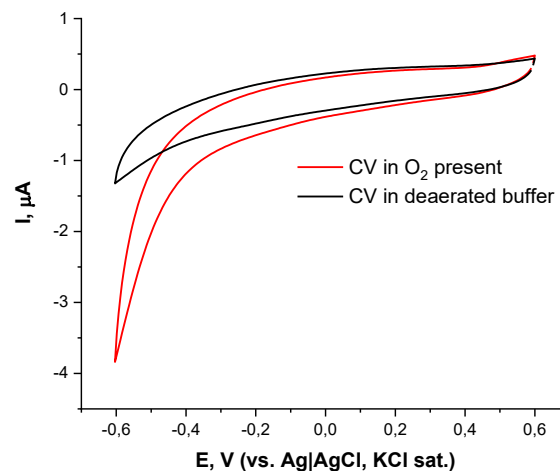
Fig. 2. Cyclic voltammograms of laccase electrode recorded in the presence (red) and in the absence (black) of dissolved O_2, electrolyte – citrate buffer, pH = 4.

Differences were noted in the variation of the electrode sensitivity with changing the polarization potential. For the electrode with immobilized laccase from *Trametes versicolor*, electrode sensitivity remains practically constant at applied potentials of -0.1 and -0.2 V, then slightly decreases at -0.3 V (Fig. 3A, black line), whilst for the other type of laccase-based electrode (*Trametes pubescens*) there is a visible sensitivity increase at an applied potential

97

of -0.2 V (Fig. 3B, black line) as compared to -0.1 V and -0.3 V. It is worth mentioning that there is a big difference in the sensitivity values for the two types of enzyme electrodes – the one for *Trametes versicolor* laccase–based electrode is almost twice as low as the sensitivity of the other type of enzyme electrode.
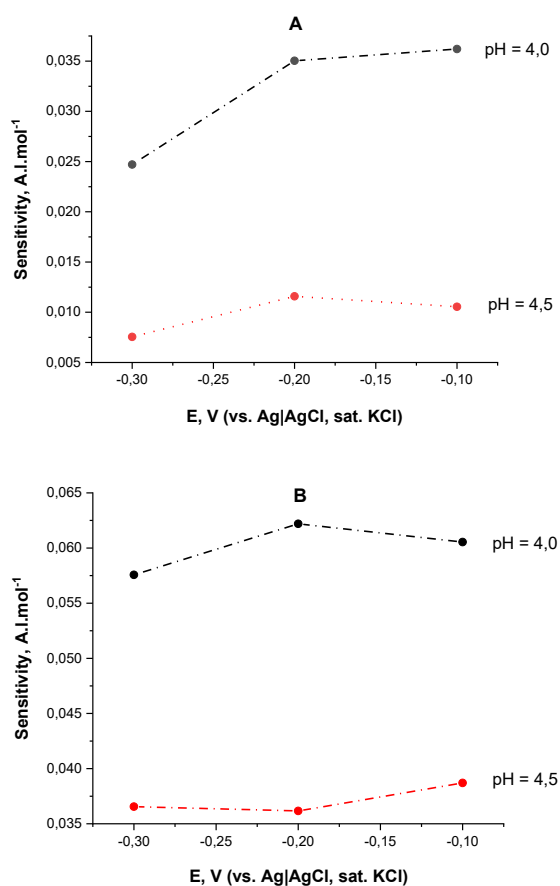
Fig. 3. Electrode sensitivities (slopes of the calibration graphs) as a function of electrode polarization potential at two different pHs of the medium for the enzyme electrode with immobilized laccase from: A) *Trametes versicolor*; B) *Trametes pubescens*.

In Fig. 4 are depicted the dependencies of the current density on the concentration of L-DOPA determined with the two types of laccase-based electrodes under the working conditions selected as optimal: working potential of -0.2 V and pH = 4.0. The similarity in the shape of the curves is obvious – both electrode types manifest hyperbolic trends of the dependencies of the electrode response on the substrate concentration. However, the apparent kinetic constants for the two immobilized laccases, determined from non-linear regression of the experimental data, show noticeable differences. The apparent Michaelis constant for immobilized laccase (*Trametes versicolor*, Fig. 4B) was found to be: $K_M^{app} = 0.89 \pm 0.012$ mM and $V_{max}^{app} = 329.8 \pm 32.8$

98

µA cm^{-2}, whilst for the immobilized laccase from *Trametes pubescens* (Fig. 4A), the apparent kinetic constants were calculated as $K_M^{app} = 1.77 \pm 0.76$ mM and $V_{max}^{app} = 273.3 \pm 7.0$ µA cm^{-2}. These differences in the apparent kinetic constants of the two identically immobilized enzymes suggest that despite biochemical similarity of the two laccases – the one isolated from *Trametes versicolor*, and the one purified from *Trametes pubescens*, there are noticeable differences in enzyme affinity towards L-DOPA, with *Trametes versicolor* laccase possessing greater enzyme affinity towards this particular substrate thus shortening the linear dynamic range within which the substrate can be determined.
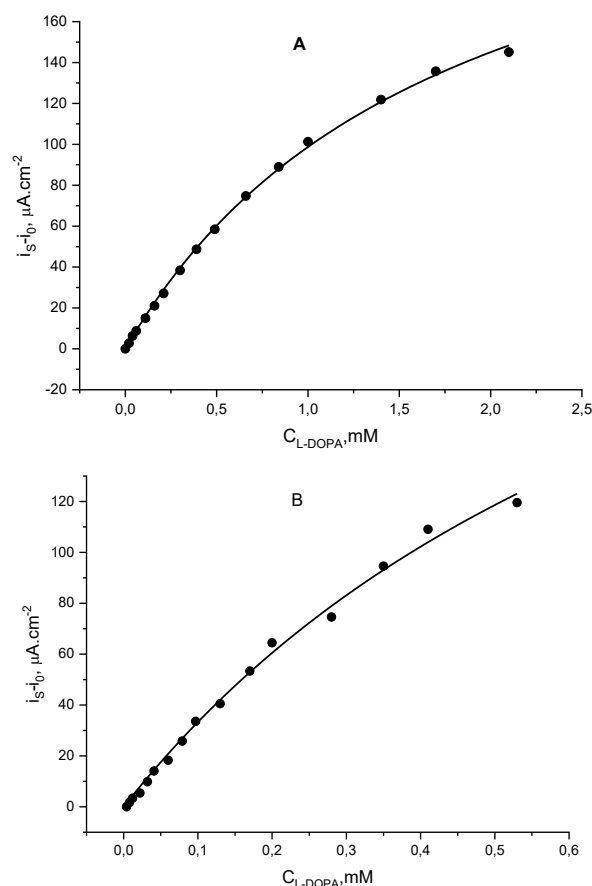
Fig. 4. Dependence of the current density of the biosensor on the L-DOPA concentration for: A) *Trametes pubescens*; B) *Trametes versicolor*; working potential E = -0.2 V.

Operational stability of the produced laccase electrode was tested over a period of 5 days and the resulting remaining activity as a function of number of measurements performed with the same electrode is depicted in Fig. 5. It could be seen that over the first four measurements the electrode gradually loses ca 7% of its activity. It retains about 30% of its initial activity after 10 measurements (on the day 2 of preparation), that can be explained with loss of catalytic activity of the enzyme due to both enzyme

leakage in the maintenance buffer and enzyme inactivation due to continuous exposure at room temperature.

The two types of laccase electrodes were tested for interference from L-ascorbic acid, dopamine, and L-epinephrine, since L-ascorbate is a usual attendant of real samples where L-DOPA is to be assayed, and the two catecholamines (dopamine and L-epinephrine) can be eventually present in pharmaceuticals containing the analyte under study.
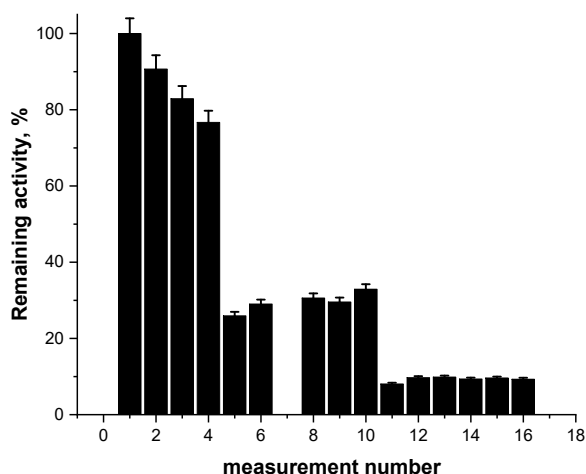
Fig. 5. Remaining electrode activity as a function of measurement number.

The results indicate that under the working potential, the interference effect of L-ascorbate on the assay of L-DOPA would not be substantial, however the presence of catecholamines may largely compromise the analysis of 3,4-dihydroxy phenylalanine.

Based on the above considerations, it can be concluded that laccase from *Trametes pubescens* is more suitable for the development of an enzyme electrode for the determination of 3,4- dihydroxy phenylalanine because of: i) wider linear dynamic range; ii) facilitated substrate penetration through the enzyme layer due to lower enzyme load in the electrode-covering membrane, and iii) greater electrode sensitivity.

REFERENCES

1. M. Dai, T. Huang, L. Chao, Y. Tan, C. Chen, W. Meng, Q. Xie, *RSC Advances*, **6**, 17016 (2016).
2. J. A. Best, H. F. Nijhout, M. C. Reed, *Theoretical Biology and Medical Modelling*, **6**, 21 (2009).
3. L. Arregui, M. Ayala, X. Gómez-Gil, G. Gutiérrez-Soto, C. E. Hernández-Luna, M. Herrera de los Santos, L. Levin, A. Rojo-Domínguez, D. Romero-Martínez, M. C. N. Saparrat, M. A. Trujillo-Roldán, N. A. Valdez-Cruz, *Microbial Cell Factories*, **18**, 200 (2019).
4. M. Tišma, P. Žnidaršič-Plazl, I. Plazl, B. Zelić, D. Vasić-Račkic, *Chemical and Biochemical Engineering Quarterly*, **22**, 307 (2008).
5. M. M. Rodríguez-Delgado, G. S. Alemán-Nava, J. M. Rodríguez-Delgado, G. Dieck-Assad, S. O. Martínez-Chapa, D. Barceló, R. Parra, *TrAC Trends in Analytical Chemistry*, **74**, 21 (2015).
6. G. Janusz, A. Czuryło, M. Frąc, B. Rola, J. Sulej, A. Pawlik, M. Siwulski, J. Rogalski, *World Journal of Microbiology and Biotechnology*, **31**, 121 (2015).
7. D. M. Ivnitski, C. Khripin, H. R. Luckarift, G. R. Johnson, P. Atanassov, *Electrochim. Acta*, **55**, 7385 (2010).
8. M. Pimpilova, K. Kamarska, N. Dimcheva, *Biosensors*, **12**, 719 (2022).
9. V. Madhavi, S. S. Lele, *BioResources*, **4**, 1694 (2009).
10. Q. Wang, L. Ding, C. Zhu, *Biotechnology & Biotechnological Equipment*, **32**, 1477 (2018).
11. T. Dhanani, R. Singh, S. Shah, P. Kumari, S. Kumar, *Green Chemistry Letters and Reviews*, **8**, 43 (2015).
12. N. Mirzanasiri, M. Hosseini, B. Larijani, H. Rashedi, *Analytical and Bioanalytical Electrochemistry*, **10**, 147 (2018).
13. M. F. Abdel-Ghany, L. A. Hussein, M. F. Ayad, M. M. Youssef, *Spectrochimica Acta - Part A: Molecular and Biomolecular Spectroscopy*, **171**, 236 (2017).
14. L. Zhang, G. Chen, Q. Hu, Y. Fang, *Analytica Chimica Acta*, 431, 287 (2001).
15. A. Moslehipour, A. Bigdeli, F. Ghasemi, M. R. Hormozi-Nezhad, *Microchemical Journal*, **148**, 591 (2019).
16. R. G. State, J.K.O.O.S.F. van Staden, *Electrochemical Science Advances*, **2,** e2100040 (2022).
17. F. Mollamohammadi, H. Faridnouri, E. N. Zare, *Biosensors*, **13**, 562 (2023).

Effect of chitosan/plant oils edible coatings on minimally processed peach quality during storage

P. Sabeva, G. Zsivanovits*, A. Parzhanova, D. Iserliyska, M. Momchilova, S. Zhelyazkov, P. Tranenska, A. Iliev

Institute of Food Preservation and Quality, Agricultural Academy, Plovdiv, Bulgaria

The edible coatings are capable to extend the shelf-life of minimally processed fruits and reduce the synthetic packaging's waste. The used coating materials are obtained from renewable plant sources and byproducts of the food production. In addition, they are functional active ingredients. In this study, low-molecular weight fungal chitosan-based coatings with plant oil emulsions were used for coating of sliced peach. For characterization of the differently coated fruit pieces physical, physicochemical, microbiological and sensorial properties were examined during refrigeration. The used coatings extended the shelf-life time up to 10 days and the coated fruits had acceptable sensory parameters even at the end of the storage.

Keywords: chitosan, plant-oil emulsions, physicochemical characterization, consumer precipitation test, fresh fruit

INTRODUCTION

The edible coating is an alternative possibility to preserve the quality and prolong the shelf-life of minimally processed (e.g. sliced) fruits [1]. The antimicrobial activity [2], and the permeability properties are the key parameters of the coating materials in the shelf-life extension [3], but the retaining of the sensory acceptance may be the biggest mission in this research field [1]. The climacteric peaches are very sensitive fruits for injuries and damages during the storage period [4]. Prolonging the shelf-life using low-molecular weight chitosan-based coatings was already studied in some of the earlier publications of this research team [5-8]. The present paper is dealing with the comparison of chitosan-grapeseed oil and chitosan-clove oil extracts, used as coating solutions [9] on sliced peaches during chilled storage.

MATERIALS AND METHODS

Chemicals

Low-molecular weight, water-soluble, fungal (mushroom origin) chitosan hydrochloride (degree of deacetylation > 85.0%) was purchased from Glentham Life Sciences Ltd, UK. Cold-pressed pure grape seed oil and clove oil were bought from Ikarov LTD, Plovdiv, Bulgaria. Tween 20 emulsifier and glycerol were delivered by Ray-Chem product LTD, Plovdiv, Bulgaria.

Fruits

Fresh peaches (*Prunus persica* L., cv. 'Glohaven') were harvested in full maturation stage at the Fruit Growing Institute – Plovdiv, Agricultural Academy of Bulgaria. The cultivar was chosen based on its ripening time (late July – early August) and resistance to rotting [10]. The intact fruits with 181±41 g average weight were carefully washed and sliced (quartered), before dipping in the coating solutions.

Treatments

Two hundred peach fruits (800 quarters) were used in four experimental series: control (not coated just washed - CONT), coated with low-molecular weight chitosan water solution (1% wt, CH), coated with an emulsion of low-molecular weight chitosan and grape seed oil (0.5% wt, CHG) and coated with an emulsion of low-molecular weight chitosan and clove oil (0.1% wt, CHC). Detailed procedure for emulsion preparation is given in Gechev *et al*. [11]. The fruit quarters were dipped in the coating liquids for 10 minutes and dried for 15 minutes at room temperature before refrigerating. Eight repetition trays (25 fruit pieces/tray) were prepared from each series and stored in a refrigerator at 4±1 °C.

Experimental methods

Visual loss (selected rotted pieces) and weight loss; texture (puncture test, peel side and pulp side);

---

color (CIELab, peel side and pulp side); BRIX; active acidity (pH); water activity, antioxidant content (DPPH method, 96% ethanol extract); microbiological safety, Total Plant Count (TPC) and sensory parameters were examined to follow the shelf-life time during 10 days. Statistical analysis was performed using the software Statistica (TIBCO Software Inc. 2020 version 14). Similar methods were used in the earlier publications [5-8].

RESULTS AND DISCUSSION

Visual loss and weight loss: The biggest losses ccould be detected in fruits without coatings. The chitosan-emulsion-based coatings reduced the intact and weight loss. The smallest losses were seen with chitosan-clove essential oil coating (Fig. 1), because it has the highest water retention ability [12].
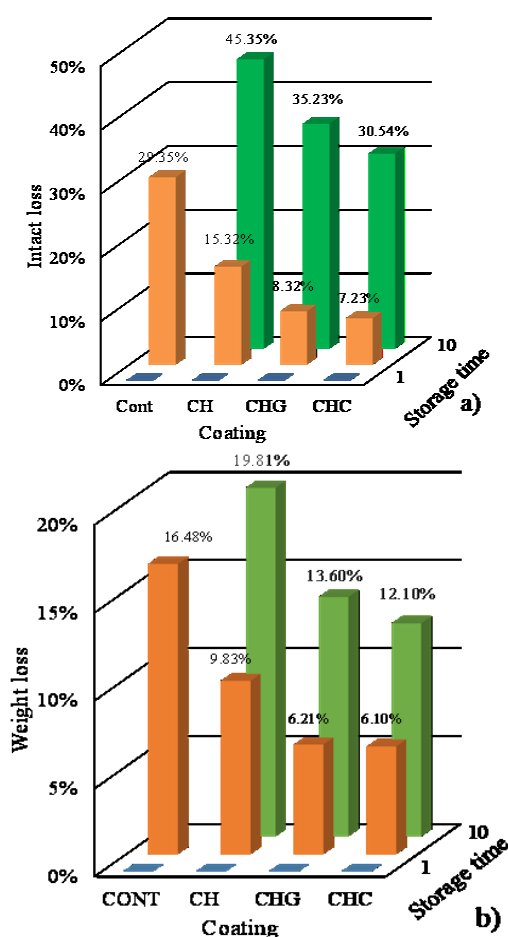
Figure 1. Visual (a) and weight loss (b) of the fruit pieces

Color changes during the shelf-life period

The coating changes the color parameters in a different range [12]. Color indicators (L – brightness; a – red-green; b – yellow-blue) depend on the packaging and change strongly during the storage (Figure 2). The water loss during the storage

can be a factor affecting fruit brightness [13]. CONT samples become lighter (L*), but packaging can delay (CH and CHG) or prevent (CHC) this process. The pulp side of the samples becomes darker during the storage, this process can also be delayed by the packaging (CH and CHC). A similar process was observed by Pizato *et al*. [14].

Color indicators a and b on the peel side show a loss of reddish color (a*). The pulp side of the peaches also becomes greener and yellower (b*). The inhibitory effect of the packages is visible; it is strongest with CHC packaging, followed by CH packaging and weakest with CHG packaging.

All of the changes are noticeable or clearly visible based on the ΔE parameter (Fig. 3a) which is defined as:

$$\Delta E = \sqrt{(L_0 - L_i)^2 + (a_0 - a_i)^2 + (b_0 - b_i)^2} \quad (1)$$

where (L_0; a_0; b_0) and (L_i; a_i; b_i) are the color parameters of the two compared samples [15].

The hairy skin and the fresh injured slice surfaces showed significant differences, because of the possibility for the deep diffusion of the coating solution. During the storage the differences were growing, but on the cut surface these did not depend on the coating (Fig. 3b). During the 10 days of storage, the color changes for samples coated with CH were significantly bigger than those of emulsion-coated samples (Fig. 3b) [15, 16].

Texture parameters of the fruit pieces

The coated samples showed higher firmness than the uncoated. The highest firmness was shown in case of CHC coating at the beginning, but during the storage, these fruit pieces softened faster. The firmness changes of the CHG coated fruit pieces were smaller than with the other coatings (Fig. 4) [17].

Physico-chemical changes

During short storage, as a consequence of drying, the soluble solid content (°Brix, Table 5) increases. Uncoated fruits dry out faster than the rest [18]. Emulsion packages better retain water and slow down losses. Similar results were obtained in our previous studies with other fruits [5-8]. CHG-coated slices also showed desiccation, but the process was slower [19]. Clove essential oil helps to retain the water content of the fruit slices. Packaged samples lose their freshness more slowly than unpackaged ones. During the storage, cell walls break down and intracellular water leaks out [20].

The drying and the pH changes depend on the water retention capability of the coating [21] (Table 1). The application of a coating containing

hydrophobic substances (oils, fats, emulsifiers, essential oils, etc.) can be used to isolate or maintain the separation of components that differ in terms of water activity in a compound food [22]. Reduction of water activity (a_w) and protection with moisture-

resistant packaging are common methods used to prevent food spoilage [23]. Based on our results, CHC packaging has a suppressive effect on the water activity.
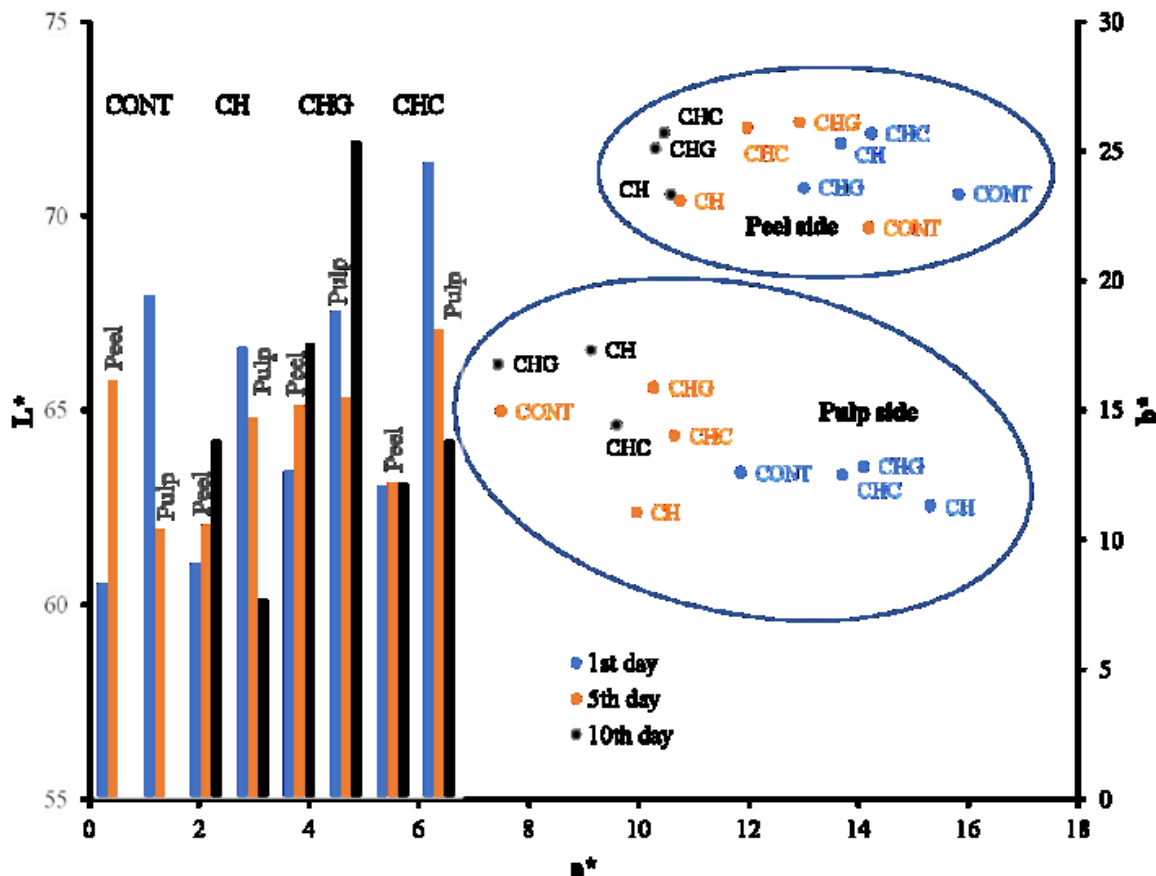
Figure 2. Changing of the CIELab parameters of the fruit pieces
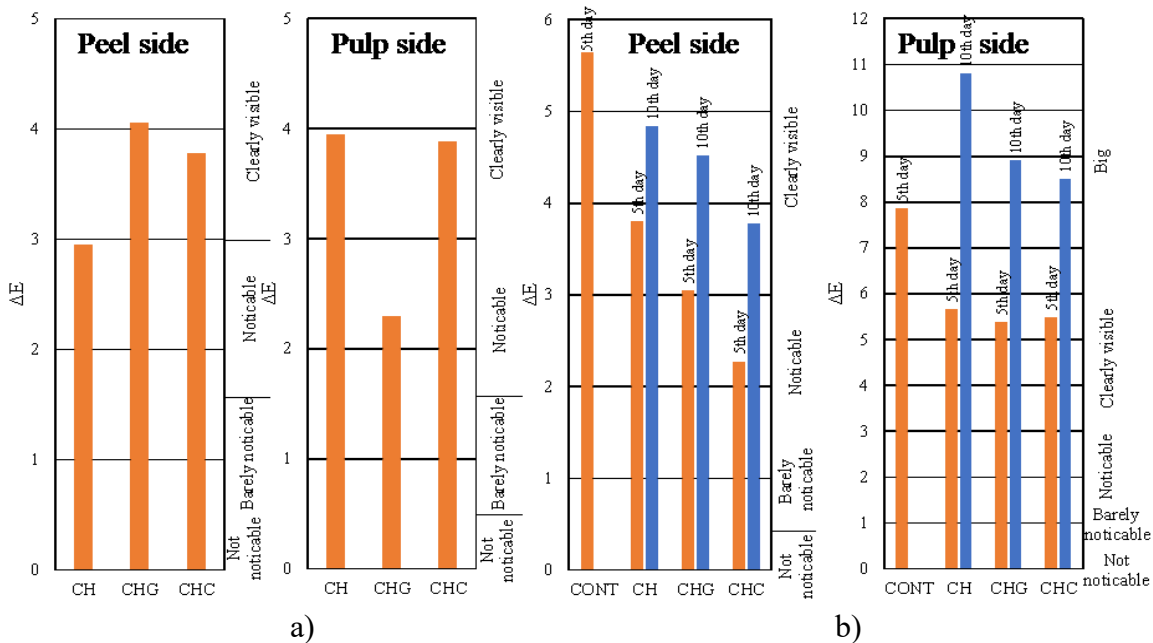
Figure 3. Total color differences (ΔE) between the control and the coated pieces on the peel and on the pulp side, after the coating (1st day, a) and between the 1st day and 5th or 10th days on the peel side and pulp side (b).
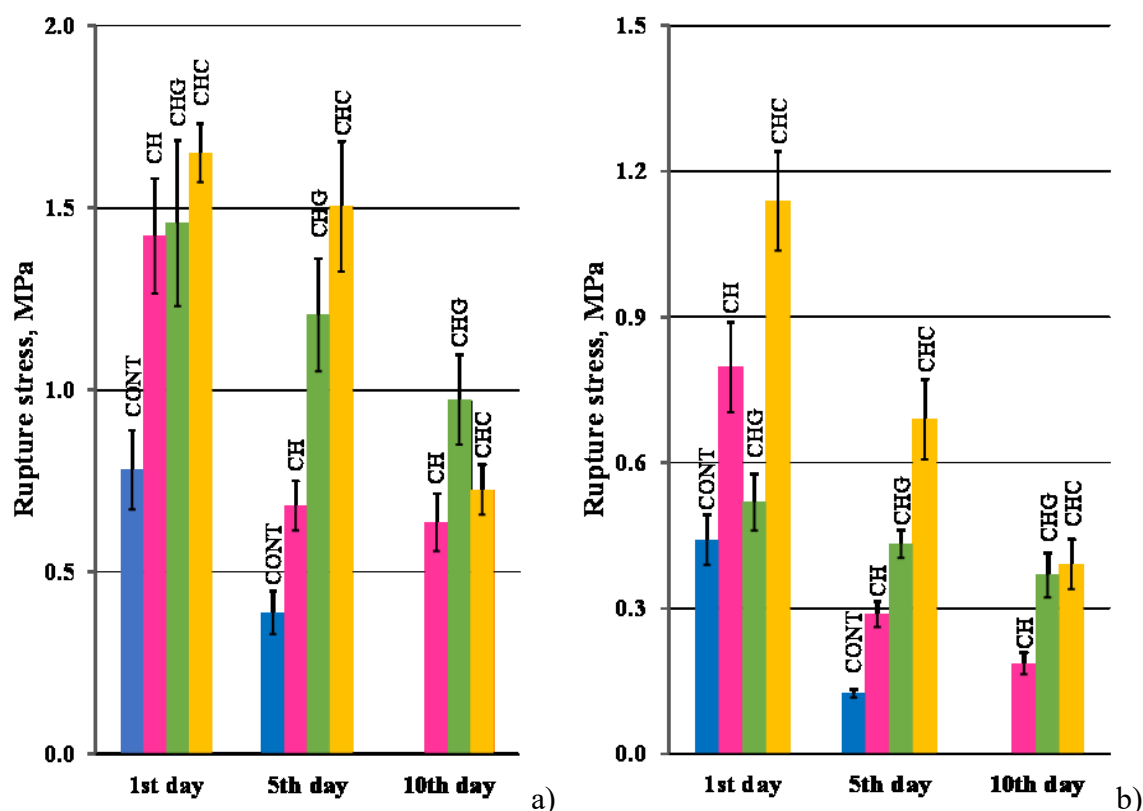
Figure 4. Firmness of the fruit pieces on the peel side (a) and on the pulp side (b)

Table 1. Physico-chemical parameters and microbiological status of the fruit pieces

	Day	°Brix	pH	a_W	AOA (DPPH), µmolTE/100g dw	TPC, cfu/g	Molds & Yeasts, cfu/g
CONT	1st	15.67 ± 0.93	3.62	0.94	240.58 ± 12.29	< 10	< 10
	5th	17.90 ± 0.52	3.86	0.94	223.37 ± 11.18	4.3×10^4	2.4×10^3
CH	1st	13.83 ± 0.32	3.48	0.94	248.17 ± 12.48	< 10	< 10
	5th	15.50 ± 2.20	3.74	0.93	233.44 ± 11.67	< 10	< 10
	10th	14.90 ± 1.04	3.97	0.89	211.25 ± 10.52	4×10^1	2×10^1
CHG	1st	13.50 ± 0.92	3.60	0.94	254.13 ± 12.76	< 10	< 10
	5th	15.27 ± 0.87	3.76	0.93	248.16 ± 12.48	< 10	< 10
	10th	15.70 ± 0.90	3.81	0.88	225.50 ± 11.27	1.9×10^2	1.1×10^2
CHC	1st	16.95 ± 1.07	3.78	0.87	258.21 ± 13.56	< 10	< 10
	5th	15.93 ± 0.92	3.84	0.88	254.62 ± 10.84	< 10	< 10
	10th	14.34 ± 0.83	3.81	0.89	232.05 ± 10.75	1.5×10^2	8×10^1

It is well known that oxidation is one of the main factors causing spoilage of fruits and vegetables [24]. The increase in pH is a consequence of enzymatic reactions during respiration. Different acidity and pH changes in fruits with chitosan-based coatings have also been reported in the literature [18, 25]. In this work, to investigate the antioxidant activity of grape seed oil and clove oil, free radical scavenging rate assays of the four systems, CONT, CH, CHG and CHC, were performed. Based on the DPPH assay, the differences in the antioxidant activity of the samples were small and not significant [26]. Storage time changes were greatest for uncoated samples. The CHC-coated series best preserved their antioxidant activity [27]. By the end of the storage, the reason for the larger changes in

antioxidant activity is most likely the volatility of these components [28].

Microbiological status of the fruit pieces

The applied coatings saved the fruit pieces from microbiological contamination (Table 1). The growing of the Total Plant Count (TPC) shows the end of the shelf-life period. The uncoated samples wasted their safety during 5 days. The emulsion coatings have a lower inhibitor effect than the pure chitosan. The CHC coating shows smaller microbiological contamination than the CHG [11, 29].

Consumer perception of samples with different packaging during storage

Storage time significantly affected the assessed sensory characteristics, as statistically significant differences (p = 0.05) were found in appearance, color and aroma; days of storage did not affect the juiciness and consistency of the fruit. The evaluated sensory characteristics were significantly affected by the type of coating during storage (p = 0.05). On the

1st day and the 5th day, significant differences with respect to the control and other samples were observed, on the 10th day there were bigger changes in the appearance and color of the samples coated with chitosan and clove oil (Fig. 5) [28, 29].

The overall score (the area of the sensory diagram) was calculated based on all sensory indicators. On the first day, the unpackaged samples received the highest overall score, followed by samples with CHG, CH and the lowest score was with CHC. By the 5th day, the loss of sensory quality was very rapid. Uncoated samples lost the most from their overall score. Retention of the overall score of CH and CHG values up to day 5 was very decent, and it was the best for CHC-coated samples. By the 10th day, the loss of sensory quality became slower. Uncoated samples were no longer tested because they lost their safety. Samples with CH packaging showed the lowest score, followed by those with CHC and CHG coatings, without significant differences. This result indicates that emulsion coatings best preserve the sensory evaluation of sliced peaches.
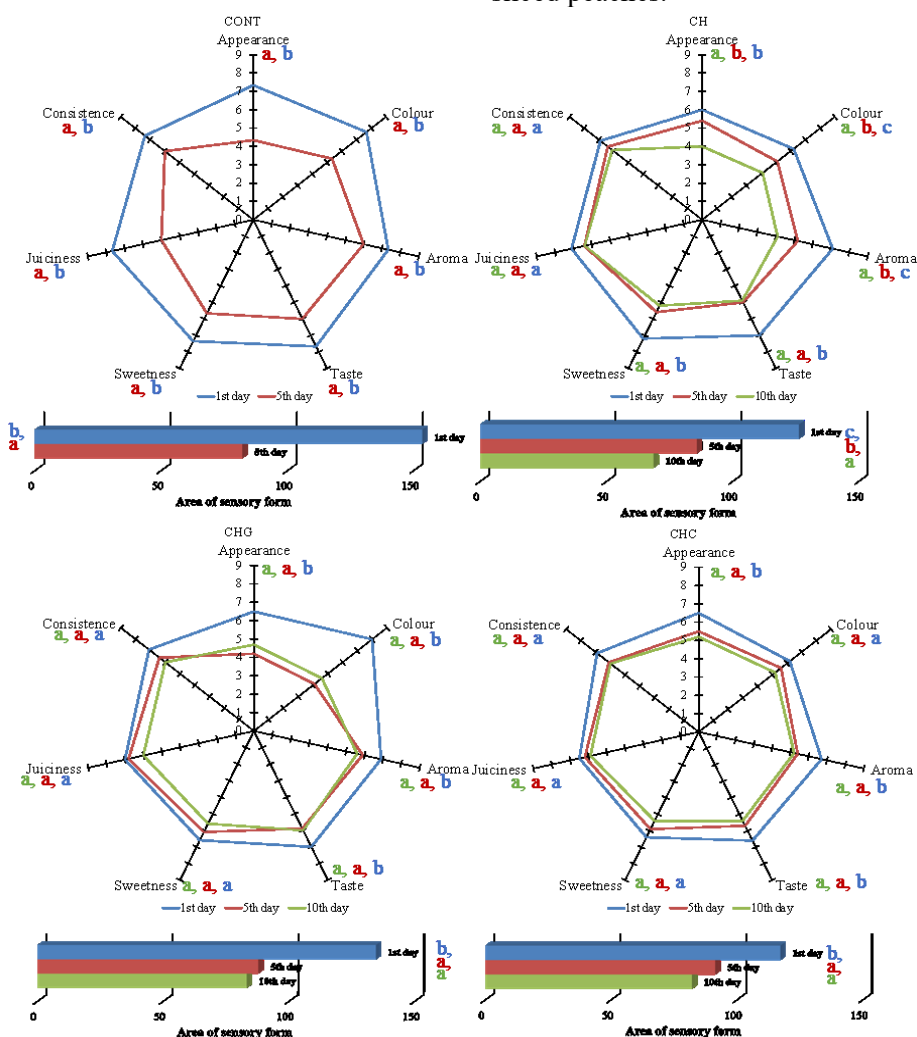
Figure 4. Consumer perception during the storage with different coatings

CONCLUSIONS

The applied multicomponent emulsion coatings saved the safety and quality of the coated pieces of peach. The observed prolonged shelf-life of the sliced peaches was 10 days. Based on the analyzed results, the clove essential oil emulsion solution was the best from the applied coatings.

REFERENCES

1. B. Maringgal, N. Hashim, I. S. M. A. Tawakkal, M. T. M. Mohamed, *Trends Food Sci. Technol.*, **96**, 253 (2020).
2. L. Salvia-Trujillo, M. A. Rojas-Graü, R. Soliva-Fortuny, O. Martín-Belloso, *Postharvest Biol. Technol.,* **105***, 8* (2015).
3. P. Jongsri, T. Wangsomboondee, P. Rojsitthisak, K. Seraypheap, *LWT,* **73***, 28* (2016).
4. G. Sortino, F. Saletta, S. Puccio, D. Scuderi, A. Allegra, P. Inglese, V. Farina, *Agriculture*, **10**(5), 151 (2020).
5. G. Zsivanovits, T. Grancharova, I. Dimitrova-Dyulgerova, D. Ivanova, S. Kostadinova, M. Marudova, *Prog. Agric. Eng. Sci.*, **14**(s1), 133 (2018).
6. G. Zsivanovits, D. Iserliyska, M. Momchilova, P. Sabeva, Z. Rankova, *Prog. Agric. Eng. Sci.,* **16**(S2), 65 (2021).
7. G. Zsivanovits, S. Zhelyazkov, M., Momchilova, D. Iserliyska, D. Aleksandrova, *Carpathian J. Food Sci. Technol.*, **13**(2), 93 (2021).
8. S. Zhelyazkov, G. Zsivanovits, M. Marudova-Zsivanovits, *BIO Web Conf.* (FoSET 2022) **58** (01012) 1 (2023).
9. G. Christian, B. P. María, *Crit. Rev. Food Sci. Nutr.*, **58**(4), 662 (2016).
10. A. Zhivondov, *Acta Hortic..* **962**, 123 (2009).
11. B. Gechev, G. Zsivanovits, A. Iliev, M. Marudova, *J. Phys. Conf. Ser.* **2436**(1), 012029 (2023).
12. ASTM D2244-23: ASTM Volume 06.01: Paint—tests For Chemical, Physical, And Optical Properties; Appearance (p1-12), 2012.
13. N. Rattanapanone, Y. W. Lee, A. E. Watada. *HortScience*, **36**, 1091 (2001).
14. S. Pizato, W. R. Cortez-Vega, J. T. Andreghetto De Souza, C. Prentice-Hernández, C. Dellinghausen Borgen, *J. Food Saf.* **33**, 30. (2013).
15. M. L. Zambrano-Zaragoza, E. Mercado-Silva, E. Gutiérrez-Cortez, M. A. Cornejo-Villegas, D. Quintanar-Guerrero, *IFSET*, **22**, 188 (2014).
16. S. K. Hasan, G. Ferrentino, M. Scampicchio, *Int. J. Food Sci. Technol.,* **55**(1), 1 (2020).
17. R. Severino, K. D. Vu, F. Donsì, S. Salmieri, G. Ferrari, M. Lacroix, *Int. J. Food Microbiol.,* **191**, 82 (2014).
18. P. Hernández-Muñoz, E. Almenar, V. D. Valle, D. Velez, R. Gavara. *Food Chem.*, **110**(2), 428 (2008).
19. L. Alandes, I. Hernando, A. Quiles, I. Pérez-Munuera, M. A. Lluch, *J. Food Sci.,* **71**(9), S615 (2006).
20. M. Ghasemnezhad, M. A. Nezhad, S. Gerailoo. *HEB*, **52**, 40 (2011).
21. P. Singh, T. Khan, F. J. Ahmad, G. K. Jain, J. Bora, *Songklanakarin J. Sci. Technol.*, **43**(5) (2021).
22. M. E. Embuscado, K. C. Huber, Edible films and coatings for food applications (vol. 9). New York, USA, Springer, 2009.
23. J. A. Torres, Microbial stabilization of intermediate moisture food surfaces, in: Water Activity, Routledge, 2017, p. 329.
24. A. Chib, N. Gupta, A. Bhat, N. Anjum, G. Yadav. *Int. J. Chem. Stud.,* **8**, 2354 (2020)
25. K. Hong, J. Xie, L. Zhang, D. Sun, D. Gong, *Sci. Hortic.,* **144**, 172 (2012).
26. L. Salvia-Trujillo, R. Soliva-Fortuny, M. A. Rojas-Graü, D. J. McClements, O. Martín-Belloso, *Annu. Rev. Food Sci. Technol.*, **8**, 439 (2017).
27. S. F. Hosseini, J. Ghaderi, M. C. Gómez-Guillén, *Food Hydrocoll.*, **124**, 107249 (2022).
28. H. Wang, Y. Ma, L. Liu, Y. Liu, X. Niu, *LWT,* **170**, 114059. (2022).
29. N. Robledo, L. López, A. Bunger, C. Tapia, L. Abugoch, *Food Bioproc. Tech.*, **11**, 1566 (2018).

Classification of apple varieties by VIS-NIR diffuse reflectance spectroscopy and chemometrics

J. Cruz[1], G. Gergov[2*], M. Tarapoulouzi[3], E. Kirilova[2], O. Kostadinova[4], K. Nikolova[5]

[1]*Escola Universitària Salesiana de Sarrià Passeig Sant Joan Bosco 74 08017 Barcelona, Catalonia, Spain*
[2]*Bulgarian Academy of Sciences, Institute of Chemical Engineering, Acad. Georgi Bontchev Str., Bl.103, Sofia 1113, Bulgaria*
[3]*Department of Chemistry, Faculty of Pure and Applied Science, University of Cyprus, P.O. Box 20537, Nicosia CY-1678, Cyprus*
[4]*Bulgarian Academy of Sciences, Institute of Electrochemistry and Energy Systems "Acad. E. Budevski", Acad. Georgi Bonchev Str. Bl.10, 1113 Sofia, Bulgaria*
[5]*Department of Physics and Biophysics, Medical University of Varna, Faculty of Pharmacy, 84 Tzar Osvoboditel Blvd, 9002 Varna, Bulgaria*

The new promising VIS NIR-ES (visible near infrared extra sensitive) spectrometer was used to identify a variety of apples. The aim of this study was to investigate the applicability of VIS-NIR spectroscopy combined with chemometric methods for the classification of different varieties of apples. The study was performed by analyzing the diffuse reflectance spectra of three different types of Chinese apples: the Fuji apple, the Red Star apple, and the Gala apple. To achieve this, after suitable preprocessing, a variable selection algorithm called interval partial least squares discriminant analysis (iPLS-DA) was used to identify the most significant spectral range. This range was then compared with the results obtained by PLS-DA (using the entire NIR spectrum) to discriminate apples of different species. The obtained results have shown that the iPLS-DA model outperforms the PLS-DA application in the entire spectral range when it comes to apple cultivar identification. The best model achieved an impressive 97.77% accuracy in the calibration set and 100% accuracy in the prediction set. These results show that the use of NIR spectroscopy is a capable method for identifying the apple variety and even the growing region.

Keywords: VIS-NIR, PLS-DA, iPLS-DA, apple varieties, classification

INTRODUCTION

There are a large number of apple cultivars available around the world. Several cultivars dominate the global supply and production: 'Fuji', 'Red star', 'Royal Gala', 'Golden Delicious', 'Granny Smith'. However, cases of mixing different varieties of fruit at harvest or in the market are observed. Therefore, incorrectly labeled or manipulated apples have become more frequent. The latter is becoming a global problem whose economic and social impact is difficult to evaluate. This fact highlights the need to implement increasingly accessible methods of detection and authentication of foods that conform to what is declared.

Numerous studies have demonstrated the effectiveness of VIS-NIR and NIR techniques in assessing apple classification and quality, showing significant potential for the food industry according to the quality of apples without damaging them [1]. Another challenge is the development of affordable and portable spectroscopic devices that can be easily integrated into fruit packaging lines for quick and real-time quality assessment, making these technologies more widely applicable.

The study of Pissard *et al.* [2] confirmed the importance of NIR spectroscopy to determine phenolic compounds and dry matter in apple peel and flesh separately to evaluate fruit quality. It was proved that different apple cultivars have different content of those parameters between the peel and pulp. The outcome of their study is in agreement with our findings which shows the differentiation of apple varieties based on NIR spectroscopy. Similarly, Beghi *et al.* [3] have used a portable VIS-NIR system in combination with PLSR to predict the total phenolic content in two apple varieties, "Stark Red Delicious" and "Golden Delicious". The latter variety had low phenolic concentration, and classification was successful. Pissard *et al.* [4] evaluated the performance of benchtop and portable devices (MicroNIR) utilizing NIR spectroscopy to explore the possibility of assessing various quality parameters in apples, including soluble solids content, titratable acidity, pulp firmness, and starch-iodine index. The results, based on Partial Least Squares (PLS) models, showed that the coefficient of determination (R^2) and the root mean square error of cross-validation (RMSECV) values were quite

---

* To whom all correspondence should be sent:
E-mail: *ggergov187@gmail.com*

similar for both devices. This suggests that MicroNIR provides performance comparable to that of the XDS device. The best results were achieved with the Least Squares Support Vector Machines (LS-SVM) chemometric method. The outcome supports the idea of our findings in terms of promoting NIR-based technologies and chemometrics in apple classification. Li *et al*. [5] studied combining NIR spectra with PCA, successive projections algorithm (SPA) in apple analysis. Three different pattern recognition methods, namely, the backpropagation neural network (BPNN), SVM, and extreme learning machine (ELM) were also applied to create models for distinguishing apples based on their varieties and geographical origins. Notably, the SPA-ELM model achieved an impressive 98.33% accuracy in identifying apples in the calibration set and 96.67% accuracy in the prediction set. This research suggests that NIR spectroscopy is a viable approach for identifying the variety and cultivation region of apple samples.

Moreover, Xu *et al*. [6] recently differentiated different varieties of apples by combining a similarity-based particle swarm optimization algorithm with the possibilistic fuzzy c-means (PFCM) algorithm, thus SPSO-PFCM. In addition, MSC and PCA chemometric methods eliminated the interference and reduced the complexity of the spectral data. Their results convincingly demonstrate that combining NIR diffuse reflectance with SPSO-PFCM clustering is an effective method for classifying different apple varieties. Cortés *et al.* [7] assessed five different apple varieties by using in-line VIS-NIR reflectance spectroscopy. To extract the most critical information from the spectra, PCA was employed. Seven principal components were then used in LDA and quadratic discriminant analysis (QDA). The results revealed that QDA was the most effective in-line classification method, achieving success rates of 98% for red apple varieties and 85% for yellow apple varieties. This study confirms that the in-line application of VIS-NIR spectroscopy is potentially feasible for accurately detecting apple varieties. Ongoing research and development in spectroscopic techniques for apple quality assessment can potentially enhance the efficiency, quality, and safety of the apple supply chain.

The aim of the present study was to evaluate the applicability of VIS-NIR spectroscopy combined with preprocessing and chemometric tools to classify three different types of Chinese apples: the Fuji apple, the Red Star apple, the Gala apple, and compare the results with the ones from Li *et al.*

article [5] where data from this study have been obtained. To achieve this, a variable selection algorithm called interval partial least squares discriminant analysis (iPLS-DA), after applying appropriate preprocessing, was used to identify the best spectral range. This range was then compared with the results obtained by applying classical PLS-DA using the entire NIR spectrum to discriminate apples of different varieties.

MATERIALS AND METHODS

Sample Preparation Procedure

For the purpose of this research, data from the article from Li *et al.* [6] were used. A total of 300 apples were selected to ensure representation and accuracy. Among these, 100 Fuji apples, 100 Red Star apples, and 100 Gala apples were used. Apples were selected from two prominent local markets. All selected apples exhibited smooth and unblemished skin, ensuring the highest quality for our study.

Before conducting any measurements, strict protocols were followed. First, all apple samples were placed in airtight polyethylene bags and stored in a refrigerator, maintaining a consistent cold temperature of $4 \pm 1°C$ for a duration of 2 days. Subsequently, after the designated storage period, the apples were removed from the refrigerator, thoroughly washed with clean water, meticulously wiped dry, and then left to acclimatize at room temperature ($24 \pm 2°C$) for approximately 3 hours. Only after these meticulous preparation steps the apples were suitable for spectral measurements.

Spectra Acquisition Procedure

An Ocean Optics USB2000-VIS-NIR-ES spectrometer was employed, sourced from Ocean Optics in the USA, equipped with HL-2000 tungsten halogen light sources also from Ocean Optics, and optical fiber reflection probes (QR600-7-VIS-NIR, Ocean Optics, USA).

NIR diffuse reflectance spectra were captured within the wavelength range of 400 to 1021nm, with an interval of approximately 0.33 nm, resulting in a total of 1888 variables for each spectrum. The data collection and transformation of spectra were facilitated using Ocean View software (Ocean Optics, USA). All measurements took place under controlled room temperature conditions, precisely at $24 \pm 2°C$.

Before the commencement of spectral measurements, a critical step involved the spectrometer being powered on for a minimum of 1 hour to stabilize and reach an optimal operating temperature. This ensured that the instrument

performed consistently throughout the data acquisition process.

During the actual spectral measurements, close proximity of the NIR optical fiber probe to the surface of the apple samples was maintained. This approach was adopted to minimize surface reflectance and eliminate any potential interference from the surrounding air.

A systematic approach was implemented to ensure robust data representation and reliability. For each intact apple sample, diffuse reflectance spectra were obtained at 15 distinct points, which were randomly selected along the equator of the apple. At each of these points, the spectral scan was repeated 10 times, resulting in a total of 150 scans. These 150 scans were then averaged to form a comprehensive and representative spectral dataset for each apple, subsequently serving as the dataset for chemometric analysis.

Data Analysis

Principal component analysis (PCA) and partial least square discriminant analysis (PLS-DA) models were applied by using Solo, version 9.2.1, a software solution developed by Eigenvector Research, Inc., headquartered in Wenatchee, WA, USA. Diverse spectral ranges were systematically explored by applying data preprocessing techniques to get the most suitable prediction models.

Principal Component Analysis (PCA)

Principal Component Analysis, often abbreviated as PCA, stands as a highly effective data mining technique that has found widespread application in spectral data analysis. The core principle behind PCA revolves around dimensionality reduction and orthogonalization of the original multidimensional dataset. The ultimate aim is to derive a set of linearly uncorrelated variables, termed principal components (PCs), with several key objectives in mind.

One primary goal is to minimize the risk of overfitting, a phenomenon where a model becomes too complex and starts fitting noise in the data rather than the true underlying patterns. Additionally, PCA enhances the training procedure's computational efficiency, making it more manageable and resource-efficient.

These principal components are calculated simultaneously through a single matrix decomposition, which extracts essential information from the original data while significantly reducing the number of variables. The first principal component is designed to capture as much variability as possible in the original dataset, thus providing a comprehensive overview of the data's main patterns.

Subsequent components follow, each exhibiting lower variance than its predecessors.

One of the key strengths of PCA is its ability to transform high-dimensional data into a lower-dimensional representation while preserving the essential information present in the original dataset. Despite this reduction in variable numbers, the principal components remain powerful descriptors that effectively encapsulate the majority of the original data's variance. This capacity to condense information while retaining its significance is a hallmark of PCA's utility in data analysis and dimensionality reduction [8].

Partial Least Squares Discriminant Analysis (PLS-DA). Partial Least Squares Discriminant Analysis, commonly called PLS-DA, is a superVISed classification algorithm that leverages the principles of PLS regression and linear discriminant analysis to effectively categorize datasets into distinct classes. This powerful technique establishes a crucial connection between predictor variables and response variables by employing a reduced number of latent variables. The primary aim of PLS-DA is to maximize the covariance between predictor variables and response variables, thus unraveling the underlying relationships within the data.

In the realm of binary classification, the PLS1 variant is frequently utilized. Here, the response variable typically assumes values of 0 or 1, signifying whether a data point belongs to a specific class or not.

iPLS-DA Classification. Interval PLS (iPLS) is a data modeling technique designed to enhance prediction accuracy by selecting a subset of variables from a dataset and optimizing performance using all available variables. iPLS employs a sequential and exhaustive search approach to identify the best individual or combination of variables for the task. In the context of iPLS, an "interval" can refer to either a single variable or a "window" encompassing adjacent variables. This concept of an "interval" is particularly relevant in situations where adjacent variables are interrelated, such as in spectroscopically correlated or time-correlated datasets, where variables in proximity exhibit related behaviors. For the discussion, an "interval" will be selected while recognizing that it may encompass one or more variables. The iPLS process initiates by creating individual Partial Least Squares (PLS) models, each utilizing only one of the predefined variable intervals. For instance, if a dataset has 100 defined intervals, the initial step involves calculating 100 models, each corresponding to a distinct interval. Cross-validation is conducted for each of

these models, and the interval yielding the lowest model root-mean-square error of cross-validation (RMSECV) is chosen as the optimal single-interval model, denoted as I1. If the objective is to select just one interval, the algorithm can conclude at this point, providing the selected interval as the outcome. However, if the aim is to incorporate multiple intervals, thereby enriching the information available to the model and potentially improving its performance, additional cycles are executed. In the subsequent cycle, the first selected interval (I1) is retained in all models and combined sequentially with each of the other remaining intervals. This process generates a new set of PLS models for each combination. Once again, using RMSECV as the guiding metric, the best combination of two intervals (I1 and an additional interval, denoted as I2) is determined. It's important to note that, at this stage, the first selected interval (I1) remains fixed. This procedure is iteratively repeated for as many intervals as needed (up to In), enhancing the model's capacity to harness information and optimize predictive performance [9].

As for the full range model, our approach started by dividing our sample dataset into two subsets, after removing one sample as outlier: a training set comprising 225 samples, meticulously selected using the Kennard & Stone algorithm [10], and a prediction set consisting of 74 samples This partitioning facilitated our models' development and subsequent evaluation, a critical step in assessing their applicability to external samples. In line with the previous methodology, we pursued developing and evaluating various chemometric models, mirroring the procedures employed in the full-range model. These models were fine-tuned to optimize performance.

Spectral Data Treatment and Model Construction

To harness the full potential of our spectral data, a comprehensive journey of data treatment and model development was performed. This encompassed the utilization of Solo, version 9.2.1, developed by Eigenvector Research, Inc. in Wenatchee, WA, USA.

Various spectral ranges and data preprocessing techniques underwent a thorough evaluation to ascertain the creation of robust prediction models.

Classification models were meticulously crafted using a split of 2/3 of the samples for calibration and 1/3 for validation, ensuring a representative dataset that included samples from all batches. Sample selection was executed with precision, employing the Kennard & Stone algorithm [9].

The exploration delved into multiple data preprocessing techniques, including Standard Normal Variate (SNV), Mean Center (MC), first and second derivatives of Savitzky–Golay, employing various window sizes and polynomial orders, Multiplicative Scattering Correction (MSC), Orthogonal Signal Correction (OSC), and combinations thereof.

In the final stages, classification models were meticulously constructed through Partial Least Squares Discriminant Analysis (PLS-DA). PLS-DA, a linear classification method rooted in the PLS regression algorithm [11], was employed for its proven effectiveness.

Performance evaluation was a paramount aspect of our methodology. This was achieved through the analysis of contingency tables and the calculation of sensitivity, specificity, and precision. Sensitivity, as defined in Equation (1), measured the model's proficiency in correctly classifying positive samples as positive:

$$\text{Sensitivity} = TP / (TP + FN) \qquad (1)$$

where: TP = number of positive samples correctly classified as positive; FN = number of positive samples erroneously classified as negative.

Specificity, captured by Equation (2), assessed the model's ability to accurately classify negative samples as negative:

$$\text{Specificity} = TN / (TN + FP) \qquad (2)$$

where: TN = number of negative samples correctly classified as negative; FP = number of negative samples erroneously classified as positive.

Precision, as per Equation (3), quantified the proportion of all samples classified as one class that genuinely belonged to that class:

$$\text{Precision} = TP / (TP + FP) \qquad (3)$$

The constructed PLS-DA models underwent rigorous internal validation through the venetian blinds cross-validation method. Key model parameters, including the R^2 model, root mean squared error of calibration (RMSEC) (as defined in Equation 4), and root mean squared error of cross-validation (RMSECV) (as defined in Equation 5), were scrutinized for the selection of the optimal model.

Further evaluation of the model's predictive capacity was executed using distinct statistical parameters, such as the root mean squared error of prediction (RMSEP), applied to the validation set samples (as defined in Equation 6). This thorough process ensured the robustness and accuracy of our predictive and classification models.

$$RMSEC = \sqrt{\frac{\Sigma_{i=1}^{n})y_i-\hat{y}_i(^2}{n}} \qquad (4)$$

$$RMSECV = \sqrt{\frac{\Sigma_{i=1}^{n}(y_i-\hat{y}_i)^2}{n}} \qquad (5)$$

$$RMSEP = \sqrt{\frac{\Sigma_{i=1}^{n}(y_i-\hat{y}_i)^2}{n}} \qquad (6)$$

In the context of our analysis, where 'yi' represents the reference value for validation set sample 'i', 'ŷi' signifies the predicted value for the same validation set sample 'i', and 'n' stands for the total number of samples within the validation set, a critical step was taken to optimize our model.

A plot illustrating the explained variance against the number of factors was generated to select the optimal number of factors. This VISual representation played a pivotal role in guiding our selection process.

Subsequently, an initial model was honed by choosing the factors that yielded the lowest Root Mean Squared Error of Prediction (RMSEP) for the validation set. Furthermore, our selection criteria incorporated a preference for factors that exhibited sensitivity and specificity coefficients that closely approached a value of 1. This comprehensive approach ensured the refinement of the final model to enhance its predictive accuracy and reliability.

RESULTS AND DISCUSSION

Vis-NIR spectra

As mentioned in the introduction and materials and methods section, Vis-NIR spectra from Li *et al.* [6] have been used for the purpose of classifying three different types of apples: the Fuji apple, the Red Star apple, and the Gala apple.

Figure 1 shows the mean apple spectra from the 3 apple classes. As it can be observed, Fuji and Red Star present similar spectra while Golden Gala, has

a slight difference due to its different color. So that by observing the spectra the principal challenge from this study would be the differentiation of Red Star and Golden Gala varieties.

Classification models. With this data, non-supervised PCA models and supervised PLS-DA models are performed, as shown in the following sections.

PLS-DA classification using the full spectral range. Our dataset was thoughtfully divided into two distinct subsets: a training set consisting of 225 (2/3) samples for the development of our predictive models and a prediction set comprising 74 (1/3) samples. This segregation was achieved utilizing the Kennard & Stone algorithm. Various chemometric models were meticulously formulated and evaluated to enhance the model's efficacy and applicability. These models were tailored using carefully selected data treatment techniques.

The array of data treatments encompassed fundamental methods such as mean centering (MC), auto-scaling, and advanced techniques, including Savitzky-Golay first (FD) and second derivative (SD), multiplicative scattering correction (MSC), standard normal variation (SNV), orthogonal signal correction (OSC), and inventive combinations thereof.

Our approach commenced with an unsupervised classification analysis, primarily employing Principal Component Analysis (PCA) to take a general overview of the samples by using the Near-Infrared (NIR) spectra. The first two principal components in the PCA model encapsulated an impressive 92.30% of the total variation. However, it was evident from Figure 2 that the unsuperVISed model revealed a predominant cluster, indicating a lack of distinct clusters for the three apple categories when the full 400 to 1021nm spectral range was used.
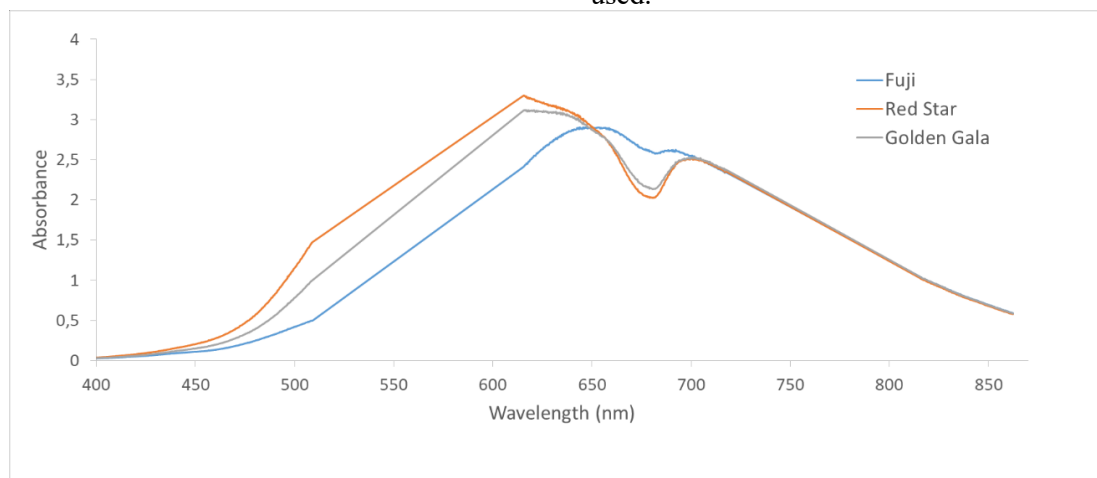
Figure 1. Mean Visible-NIR spectra from Fuji apple, Red Star apple, and Golden Gala apple.
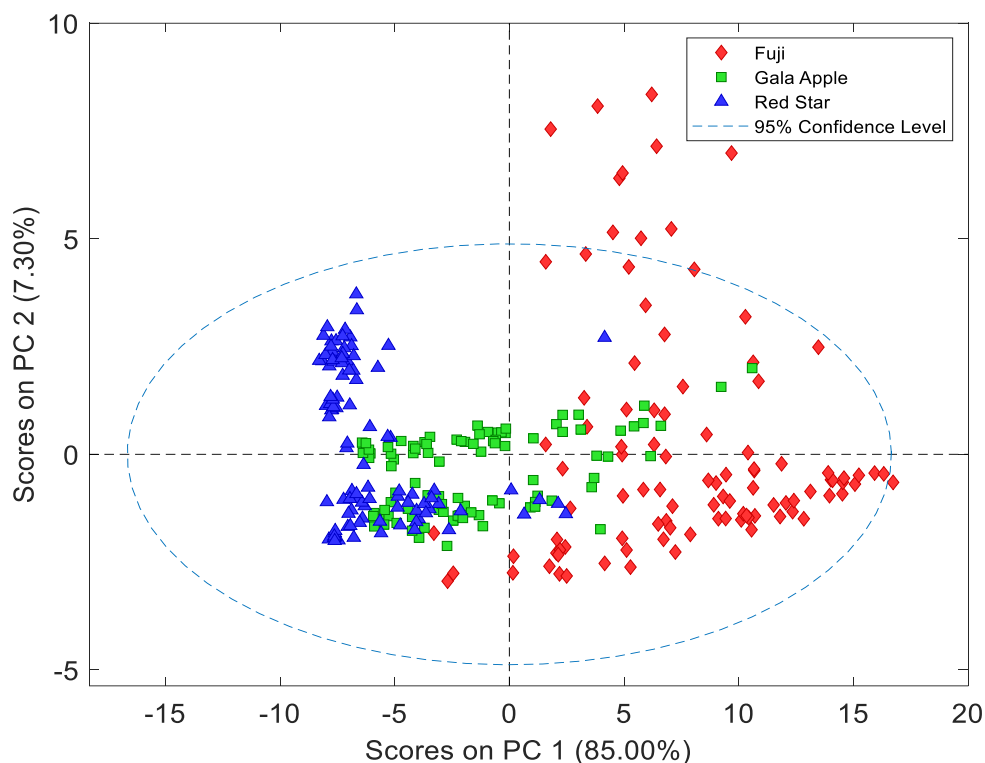
Figure 2. PCA score plot PC1 *vs*. PC2 of all apple SNV pretreated full VIS-NIR spectra data.

Table 1. Key model parameter from the SNV full range PLS-DA.

	Calibration			Cross Validation			Prediction		
	Fuji	Gala	Red Star	Fuji	Gala	Red Star	Fuji	Gala	Red Star
RMSE	0.194	0.264	0.263	0.198	0.272	0.268	0.288	0.339	0.306
R^2	0.814	0.704	0.693	0.806	0.685	0.680	0.687	0.442	0.582

Table 2. Confusion Table obtained from the SNV full range PLS-DA.

	Cross Validation			Prediction		
	Actual class			Actual class		
	Fuji	Gala	Red Star	Fuji	Gala	Red Star
Predicted as Fuji	62	4	0	37	1	0
Predicted as Gala	1	81	1	0	13	2
Predicted as Red Star	0	0	76	0	1	21
Sensitivity	1.000	0.988	0.909	0.973	1.000	0.957
Specificty	0.981	0.993	0.973	0.946	0.900	0.961

A Partial Least Squares Discriminant Analysis (PLS-DA) supervised classification model was performed to refine the classification. By utilizing predictive components, PLS-DA significantly improved class separation. The selection of the most suitable number of latent variables was determined based on the lowest value of the Root Mean Square Error of Cross-Validation (RMSECV). In our case, 6 latent variables were chosen to construct the classification model.

The performance evaluation of our classification model encompassed both internal validation (cross-validation) and external validation using the prediction set. Our model exhibited commendable R2 values for calibration, cross-validation, and prediction, as showcased in Table 1.

Furthermore, the Root Mean Square Error of Calibration (RMSEC), Root Mean Square Error of Cross-Validation (RMSECV), and Root Mean Square Error of Prediction (RMSEP) for all three apple classes demonstrated excellent agreement. This alignment indicated that the RMSECV value effectively approximated the standard error of prediction observed for the test set.

Table 2 shows the confusion table for the 3 categories with very good results. Only 2 samples for Gala apples and 2 for Redstar are misclassified in the validation set, while in the cross-validation, only 1 sample for Fuji apples, 4 for Gala apples, and 1 for Redstar are misclassified.

The ROC curves provided a comprehensive view of the models' performance. Sensitivity and specificity (Table 2) were integral components of our evaluation criteria. Sensitivity, indicative of the rate of correctly identified samples within a specified class, was plotted against 1-specificity, representing the rate of correctly identified samples within different classes.

The Area Under the Curve (AUC) of the ROC plots was instrumental in assessing method performance. The AUC value, which ranges from 0.5 (indicative of random decision) to 1 (representing a perfect model), offered insights into the model's accuracy. Remarkably, the AUC values for the full range PLS-DA model ranged from 0.975 for Gala apples to an impressive 0.996 for Fuji apples. According to the suggestion of Swets, models could be classified as non-informative (AUC=0.5), less accurate (0.5<AUC≤0.7), moderately accurate (0.7<AUC≤0.9), highly accurate (0.9<AUC<1) and perfect tests (AUC=1).

In addition to the confusion table, sensitivity and specificity values for the validation set and the cross-validation are close to 1. Table 3, with the Total positive results (TPR), false positive results (FPR), total negative results (TNR), false negative results (FNR), and % classification error (Err), shows for both prediction and cross-validation values close to 1 for TPR and TNR and 0 for FPR and FNR. Receiver-operating characteristic (ROC) curves were created for the data sets following the external prediction set to determine the performance of the chosen models, which can be seen in Figure 3.

Table 3. Total positive results (TPR), false positive results (FPR), total negative results (TNR), false negative results (FNR), and % classification error (Err) obtained from the cross-validation and prediction sets from the SNV full range PLS-DA

		N	TPR	FPR	TNR	FNR	Error
Cross Validation	Fuji	63	0.968	0.049	0.951	0.032	0.058
	Gala	85	0.894	0.029	0.971	0.106	0.058
	Red Star	77	0.974	0.007	0.993	0.026	0.013
Prediction	Fuji	37	1.000	0.027	0.973	0.000	0.014
	Gala	14	0.929	0.033	0.967	0.071	0.041
	Red Star	23	0.913	0.000	1.000	0.087	0.027
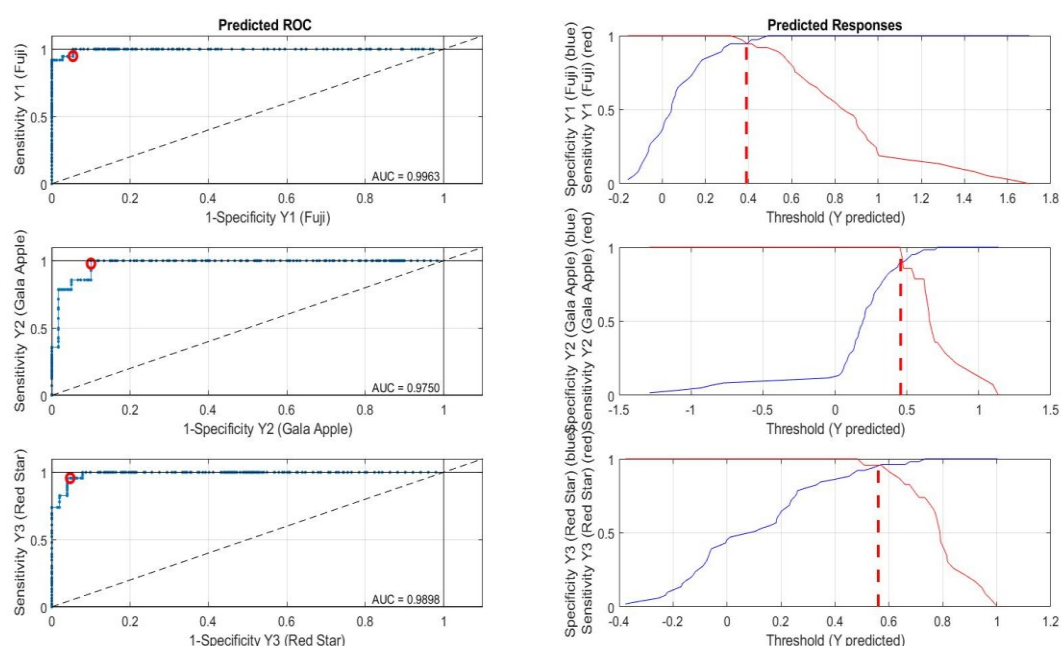
**Figure 3.** ROC curves obtained for full range SNV PLS-DA model
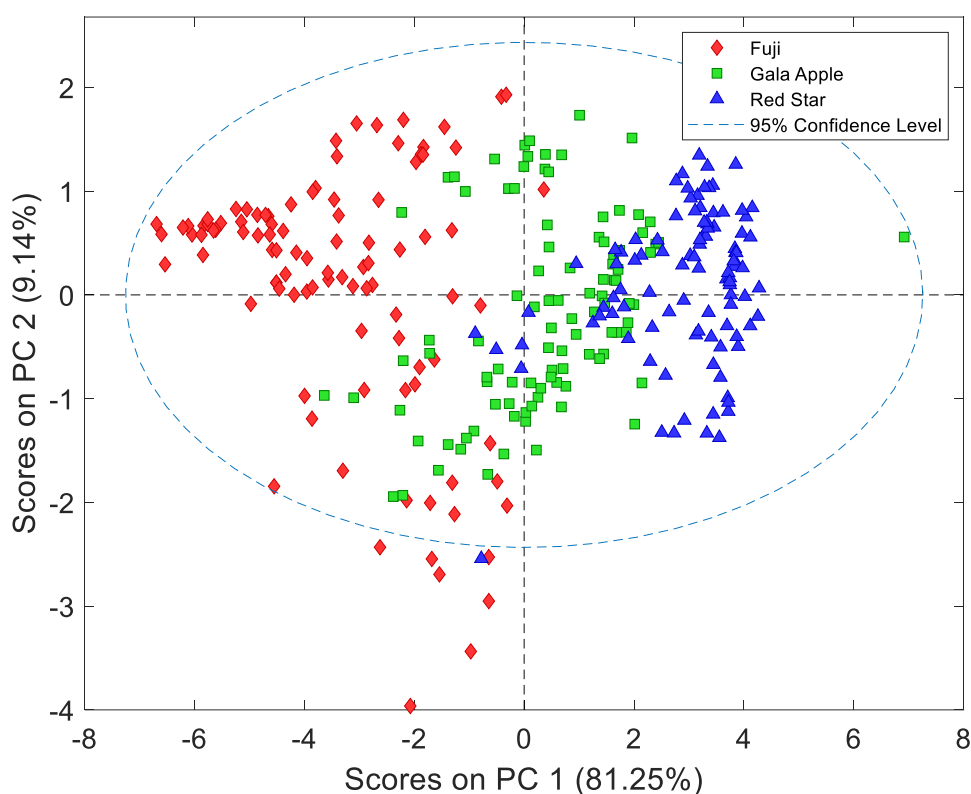
Figure 4. PCA score plot PC1 vs. PC2 of all apple SNV pretreated selected ranges of VIS-NIR spectra.

Table 4. Key model parameter from the SNV full range PLS-DA.

	Calibration			Cross Validation			Prediction		
	Fuji	Gala	Red Star	Fuji	Gala	Red Star	Fuji	Gala	Red Star
RMSE	0.166	0.275	0.183	0.195	0.323	0.202	0.267	0.412	0.269
R^2	0.864	0.679	0.851	0.812	0.556	0.818	0.730	0.276	0.663

In accordance with Swets' classification, the models were unequivocally classified as highly accurate.

iPLS-DA classification using the selected spectral range. After application of PCA method, the first two principal components (PC1 and PC2) accounted for an impressive 90.39% of the total variation. While the score plot in Figure 4 indicated the presence of a predominant cluster, a closer examination revealed that the three apple categories were distinguishable within this cluster. This observation underscored that, although PCA did not delineate specific clusters for the three apple categories, it exhibited the ability to differentiate them more effectively when the iPLS-DA 400.093-508.864, 615.223-716.993, and 815.113-861.991 nm spectral ranges were only chosen.

The implementation of the PLS-DA superVISed classification model notably enhanced the separation of distinct classes. Following a meticulous

evaluation process, which considered the lowest Root Mean Square Error of Cross-Validation (RMSECV), three latent variables as the optimal number for constructing the classification model. This selection of latent variables laid the foundation for a robust classification model, and its performance was rigorously scrutinized through both internal validation (cross-validation) and external validation using the prediction set.

The results of this assessment were indicative of the model's excellence, as reflected in Table 4. Therefore, the SNV full range PLS-DA model consistently demonstrated good performance across multiple metrics, including R2 for calibration, cross-validation, and prediction. Moreover, the Root Mean Square Error of Calibration (RMSEC), Root Mean Square Error of Cross-Validation (RMSECV), and Root Mean Square Error of Prediction (RMSEP) for all three apple classes exhibited strong agreement. Table 5 presents the confusion table for the three

apple categories, yielding excellent results with no misclassifications in the validation set. In cross-validation, only 5 misclassifications were observed for the Red Star category. Supplementing the confusion table, sensitivity and specificity values for both the validation set and cross-validation were found to be closely approaching a value of 1.

Table 6 shows the model's proficiency, with values of 1 for True Positive Rate (TPR) and True Negative Rate (TNR) in the prediction set, alongside 0 values for False Positive Rate (FPR) and False Negative Rate (FNR). Cross-validation results mirror this performance, with TPR and TNR values nearing 1 and FPR and FNR registering close to 0.

To further evaluate the efficacy of our chosen models, Receiver-Operating Characteristic (ROC)

curves have been created, a key step for external prediction using the prediction set. Figure 4 graphically represents the ROC curves, providing an insightful assessment of model performance. The Area Under the Curve (AUC) for the iPLS-DA range model ranged from 0.9569 for Red Star apples to 1 for Gala apples. In accordance with Swets' classification, our model for Gala apples would be classified as excellent, while the models for the other two apple varieties would be deemed highly accurate. This extensive evaluation reaffirmed the excellence and reliability of our classification model in classifying apple varieties. The classification performance of the model was also evaluated through sensitivity and specificity, as presented in Table 5.

Table 5. Confusion Table obtained from the SNV full range PLS-DA.

	Cross Validation			Prediction		
	Actual class			Actual class		
	Fuji	Gala	Red Star	Fuji	Gala	Red Star
Predicted as Fuji	63	0	3	37	0	0
Predicted as Gala	0	85	2	0	14	0
Predicted as Red Star	0	0	72	0	0	23
Sensitivity	0.984	0.882	0.987	1.000	1.000	1.000
Specificty	0.957	0.871	1.000	0.973	1.000	0.863

Table 6. Total positive results (TPR), false positive results (FPR), total negative results (TNR), false negative results (FNR), and % classification error (Err) obtained from the cross-validation and prediction sets from the SNV full range PLS-DA.

		N	TPR	FPR	TNR	FNR	Error
Cross Validation	Fuji	63	1.000	0.019	0.981	0.000	0.013
	Gala	85	1.000	0.014	0.986	0.000	0.009
	Red Star	77	0.935	0.000	1.000	0.065	0.022
Prediction	Fuji	37	1.000	0.000	1.000	0.000	0.000
	Gala	14	1.000	0.000	1.000	0.000	0.000
	Red Star	23	1.000	0.000	1.000	0.000	0.000
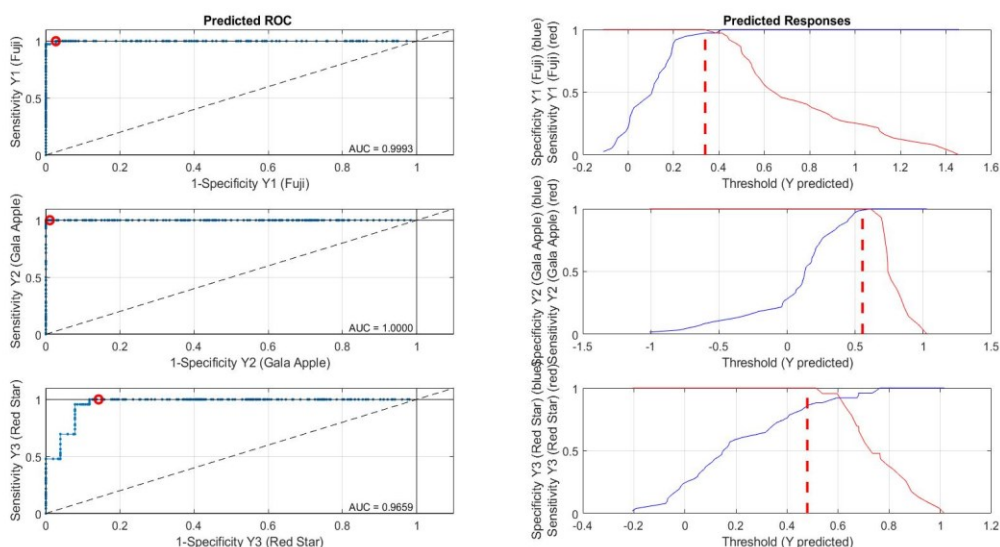
Figure 5. ROC curves obtained for iPLS-DA SNV model

Comparing the obtained results with the ones of Li *et al.* [6], we can affirm that with less complex models, PLS-DA and iPLS-DA, similar or even better accuracies are obtained than the ones obtained by SVM models and ELM models in Li *et al.* manuscript. So, models with less computation complexity can give us similar results in classifying apples among their variety.

In addition, these more complex models are more potent in classifying the apples regarding their origin. The next step in our study will be the research of the optimal conditions for obtaining comparable classification accuracies to those obtained by SVM and ELM, classifying apples regarding their origin with a more straightforward classification method.

CONCLUSIONS

In conclusion, this study highlights the efficacy of employing chemometrics in tandem with VIS-NIR direct analysis to effectively differentiate between various apple varieties, as exemplified by the successful application of PLS-DA particularly. The encouraging outcomes of the green methodology notably add another advantage to this approach.

Nevertheless, a pivotal juncture in our journey toward enhancing the classification model was the judicious selection of the most pertinent spectral range. In this crucial endeavor, the introduction of iPLS-DA emerged as a game-changer, leading to significant advancements in classifying the three distinct apple categories. This improvement was not solely confined to eliminating prediction errors within the prediction dataset; it also entailed reducing the number of latent variables within the model.

It becomes evident that the choice of an optimal spectral range not only simplifies the final model in terms of latent variables but also plays a pivotal role in elevating the predictive prowess of the model. This observation highlights the pivotal importance of spectral range optimization in refining classification models and further reaffirms its central role in improving the accuracy and efficacy of such models. Subsequently, this research demonstrates the power of precision and optimization in the field of apple spectral analysis and classification.

As mentioned in the Results section, the results obtained with PLS-DA and iPLS-DA have similar or evern better accuracies than those obtained by more complex algorithms in [6].

REFERENCES

1. J. Grabska, K. B. Beć, N. Ueno, C.W. Huck, *Foods*, **12**(10), 1946 (2023).
2. A. Pissard, V. Baeten, P. Dardenne, P. Dupont, M. Lateur, Use of NIR spectroscopy on fresh apples to determine the phenolic compounds and dry matter content in peel and flesh. BASE, 2018.
3. R. Beghi, A. Spinardi, L. Bodria, I. Mignani, R. Guidetti, *Food and Bioprocess Technology*, **6**, 2547 (2013).
4. A. Pissard, E. J. N. Marques, P. Dardenne, M. Lateur, C. Pasquini, M. F. Pimentel, J. A. F. Pierna, V. Baeten, *Postharvest Biology and Technology*, **172**, 111375 (2021).
5. Q. Xu, X. Wu, B. Wu, H. Zhou, *J. Food Process. Eng.*, **45**, e13993 (2022).
6. C. Li, L. Li, Y. Wu, M. Lu, Y. Yang, L. Li, *J. Spectrosc.*, 6935197 (2018).
7. V. Cortés, S. Cubero, J. Blasco, N. Aleixos, P. Talens, *Food Bioprocess. Technol.*, **12**, 1021 (2019).
8. N. Salem, S. Hussein, *Procedia Computer Science*, **163**, 292 (2019).
9. R. W. Kennard, L. A. Stone, *Technometrics*, **11**(1), 137 (1969).
10. L. Nørgaard, A. Saudland, J. Wagner, J. P. Nielsen, L. Munck, S. B. Engelsen, *Applied Spectroscopy*, **54**(3), 413 (2000).
11. S. Wold, M. Sjöström, L. Eriksson, *Chemometrics and Intelligent Laboratory Systems*, **58**(2), 109 (2001).

Electrochemical response of gallic acid on activated glassy carbon electrode

D. T. Hadzhiev, T. M. Dodevska*, I. G. Shterev

*Department of Organic Chemistry and Inorganic Chemistry,
University of Food Technologies, 26, Maritsa Blvd., Plovdiv 4002, Bulgaria*

A simple and sensitive electrochemical method for the quantitative determination of gallic acid (GA) using an electrochemically activated glassy carbon electrode (EAGCE) is reported. The electrochemical pre-treatment of the electrode was carried in 0.1M H_2SO_4 by cycling between 0.0 and 1.5 V (*vs.* Ag/AgCl, 3M KCl) for 10 cycles using cyclic voltammetry technique. The electrochemical properties of the suggested electrode and the voltammetric behavior of GA were investigated by cyclic voltammetry (CV) and differential pulse voltammetry (DPV). The prepared electrode EAGCE exhibited good sensitivity, selectivity and reliability in the electroanalysis of GA. Interference studies indicate that common ions (Na^+, NH_4^+, Mg^{2+}, Cu^{2+}, Cl^-, NO_3^-, CO_3^{2-}, and PO_4^{3-}), as well as some organic acids (ascorbic, oxalic, citric, salicylic, and tartaric acid) do not interfere with the GA assay. The proposed metal-free catalyst has cost-effective and good performance to GA determination.

Keywords: gallic acid; sensor; electrochemical sensor; electrochemical analysis; electrochemical activation, electrocatalysis

INTRODUCTION

Recently, gallic acid (3,4,5-trihydroxybenzoic acid, GA) has received considerable attention because of its multiple applications. GA is a strong natural antioxidant present in a wide variety of fruits, vegetables, green tea, black tea and several other plants. A number of studies confirmed that GA possesses various biological functions such as scavenging of free radicals, anti-inflammatory and antitumor activity, protection against cardiovascular diseases, which lead to its popularity and rapid adoption in medical and pharmaceutical industries [1-5]. Additionally, GA is generally accepted as a reference standard when determining the total polyphenolic content in plants, and the resultant GA equivalents are used to indicate the antioxidant level of the plant extracts. Thus, GA content in many natural products and beverages is considered as a benchmark for their quality.

Owing to the bioactive and pharmacological importance of GA, the development of new reliable, sensitive, easy to use, and time-saving analytical methods for GA determination is of great interest [6]. The presence of three hydroxyl groups (-OH) and one carboxylic group (-COOH) in GA molecule make it highly electroactive, thus electroanalytical methods are appropriate for its assessment [7]. Several research papers report on the application of electrochemical methods for the quantification of GA using, in particular, carbon-based electrodes modified with different electrocatalytic materials: metal nanoparticles [8], metal oxide nanoparticles [9, 10], carbon nanotubes [11, 12], graphene [13, 14], graphene oxide [15, 16], metal-organic frameworks [17, 18], conductive polymers [19].

Herein, we report a cost-effective, simple and sensitive electrochemical method for the quantitative detection of GA using an electrochemically activated glassy carbon electrode (EAGCE). The electrochemical activation process may generate various oxygen-containing functional groups (hydroxyl, carbonyl, carboxyl, quinone, etc.) on the surface of the glassy carbon. These functional groups could act as electron acceptors in the target reaction of oxidation of GA that can improve the sensitivity and selectivity of the sensing platform. In fact, the sensing platform is non-expensive, no hazardous or highly pure solvents are required, and no modifications are necessary. The electro-activation method used in this work only requires the application of a potential on the bare GCE immersed in the supporting electrolyte before measurements. The electrochemical activation of the GCE is fast, easy and reproducible, and the measurement of GA by DPV shows considerable sensitivity and reliability.

EXPERIMENTAL

Materials and Apparatus

H_2SO_4, $NaNO_3$, NaCl (Merck); NH_4Cl, $MgCl_2$, $CuSO_4.5H_2O$, Na_2CO_3, Na_3PO_4, $Na_2HPO_4.12H_2O$,

---

* To whom all correspondence should be sent:
E-mail: *dodevska@mail.bg*

NaH$_2$PO$_4$.2H$_2$O, (Fluka). Gallic acid, ascorbic acid, oxalic acid, citric acid, salicylic acid, and tartaric acid were purchased from Sigma-Aldrich. All the chemicals were of analytical grade and used without any further purification. Double distilled water was used to prepare aqueous solutions. Phosphate buffer solutions (pH = 1.0, 3.0, and 7.0) were ready by mixing of 0.1M NaH$_2$PO$_4$ and 0.1M Na$_2$HPO$_4$ and adjusting the solution pH to the required value with H$_3$PO$_4$ and/or NaOH.

EmStat2 potentiostat (PalmSens BV, The Netherlands) controlled by a PC running PSTrace software version 5.5. The electrochemical cell was composed of a common three-electrode system: GCE with a surface diameter of 3 mm (Metrohm Autolab BV, The Netherlands) as a working electrode, platinum wire as a counter-electrode, and Ag/AgCl (3M KCl) as a reference electrode. All potentials in this study were reported *vs.* this reference electrode.

Procedures

The surface of the GCE was mechanically cleaned *via* polishing using 0.05 μm alumina slurry on a microcloth, sonicated in double distilled water for 5 min, followed by thorough rinsing with ethanol and double distilled water. The cleaned GCE was immersed in 0.1 M H$_2$SO$_4$ and conditioned by cyclic voltammetry. The activation process was carried out by sweeping the GCE in the potential range between 0.0 V and +1.5 V (*vs.* Ag/AgCl, 3M KCl) for 10 cycles at a scan rate of 100 mV s^{-1}. The electrochemically activated electrode (EAGCE) was then directly used for the measurements.

The measurements were carried out at ambient temperature (25 ± 3 °C). The experimental data analysis was performed using software package 'OriginPro 2015'. For the calibration curve, each point was obtained by the average peak intensity of three consecutive DPV measurements. The linearity was evaluated using the least-square regression method.

RESULTS AND DISCUSSION

Electrooxidation of GA on bare GCE

The electrochemical behavior of GA on bare GCE was initially investigated in 0.1M H$_2$SO$_4$ using cyclic voltammetry at a scan rate of 100 mV s^{-1}. As shown in Fig. 1, in the presence of GA (500 μM) one oxidation peak appears at about 0.63 V, but no reduction peak can be detected over the whole potential range. This finding suggests irreversibility of the GA oxidation process at the GCE surface.
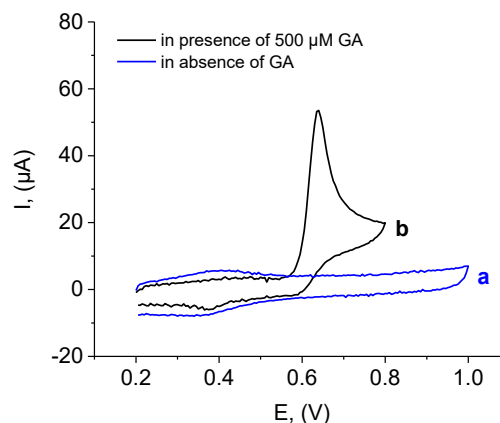
Figure 1. CVs of the bare GCE in the absence (curve a) and presence of 500 μM GA (curve b). Supporting electrolyte 0.1M H$_2$SO$_4$; scan rate 100 mV s^{-1}.

The effect of pH value of the supporting electrolyte on the electrochemical response of GCE toward GA oxidation was investigated by DPV in phosphate buffer of different pHs (1.0, 3.0, and 7.0) in the presence of GA. The obtained results are presented in Fig. 2. The anodic peak potentials of GA are shifted toward the more negative direction with decreasing proton concentration. It can be observed that the relationship of peak potential Ep *vs.* pH is linear and described by equation Ep (V) = −0.05214 pH + 0.5899. According to the Nernst equation, the slope of 0.0521 V pH^{-1} is close to the expected theoretical value of 0.0591 V pH^{-1} which indicates the transfer of an equal number of electrons and protons in the electrooxidation process. The oxidation mechanism of GA in acidic solutions occurs *via* two electrons and two protons transfer. The results were in line with the findings of previous studies [9-12].
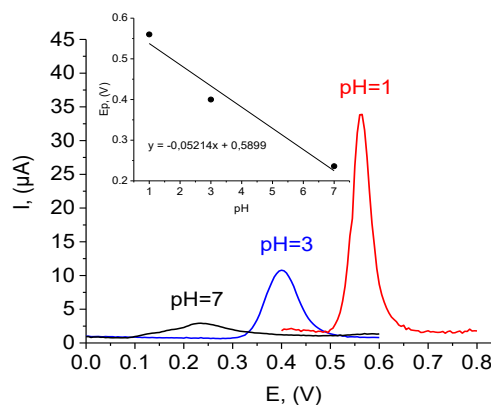
Figure 2. DPVs obtained at the bare GCE in the presence of 300 μM GA in supporting electrolyte phosphate buffer of various pHs. Inset: the relationship of the anodic peak potential for GA oxidation as a function of pH of the buffer solution.

Direct electrochemical oxidation of GA at the GCE is facile; at pH ≤ 4.24 GA undergoes a $-2e^-$, $-2H^+$ process to form quinone (Scheme 1). As can be seen from the results presented in Fig. 2, the oxidation peak of GA becomes lower with the increase of pH from 1.0 to 7.0. It was found that at pH 1.0 the well-shaped, the most symmetrical and intense peak of GA oxidation was obtained.
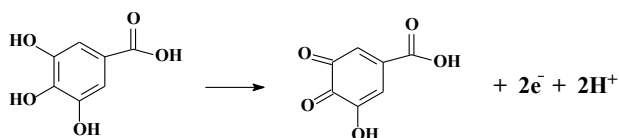
Scheme 1. Oxidation of GA.

Electrooxidation of GA on EAGCE

The electrochemical oxidation of GCE altered the surface chemistry of the electrode because of the increased number of different oxygen functionalities which affect hydrophilicity. This procedure activates the electrode surface, leading to faster electron transfer kinetics.

Immediately after the electrochemical activation, the electrode EAGCE was directly used for the measurements in the same electrolyte (0.1M H_2SO_4 solution). The experimental results clearly show that the electrochemical signals of GA were increased by the application of the electro-activation procedure. Fig. 3 presents CV curves of GCE and EAGCE in supporting electrolyte 0.1M H_2SO_4 in the presence of 300 µM GA under certain testing conditions (pH = 1.0; potential range from 0.2 to 0.8 V; scan rate of 100 mV s^{-1}). It can be clearly observed that the peak current at EAGCE (curve b) is twice as high as that at GCE (curve a). Owing to the specific oxygen-containing functional groups and the outstanding conductivity of EAGCE, the proposed sensing platform exhibits an enhanced oxidation peak current of GA when compared with non-activated GCE. This indicates that the electrochemical activation of GCE can facilitate the electron transfer at the electrode surface and enhance the adsorption of GA. Thus, the peak current enhancement at EAGCE is attributed to the increased adsorption active sites and effective surface area, as well as to the improvement of electron transfer ability and high electrocatalytic activity of the EAGCE.

Using EAGCE a series of DPVs for increasing concentrations of the analyte GA were recorded. The measurement signal was the current value read at 0.59 V, which corresponds to the potential of the GA peak maximum. The peak height was used for quantification, and each analytical signal was recorded in triplicate.
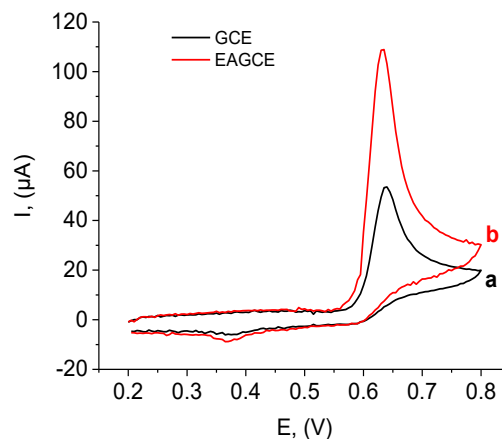
Figure 3. CVs of 500 µM GA in 0.1M H_2SO_4 on bare GCE (a) and EAGCE (b).

From the records presented in Fig. 4 it can be observed that the current linearly increases with the concentration of GA in two ranges. The first one is up to 0.5 mM GA with a linear regression equation I (µA) = 0.1154C (µM) + 4.3622 and a correlation coefficient of 0.988. The electrode shows electrochemical sensitivity of 1.6323 µA µM^{-1} cm^{-2} (normalized to the electrode geometric surface area). In the concentration range from 0.5 to 1.5 mM GA the linear regression equation is I (µA) = 0.03063C (µM) + 48.16; the sensitivity and the correlation coefficient are 0.4332 µA µM^{-1} cm^{-2} and 0.999, respectively. The limit of quantification (LOQ) was calculated to be 8 µM (S/N = 10).
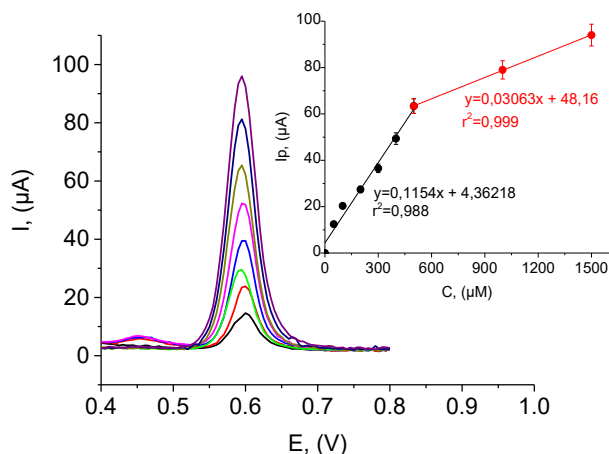
Figure 4. DPV response for various concentrations of GA at EAGCE. Inset: corresponding calibration plot (n=3). Supporting electrolyte: 0.1M H_2SO_4.

The selectivity of the EAGCE-based sensing platform was examined with common interfering organic substances and inorganic ions that may alter the registered DPV signals. The influence of each possible interfering compound was examined by the comparison between peak current of 500 µM GA

and peak current of GA in the presence of interfering ion/molecule. Results indicated that 6-fold amounts of ascorbic acid (AA), oxalic acid (OA), citric acid (CA), salicylic acid (SA), and tartaric acid (TA) and 30-fold amounts of $NaNO_3$, NaCl, NH_4Cl, $MgCl_2$, $CuSO_4$, Na_2CO_3, and Na_3PO_4 did not practically affect the detection of GA (signal change below 5%). Fig. 5 shows the effect of 6-fold addition of AA, OA, and CA on the DPV-response toward 500 µM GA. These findings suggest that the proposed electrode EAGCE has a good selectivity for GA and could be used as a reliable and cost-effective sensing platform for selective detection of GA in real samples.
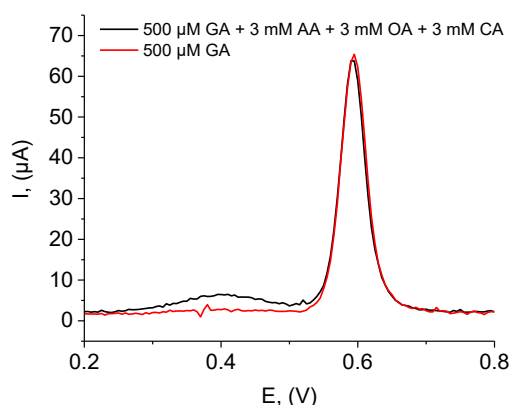
Figure 5. Effect of addition of 3 mM AA, OA, and CA on DPV response toward 500 µM GA. Supporting electrolyte: 0.1M H_2SO_4.

Usually, poor reproducibility of the current signal was encountered when carbon-based electrodes were applied in the determination of phenol derivatives by means of electrochemical oxidation, and the same electrode could not be used for the next measurement. In regard to the electrochemical oxidation of GA, a number of researchers reported a severe surface fouling accompanied by the adsorption of oxidized products.

In this work potential cycling was employed as a regeneration and activation process, i.e. the electrode surface could be renewed by activation process and it was found to give reproducible results. Good reproducibility (RSD of 4.2%) was observed for 5 replicate DPV measurements in the presence of 100 µM GA. The low RSD value reveals the fact that EAGCE used in this work provides precise measurements for GA sensing. The sensitivity could be restored even after an intensive fouling of electrode surface using the electrochemical activation procedure to generate new active sites for use in subsequent experiments.

Here we outline future research directions in the upcoming study. Our future work will be oriented toward optimization of the various parameters such as electrolyte concentration, number of cycles, and oxidation potential window to achieve the best performance against GA. The second direction of the research will be to demonstrate the application of the proposed platform for direct electrochemical sensing of GA in a real sample (green tea extract).

CONCLUSION

Electrochemical oxidation is a simple, controllable and reproducible method for processing a GCE. In the present work, an electrochemically activated GCE was proven to be a useful sensing platform for GA quantitative detection. The electroanalytical properties were improved after the working electrode was activated which was ascribed to the attribution of surface oxygen containing functional groups and increased hydrophilicity. By incorporating electrochemical activation of GCE as a part of the analysis procedure, the effect of fouling of electrode surface was sufficiently minimized to achieve reliable measurements. The benefits of using the EAGCE presented here instead of the more complex modified ones are based on the absence of obstructions related to long-term stability. As the working electrode can be regenerated by a fast, simple electrochemical procedure *in situ*, this method of reactivating the electrode surface will keep the catalyst active in long-term experiments and repeated measurements. Furthermore, the use of EAGCE avoids the use of costly and time-consuming surface functionalization procedures.

REFERENCES

1. B. Badhani, N. Sharma, R. Kakkar, *RSC Adv.*, **5**, 27540 (2015).
2. N. Nayeem, S. M. B. Asdaq, H. Salem, S. Ahei-Alfqy, *J. App. Pharm.*, **8**, 213 (2016).
3. J. Bai, Y. Zhang, C. Tang, Y. Hou, X. Ai, X. Chen, Y. Zhang, X. Wang, X. Meng, *Biomed. Pharmacother.*, **133**, 110985 (2021).
4. N. Jabbari, M. Feghhi, O. Esnaashari, H. Soraya, J. Rezaie, *BioImpacts*, **12(6)**, 549 (2022).
5. M. S. Bhuia, M. M. Rahaman, T. Islam, M. H. Bappi, M. I. Sikder, K. N. Hossain, F. Akter, A. A. S. Prottay, M. Rokonuzzman, E. S. Gürer, D. Calina, M. T. Islam, J. Sharif-Rad, *Chin. Med.*, **18**, 27 (2023).
6. F. H. Fernandes, H. R. Salgado, *Crit. Rev. Anal. Chem.*, **46**, 257 (2016).
7. M. Badea, F. Di Modugno, L. Floroian, D. M. Tit, P. Restani, S. Bungau, L. Aleya, *Sci. Total Environ.*, **672**, 129 (2019).
8. S. A. Shahamirifard, M. Ghaedi, Z. Razmi, S. Hajati, *Biosens. Bioelectron.*, **114**, 30 (2018).
9. F. Gao, D. Zheng, H. Tanaka, F. Zhan, X. Yuan, F. Gao, Q. Wang, *Mater. Sci. Eng. C*, **57**, 279 (2015).
10. J. Tashkhourian, S. F. Nami-Ana, *Mater. Sci. Eng. C*, **52**, 103 (2015).

11. H. Zhao, Q. Ran, Y. Li, B. Li, B. Liu, H. Ma, S. Komarneni, *J. Mater. Res. Technol*., **9(4)**, 9422 (2020).

12. H. Zhao, Y. Liu, F. Li, G. Zhu, M. Guo, J. Han, M. Zhao, Z. Wang, F. Nie, Q. Ran, *Ceram. Int.*, **49(16)**, 26289 (2023).

13. M. Chen, H. Lv, X. Li, Z. Tian, X. Ma, *Int. Electrochem. Sci*., **14**, 4852 (2019).

14. Z. Liang, H. Zhai, Z. Chen, H. Wang, S. Wang, Q. Zhou, X. Huang, *Sens. Actuat. B: Chemical*, **224**, 915 (2016).

15. J. Węgiel, B. Burnat, S. Skrzypek, *Diam. Relat. Mater*., **88**, 137 (2018).

16. R. Abdel-Hamid, A. Bakr, E. F. Newair, F. Garcia, *Beverages*, **5(1)**, 11 (2019).

17. J. Chen, Y. Chen, S. Li, J. Yang, J. Dong, *Colloid. Surface.,* **650**, 129318 (2022).

18. J. Li, Y. Yang, Y. Li, P. Zhao, J. Fei, Y. Xie, *Food Chem.*, **429**, 136900 (2023).

19. V. Krishnan, E. Gunasekaran, C. Prabhakaran, P. Kanagavalli, V. Ananth, M. Veerapandian, *Mater. Chem. Phys.*, **295**, 127071 (2023).

Synthesis and luminescence characteristics of yttrium, aluminum and lanthanum borates doped with europium ions (Eu^{3+})

K. Hristova[1]*, I. Kostova[1], T. Eftimov[2, 3], D. Tonchev[1]

[1]University of Plovdiv "Paisii Hilendarski", Department of Chemical Technology, 24 Tsar Asen Str., Plovdiv, Bulgaria
[2]Centre de Recherche en Photonique, Université du Québec en Outaouais, 101 rue Saint-Jean-Bosco, Gatineau, Québec, J8X 3X7, Canada
[3]Central Laboratory for Applied Physics, Bulgarian Academy of Sciences, 61 Saint Petersburg Blvd, Plovdiv, Bulgaria

Inorganic materials doped with rare earth (RE) ions are an object of intense research due to their optical and electrical properties. These materials have the potential for various applications, such as solid-state lasers, active planar waveguides, optical fiber amplifiers, light-emitting diodes (LEDs), displays, ink fillers, security features, etc. RE trivalent ions can emit light from the ultraviolet (UV) to the near-infrared (NIR) regions due to electronic transitions of the *4f-5d* levels.

Yttrium borate doped with europium ions was prepared by solid-state synthesis in a muffle furnace at 900°C for 4 hours, while lanthanum and aluminum borates doped with europium ions were prepared at 1000°C for 6 hours again in a muffle furnace. The resulting materials are fine white powders. Among the rare earth ions, europium is one of the most commonly used activators because the ions of Eu^{3+} and Eu^{2+} can be used as emission sites in the host lattices. Eu^{3+} ions can produce effective sharp emission peaks in different matrix compositions. Photoluminescence analysis of the samples was performed, based on which the luminescence intensity of the Eu^{3+} ion was determined through a comparative characteristic. YBO$_3$:Eu^{3+} phosphor is optically active and chemically stable. It is characterized by a strong orange-red emission at $\approx$ 591 nm, $\approx$ 612 and $\approx$ 696 nm due to the $^{5}D_0\rightarrow^{7}F_1$ and $^{5}D_0\rightarrow^{7}F_2$ electronic transitions, respectively. Red emission is also observed for LaBO$_3$:Eu^{3+} at $\approx$ 592 and $\approx$ 615 nm, characterizing the $^{5}D_0\rightarrow^{7}F_1$ and $^{5}D_0\rightarrow^{7}F_j$ (j=0, 1, 2, 3, 4) transitions. While aluminum borate doped with europium ion shows intense emission at $\approx$ 612 nm, making this material suitable for lighting devices. The technique of Fourier transform infrared spectroscopy (FTIR) was used to study the structure of the obtained materials.

Keywords: Europium ion, solid-state reaction, fluorescence analysis, rare earth borates, aluminum borate, red emission.

INTRODUCTION

Rare earth elements are widely used as luminescent materials in various fields of practice. These materials are indispensable in the production of fluorescent lamps, scintillators, lasers, diodes, etc. [1, 2]. Of importance among them is europium, which in the +3 oxidation state is one of the most interesting and applicable elements. Upon irradiation with an ultraviolet source, the trivalent europium ion exhibits intense red fluorescence due to various electronic transitions [3]. This photoluminescence is observed not only for Eu^{3+} ions doped in crystalline inorganic matrices or glasses but also for europium (III) complexes with organic ligands. These ligands can act as a source to absorb the excitation light and to transfer the excitation energy to the higher energy levels of Eu^{3+} ion, where the emitting excited levels can be populated [4]. The lines of the emission spectra are usually sharp and depend on the crystal field around the metal ions [5]. In this work we synthesized different borates, which are optically apparent up to

140–180 nm, therefore, the UV light can openly excite impurity activator in such kind of host lattice. The energy transmission from a borate host crystal excited by UV light to the trivalent rare-earth activators leads to host-excited luminescence. The doping with europium ion in various matrices yields luminescent materials for biochemical or biomedical applications [6]. Europium ions have interesting optical characteristics such as well-defined spectral lines and red/orange emission, which have been used for technological applications in displays, lamps, etc. [7]. Most of the standard commercial red phosphors are based on Eu^{3+}-doped oxides. With an appropriate selection of the matrix, it is possible to use low concentrations of the activating ion and achieve high fluorescence intensity [8]. An interesting and very important application of europium as a main component is in the anti-counterfeiting ink of banknotes, as well as QR codes [9].

The aim of the present work is to study the influence of different inorganic matrices - yttrium, lanthanum and aluminum borates, on the activation

---

of europium 3+ (Eu^{3+}) ion after establishing optimal synthesis conditions in terms of temperature and duration [10, 11]. By means of photoluminescence analysis, a comparative characterization of the influence of these factors on the luminescence intensity of the Eu^{3+} ion was performed. The technique of Fourier transform infrared spectroscopy (FTIR) was used to study the structure of the obtained materials.
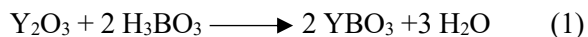
EXPERIMENTAL

Materials

For the synthesis of luminescent materials, the following reagents of analytical grade purity were used: Y_2O_3 (yttrium (III) oxide, 99.99 % (trace metal basis), CAS: 1314-36-9, Acros organics); H_3BO_3 (boric acid, 99%, Index # 005-007022-2); Eu_2O_3 (europium (III) oxide, 99.99% (trace metal basis), Acros, CAS: 1308-96-9), La_2O_3 (lanthanum (III) oxide, 99.9%), Al_2O_3 (aluminum oxide for chromatographic purposes 99%), purchased from Alfa Aesar.

Sample preparation

For the synthesis of materials, the necessary quantities of the starting substances were stoichiometrically calculated for 1 gram of sample, as shown in equations (1), (2), (3).

$$Y_2O_3 + 2\ H_3BO_3 \longrightarrow 2\ YBO_3 + 3\ H_2O \qquad (1)$$
$$La_2O_3 + 2\ H_3BO_3 \longrightarrow 2\ LaBO_3 + 3\ H_2O \qquad (2)$$
$$Al_2O_3 + 2\ H_3BO_3 \longrightarrow 2\ AlBO_3 + 3\ H_2O \qquad (3)$$

Description of sample composition is given in Table 1. The solid-state synthesis was carried out in a muffle furnace LM 312.07 with a G400 controller with a temperature range of 0-1200°C. Sample S29 SS was prepared by mixing stoichiometric amounts of Y_2O_3 and excess of H_3BO_3 45% as shown in equation (1) with 2 mol % Eu_2O_3 as doping agent at 900°C for 4 hours at a heating rate of 15°C/min. For samples S60 SS and S70 SS, the synthesis was carried out again in a muffle furnace at temperature of 1000°C for 6 hours, with a heating rate of 15°C/min by mixing stoichiometric amounts of the starting substances - La_2O_3/Al_2O_3, H_3BO_3 - 45% excess and 2 mol % Eu_2O_3 as shown in equations (2) and (3). The reagents were weighed, mixed, and well-homogenized. The prepared mixtures were placed in porcelain crucibles and heated. After 4 hours for sample S29 SS and 6 hours for S60 SS and

S70 SS, they were left in the furnace and slowly cooled for 16 hours.

Photoluminescence measurements

The photoluminescence spectra were measured at room temperature by an Ocean Optics fiber optic QEB1104 spectrometer in the range 200–990 nm and a combination of an Energetic Laser driven white light source (190 nm – 2500 nm) and a fiber-optic monochromator (MonoScan 2000, Ocean Optics). The main advantage of this scheme is that it minimizes reflection from the samples and maximizes the luminescence spectrum. The synthesized samples are fine white powders, which makes them suitable for fillers in polymers, paper, inks, etc.

Fourier transform-infrared (FTIR) spectroscopy

FTIR Bruker Vertex 70 spectrometer was used for the FTIR analyses, which provided peak sensitivity in the MIR 4000-400 cm^{-1} region. The IR data were analyzed to compile the structure spectra, and to get information about the interatomic forces and the reasons for the appearance of the different types of structures in the rare earth borates.

RESULTS AND DISCUSSION

It was found that temperature of synthesis affects the substitution of the activator, that is, the europium ion can replace yttrium, aluminum, or lanthanum ion in the host lattice. This occurs when the ionic radii of the activator and the host are sufficiently different. It is known that replacing Eu^{3+} with Y^{3+} results in a larger unit cell volume due to the difference in radii (0.95 and 0.90 Å, respectively) [12]. The same can be said for lanthanum, whose ionic radius is 1.06 Å, and for aluminum – 0.54 Å [13, 14]. From the observed excitation-emission scan of the sample S29 SS, the most intense emission peaks are at ≈ 591 nm (2.10 eV) (orange region) due to the $^5D_0 \rightarrow {}^7F_1$ transition, ≈ 612 nm (2.03 eV) (red) corresponding to the $^5D_0 \rightarrow {}^7F_2$ transition and 696 nm (1.78 eV) due to $^5D_0 \rightarrow {}^7F_4$ as shown in Fig. 1(a and b). Very intense and hypersensitive transition $^5D_0 \rightarrow {}^7F_2$ indicates that Eu^{3+} is not on a site with a center of symmetry [15, 16]. For the S_6 symmetry, which has an inversion center, the rule forbids an electron-dipole transition within the 4f subshells. This transition is allowed only under the condition that the europium ion occupies a site without an inversion center and is sensitive to local symmetry.

Table 1. Description of sample composition

Samples	Y_2O_3 (g)	La_2O_3 (g)	Al_2O_3 (g)	H_3BO_3 excess %	H_3BO_3 (g)	Eu_2O_3 (mol %)	Eu_2O_3 (g)
S29 SS	0.7850			45	0.6232	2	0.007
S60 SS		0.7249		45	0.3987	2	0.007
S70 SS			0.4519	45	0.7946	2	0.007
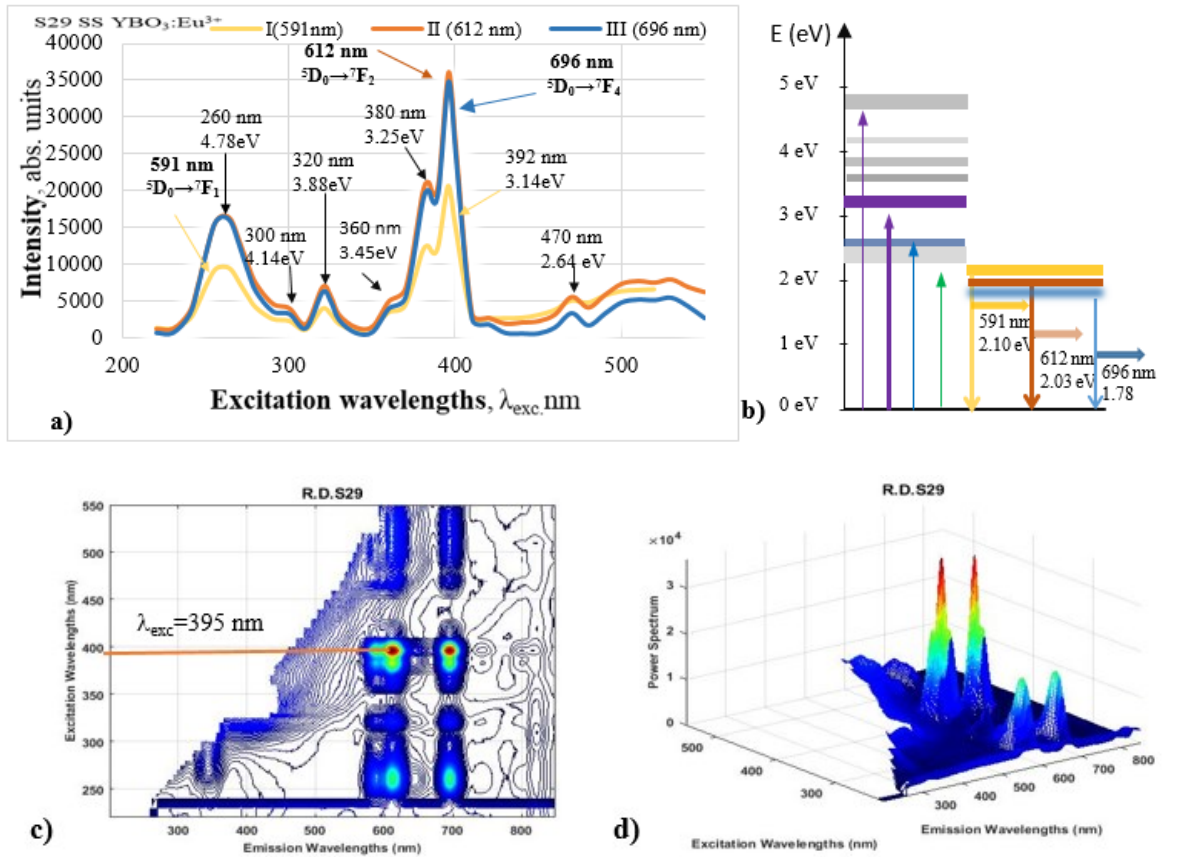
Fig. 1. a) Graphic representation of the emission intensity at 591 nm, 612 nm and 696 nm *vs*. excitation wavelength; **b)** corresponding energy levels of yttrium borate doped with Eu³⁺; **c)** excitation-emission 3D spectra of YBO₃:Eu³⁺ topographic representation; **d)** side view presentation.
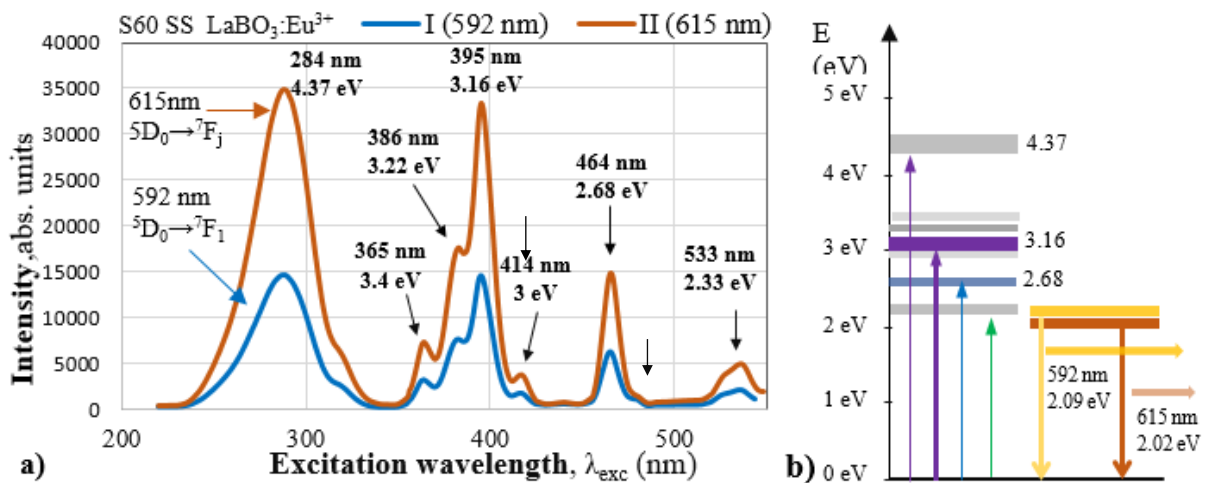
Fig. 2. a) Graphic representation of the emission intensities at 592 nm and 615 nm on the excitation wavelength; **b)** energy levels (eV) of lanthanum borate doped with europium ion; **c)** 3D excitation-emission spectra of LaBO₃: Eu³⁺: topographic presentation; **d)** side view

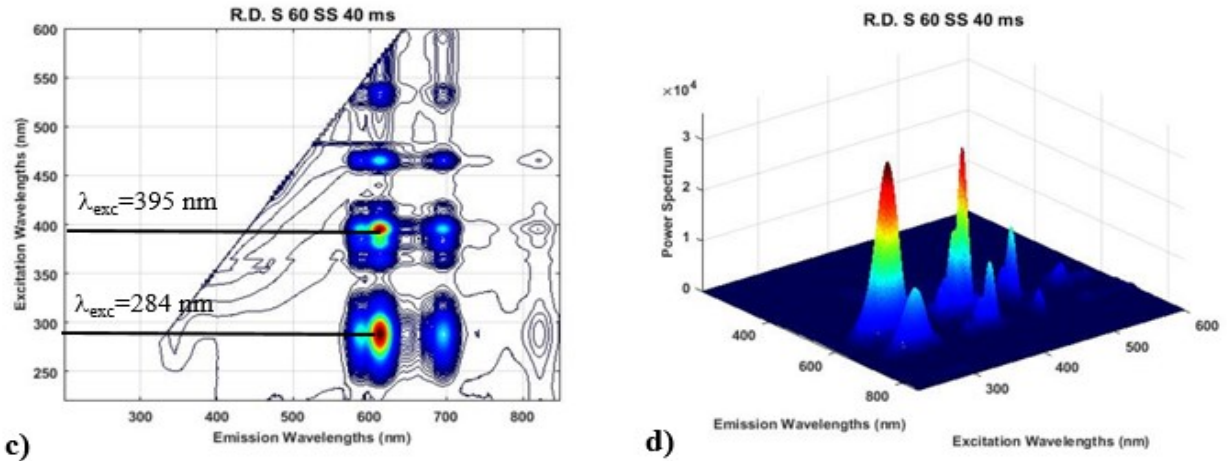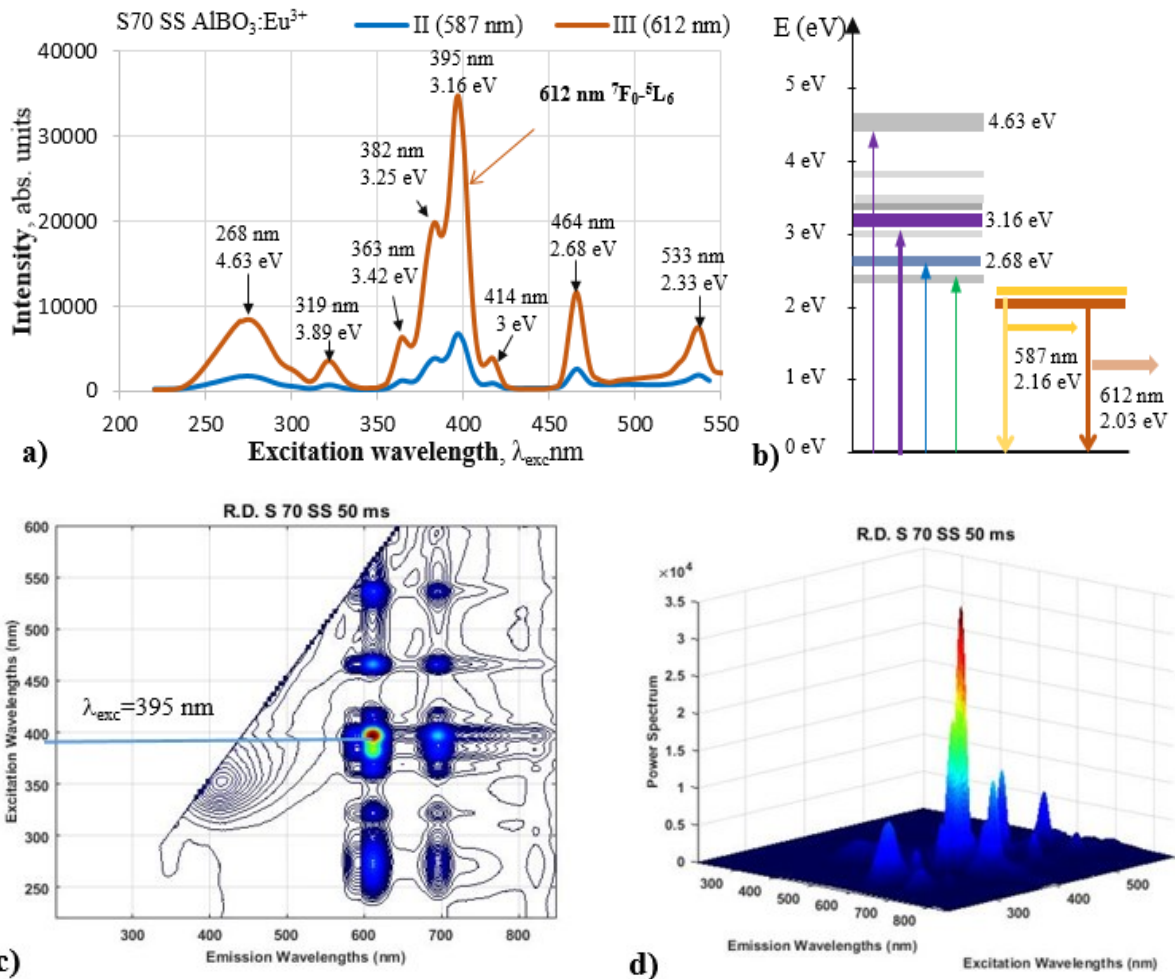**Fig. 3. a)** Graphic representation of the emission intensity at 587 nm and 612 nm on the excitation wavelength; **b)** energy levels (in eV) of aluminum borate doped with europium ion. Eu³⁺: **c)** 3D excitation-emission graph of AlBO₃: topographic representation; **d)** side view.

When Eu^{3+} ions occupy sites of inversion centers, the $^5D_0 \rightarrow {}^7F_1$ transitions should be relatively strong and the $^5D_0 \rightarrow {}^7F_2$ transitions should be relatively weak [17]. In our case, we observed the opposite statement and concluded that the europium ion isn't at the site with the center of inversion for 284 nm (4.37 eV) with emission at $\approx$ 592 nm (orange region) due to the $^5D_0 \rightarrow {}^7F_1$ transition and with emission at $\approx$ 615 nm (2.02 eV) due to the $^5D_0 \rightarrow {}^7F_j$ transition (red region). In the excitation source of 395 nm we observed emission at 595 and 615 nm and the weakest fluorescence upon excitation at 464 nm (2.68 eV) again 615 nm (red), as shown in Fig. 2a) and b). The peaks at 615 nm correspond to $^5D_0 - {}^7F_j$ transitions between multiplets (j = 0, 1, 2, 3, 4) characteristic of the Eu^{3+} ion as shown at Fig. 2(a and b) [18]. For an excitation at $\lambda_{max} \approx$ 290 nm, excitation energy transferred from the 2p orbital of the O^{2-} to the–4f of Eu^{3+} is observed, the energy of which depends on the stability of the fields of the surrounding O^{2-} ions. The peaks in the range 350–430 nm (365, 386 nm) (3.40, 3.22 eV) correspond to transitions of Eu^{3+} f−f electrons from the ground state $^7F_0$ to the excited levels $^5D_4$, $^5L_6$ и $^5G_{4,5}$ [19]. In the excitation spectra, the charge transfer is much more intense when in the matrix the alloying element is the europium ion as shown in Fig. 2c) and d) [5]. The displacement of the charge transfer peaks to longer wavelengths may also be caused by a decrease in the distance between Eu^{3+} and O^{2-} and therefore a decrease in the electronegativity difference between the ions [20]. Aluminum borate is characterized by highly efficient radiation in the visible region. Upon excitation with 395 nm, emission at 612 nm was observed, corresponding to the $^7F_0 - {}^5L_6$ transition characteristic of the europium ion in the aluminum borate matrix and which is the most intensive peak [21]. Typical emission from $^5D_0$ to $^7F_{0, 1, 2, 3, 4}$ was measured in the range of 276-536 nm as shown in Fig. 3a and b [22]. An important feature observed in the emission spectra is that when considering all the transitions from $^5D_0$ to $^7F_{0, 1, 2, 3, 4,}$ peak broadening takes place [23]. This can be attributed to the distribution effect of the different microenvironments around Eu^{3+}, i.e. separate symmetry sites occupied by Eu^{3+} in the host lead to inhomogeneous broadening. When the $AlBO_3$ host consists of octahedra, it can be assumed that Eu^{3+} replaces Al^{3+} in the octahedral sites. The magnetic dipole character of $^5D_0 \rightarrow {}^7F_1$ makes it possible to determine the intensity parameters of the emission spectrum since this transition does not depend on the local ligand field and can be used as a reference for the entire spectrum.

FTIR analysis

Depending on the size of the cations, rare earth borates crystallize in 3 spatial structures – vaterite, calcite, and aragonite [24]. It is believed that the vibrational spectra of vaterite-type orthoborates significantly differ from calcite and aragonite types. Borate compounds of vaterite type are characterized by extremely broad and intense absorption peaks in the range from 800 cm^{-1} to 1200 cm^{-1}. These peaks can be attributed to the vibration of the $B_3O_9^{9-}$ groups in the vaterite-type orthoborates. For the isolated XO_3 (X=yttrium, lanthanum, aluminum) planar ion having trigonal symmetry, there are four main modes of vibration: symmetric stretching v_1, out-of-plane bending v_2, doubly degenerate antisymmetric stretching v_3, and doubly degenerate antisymmetric planar bending, v_4 [25]. Of these, three are active in the infrared region, while v_1, a symmetric stretch, is inactive in isolated ions. In a crystalline solid containing more than one molecule per unit cell, symmetry considerations indicate that all modes can be active and coupling between different modes can even eliminate degeneracies [26, 27]. Six bands are expected in aragonite because in this structure v_1 is active and degeneracies have been removed from v_3 and v_4. Vaterite is known to possess a hexagonal structure containing two or more molecules per unit cell [28-30].

For the sample S29 SS, (Fig. 4, S29 SS), the weak peak at 570 cm^{-1} is attributed to in-plane bending of the BO_4 group or the BO_3 group in vaterite-type orthoborates [31]. The bending vibrations of the B–O–B bond in the borate network are located at 710 cm^{-1}. In the range 731 – 873 cm^{-1} the YBO_3 vibrations appear. The peaks located in the region from 916 cm^{-1} to 1250 cm^{-1} are due to B-O symmetric stretching vibrations of the bond in BO_4 units of diborate and tetraborate groups [32]. B–O stretching vibrations are best expressed at 1250 cm^{-1} [33]. The intense peak at 1270 cm^{-1} corresponds to the B–O stretching vibration in BO_3 units of various types of borate groups appearing in the weaker band at 1381 cm^{-1} [34]. The peak at 1409 cm^{-1} represents the stretching vibrations of the B–O bonds for the tetrahedral BO_4 groups [35]. The band centered at 1463 cm^{-1} corresponds to B-O$_{sym}$ symmetric stretching of BO_3 in ortho-borate groups [36]. The most intense peak at 1724 cm^{-1} is due to pentaborate arising from the B – O stretching vibration of $[BO_3]^{3-}$ [31]. Data from the IR spectrum of the lanthanum borate are shown in Fig. 4, S60 SS. The IR spectrum of $LaBO_3$ doped with Eu^{3+} shows strong absorption peaks in the range 1269–592 cm^{-1}, inherent to the vibrations of planar trigonal $[BO_3]^{3-}$ groups [37-40]. Two weak absorption bands at 592 and 611 cm^{-1} are

due to in-plane (v_4) and the strong peak at 714 cm^{-1} is due to out-of-plane (v_2) B–O-B bending modes. The peak at 940 cm^{-1} (v_1) refers to the symmetric stretching of the three-coordinate bands [$v_s(B_{(3)}–O)$] modes of the [BO_3]$^{3-}$ groups. The most intense and sharp peak appears at 1269 cm^{-1}, which is characteristic of the B-O asymmetric stretching of BO_3 [20]. For aluminum borates doped with europium ion, the weak peak observed in the range of 448–505 cm^{-1} is attributed to the bending of BO_4 units as shown in Fig. 4, S70 SS. The peak at 547 cm^{-1} is attributed to the formation of Eu^{3+} borate. The following are bands that correspond to the different

phases and stretching modes: 648 cm^{-1} B-O-B in BO_3 [36]. The band at 717 cm^{-1} for the formation of the B_2O_3 glassy body due to the bending vibration of the B–O–B bond in the borate network was determined. The stretching vibration of Al–O in AlO_4 appears at 780 cm^{-1}[37]. The bands in the range of 884–1052 cm^{-1} can be assigned to B–O bond stretching vibration in BO_4 units of di-, tri-, tetra- and penta-borate groups as shown in [40 Fig. 6.]. The band at 1437 cm^{-1} corresponds to B–O asymmetric stretching vibrations in BO_3 units.
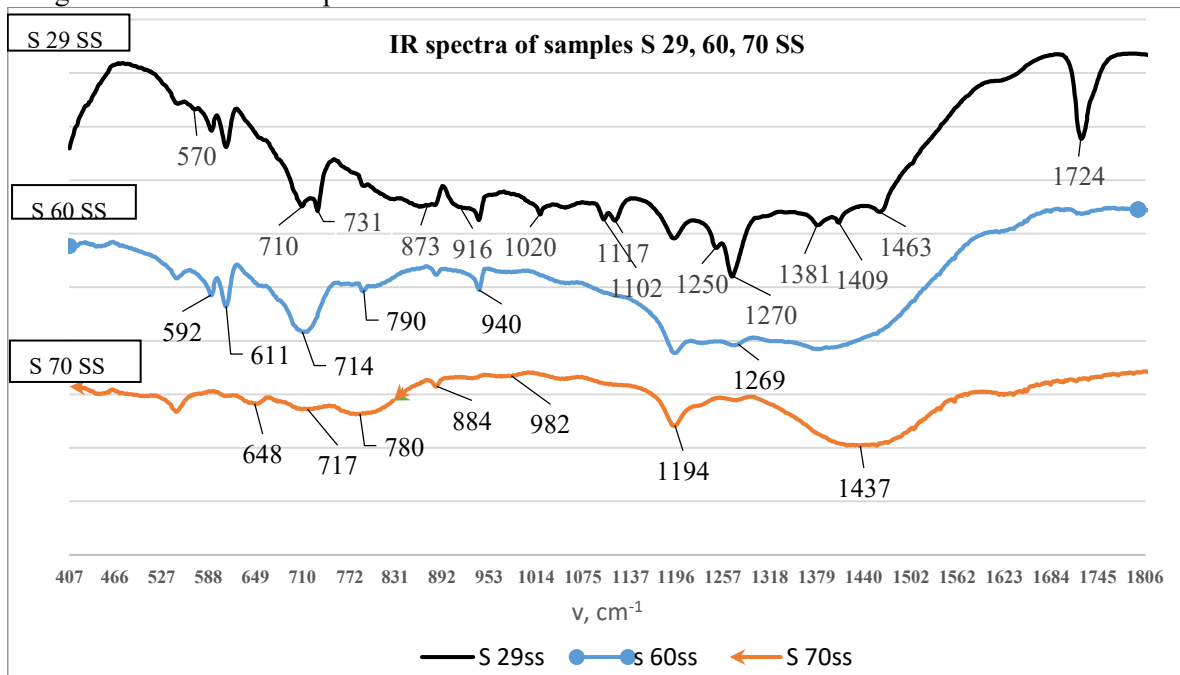
Fig. 4. FTIR spectra of yttrium, lanthanum and aluminum borates doped with europium ion.

CONCLUSION

Three samples with different matrix compositions - YBO_3, $LaBO_3$, and $AlBO_3$ doped with europium oxide were synthesized by a solid-state reaction. The samples were analyzed with a spectrometer to establish the highest emission intensity resulting from europium ion activation in the different matrices. The excitation spectra of the obtained materials show transitions from $^5D_0$ to $^7F_1$ $^7F_2$ $^7F_3$ and $^7F_4$ states. When comparing the spectra of aluminum, lanthanum, and yttrium borate, for excitation at ≈ 284 nm, only europium-doped lanthanum borate produces an intense peak with emission at 615 nm. Two intense peaks are also observed in the yttrium borate matrix, which, under the excitation with ≈ 395 nm, emit at ≈ 612 and 696 nm, respectively, due to different electronic transitions. For the aluminum borate matrix, upon excitation with ≈ 290 nm, an extremely weak, undetectable fluorescence is observed at 590 nm, the

most intense peak for this matrix is at 612 nm when the excitation source is ≈ 395 nm. It was found that the matrix with yttrium borate, europium ion is well activated and gives peaks in the orange and red region of the spectrum, for the matrix with lanthanum borate two strong peaks are observed in the red region, but when irradiated with sources of different wavelength, for the aluminum borate matrix we observe one intense peak in the red region. Based on these studies, depending on the target product, a suitable matrix can be selected for different areas of application. Of the lanthanide group, europium oxide itself has fluorescence in the red region. FTIR spectra evidence the presence of BO_4 vibrations, B–O deformation mode, and stretching vibrations of BO_4 units in tri-, tetra, and penta-borate groups in all RE-doped materials, absorption peaks arise due to electronic transition between inner orbitals. The addition of rare earth

oxide to different matrices leads to the activation of the europium ion and a shift of the absorption peaks.

REFERENCES

1. M. V. Nazarov, J. H. Kang, D. Y. Jeon, S. Bukesov, T. Akmaeva, *Optical Materials,* **27**, 1587 (2005).
2. R. Srinivasan, N. R. Yogamalar, J. Elanchezhiyan, R. J. Joseyphus, A. C. Bose, *Journal of Alloys and Compounds,* **496** (1-2), 472 (2010).
3. H. Qi, Z. Zhao, G. Zhan, B. Sun, W. Yan, C. Wang, L. Wang, Z. Liu, Z. Bian, C. Huang, *Inorg. Chem. Front.*, (2020), doi: 10.1039/D0QI00762E
4. Poonam, S. P. Khatkar, R. Kumar, Avni Khatkar, V. B. Taxak *Journal of Materials Science: Materials in Electronics,* (2015) doi:10.1007/s10854-015-3330-7
5. M. V. Nazarov, J. H. Kang, D. Y. Jeon, E. J. Popovici, L. Muresan, B. S. Tsukerblat, *Solid State Communications,* **133**, 183 (2005).
6. R. L. Kohale, V. B. Pawade, A. H. Deshmukh, *Electronic and Optical Materials* (2021).
7. A. K. Gangwar, K. Nagpal, P. Kumar, N. Singh, B. K. Gupta, Bipin. *J. Appl. Phys.* **125,** 074903 (2019)
8. M. J. Q. Lauro, F. F. M. Fausto *Nanocomposites for Photonic and Electronic Applications,* **31–44** (2020), doi:10.1016/B978-0-12-818396 0.00002 9
9. D. J. Kim, S. H. Hyun, S. G. Kim; M. Yashima, *J. Am. Ceram. Soc,* **77** (2), 597 (1994).
10. E. A. Tkachenko, R. Mahiou, G. Chadeyron, D. Boyer, P. P. Fedorov, S. V. Kuznetsov, *Russian Journal of Inorganic Chemistry*, **52**(6), 829 (2007).
11. K. Hristova, S. Nachkova, Al. Peltekov, Zh. Simeonova, I. Kostova, *Technics, Technologies, Education. Safety,* **2**, 128 (2021).
12. A. A. Al-Juaid, M. A. Gabal; *Journal of Materials Research and Technology,* **14**, 10 (2021).
13. K. Chandra, V. Singh, S. K. Sharma, P. K. Kulriya, **937** 168311 (2023), doi: 10.1016/j.jallcom.2022.168311
14. J. H. Lin, S. Zhou, L. Q. Yang, G. Q. Yao, M. Z. Su, *Journal of Solid State Chem*., **134**(1), 158 (1997).
15. K. Binnemans, *Coordination Chemistry Reviews,* **295***, 1 (2015)* doi: 10.1016/j.ccr.2015.02.015
16. N. C. Chang, *J. Appl. Phys*., **34**, 3500 (1963) doi: 10.1063/1.1729247
17. S. Sari, F. T. Senberber, M. Yildirim, A. S. Kipcak, S. A. Yuksel, E. M. Derun, *Materials Chemistry and Physics*, **200,** 196 (2017) doi: 10.1016/j.matchemphys.2017.07.056
18. N. V. Klassen, S. Z. Shmurak, I. M. Shmyt'ko, G. K. Strukova, S. E. Derenzo, M. J. Weber, *Nuclear Instruments and Methods in Physics Research A,* **537,** 144 (2005).
19. N. I. Steblevskaya, M. V. Belobeletskaya, M. A. Medkov. *Russian Journal of Inorganic Chemistry*, **66**, 468 (2021)
20. P. J. Yadav, N. D. Meshram, S. V. Maharil. *Optical Materials*: X, **19**, 100252 (2023).
21. S. P. Ray, *J. Am. Ceram. Soc,* **75(9)**, 2605 (1992).
22. A. S. Kipcak, D. Y. Baysoy, E. Derun, S. Piskin, *Advances in Materials Science and Engineering*, **1-9** (2013).
23. R. Srinivasan, N. R. Yogamalar, J. Elanchezhiyan, R. J. Joseyphus, A. C. Bose*, Journal of Alloys and Compounds,* **496**(1-2), 1 (2010).
24. G. Hertzberg, Molecular spectra and molecular structure, vol II*,* 7th edn. D. van Nostrand Co, **178,** ,\N.Y.,1956.
25. C. E. Weir, E. R. Lippincott, *J. Res. Natl. Bur. Stand. A, Phys. Chem.,* **65**A(3), 173 (1961).
26. R. S. Halford, *The Journal of Chemical Physics,* **14**, 395 (1946), doi: 10.1063/1.1724158
27. R. W. G. Wykoff, The Chemical Catalog Co, 2nd edn., **80**, N.Y., 1931.
28. H. J. Meyer. *Angew. Chem.,* **71,** 678, (1959).
29. L. H. Ahrens, *Geochim. Cosmochim. Acta,* 155 (1952) doi:10.1016/0016-7037(52)90004-5
30. A. G. Christy, *Crystal Growth & Design, acs.cgd.7b00481* (2017). doi: 10.1021/acs.cgd.7b00481
31. V. Hegde, N. Chauhan, V. Kumar, C. S. D. Viswanath, K. K Mahato, S. D. Kamath, *Journal of Luminescence*, (2018) doi: org/10.1016/j.jlumin.2018.11.023
32. A. Y. Madkhli, Ü. H. Kaynar, M. B. Coban, M. Ayvacikli, A. Canimoglu, N. Can, *Materials Research Bulletin,* **161** (2023). https://doi.org/10.1016/j.materresbull.2023.112167
33. P. Pascuta, S. Rada, G. Borodi, M. Bosca, L. Pop, E. Culea, *Journal of Molecular Structure,* **924–926,** 214 (2009).
34. P. O. Ike, A. C. Nwanya, K. K. Agwu, F. I. Ezema. *Optical Materials,* **127**, 112263 (2022) https://doi.org/10.1016/j.optmat.2022.112263
35. A. S. Oreshonkov, E. M. Roginskii, N. P. Shestakov, I. A. Gudim, V. L. Temerov, I. V. Nemtsev, M. S. Molokeev, S. V. Adichtchev, A. M. Pugachev, Y. G. Denisenko, *Materials,* **13** (3) 545 (2020).
36. A. Szczeszak, K. Kubasiewicz, S. Lis, *Optical Materials,* **35**(6), 1297 (2013).
37. N. I. Steblevskaya, M. A. Medkov, M. V. Belobeletskaya, RF Patent 2651028, *Russian Journal of Inorganic Chemistry,* Publ. 11 (2017).
38. C. Badan, O. Esenturk, A. Yilmaz, *Solid State Sciences,* **14**(11-12), 1710 (2012).
39. G. Heymann, T. Soltner, H. Huppertz, *Solid State Sci*. **8**, 827 (2006).
40. P. Su. Wong, M. H. Wan, R. Hussin, H. O. Lintang, S. Endud, *Journal of Rare Earths,* **32**(7), 585 (2014).

Ion-specific effects on foam films and foam from diluted solution of sodium dodecyl sulfate

N. K. Petkova[1], D. S. Ivanova–Stancheva[1*], N. A. Grozev[2], K. M. Mircheva[2], S. I. Karakashev[1]

[1]Faculty of Natural Sciences, Shumen University, 115 Universitetska Str. 9712 Shumen, Bulgaria
[2]Department of Physical Chemistry, Sofia University, 1 James Bourchier Avenue, 1164 Sofia, Bulgaria

The ion-specific effects on extremely diluted solutions of surfactants are poorly studied. The effect of Li^+, Na^+ and K^+ ions on the properties of foam films and foam stabilized by 0.05 mmol/L sodium dodecyl sulfate (SDS) was studied. Each one of the salts LiCl, NaCl and KCl in the concentration range of 1.1 mmol/L to 50 mmol/L was added to 0.05 mmol/L solution of SDS, for studying the properties of its foam films and foams. It was established that the surface potential of the foam films does not depend on the type of salt added, which means that no ion-specific effects are registered. On the contrary, such effects are evident in the case of foam produced by sparging of gas through porous bottom of column containing the same solutions. Thus, the rates of foaming, foam decay and the foam lifetime *vs.* the concentration of added salt (LiCl, NaCl and KCl) were studied by means of Dynamic Foam Analyzer (DFA-100, Kruss Ltd, Germany). The foam production number for each one of these cases was calculated as well. It was established that both NaCl and KCl boost the foam, the first one of which being stronger than the second one. On the contrary, LiCl has no effect on the foamability of the system. The present study is an example for manifestation of a salt-specific effect under dynamic conditions, which vanishes under static conditions.

Keywords: ion-specific effects, foam films, foam, adsorption layer, surfactant

INTRODUCTION

It has been established since long time ago that different salts differently affect the physico-chemical properties of solvents, solutes, dispersed systems and biological cells. For example, Ostwald [1] reported that the vapor pressure of the solvent weakly depends on the type of the added salt. Raoult [2] had similar observation for the freezing points of the solutes in presence of different salts. De Vries [3] explored the specific effect of different salts on live plant cells and established that there exist a certain concentration specific for each salt, at which the protoplasm of the cell peels away from the cell wall (plasmolysis). The same effect has been confirmed by Hamburger [4] for the red blood cells. Hofmeister [5-7] established that the blood proteins salt out at a certain concentration specific for each salt. He succeeded to separate the effects of the anions and those of the salts and ordered them in the following series of increasing strength for precipitation of the blood proteins:

Cations:
$Li^+<Na^+<K^+<Rb^+<Cs^+ NH_4^+<N(CH_3)_4^+$
Anions:
$ClO_4^-<BF_4^-<NO_3^-<Br^-<Cl^-<OH^-<F^-<CH_3COO^-$
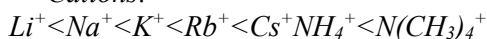
The effect of the anions has been found to be stronger than that of the cations. Significantly later on, the same systems were explored by means of small-angle X-ray scattering (SAXS) [8]. Thus, it was established that the addition of salt generally initiates attraction between the protein molecules, but with a power specific for each salt [8, 9]. Surprisingly, it was found out that some salts have the ability to slow down the coalescence of bubbles in aqueous medium at a certain specific concentration, while other salts do not have such an effect [10, 11]. The same observations were made on aqueous foam films [12, 13]. Recent studies on the effect of co-ions [14-16] and counter-ions [17, 18] on the properties of foam, wetting and emulsion films indicated a specific adsorption of the ions on the interface boundaries depending on their specific energy of adsorption, sizes and hydration shells, thus affecting the surface potentials of the interface boundaries. The higher the value of the specific adsorption energy of the ion, the larger is its adsorption on the film surfaces. Hence, counter-ions with larger specific adsorption energy should contribute for thinner films and less stable dispersed systems and *vice versa*. Indeed, our theoretical expectations regarding the thickness of the thin films are fulfilled [14-18], but the experiments on foam's and emulsion's stability show the opposite effect – counter-ions with larger specific energy of adsorption contribute for more stable foams and

---

emulsions [17, 19, 20]. The systems, which have been studied in these cases contain ionic surfactants with concentrations close to C/CMC≈ ½. It is not clear if the ion-specific effect will be manifested at more diluted surfactant solutions (e.g. C/CMC≈0.05). For this reason, we explored the effect of LiCl, NaCl and KCl on the properties of foam films and foam stabilized by 0.05 mmol/L SDS.

EXPERIMENTAL

Interferometric study of foam films

The interferometric method for studying thin liquid films allows one to calculate the surface potential of the film surfaces [21]. The setup consists of two units: (i) the cell in which the film is formed, and (ii) the optic-electronic system for monitoring the film and registration of its interferometric image.

The cell contains a film holder with radius of 2.15 mm, which has an orifice aside, connected to a capillary tube and a mercury pump. The film holder is dipped into the surfactant solution and pulled out, thus forming a double concave drop. After this the two tips of the double concave drop are approached toward each other by gentle suction of the liquid using the mercury pump until the formation of the foam film. Immediately after its formation, it starts draining due to the action of the capillary pressure. The foam film is vertically illuminated with a beam of coherent monochromatic light (λ = 551 nm) generated by an inverted microscope (Carl Zeiss, Germany) and reflected by the two surfaces of the film, thus causing the appearance of two phase-shifted beams of reflected light, which are collected together and captured by a Sony – SSC-M388CE photo-camera as a temporal general interferogram. The latter one is recorded on computer as a movie in "avi" format. "Image J" software is used for processing the movie. Hence, the movie of the evolution of the general interferogram is split to pictures in a 0.083 seconds-time frame. The software extracts the signal from a small spot on the general interferogram, chosen by us through all of the frames of the movie. Once, we produce the spatial interferogram (signal *vs.* pixel) we use the interferometric formula (see Eq. 1) integrated as code in VBA macros in Microsoft Excel. The formula is as follows:

$$h = \frac{\lambda}{2\pi n_0} \left[l\pi \pm \arcsin \sqrt{\frac{\Delta(1+r)^2}{(1-r)^2 + 4r\Delta}} \right] \quad (1),$$

where λ is the wavelength of the monochromatic light after digital filtration (for green light λ =551 nm), n_0 is the refractive index of water (n_0 =1.333

at T=20°C), l is order of interference, $\Delta=(I-I_{min})/(I_{max}-I_{min})$, where I is the transient strength of the signal, I_{max} and I_{min} are its maximal and minimal values, $r=(n_0-n_1)^2/(n_0+n_1)^2$ is the Fresnel reflection coefficient, n_1 is the refractive index of the air (n_1=1). The minimal signal for the foam film is usually taken from the signal of a ruptured film while the maximal signal is taken from the digital interferogram.

Study of pneumatic foams

Dynamic foam analyzer (DFA – 100, Kruss ltd, Germany) was used to study the foams. The pneumatic foams were produced by means of sparging of gas (0.3 L/min) through the porous bottom of a column containing the foaming solution. After turning on the gas flux, the foam column starts raising up until reaching a certain maximal height at which the gas delivery is switched off, thus allowing the foam to decay. Both, the foam upraise and the foam decay are monitored by means of scanline camera which delivers the foams image to a computer whose specialized software digitalizes this image and records it. This allows us to record the height of the foam *vs.* time and calculate in this the rates of foam upraise and decay, its lifetime and the foam production number:

$$f = V_{foaming} / V_{defoaming} \quad (2)$$

The chemicals LiCl, NaCl and KCl were purchased from Sigma-Aldrich.

RESULTS AND DISCUSSION

Foam films and foams stabilized by 0.05 mmol/L SDS in presence of LiCl, NaCl and KCl in the concentration range of 1.1 mmol/L to 50 mmol/L were explored.

Exploration of the ion-specific effects on foam films stabilized by 0.05 mmol/L SDS

The equilibrium foam films for each one of the cases were obtained by means of the above-mentioned interferometric method. The surface potentials of the foam films in presence of each one of the salts were calculated by means of the DLVO theory [22]. The equilibrium foam film thickness and its correspondent surface potential values *vs.* the added salt concentration are presented in Fig. 1. One can see that both the equilibrium film thickness and the surface potential values in the cases of LiCl, NaCl and KCl practically coincide in their whole concentration range. This is an indication that no counter ion-specific effect in the particular case of 0.05 mmol/L SDS can be registered.
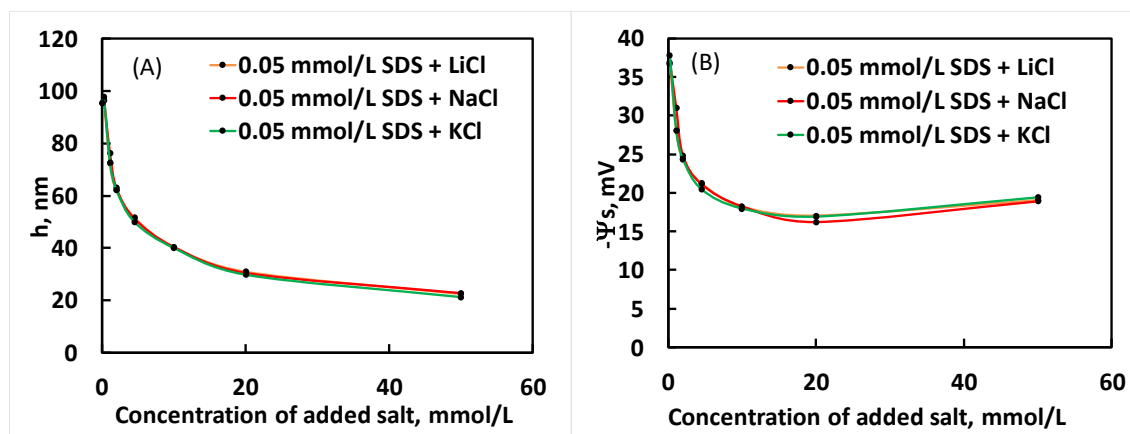
Figure 1. Equilibrium foam film thickness (A) and surface potential (B) of foam films stabilized by 0.05 mmol/L SDS *vs.* concentration of the added salt (LiCl, NaCl, KCl).
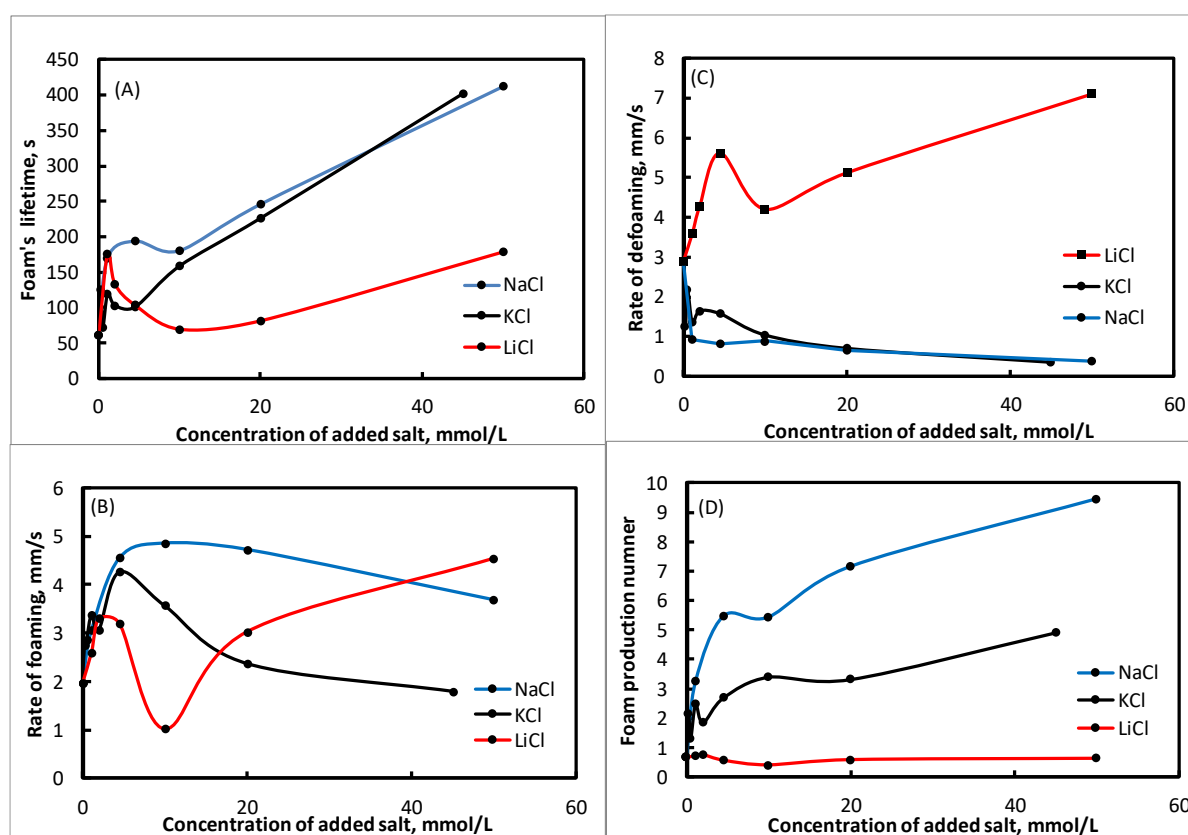
Figure 2. Foam's lifetime (A), rate of foaming (B), rate of defoaming (C) and foam production number (D) *vs.* the concentration of the added salt.

Exploration of the ion-specific effects on pneumatic foam stabilized by 0.05 mmol/L SDS

The foam's lifetime, the rate of foaming, the rate of foam decay and the foam production number versus the added salt concentration for the three different cases (0.05 mmol/L SDS + LiCl, NaCl, KCl) is presented in Fig. 2. The salt – specific effect on the foam films stabilized by 0.05 mmol/L SDS was not observed, but it was registered in the case of the pneumatic foams produced from the same SDS + MCl (M = Li, Na, K) aqueous solutions. Obviously, the ion-specific effect for this very

diluted solution of SDS (0.05 mmol/L) emerges under dynamic conditions, while it vanishes under static conditions. In short, both NaCl and KCl significantly increase the foam's lifetime, while LiCl moderately increases the latter (see Fig. 2A). The rate of foaming reaches a maximum at certain concentrations of NaCl and KCl, above which it diminishes, while in the case of LiCl a peculiar and opposite trend is observed (see Fig. 2B). The rate of foam decay weakly diminishes upon the increase of the concentrations of NaCl and KCl, while it raises steeply in the case of LiCl (see Fig. 2C). One can see

most clearly the effect of the type of salt on the foam's behavior in Fig. 2D. The foam production number steeply increases with the increase of the concentration of NaCl, followed by KCl, in which it increases weaker than in the case of NaCl. In the case of LiCl the foam production number practically does not depend on the concentration of LiCl, but it is below unity, which means that LiCl acts as a weak foam suppressor. On the contrary, KCl and NaCl act like foam boosters with NaCl being the strongest one.

CONCLUSIONS

The counter-ion-specific effect on a very diluted solution of SDS (0.05 mmol/L) was studied by means of added LiCl, NaCl and KCl. No effect of the type of the salt on the equilibrium foam films was established, while in the case of pneumatic foams NaCl acted as a strong foam booster, followed by KCl. The third salt (LiCl) showed a peculiar effect on the foam but generally it acted as a weak foam suppressor not depending on the LiCl concentration.

REFERENCES

1. W. Ostwald, Lehrbuch der allgemeinen Chemie. Vol. 1, 1885.
2. F.-M. Raoult, By Raoult's method of determining the lowering of the freezing point in very dilute solutions. Brown and Morris, London, 1888, p. 610.
3. N. Pringsheim, *Jahrbücher für wissenschaftliche Botanik,* Gebrüder Bornträger, Berlin, **XIV**, 1884, p. 601,.
4. H. J. Hamburger, *Archiv für Physiologie*, 486 (1886).
5. F. Hofmeister, *Archiv für experimentelle Pathologie und Pharmakologie,* XXIV, 247 (1887).
6. F. Hofmeister, *Archiv für experimentelle Pathologie und Pharmakologie,* XXV, 1 (1888).
7. F. Hofmeister, *Archiv für experimentelle Pathologie und Pharmakologie,* XVII, 395 (1890).
8. S. Finet, F. Skouri-Panet, M. Casselyn, F. Bonnete, A. Tardieu, *Curr. Opin. Colloid Interface Sci.,* **9** (1-2), 112 (2004).
9. M. Bostrom, D. R. M. Williams, B. W. Ninham, *Current Opinion in Colloid & Interface Science,* **9** (1-2), 48 (2004).
10. V. S. J. Craig, B. W. Ninham, R. M. Pashley, *J. Phys. Chem.,* **97**, (39), 10192 (1993).
11. V. S. J. Craig, *Curr. Opin. Colloid Interface Sci.,* 9, (1,2), 178 (2004).
12. V. V. Yaminsky, S. Ohnishi, E. A. Vogler, R. G. Horn, *Langmuir,* **26**, (11), 8061 (2010).
13. V. V. Yaminsky, S. Ohnishi, E. A.; R. G.Horn, *Langmuir,* **26**, (11), 8075 (2010).
14. N. Schelero, G. Hedicke, P. Linse, R. V. Klitzing, *J. Phys. Chem. B,* **114**, (47), 15523 (2010).
15. W. Kunz, Specific Ion Effects, World Scientific, 2010.
16. N. Schelero, R. von Klitzing, *Curr. Opin. Colloid Interface Sci.,* **20** (2), 124 (2015).
17. I. B. Ivanov, R. I. Slavchov, E. S. Basheva, D. Sidzhakova, S. I. Karakashev, *Adv Colloid Interface Sci,* **168** (1-2), 93 (2011).
18. R. I. Slavchov, S. I. Karakashev, I. B. Ivanov, in: Surfactant Science and Technology: Retrospects and Prospects, L. S. Romsted (ed.) Taylor & Francis Group, 2013; p 53.
19. S. Sett, S. I. Karakashev, S. K. Smoukov, A. L. Yarin, *Adv. Colloid Interface Sci.,* **225**, 98 (2015).
20. P. Amani, S. I. Karakashev, N. A. Grozev, S. S. Simeonova, R. Miller, V. Rudolph, M. Firouzi, *Adv. Colloid Interface Sci.,* 295 (2021).
21. P. M. Kruglyakov, D. R. Ekserova, *Foam and Foam Films,* 1990, p 425.
22. A. V. Nguyen, H. J. Schulze, Colloidal Science of Flotation, Marcel Dekker, New York, 2004, p 840.

Effect of endogenic and exogenic oxidative stress changes during spontaneous preterm birth

I. M. Koleva-Korkelia[1], R. J. Jasem[1], D. S. Kostadinova[1], M. Angelova[1], K. Petkova-Parlapanska[2], E. D. Georgieva[2], G. D. Nikolova[2], Y. D. Karamalakova[2*]

[1]*Obstetrics and Gynaecology Clinic, UMHAT "Prof. St. Kirkovich" 6000, Stara Zagora, Bulgaria*
[2]*Department of Chemistry and Biochemistry, Medical Faculty, Trakia University, 11 Armeiska Str., 6000 Stara Zagora, Bulgaria*

This study aimed to assess the effect of endogenic and exogenic oxidative stress (OS) changes in the maternal response and establish the relationship to plasma non-infectious OS-associated inflammation in spontaneous preterm birth (SPTB), (in declared active labor with an intact amniotic sac and no recorded inflammation) beginning at $32–34^{+6}$ gestational weeks. Results were compared with women who gave birth at term (TB) in the active phase. To assess changes in OS, the reactive oxygen-nitrogen (RONS) species, as nitric oxide ($•NO$), superoxide ($•O_2^-$) radicals, albumin SH-malformation (5-MSL), and ROS peroxidation were investigated by electron paramagnetic resonance (X-band-EPR-Emxmicro spectrometer, Bruker) spectroscopy. The antioxidant enzymes (GSH, GPs1, and TAC) were evaluated by ELISA kits. The present study shows significant associations between the endogenic and exogenic non-infectious OS elevation due to the RONS up-regulation and the secondary OS generation associated with a lack of antioxidant protection in SPTB.

Keywords: inflammation, oxidative stress, birth, free radicals

INTRODUCTION

Spontaneous preterm birth (SPTB) is defined as a birth before <37 gestational weeks (GW), representing a significant contribution to perinatal morbidity and mortality in newborns [1-3]. Clinical studies confirmed that this group includes spontaneous births (mid-second trimester) and resembles miscarriages due to similarities with the main risk factors characteristic for SPTB: *increased uterus contractility, structural changes in the cervix, changes in the fetal membrane, decidual processes of the uterus and hormonal changes* [4]. SPTB onset results in a preterm infant with developmental complications, respiratory distress, pneumonia, bronchopulmonary dysplasia, neurological complications, arthritis, necrotizing enterocolitis, etc. [5-7]. The SPTB reasons are still not fully understood. The ascending bacterial infection of the amniotic membranes, amniotic fluid, placenta, umbilical cord, and the fetus is the main etiological cause of SPTB. Further, the fetus can independently modulate the exact moment of preterm/SPTB initiation, as a result of collapsed feto-maternal communication [7, 8]. Reduced local immunity in the vaginal cavity and cervical canal is thought to lead to intrauterine bacterial infection, an additional indicator of infection in the fetus, increasing fetal plaque, and a strong risk factor for spontaneous hemorrhage and SPTB activation [9]. SPTB can be considered as a „syndrome" due to multiple pathological processes, such as inflammatory cytokines overexpression in the chorion, amnion, and trophoblasts [10]; high mobility proteins modulation, enhanced placental inflammatory responses and SPTB activation [11]. The stable vaginal microbiota during pregnancy at term (TB) is replaced by altered estrogen levels, carbohydrate structures, and glycogen induction in the vaginal epithelium, i.e. possible factors causing vaginal injuries and acute intra-amniotic infection in spontaneous birth. The only proven mechanism in SPTB cases is induced fetoplacental inflammation associated with earlier gestational age, damage to gestational tissues and maternal circulation; an expression of the defense mechanism after cellular stress and activation of an intense immune response [2, 3, 12].

In contrast, multiple clinical studies associated "non-infectious" OS, endogenic and exogenic antioxidant disturbances, and accumulated reactive oxygen-nitrogen species (RONS) in the intrauterine space, plasma, and fetal aging as additional/ secondary promotors in SPTB activation. Specifically, OS-induced placental RONS (i.e., superoxide ($•O_2^-$), hydrogen peroxide (H_2O_2), hydroxyl ($•OH$), nitric oxide ($•NO$) radicals) cause a cascade of irreversible cellular dysfunctionality and premature cervical ripening [13, 14] by acute redox modifications. Tantengco *et al*., and Moore *et al*., [13, 14] comment on the OS/ RONS association in direct contribution to SPTB. More specifically, increased OS provokes modulation of proteins, lipids and DNA oxidation through the altered activity of ion channels in cell membranes. Additional SPTB prerequisite is RONS-

---

* To whom all correspondence should be sent:
E-mail: ykaramalakova@gmail.com

induced permanent structural damage to carbonylated proteins and activation of collagen degradation in the amniotic membrane [15]. The interrelationship between OS and increased uterine contractility was established in lysine/arginine/proline glycoxidation; C-reactive protein (CRP) elevation in combination with specific pro-inflammatory and immune proteins degradation [16], the typical SPTB complications. Retrospectively, locally induced OS has been predicted to stimulate changes in immune and acute-phase-inflammatory proteins, prostaglandins, and matrix metalloproteinases leading to increased uterine contractility, subsequent intra-amniotic infection, and SPTB [16, 17]. Simultaneously, early fetoplacental development initiated a cascade of "non-infectious" OS accompanied by increased lipid peroxidation (MDA) and RONS, intracellular protein dynamics, leptin up-regulations, and inability of the pregnant mother to respond to the decrease in enzymatic/ non-enzymatic antioxidants [2, 3, 18]. The endo- and exogenous antioxidants incapacity toward protected cellular response against increased OS and RONS [2, 3] leads to non-infectious cellular atrophy due solely to OS-induced senescence, which in turn causes sterile inflammation, generating an immunocompromised intrauterine environment and SPTB induction.

To better understand endogenic and exogenic non-infectious OS changes in SPTB, for the first time, we investigated the following RONS species: nitric oxide ($\cdot$NO), superoxide ($\cdot O_2^-$) radicals, 5-MSL disorders, ROS peroxidation and compared to antioxidant enzymes (GSH, GPs1, and TAC) in pregnant women from Southern Bulgaria, during 32–34^{+6} GW.

EXPERIMENTAL

The study was conducted in the period June 2019 - June 2022, on pregnant women from Southern Bulgaria; and approved by the Institutional Review Boards under all applicable state regulations at the Obstetrics and Gynecology Clinic, Stara Zagora. All 440 patients underwent a routine gynecological examination by the same medical specialist and provided written informed consent. *The exclusion criteria*: ruptured amniotic sac; systemic infection (respiratory, renal, and cardiovascular); nonsmokers; cesarean delivery; previous pregnancy; fetal anomaly; fetal mortality; organ transplant; chronic steroid use; multiple gestations; vaginal intercourse; congenital or chromosomal abnormalities; gestational/ pregestational diabetes; preeclampsia. *The inclusion criteria*: SPTB and TB women (18–42.5 maternal ages) were divided into two groups (Table 1).

Table 1. Obstetric and clinical characteristics of SPTB (n=220) and TB (n=220) participants. To define the difference between both groups the Student t-test was used. The results are presented as mean ± S.E. p < 0.05; b -values are means and c values are percentages; 1*NSVD, normal spontaneous vaginal delivery; **NA, not applicable.

Characteristics	SPTB (n=220) 32-34^{+6} g.w.	TB (n=220) 37-39^{+6} g.w.	p
Age (years)	31 ± 4.1	26.6 ± 5.8	0.042[a, b]
Gestational age, weeks	32.6± 4.11	38.3 ± 1.5	≤0.004 [a, b]
Body mass index (BMI), kg/m^2	19.6± 0.84	39.4 ±2.9	≤0.051[a, b]
Eclampsia/ pre-eclampsia	None	None	≤0.00
Infectious Diseases History	None	None	≤0.00
Parity	None	None	≤0.00
Gravidity	1	None	≤0.00
Abortion	None	None	-
previous SPTB	**NA	**NA	-
Family history of diabetes	0.00(0-5)	0.00(0-8)	-
Pelvic score	7-11 (7%)	9-13 (8%)	≤0.002 [a, c]
Bishop score (median)	12 (1–18)	-	≤0.00
Papiernik score (CRAP)	>10, 110 (75.2%)	-	≤0.0065[a,c]
*NSVD	220	220	0.99 [a,]
Cesarean section	0	0	

(I) SPTB (n = 220); 32–34^{+6} GW; entered with declared active birth with preserved amniotic sac integrity and gave birth within 24 hours. The fetus gestational week was calculated from the date of the last regular menstrual period (LMP) and was confirmed by a transabdominal ultrasound AFI examination (Aloka pro sound alpha 6–IPF-1503).

(II) TB (n = 220), singleton pregnancy at 37^{+1}-39^{+6} GW; meeting the above-described criteria; with birth in its active phase at the hospitalization and preserved the amniotic sac integrity; no inflammation registered.

Both groups received supplemental amounts of folic acid (≤300 mg/day), vitamins (D, B6) (≤350 mg/day), and magnesium (≤360 mg/day), during pregnancy.

Venous blood samples (10 mL/plasma) taken from *v. cubitalis* were collected during birth and examined up to 2 h, after 3500 rpm centrifugation at 4°C/15 min. All patients were with 7-13 Pelvic score; and underwent ultrasound fetal biometry (Aloka Prosound alpha 6-IPF-1503) to assess the expected newborn weight, the placenta location, and the amniotic fluid amount.

3-Nitrotyrosine peroxidation (3-NT, mM, at 450 nm/620 nm, 20 nM detection limit) [19]; glutathione (GSH; nmol/ml), glutathione peroxidase (GPx1; ng/ml); total antioxidant capacity (TAC, 0.004 mM detection limit) were assessed by commercially available assay kits (BioVision Inc., CA, USA) according to the manufacturer's instructions.

The albumin oxidation was evaluated using spin-conjugation with 10 mM 5-MSL dissolved in saline (pH=7.4). The mixture was added to 70 mL of plasma, centrifuged at 4000 rpm/10 min, at 4°C; by EPR characteristics: 3505 G centerfield, 6.42 MW power, 5 G amplitude, 1-5 scans [20].

ROS production was examined by a mixture of 900 μl phenyl N-tert-butylnitrone (PBN) (50 mM) in dimethyl sulfoxide (DMSO) to 100 mL plasma, centrifuged at 4000 rpm (10 min), at 4°C [21].

•NO radicals generation: The mixture of 50 μM carboxy-PTIO.K solution, 30 μl plasma, 50 mM Tris (pH 7.5) and DMSO at a ratio 9:1, was centrifuged at 4000 rpm, 10 min, 4°C. The spin adduct between carboxy-PTIO and the •NO radicals was measured, by [22, 23]. •O_2^-concentration: 30 μl plasma was activated by 30 μl (30 μM) 1-hydroxy-3-methoxycarbonyl-2,2,5,5-tetramethylpyrrolidine (CMH) (1:1) on an ice bath, after 5 min incubation [24, 25].

All RONS formation was read in EPR-Emxmicro spectrometer (Bruker) triplicate, in arbitrary units with characteristics: 3505 G centerfield, 6.42 MW power, 5 G amplitude, 1-5 scans.

Statistical analysis. The clinical data were analyzed using Statistica (Version 10.0 software, StaSoft, Inc., USA), and performed using one-way ANOVA. Student's t-test or Mann-Whitney–U test was used to compare the baseline characteristics between groups. EPR spectral processing was performed using Win-EPR and Sim-Fonia software after consecutive replicates. The p≤0.05 was considered statistically significant. The primary analysis was performed on GraphPad Prism 9 including log-odds (log2) data of the study components and comparison with

birth outcomes (SPTB *vs.* term birth). For the sensitivity of analyses two-tailed Student's t-test was used, and resulting p-values were adjusted by false discovery rates calculated using the Benjamini-Hochberg (BH) method with a threshold ≤ 0.1. Only a p-value ≤ 0.05 and absolute changes ≥ 1.5 were considered significant.

RESULTS AND DISCUSSION

Inflammation and OS are the primary and secondary pathophysiological initiators of changes in the gestational membrane structures and activation of myometrium contractions and cervical maturation, i.e. directly contribute to SPTB activation [2, 3, 16, 17]. The homeostatically - induced endogenous and exogenous OS and RONS activate redox-sensitive transcription factors that are responsible for "non-infectious" inflammation. Furthermore, behavioral risk factors increase RONS and OS, consuming the antioxidant enzymes. Induced "hidden" inflammation activates spontaneous birth [2, 3, 26, 27].

The obstetric and socio-clinical data are reported in Table 1. The average gestational age in SPTB was significantly lower vs. TB (p ≤ 0.004), and 100% of women in both groups delivered naturally. We observed statistically significant differences between BMI (p ≤ 0.005) and in the mean age of patients with premature uterine contractions ending in SPTB (p ≤0.042), for the two groups, respectively. We also found a significant association between SPTB and TB in all three measured factors, respectively (^{a}p < 0.002; ^{a}p < 0.002; ^{a}p < 0.005).

The peroxynitrite (ONOO$^-$)-mediated tyrosine nitration has pathological significance in OS monitoring. The one-electron 3-NT oxidation is supported by oxidants such as •OH, •NO, alkyl, carbonyl (•CO_3^-), lipid (LO•), peroxyl (LOO•) radicals and originates in two ways: 1) by ONOO$^-$ generation; and 2) by heme peroxidases, catalyzed processes and activities of myoglobin, hemoglobin, catalase, copper/zinc superoxide dismutase. Placental •NO and •O_2 result in increased ONOO$^-$ formation due to reduced antioxidant activation [28, 29]. A higher 3-NT (Figure 1a) concentration was observed in the SPTB group (40.89 ± 30.22 nM *vs.* 61.4 ± 44.7 nM; p < 0.02, t-test; p≤ 0.0021).

The registered 3-NT-dependent OS was almost two-fould in the SPTB group with a positive correlation registered to •NO radicals. Increased protein nitrosation and the endogenous antioxidants inability to process generated •NO and ONOO$^-$ and to balance amino acid changes in the fetoplacental system in SPTB, is consistent with other studies [27, 30].

5-MSL conjugates (Patent: BG/U/2022/5487) readily to maternal plasma *via* its conjugation to weakened SH-albumin sites and has been used to assess oxidatively induced conformational changes in amyloid albumin aggregates leading to structural disruption [20] and likely SPTB induction. The 5-MSL albumin expression (Figure 1b), was statistically significantly 2.3-fold lower in the SPTB, compared to TB groups (3.97 ± 0.037 a.u. *vs.* 1.11 ± 0.027 a.u.; p < 0.003, t-test; p≤ 0.0001). Plasma albumin as transporter scavenging OS and RONS, promoted spontaneous birth [31, 32]. We observed a

three-fold decrease in albumin (>67%) and SH- disrupted albumin sites, e.g., peroxyl RS• / RSOO• overproduction, additional initiators of lipid peroxidation, and characteristic hypoalbuminemia, in SPTB women. In agreement with our results, a significant association was observed between reduced albumins during OS induction [33].
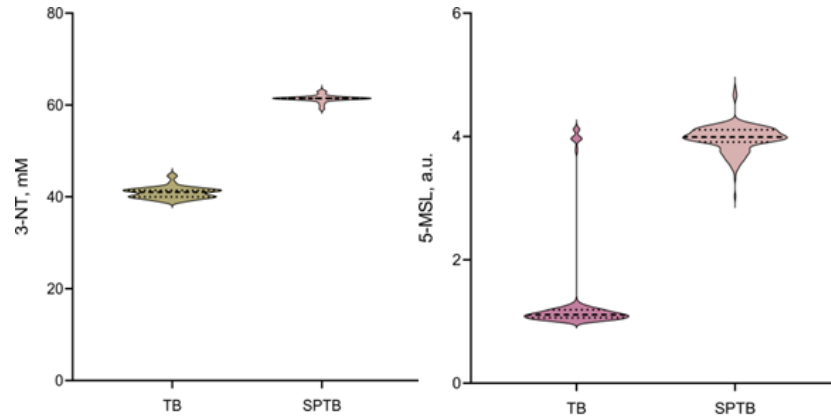
Figure 1. Violin plots of plasma 3-NT (a) and 5-MSL-conjugated albumin levels (b) as a modified protein peroxidation marker followed in patients with SPTB and TB. All data are presented as MFI. To define difference per groups the log2 and two-sided Student t-tests were used; a p-value ≤ 0.05 and changes ≥ 1.5 were considered significant.
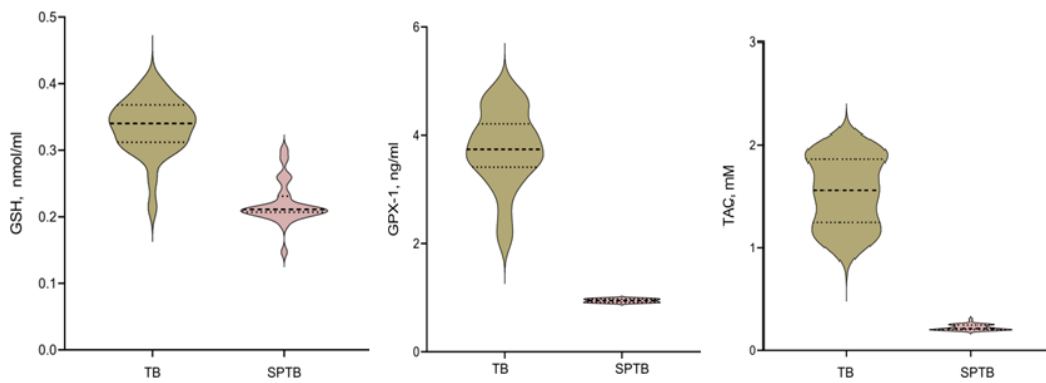
Figure 2. Violin plots of plasma antioxidant enzymes GSH (a), GPx1 (b), TAC (c), in SPTB and TB. To define which groups are different from each other the log2 and two-sided Student t-tests were used; a p-value ≤ 0.05 and changes ≥ 1.5 were considered significant.
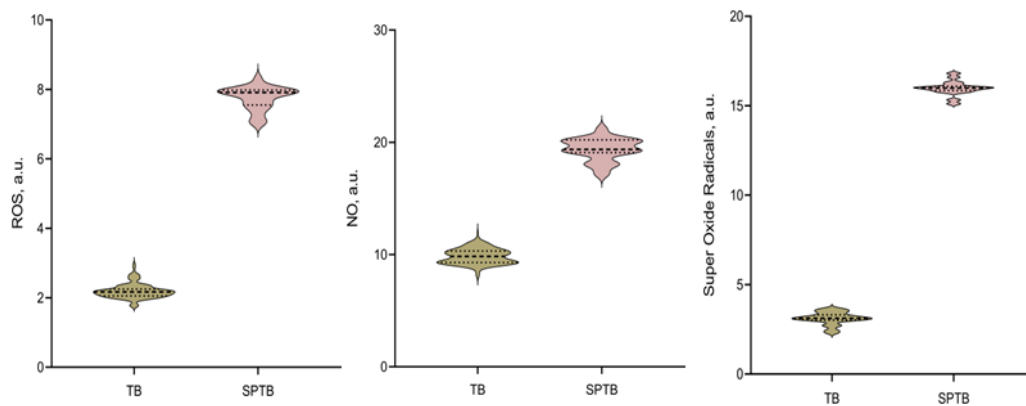
Figure 3. Violin plots of plasma ROS (a), •NO (b) and •O$_2^-$(c) concentrations in SPTB vs TB. To define which groups are different from each other the log2 and two-sided Student t-tests were used; a p-value ≤ 0.05 and changes ≥ 1.5 were considered significant.

Maternal OS competitively consumes endo-exogenous antioxidants, through RONS expression, altering placental and intrauterine redox status, and contributes to SPTB induction [2, 3]. The RONS-mediated collagen damage in the maternal gestational tissue increases uterine centrality and rupture of the chorio-amnionitis sac, which is a sure SPTB sign [34]. Plasmatic GSH (0.219±0.007 nmol/ml *vs*. 0.335±0.02 nmol/ml, p<0.003, t-test; p≤0.145), GPx1(0.94±0.07 ng/ml *vs*. 3.74±0.01 ng/ml, p<0.02, t-test; p≤ 0.0411) and TAC (0.227±0.07 mM *vs*. 1.54±0.06 mM, p<0.05, t-test; p≤ 0.0297) showed statistically significant decreased SPTB, 1.7-fold, 2.9-fold, 4.2-fold, respectively (Figure 2a, 2b, 2c). We further hypothesized that RONS activated lipid peroxidation, altered cellular function through tyrosine and glutathione nitration, in the SPTB cases. GPx1 promotes ROS detoxification of labile lipid hydroperoxides and utilizes reduced non-enzymatic GSH [2, 3, 34]. In two consecutive studies, GSH and GPx1 decreased expression in maternal blood was reported in the delivery of preterm infants (>37 GW), a likely consequence of increased OS. This is consistent with our study, where maternal GPx1 concentrations were dramatically decreased in SPTB, i.e. cellular redox-buffering antioxidant GSH may be associated with SPTB. Interestingly, sharp decreases in the non-enzymatic antioxidants are directly related to OS, reduced gestational weeks, and likely contribute to SPTB pathogenesis [35, 36]. Dysregulation in the endogenic-exogenic maternal antioxidants leads to intracellular TAC decrease [37] in SPTB.

With respect to OS mediation as a possible SPTB factor, the local formation of ROS, •NO and •O_2^- was monitored. The plasmatic ROS production was almost three-fold, statistically significantly increased in SPTB (7.75±0.2 *vs*. 2.19±0.4, p<0.001, t-test; p≤ 0.0001) *vs*. TB. Also, an endogenous metabolic 2.1-fold increase in plasmatic •NO, (19.34±3.51 *vs*. 9.83±2.11, p< 0.003, t-test; p≤ 0.0001); and a 3.9-fold increase in •O_2^- maternal circulation (15.9±2.49 *vs*. 3.11±0.41, p< 0.003, t-test; p≤ 0.0002) was recorded in SPTB *vs*. TB (Figure 3a, 3b, 3c). The 2.89-fold increase in ROS production found in late SPTB cases vs. TB is consistent with other studies [2, 3, 18, 19]. Notably, lipid peroxidation predominance plays a known role in cervical ripening <34 GW and the OS-directed immune response in spontaneous labor [38]. OS-induced late inflammation can be explained, at least in part, by the significant increase in the amplitudes of •NO and •O_2^- radicals and compared to their circulation in cellular endogenous enzymes and TAC, <34 GW. In addition, maternal antioxidants were unable to normalize metabolic changes and deactivate H_2O_2, i.e., OS enhances the non-immune response and SPTB activation. Specifically, dysregulated plasmatic •NO/ •O_2^- suggests the generation of additional OS in the uterine tissue and cervix associated with oxygen species and nitric oxide synthase (NOS) and spontaneous early/late preterm birth [3, 38, 39]. In addition, the inability of GSH, GRx1 and GSH-reductases to donate free –SH/thiols to detoxify •NO/•O_2^- into protein, lipid and amino acid catabolites leads to local placental OS [3, 38-40].

CONCLUSIONS

The present study has several advantages: First, the investigations contribute to building upon the assumption that OS is the causal pathway to spontaneous preterm birth, in pregnant women. Second, the significant RONS elevation increased proteins and glycation products by decreasing the specific endo/exogenous enzymes and TAC in the SPTB group. Third, plasma RONS accumulations disclose additional OS mechanisms in uterine tissue and cervix associated with increased lipid peroxidation, hypoalbuminemia, and NOS dysregulation elevating the SPTB chances. Fourth, the SPTB and TB group in the study were from the same population, and their baseline characteristics were basically similar, probably mediating spontaneous birth progression, at 32–34^{+6} GW. Fifth, importantly, this research considering OS as the important SPTB causes is conducted for the first time on Bulgarian women.

PATENTS

The patent resulting from the work reported in this manuscript is with the incoming number of the patent application: BG/U/2022/5487

REFERENCES

1. A. V. Glover, T. A. Manuck, *Semin Fe.t Neonat. Med*., **23** (2), 126 (2018).
2. R. Menon, *Acta Obstet. Gynecol. Scand*., **87** (6), 590 (2008).
3. R. Menon, *O.G.S.*, **62** (4), 199 (2019).
4. M. S. Vidal, R. C. V. Lintao, M. E. L Severino, O. A. G Tantengco, R. Menon, *Front. Endocrinol.,* **13**, https://doi.org/10.3389/fendo.2022.1015622 (2022).
5. A. G. Paquette, J. MacDonald, T. Bammler, D. B. Day, C. T. Loftus, E. Buth, S. Sathyanarayana, *A.J.O.G.*, https://doi.org/10.1016/j.ajog.2022.07.015 (2022).
6. X. Chen, X. Zhang, W. Li, W. Li, Y. Wang, S. Zhang, C. Zhu, *Front. Neurol.*, **12**, https://doi.org/10.3389/fneur.2021.649749 (2021).
7. M. Panayotova, M. Muhtarov, P. Dragomirova, V. Bangyozov, V. Boeva-Bangyozova, *Gen. Med.*, **20** (3), 47 (2018).
8. G. K. Cunha, L.B. Bastos, S.F. Freitas, R. Cavalli, S.M. Quintana, *A.J.O.G.,* **129** (2), 273 (2021).
9. S. Huang, J. Tian, C. Liu, Y. Long, D. Cao, L. Wei, Z. Mo, *BMC Pregn Childb.*, **20** (1), 1 (2020).
10. D. S. Yoon, Y. H. Kim, C. H. Kim, M. K. Cho, J. W. Kim, H. Y. Cho, S. M. Kim, W. D. Kang, K. H. Lee, T. B. Song, *OGS.*, **54** (1), 26 (2011).
11. K. Shirasuna, K. Seno, A. Ohtsu, S. Shiratsuki, A. Ohkuchi, H. Suzuki, T. Kuwayama, *Am. J. Reprod. Immunol.,* **75** (5), 557 (2016).

12. K. Hočevar, A. Maver, M. Vidmar Šimic, A. Hodžić, A. Haslberger, T. Premru Seršen, B. Peterlin, *Front. Medic.*, **6**, 201 (2019).

13. O. A. Tantengco, J. Vink, P. M. Medina, R. Menon, *Biol. Reprod.,* doi.org/10.1016/j.mehy.2020.110336 (2021).

14. T. A. Moore, I. M. Ahmad, M. C. Zimmerman, *C.*, **20** (5), 497 (2018).

15. J.S. Cuffe, Z.C. Xu, A.V. Perkins, *Biomark. Med*., **11** (3), 295-306 (2017).

16. S.A. Kim, K.H. Park, S.M. Lee, Y.M. Kim, S. Hong, *Am. J. Perinatol.*, DOI: 10.1055/s-0040-1718575 (2020).

17. A. Cooley, S. Madhukara, E. Stroebele, M.C. Caraballo, L. Wang, G. Hon, M. Mahendroo, *Bio. Rxiv.*, https://doi.org/10.1101/2022.07.26. 501609 (2022).

18. O. A. G. Tantengco, R. Menon, *Front. Glob. Women's Health.,* **2**, (2022).

19. L.F. Martin, N.P. Moço, M.D. de Lima, J. Polettini, H.A. Miot, C.R. Corrêa, R. Menon, M.G. da Silva, *BMC Pregn. Childb.*, **17** (1), 1 (2017).

20. K. Takeshita, K. Saito, J.I. Ueda, K. Anzai, T. Ozawa, *Biochim. Et Biophys. Acta (BBA)-Gen. Subj.,* **1573**, 156 (2002).

21. H. Shi, Y. Sui, X. Wang, Y. Luo, L. Ji,*Comp. Biochem. and Physio.l Part C: Toxicol & Pharmacol.,* **140** (1), 115 (2005).

22. T. Yoshioka, N. Iwamoto, K. Ito, *J. Am. Soc. Nephr.,* **7** (6), 961 (1996).

23. K. Yokoyama, K. Hashiba, H. Wakabayashi, K. Hashimoto, K. Satoh, T. Kurihara, N. Motohashi, H. Sakagami, *Antican. Res.*, **24** (6), 3917 (2004).

24. J. F. Gielis, G. A. Boulet, J. J. Briedé, T. Horemans, T. Debergh, M. Kussé, P. E. Van Schil, *Eur. J. Cardioth. Surg.*, **48** (4), 622 (2015).

25. D. Mannaerts, E. Faes, J. Gielis, E. Van Craenenbroeck, P. Cos, M. Spaanderman, Y. Jacquemyn, *BMC Pregn. Childb.*, **18** (1), 1 (2018).

26. J. Pan, X. Tian, H. Huang, N. Zhong, *Front Physiol*., **21** (11), 800 (2020).

27. S. M. Eick, S. D. Geiger, A. Alshawabkeh, M. Aung, E. Barrett, N. R. Bush, J. F. Cordero, K. K. Ferguson, J. D. Meeker, G. L. Milne, R. H. Nguyen, *Sci. Total Environ.*, **835**, 155596 (2022).

28. M. Jiang, X. M. Zhao, Z. S. Jiang, G. X. Wang, D. W. Zhang, *Anal. Chim. Acta.,* **529**, 34 (2022).

29. J. He, E. R. Becares, P. W. Thulstrup, L. F. Gamon, J. N. Pedersen, D. Otzen, P. Gourdon, M. J. Davies, P. Hägglund, *Redox. Biol.,* **36** (2020).

30. D. Weber, W. Stuetz, W. Bernhard, A. Franz, M. Raith, T. Grune, N. Breusing, *Europ. J Clin. Nutr*., **68**, 215–222 (2014).

31. J. Malik, S. Ahmad, H. Aziz, N. Roohi, M.A. Iqbal, *Curr. Proteom.*, **19** (3), 274 (2022).

32. Q. Ying, X.Q. You, F. Luo, J.M. Wang, *Front Pediatr.,* **9** (2021).

33. M. Saleh, M. Compagno, S. Pihl, H. Strevens, B. Persson, J. Wetterö, B. Nilsson, C. Sjöwall, *J. Clin. Med.,* **11** (2022).

34. M. A. Kim, E. J. Lee, W. Yang, H. Y. Shin, Y. H. Kim, J. H. Kim, *Sci. Rep.,* **12** (1), 1 (2022).

35. L. Cannavò, S. Perrone, V. Viola, L. Marseglia, G. Di Rosa, E. Gitto, *Int. J Mol. Sci.,* **22**, 12504 (2021).

36. A. Arslan, K. Uckan, K. Turan, H. Demir, C. Demir, *Birth*, **11**, 12,

37. C. Abiaka, L. Machado, *Sultan Qaboos Univ. Med. J.*, **12**, 300 (2012).

38. E. H. Joo, Y. R. Kim, N. Kim, J. E. Jung, S. H. Han, H. Y. Cho, *Int. J. Mol. Sci.,* **22**, 18 (2021).

39. L. Cannavò, S. Perrone, V. Viola, L. Marseglia, G. Di Rosa, E. Gitto, *Int. J. Mol. Sci.,* **22**, 12504 (2021).

40. M. Phillippe, *AJ.O.G.,* **227** (2), 148 (2022).

Maternal oxidative imbalance in symptomatic SARS-COV-2 during pregnancy

R. J. Al-Dahwi[1], D. Kostadinova[1], M. Angelova[1], E. D. Georgieva[2], K. Petkova-Parlapanska[2], G. D. Nikolova[2], Y. D. Karamalakova[2*]

[1]*Obstetrics and Gynaecology Clinic, UMHAT "Prof. St. Kirkovich" 6000, Stara Zagora, Bulgaria*
[2]*Department of Chemistry and Biochemistry, Medical Faculty, Trakia University, 11 Armeiska Str., 6000 Stara Zagora, Bulgaria*

The coronavirus infection (Covid-19) leads to overactive immune responses, resulting in oxidative stress (OS), excessive reactive oxygen/ nitrogen (ROS/RNS) production, reduced antioxidant enzymes, and disrupted total redox balance. Pregnant women are more susceptible to respiratory pathogens, i.e. to Covid-19. The aim of the study was to investigate the effects of symptomatic Covid-19 during pregnancy on oxidative/antioxidant status in blood during pregnancy and the consequences for the mother. The patients were divided: 1) Controls (n = 100); singleton pregnancy, without Covid-19; and 2) Covid-19 group (n = 65), singleton pregnancy, with symptomatic Covid-19 (>30 gestational weeks). Serum superoxide dismutase ($p < 0.01$), catalase ($p < 0.01$), protein carbonylation ($p < 0.001$), ROS production ($p < 0.01$) and albumin oxidation ($p < 0.05$) were increased in symptomatic Covid-19 pregnancies *vs*. controls. The increased maternal OS/ redox imbalance in pregnant mothers with symptomatic Covid-19 could be associated with preterm labour.

Keywords: symptomatic CoV-19 pregnancies, health pregnancies, OS, ROS/RNS

INTRODUCTION

The acute respiratory syndrome coronavirus 2 (SARS-CoV-2) is the cause of coronavirus disease 2019 (Covid-19). Advanced age, increased body mass index (BMI), type 2 diabetes (T2D), hypertension, and ineffective immune responses are significant risk factors that contribute to SARS-CoV-2 cytokine hyper-inflammation [1, 2]. SARS-CoV-2 infection leads to overactive immune responses, resulting in oxidative stress (OS), excessive production of reactive oxygen/nitrogen species (ROS/RNS), reduced antioxidant enzymes, and disrupted total redox balance [2, 3]. OS damages tissues and blood components through oxidation of nucleic acids, proteins, and lipids, mainly macromolecules involved in the SARS-CoV-2 pathogenesis [2, 4]. Viral infections alter the cellular structures and function through lipid peroxidation, resulting in increased ROS/RNS production and acute metabolic dysfunction [2, 5, 6].

Pregnant women are more susceptible to respiratory pathogens and severe pneumonia [7]. This is due to the physiological changes in the respiratory system during pregnancy and increased oxygen consumption. Physiological diaphragm elevation leads to restrictions in the lung expansion, hormonal inducement of edema of upper respiratory tract mucosa. As the pregnancy progresses, other changes like closure of small airways and sub-

sequent reduction of functional residual capacity (FRC) and expiratory reserve volume (ERV). This makes pregnant women more sensitive to hypoxia and generally more susceptible to respiratory pathogens [8, 9]. Pregnancy is associated with changes in the functioning of the immune system. All these facts increase the risk of Covid-19 [8, 9]. Pro-inflammatory cytokines release is inhibited by hormonal cues in pregnancy, mainly due to high progesterone level. A Th2-polarization phenomenon allows for the suppression of dominant cell-mediated pro-inflammatory Th1 immunity in favour of a physiological shift to humoral Th2-dominant immunity. As a result, there is an increase in the intercellular susceptibility to infection weather viruses, bacteria and parasites and this can explain why pregnant women are more vulnerable to viral infection in comparison to non-pregnant women. Pregnant women with pneumonia are at high risk for miscarriage, preterm delivery, premature rupture of membranes, preeclampsia (PE), foetal distress, low birth weight (<2500 g), small-for-gestational-age (SGA) and neonates with low Apgar score [8, 9]. However, increased systemic inflammatory response, hyper-coagulation, decreased arterial oxygen saturation, and increased OS are considered risk factors directly related to poor obstetric outcomes [8, 9]. Despite the importance of OS for the proper macromolecule metabolism and for foetal development, there are only a few studies on the role

---

* To whom all correspondence should be sent:
E-mail: *yanka.karamalakova@trakia.uni-bg*

of OS changes in symptomatic Covid-19 in pregnant women, leading to preterm labour [10, 11].

According to the above, the aim of the present study was to investigate the effects of CoV-19 during pregnancy on the oxidative/antioxidant status and to clarify the crucial role of both factors during pregnancy and their consequences for the mother and foetus.

EXPERIMENTAL

The 165 pregnant women were examined after admission to the Obstetrics and Gynaecology Clinic, Stara Zagora, Bulgaria, between June 2021- October 2023. The inclusion criteria were: pregnant patients without previous chronic pathologies, singleton pregnancy; body mass index 18–30 kg/m^2; experienced symptomatic Covid-19 infection with (PCR (+)) test, from the >30th gestational week onwards and the control group with Covid-19 and PCR (−) test, again with singleton and body mass index 18–30 kg/m^2. Exclusion criteria were: chronic disease with long-term treatment; previous infectious diseases; body mass index <18 or >30 kg/m^2; malnutrition; previous foetal demise. All symptomatic Covid-19 pregnant patients enrolled in the study reported severe symptoms (cough (31%), fever ≥ 38.5 °C (50.6 %); respiratory rate ≥ 20 (9%); heart rate ≥ 100 bpm (13%); oxygen saturation SpO_2 less than 92% (7%)) requiring hospital stay and antiviral therapy with Ritonavir and Lopinavir.

The study included: 1) Controls (n = 100); singleton pregnant women, who have not suffered from Covid-19 and gave birth at term; 2) Covid-19 group (n = 65), singleton pregnant women who suffered from symptomatic Covid-19 during pregnancy (>30 gestational weeks). The study was approved by the Ethics Committee of the University Multidisciplinary Hospital for Active Treatment "St. Kirkovich" (referenced 10/816 -12 Oct. 2019). Serum samples (5 mL) taken from *v. cubitalis* were collected during birth and examined up to 2 h, after 3500 rpm centrifugation at 4°C, 15 min.

Serum superoxide dismutase (SOD) and catalase (CAT) activities were assayed according to the spectrophotometric methods described earlier [12, 13], at 550 nm and at 240 nm. Protein carbonylation (PCC; nmol/mg) was evaluated by an immune-enzyme method using commercially available ELISA kits (126287/BioVision Inc., USA). ROS production was examined by a mixture of 900μl phenyl N-test-butyl nitrone (PBN) (50 mM) in dimethyl sulfoxide (DMSO) to 100 mL plasma, centrifuged at 4000 rpm (10 min), at 4°C [14].

The albumin oxidation was evaluated using spin-conjugation with 10 mM 5-MSL dissolved in saline (pH=7.4). The mixture was added to 70 mL serum, and centrifuged at 4000 rpm/10 min, at 4°C [15]. The ROS formation and albumin oxidation were read in EPR-Emxmicro spectrometer (Bruker) in triplicate, in arbitrary units with characteristics: 3505 G centerfield, 6.42 MW power, 5 G amplitude, 1-5 scans.

Statistical Analysis

The clinical data were analysed using Statistica (Version 10.0 software, StaSoft, Inc., USA), and performed using one-way ANOVA. Student's t-test and Mann–Whitney U test were used to compare the baseline characteristics between groups. EPR spectral processing was performed using Win-EPR and Simfonia software after consecutive replicates and p≤0.05 was considered statistically significant. The primary analysis was performed on GraphPad Prism 9 including log-odds (log2) data of the study components and comparison with birth outcomes. Only a p-value ≤ 0.05 and absolute changes ≥ 1.5 were considered significant.

RESULTS AND DISCUSSION

SARS-CoV-2 infection causes OS disorder and metabolic dysfunctions during pregnancy, which is followed by changes in the condition and development of the fetus. Respiratory infections, including Covid-19, are associated with increased ROS/RNS production, increased antioxidant consumption, and a long-term impaired immune response [7, 8, 16]. Physiologically, Delgado-Roche and Mesta [16] comment that long-term accompanied OS plays a critical role in Covid-19 viral infection. The clinically measured haematological and biochemical characteristics of the symptomatic SARS-CoV-2 pregnant mothers *versus* controls are shown in Table 1.

No statistically significant differences were observed between both groups in age, weight, BMI, parity, and delivery. Statistically, significant changes were found in serum Fe (p < 0.01), ferritin (p < 0.001), and CRP (p < 0.001) concentrations with lower/higher values in the Covid-19 mothers compared to controls. It should be emphasized that the serum samples were collected from groups with no statistical differences between vaginal delivery and Caesarean section. Therefore, differences from endogenous OS due to birth outcome are minimized [8].

The antioxidant SOD and CAT activities showed a decrease in serum capacity in mothers suffering of Covid-19 compared to controls; 1.5-fold (p < 0.01) and 1.7-fold (p < 0.01), respectively (Table 2).

Table 1. Obstetric and clinical characteristics of healthy controls ($n = 100$) and pregnant mothers suffering from symptomatic CoV-19 ($n = 65$). Significantly different *vs.* controls, *p < 0.01, Student t-test; *p < 0.001, Student t-test.

Obstetric and clinical characteristics	Controls (n=100)	Symptomatic CoV-19 (n=65)
Age (years)	31.22 ± 1.4	29.91 ± 1.88
Body mass index (BMI), kg/m^2	28.6 ± 0.84	27.4 ± 2.91
Infectious diseases	None	None
Vaginal delivery (%)	50.2	60.7
Cesarean delivery (%)	50.1	49.9
Hemoglobin (g/L)	12.98 ± 0.51	12.21 ± 0.6
Hematocrit (%)	36.2 ± 0.77	32.11± 0.07*
Serum Fe (µg/dL)	96.13 ± 11.35	62.33 ± 10.11 *
Ferritin (ng/mL)	273 ± 11.54	1307 ± 451.5 **
CRP (mg/dL)	4.34 ± 0.12	183 ± 13.55 **

Table 2. Antioxidant and oxidative parameters in serum of healthy controls ($n = 100$) and pregnant mothers suffering from symptomatic CoV-19 ($n = 65$). Significantly different *vs.* controls, *p < 0.01, Student t-test; *p < 0.001, Student t-test. The primary analysis was performed on log-odds (log2) data of the study components and birth outcomes.

Antioxidant / Oxidative parameters	Controls (100)	Symptomatic CoV-19 (n=65)	log2 Analysis
SOD (mU/mg)	5.73 ± 0.91	2.91 ± 0.37 *	≥ 1.6 fold
CAT (mU/mg)	81.01 ± 6.12	54.86 ± 3.966*	≥ 1.5 fold
Protein carbonyl groups (nmol/mg)	6,711 ± 0.22	14.53 ± 0.54**	≥ 2.1 fold
ROS production (arb. units)	2.371 ± 0.51	8.14 ± 0.81**	≥ 3.2 fold
5-MSL (-SH/ albumin changes) (arb. units)	4.27 ± 0.012	1.033 ± 0.05**	≥ 3.1 fold

As a result of Covid-19 viral infection, an interplay between mitochondrial ROS/RNS and endothelial damage leads to vasoconstriction, OS-enhanced inflammation, and redox imbalance [17].

Placental ROS coupled with OS directly damage macromolecules, inhibit their versatility and compromise cellular antioxidant defences. This exacerbates OS values and OS impairments. Therefore, in the blood of pregnant females with symptomatic Covid-19, oxygen desaturation and improper placental perfusion will activate a redox imbalance [16, 18-19]. Different studies have reported increased OS and gestational disorders such as intrauterine growth retardation, gestational diabetes, maternal obesity, and preeclampsia [20, 21]. Mandò et al., [21] hypothesized that increased inflammation and OS in the Covid-19-altered intrauterine environment may alter antioxidant dynamics, depending on the severity of Covid-19. In addition, SARS-CoV-2 provokes enzymatic and redox imbalance even in non-pregnant patients [21].

Berktas et al., [9] comment that lipid peroxides from the placenta are secreted into the maternal blood circulation. Placental antioxidant defence systems (SOD, CAT, GST, and glutathione reductase (GR)) maintain lipid peroxide levels in normal pregnancy, while in symptomatic CoV-19 pregnancy, ROS production increases [9, 21]. ROS production in blood serum is shown in Table 2. The results show that the ROS production/ residual lipid peroxidation concentration increased almost 3.1-fold (p < 0.001) in the pregnant woman with symptomatic Covid-19, compared to controls.

Blood serum and placenta are extremely susceptible to OS, especially when SOD and CAT metabolism is impaired. As a result, if the unique immunological response of the pregnant woman with SARS-CoV-2 does not minimize the ROS generation and lipid peroxides, this may lead to improper implantation and restriction of embryo growth especially when the infection occurs during the first trimester [21, 22].

Solis-Paredes et al., [23] commented that oxidation of structural proteins in pregnant women who developed severe Covid-19 occurs in red blood cells and activates coagulopathic and thromboembolic events, due to increased ROS production. Pregnant women with severe Covid-19 had a 2.1-fold (52%) increase in the levels of carbonylated proteins (p < 0.001, Table 2). In this regard, a statistically significant increase in protein oxidative damage and ROS production in SARS-CoV-2 pregnant women has been reported in other studies [23, 24].

Blood albumin is a negative acute-phase reactant, multifunctional transporter of scavenged ROS, and promoted vascular permeability in normal labour [25]; used as a biomarker with significant prognostic value in severe Covid-19 infection during pregnancy. We used 5-MSL and by conjugating it to the weakened SH-albumin regions we used it to assess the conformational changes (*Patent:*

BG/U/2022/5487) occurring upon oxidation in amyloid albumin aggregates [26]. We observed a 3.1-fold decrease in albumin, i.e. > 69% SH-disrupted sites, and RS•/ RSOO• overproduction, additional initiators of lipid peroxidation, and characteristic hypoalbuminemia in Covid-19 pregnant women. In agreement with our results, a significant association was observed between OS-decreased albumins during severe Covid-19 infection [25] during pregnancy.

CONCLUSIONS

In the present study, we reported for the first time that maternal OS imbalance could be associated with preterm labour, in Bulgarian population. In this report, maternal OS imbalance was significantly elevated in pregnant mothers with symptomatic Covid-19 compared to control group. To our knowledge, this is the first evidence of the OS biomarkers expression in symptomatic Covid-19 pregnancy in the Bulgarian population.

PATENTS

The patents resulting from the work reported in this manuscript are with the incoming number of the patent application: BG/U/2022/5487

REFERENCES

1. X. Li, S. Xu, M. Yu, K. Wang, Y. Tao, Y. Zhou, J. Shi, M. Zhou, B. Wu, Z. Yang, C. Zhang, *J. Clin. Immunol.*, **146**, 1, 110 (2020).
2. A. Avila-Nava, A. Geovanny Pech-Aguilar, R. Lugo, I. Medina-Vera, M. Guevara-Cruz, A. L.Gutiérrez-Solis, *Oxid Med Cell Long.*, **2022**, ID 1058813 (2022).
3. G. E. Forcados, A. Muhammad, O. O. Oladipo, S. Makama, C. A. Meseko, *Front. Cell. Infect. Microbiol.*, **11**, 654813 (2021).
4. R. Cecchini, A. L. Cecchini, *Med. Hypot.*, **143**, 110102 (2020).
5. M. A. Beck, J. Handy, and O. A. Levander, *Annals New York Acad. Sci.*, **917**(1), 906 (2000).
6. N. Žarković, B. Orehovec, L. Milković, B. Baršić, F. Tatzber, W. Wonisch, M. Tarle, M. Kmet, A. Mataić, A. Jakovčević, T. Vuković, *Antiox.*, **10** (9),1341 (2021).
7. M. Behram, S. C.Oğlak, Y. Başkıran, S. S. Çaypınar, S. Akgöl, Ş. Tunç, Z. G. Özköse, E. Akay, I. Dağ, *Ginekol. Pol.,* **92** (9), 631 (2021).
8. J. Moreno-Fernandez, J. J. Ochoa, C. De Paco Matallana, A. Caño, E. Martín-Alvarez, J. Sanchez-Romero, J. M. Toledano, M. Puche-Juarez, S. Prados, S. Ruiz-Duran, L. Diaz-Meca, *Antiox.*, **11** (2), 184 (2022).
9. O. A. Berktas, S. O. Tutar, E. G. G. Peker, C. Kaya, *Aeg. J. Obst. Gynecol.*, **4** (2), 26 (2022).
10. M. Mirbeyk, A. Saghazadeh, N. A. Rezaei, *Arch. Gynecol. Obstet.*, **304**, 5 (2021).
11. G. Capobianco, L. Saderi, S. Aliberti, M. Mondoni, A. Piana, F. Dessole, M. Dessole, P. L. Cherchi, S. Dessole, G. Sotgiu, *Eur. J. Obstet. Gynecol. Reprod. Biol.*, **252**, 543 (2020).
12. J. D. Crapo, J.M. McCord, I. Fridovich, *Meth. Enzymol.*, **53**, 382 (1978).
13. H. Aebi, *Meth Enzymol.*, **105**, 121 (1984).
14. H. Shi, Y. Sui, X. Wang, Y. Luo, L. Ji, *Comp. Biochem. Physiol. Part C: Toxicol. & Pharmacol.*, **140** (1), 115 (2005).
15. K. Takeshita, K. Saito, J.I. Ueda, K. Anzai, T. Ozawa, *Biochim. Et. Biophys. Acta (BBA)-Gen. Subj.*, **1573**, 156 (2002).
16. L. Delgado-Roche, F. Mesta, *Arch. Med. Res.,* **51**, 384 (2020).
17. O. Holland, M. Dekker Nitert, L. A. Gallo, M. Vejzovic, J. J. Fisher, A. V. Perkins, *Placenta*, **54**, 2 (2017).
18. H. C. Lee, Y. H. Wei, *Int. J. Biochem. Cell Biol.* **37**, 822 (2005).
19. L. Loffredo, F. Violi, *Int. J. Cardiol.*, **312**, 136 (2020).
20. M. Zambon, C. Mandò, A. Lissoni, G. M. Anelli, C. Novielli, M. Cardellicchio, R. Leone, M. N. Monari, M. Massari, I. Cetin, S. Abati, *Reprod. Sci.*, **25**, 1474 (2018).
21. C. Mandò, V. M. Savasi, G. M. Anelli, S. Corti, A. Serati, F. Lisso, C. Tasca, C. Novielli, I. Cetin, *Antiox.*, **24**(10),1517 (2021).
22. K. Toboła-Wróbel, M. Pietryga, P. Dydowicz, M. Napierała, J. Brązert, E. Florek, *Oxidative Med. Cell. Longev,.* **2020**, 6398520 (2020).
23. J. M. Solis-Paredes, A. Montoya-Estrada, A. Cruz-Rico, E. Reyes-Muñoz, J. Perez-Duran, S. Espino y Sosa, V. R. Garcia-Salgado, R. Sevilla-Montoya, R. J. Martinez-Portilla, G. Estrada-Gutierrez, J. A. Gomez-Ruiz, *Viruses*, **14** (4), 723 (2022).
24. S. Espino-Y-Sosa, R. J. Martinez-Portilla, J. Torres-Torres, J. M. Solis-Paredes, G. Estrada-Gutierrez, J. A. Hernandez-Pacheco, A. Espejel-Nuñez, P. Mateu-Rogell, A. Juarez-Reyes, F. E. Lopez-Ceh, *Viruses*, **13,** 1906 (2021).
25. T. Okamoto, K. Watanabe, T. Banno, T. Saitou, K. Sugiura, A. Iwasaki, A.Wakatsuki, *PIH*, (2022) https://doi.org/10.1016/j.preghy.2022.05.009
26. E. Georgieva, Y. Karamalakova, G. Arabadzhiev, V. Atanasov, R. Kostandieva, M. Mitev, V. Tsoneva, Y. Yovchev, G. Nikolova, *Antioxidants*, **11** (12), 2311 (2022).

Measurement of oxidative stress-related markers in gastro-intestinal damages in Bulgarian pediatric patients

M. Panayotova[1]*, M. Penkova[2]

[1]*Pediatrics Department, Medical Faculty, Trakia University, 11 Armeiska Str., 6000 Stara Zagora, Bulgaria*
[2]*Gastroenterology Department, Medical Faculty, Trakia University, 11 Armeiska Str., 6000, Stara Zagora, Bulgaria*

Cow's milk allergy (CMA), affects ~2 - 7.5% of the infants, and results in an immunological response to casein and α-/β-lactalbumins such as: skin rashes, respiratory and gastrointestinal disturbances. Inflammatory bowel disease (IBD), affecting adolescents, is sustained by an impaired immune/ inflammatory response against intestinal microorganisms. Reactive oxygen/nitrogen (ROS/RNS) overproduction in the gastrointestinal tract damages the mucosa in CMA and IBD. The aim of the present study was to determine ROS/RNS and oxidative disturbances in the intestinal mucosa influence in CMA and IBD. We investigated the levels of advanced protein (OPC), protein carbonyls (PCC), nitric oxide (•NO) and total antioxidant capacity (TAC) in blood serum in CMA and IBD patients. The results showed a significant increase in PCC ($p < 0.0001$), OPC ($p < 0.0001$), and increased •NO deposition ($p < 0.001$) and TAC ($p < 0.0001$) that likely induce oxidative damage in CMA *versus* IBD patients. In conclusion, the ROS/RNS accumulation, and oxidative damage to the protein skeleton in the colonic mucosa play a key role in the CMA and IBD pathophysiology, especially in the initiation, duration and maintenance of mucosal inflammation.

Keywords: CMA, IBD, OPC, PCC, oxidative damages

INTRODUCTION

Cow's milk protein allergy (CMA) is a form of food allergy in infants and children and is a common cause for gastrointestinal mucosal inflammation (2 - 7.5 % frequency) [1-3]. Epidemiological studies indicate that 5-15% of children exhibit symptoms suggestive of CMA [4]. The most common allergens are β-lactoglobulin, α-lactoalbumin, bovine serum albumin, globulin and casein. Other important allergens are egg whites, ovalbumin, soy protein, peanuts, fish, and (beef, pork, chicken) meat [5].

Clinical presentation includes general and gastro-intestinal symptoms; skin manifestations; respiratory injuries; and the complaints start in the first two hours in case of IgE-mediated allergy and several days/weeks in the case of non-IgE-mediated allergy [3, 5] after CMA ingestion. Gastrointestinal food allergy is usually considered as non-IgE mediated, whereas eosinophilic dominant disorders could be mixed IgE and non-IgE allergies. Infants less than <1 year, are victims of gut-affecting non-IgE-mediated allergies [2, 6]. The antigens cross the intestinal barrier and are recognized by M-cells in the mucosa, which convey the information to antigen presenting cells. Thus, APCs present the antigen to T-helper lymphocytes (Th0), which cause overexpression of the Th2 response, so that cytokines such as interleukins- IL-4 and IL-13, are released and stimulate B-lymphocytes to synthesize specific IgE [7]. In cases of non-IgE-mediated allergy, IL-5 and TNF-α are synthesized which promote recruitment of neutrophils and eosinophils activation and infiltration and determine the appearance of edema, pain and abnormal functioning [6-8]. CMA induces an increase in eosinophils in the intestinal mucosa, with affection on the rectum and duodenum. Focal erythema, erosions, lymphoid nodular hyperplasia and partial villous atrophy were reported [6, 8]. In 62% of the gastrointestinal biopsies inflammation and eosinophilic infiltration were found [3, 6-8]. The allergic inflammation in the intestinal mucosa leads to an increase in some oxidative stress (OS) markers, in particular nitric oxide (•NO) and protein levels [9].

Inflammatory bowel diseases (IBD) are chronic, idiopathic and complex diseases of the gastro-intestinal tract, with two forms: ulcerative colitis (UC) and Crohn's disease (CD) [10, 11]. The IBD incidence and prevalence was increased [12, 13] and CD/ UC pathogenesis involves genetic, immune, and environmental factors leading to disruption of the delicate homeostasis between host immunity and the gastrointestinal microbiome [10, 11, 13, 14]. Mucosal tissue infiltration with activated phagocytic immune cells generating ROS/RNS induces

---

prooxidants generation [15, 16]. In addition, ROS/ RNS are predominant mediators responsible for the intracellular damages of proteins, lipids, nucleic acids, and being highly reactive, upregulate the gene expression and reduce immune responses adaptation [16-19]. ROS/ RNS and OS are related to inflammatory responses [20] and have been implicated in the IBD exacerbation [14, 21-23]. The increased intracellular ROS/ RNS production, but higher superoxide dismutase (SOD), glutathione peroxidase (GP_X) and catalase (CAT) activities [15] and higher nitric oxide (•NO) [24] were found in UC patients, than in controls. Moreover, Lih-Brody *et al.* [25] observed increased protein carbonyls content, DNA oxidation and iron content, but decreased/ increased activity of copper and Cu-Zn SOD in CD and UC biopsies. The study concluded that an imbalance in the formation of ROS and antioxidant trace elements may be important in the pathogenesis

of tissue damage in IBD and may provide a rationale for therapeutic modulation with antioxidants.

On these bases, the aim of the present study was to investigate and compare the oxidative stress biomarkers and the clinical characteristics of a group of children with gastrointestinal problems, e.g. CMA and IBD.

EXPERIMENTAL

The group included 35 CMA patients (15 boys, 20 girls), at age 1 month - 12 years (29 infants – median age range 5.2 months; and 6 toddlers at 2 - 12 years, median age range 7.6 years) and 18 IBD patients (8 males; 10 females) at age 13 - 17 years (median age range 14.1 years). All patients have been treated in Trakia Hospital and UMAT Hospital "Stoyan Kirkovich", Stara Zagora, Bulgaria, between 2022-2023 (Table 1).

Table 1. Demographic and clinical characteristics of CMA and IBD patients; p-values *p < 0.01, **p < 0.001, **p < 0.0001 by Students t-test or Mann–Whitney test.

Demographic and clinical characteristics	CMA (n= 35)	IBD (n= 18)	p
Gender			
-male	15 (39 %)	8 (49 %)	p < 0.0001
-female	20 (61 %)	10 (52 %)	p < 0.0001
BMI (kg/m²)	≤ + 1 SD	≤+1SD, ~34,9%	-
Age (years) :			-
Infants	~5.2 months	-	
Toddlers	~7.6 years	~14.1 years	-
Disease duration (months/years)	2 months	3 years	p < 0.001
			p = 0.01
Diagnostic delay (months)	1 month	6 months	
			p = 0.083
Disease behavior			
Clinical signs of inflammation	100%	100%	
Colonoscopy	-	(+) positive	p = 0.00
Histological study	-	-	-
Active IBD	-	2 (9%)	-
Remission	1	16 (95%)	-
Fecal calprotectin	-	~1290 µg/g	p <0.0001
			-
Extra-intestinal disease			
-Skin	14 (47 %)	No	
-Arthritis			-
Allergies yes/no			
Esonophilia	21 (64%)	No	
Atopic dermatitis	14 (47 %)	-	-
Bronchial asthma	2 (3.9 %)	-	
Eosinophilic esophagitis	3 (4.3 %)	-	
Familial CMA/ IBD yes/no	16 (49%)	No	
			-
Pharmacotherapy			
5-aminosalicylates (5-ASA)	No	10	
Steroids	No	1	
Azathioprine	No	4	
Biologics	No	3	

The assessment of patient health status was based on medical history, physical examination, laboratory data and imaging studies.

The exclusion criteria were: 1) evidence of intestinal infection; 2) other acute infection.

The inclusion criteria were: 1) CMA group - positive elimination and challenge test for cow milk (infant formula) with/ without blood eosinophilia and increased IgE; 2) IBD group - positive colonoscopy findings and histology and increased fecal calprotectin.

The study was conducted in accordance with the Declaration of Helsinki, and approved by the Ethic Committee by Trakia Hospital and UMAT "St. Kirkovich" Hospital (code: 10-816/ 12 Oct. 2019). All subjects or legal guardians gave written consent.

Serum samples (1.2 ml) were collected from patients after an all-night rest, at 7.30 a.m., and centrifuged (2000×g; 4 ℃, 10 min).

Advanced oxidation protein content (OPC): 30 µl serum, 970 µl PBS, 50 µl KI (1.20 M) and100 µl acetic acid were mixed and immediately read at 340 nm. OPC were quantified in µmol/mg proteins by using the standard chloramine-T (Sigma-Aldrich, Germany) [26].

Protein carbonyl content (PCC): Serum PCC was evaluated by an immune-enzyme method using commercially available ELISA kit in nmol/mg (126287/BioVision Inc., CA, USA) [27].

Total antioxidant capacity (TAC): The 30 µl serum was mixed to ABTS•$^+$ solution (3-ethylbenzothiazoline-6-sulfonic acid) immediately read at 660 nm in µmol/mg protein, by using the standard Trolox (Sigma-Aldrich, Germany) [28].

Nitric oxide generation (•NO): The mixture of 30 µl serum, 50 µM carboxy-PTIO.K, 50 mM Tris (pH 7.5) and DMSO at a ratio 9:1, was centrifuged at 4000 rpm, 10 min, 4°C. The spin-adduct between carboxy-PTIO and •NO radicals was measured in a.u. [29].

Statistical analysis: The data were analyzed using Statistica (Version 10.0, StaSoft, Inc., USA), and performed using one-way ANOVA. Student's t-test or Mann-Whitney–U test was used to compare the groups. EPR spectral processing was performed using Win-EPR and Simfonia software after consecutive replicates. The $p \leq 0.05$ was considered statistically significant.

RESULTS AND DISCUSSION

OS is not only a consequence of acute and chronic inflammation, but has an essential role in the development and maintenance of inflammation levels, and therefore, abnormal immune response in CMA and IBD in infants and toddlers [5, 20, 30]. Our results demonstrated significant differences in gender ($p < 0.0001$), in median age range ($p < 0.0001$), in disease duration ($p < 0.01$), in diagnostic delay ($p = 0.083$), and in inflammation level ($p = 0.01$), (Table 1). In our study, only 2 patients of the CMA group presented bronchial asthma (3.8%); tree more patients (4.3 %) had eosinophilic esophagitis; 14 patients (47 %) had presents of atopic dermatitis; 21 patients (64%) had presents of esonophilia. The clinical data demonstrated significant differences in familial CMA presents in 16 (49%) infants, and no familial history for IBD group. Based on the international WHO norms for age/ sex-specific BMI, the significant differences were not measured. Ambulatory fecal calprotectin (~1290 µg/g; FC) and 18 positive (+) colonoscopy were used for IBD confirmation. Patients in active IBD were 2 (9%) and in IBD remission - 16 (95%; $p < 0.0001$) *versus* CMA children.

It is widely accepted that the use of >3 medicaments significantly taints a clinical study. For this reason, we used patients in IBD group, taking only 1 medicament: 10 patients took 5-aminosalicylates (5-ASA) medicaments; 1 patient ttook steroids medicaments; 4 patients took azathioprine medicaments; 3 patients had biologics pharmacotherapy.

In regard to OS, our results show an overall increase in oxidative biomarkers in patients with CMA compared to IBD, highlighting that severe allergic activity directly reflects acute oxidative stress-induced protein damages (Table 2). Among the markers analyzed, OPC (mean 12.73 (4.12 – 16.19) µmol/g *vs.* 9.47 (3.75 – 10.71) µmol/g of oxidize proteins; $p < 0.0001$) and PCC (mean 11.48 (7.53 – 12.49) nmol/mg *vs.* 7.69 (5.42 – 11.061) nmol/mg of oxidize proteins; $p < 0.0001$) demonstrated the greatest statistically significant difference in CMA from IBD patients. In CMA children, probably the acute-phase induced excessive formation of di-tyrosine-containing cross-linked products, after the activation of serum proteins (albumin) with chlorinated compounds [30, 31], compared to IBD children.

Table 2. Mean values of oxidative markers in serum samples from CMA patients and IBD patients. The means ± SD and **p < 0.0001 by Student's t-test or Mann–Whitney test were statistically significant; a.u.: arbitrary units.

Oxidative stress markers	CMA (n =35)	IBD (n = 18)	p
OPC (μmol/mg advanced proteins)	12.73 (range 4.12 – 16.15)	9.477 (range 3.75 – 10.14)	p < 0.0001
PCC (nmol/mg)	11.46 (range 7.12 – 12.49)	7.78 (range 5.13 – 11.06)	p < 0.0001
TAC (μmol/mg protein)	3.97 (range 0.87 – 4.11)	1.59 (range 0.91 – 2.07)	p < 0.0001
•NO deposition (a.u.)	7.39 (range 5.16 – 8.22)	5.09 (range 2.99 – 6.044)	p < 0.0001

In this sense, OS-induced protein damage in CMA allergy is associated with excessive ROS/RNS production that depletes serum antioxidants two-fold. As in the IBD disorders, mucosal ROS-infiltration only overwhelms tissue antioxidant defenses [30, 32]. AOPP and PCC contents activate protein kinase C and nicotinamide adenine, NADPH oxidase, as well as the NF-κB-dependent oxidative and inflammatory pathways [30, 33].

Increased OS damages and protein modification (↑ OPC and ↑ PCC) in serum correlated with reduced antioxidant barrier, significantly increased TAC (mean 9.37 (0.78–4.11) μmol/mg *vs.* 1.58 (0.9–2.03) μmol/g proteins; p < 0.001), in children with CMA, compared to IBD children. The TAC content was almost 8-fold higher in the blood of children with CMA (~5.2 months age), which suggests an un-adaptive antioxidant response of the organism to ROS/ RNS overproduction. Although we did not directly evaluate ROS concentration, our hypothesis can be confirmed by a positive correlation between increased protein content and and TAC levels in CMA children, compared to IBD children.

The nitric oxide (NO/ •NO radical) is the most important vasodilator helping the proper function of blood vessels [34, 35]. Interestingly, we found a sharp increase in serum •NO radical concentration (mean 7.44 (5.14 – 8.25) a.u. *vs.* 5.07 (2.99 – 6.04) a.u.; p < 0.001) in CMA children, compared to IBD children. The main mechanism increasing the •NO radical bioavailability is direct oxidation with superoxide anion radical ($•O_2^-$) leading to the formation of highly reactive peroxynitrite with strong oxidizing properties, which interferes with mitochondrial function and further oxidizes thiol groups of enzymes and signaling proteins [33, 36, 37]. This can be confirmed by a positive correlation between increased TAC *vs.* •NO (r = 0.86, p < 0.005), PCC vs •NO (r = 0.81, p < 0.002), •NO *vs.*

OPC (r = 0.81, p < 0.001) levels in CMA children, compared to IBD children. Intestinal mucosal inflammation promotes ROS/RNS through the activation of NOX systems and inducible nitric oxide (iNOS) synthase, which directly damages cytoskeletal proteins and escalates OS-induced intestinal inflammation, probably in both groups, CMA and IBD children [15].

A positive correlation between markers was observed for: PCC vs •NO (r = 0.81, p< 0.002); TAC *vs.* •NO (r = 0.86, p< 0.005); TAC *vs.* PCC (r = 0.81, p< 0.003); PCC *vs.* OPC (r = 0.81, p< 0.0002); •NO *vs.* OPC (r = 0.81, p < 0.001) in CMA children, compared to IBD children.

In fact, OS and ROS/RNS uncontrolled production are a key pathologically-contributing factors responsible for the development of several gastrointestinal tract pathological disorders, such as CMA and IBD. In the context of mucosal (intestinal epithelium) inflammation (CMA and IBD), the activation by inflammatory cytokines leads to the superoxide anion radical ($•O_2^-$) and nitric oxide radical (•NO) production by IEC cells, neutrophils, and macrophages [15]. However, Maor *et al.* and Beltran *et al.* [36, 37] identified that OS rates were higher in active IBD phase compared to patients in remission. In our study, 16 patients (95%) were in IBD remission phase; probably the reduced inflammation levels, as well as the application of pharmaceutical treatment (5-ASA, steroids) dually regulate ROS/ RNS concentrations and reduce OS disorders. We hypothetize that the statistical increase of OS markers in the CMA group (infants and toddlers) is directly affected by the duration of the symptomatology, by the distinct diagnosis at a younger age, but in the CMA allergic condition, to the inflammation and OS maximum [15, 36, 37]. In addition, the high OS observed in CMA patients, witnessed by the increase in OPC, PCC, •NO radical

and TAC [38-39] markers measured, correlated to CMA patients examined before starting drug treatment and implementing a diet.

The limitations of our study are: 1) the relatively small sample size; 2) the relatively low uniformity of the lips; 3) repeated measurements during the course of the disease, necessary to validate the relevance of the use of OS markers in clinical settings.

CONCLUSIONS

Despite limitations, our results provide evidence that circulating OPC, PCC, •NO radical and TAC are significantly elevated in CMA patients, suggesting that these parameters could be evaluated in a prospective, larger study on the CMA and IBD progression, as biomarkers for diagnosis or monitoring of CMA and IBD patients. The search for new non-invasive diagnostic methods is of great importance, especially for children and adolescents with CMA and IBD.

REFERENCES

1. M. D'Apolito, A. Campanozzi, I. Giardino, M. Pettoello-Mantovani, *Turk. Pediatri. Ars.*, **52** (4), 208 (2017).
2. Y. Vandenplas, I. Broekaert, M. Domellöf, F. Indrio, A. Lapillonne, C. Pienar, C. Ribes-Koninckx, R. Shamir, H. Szajewska, N. Thapar, R. A. Thomassen, E. Verduci, C. West, *J. Pediatr. Gastroenterol. Nutr.*, **26** (2023).
3. R. Meyer, C. Venter, A. Bognanni, H. Szajewska, R. Shamir, A. Nowak-Wegrzyn, A. Fiocchi, Y. Vandenplas, *World Allergy Organ. J.,* **24**, 16 (7), 100785 (2023).
4. R. Martín-Masot, J. J. Díaz-Martín, A. Santamaría-Orleans, V. M. Navas-López, *Nutrients,* **15** (16), 3586 (2023).
5. M. Panayotova, T. Velikova, E. Ivanova-Todorova, *Medinfo*, **8**, 44 (2015).
6. N. Shah, M. Foong Ru-Xin, O. Borrelli, E. Volonaki, R. Dziubak, R. Meyer, M. Elawad, N. J. Sebire, *BMC Clin. Pathol.*, **15** (1), 1 (2015).
7. J. Noh, J. H. Lee, G. Noh, S. Y. Bang, H. S. Kim, W. S. Choi, S. Cho, S.S. Lee, *Cell Immunol.,* **264** (2), 143 (2010).
8. R. Cervantes-Bustamante, I. Pedrero-Olivares, E. M. Toro-Monjaraz P. Murillo-Márquez J. A. Ramírez-Mayans, E. Montijo-Barrios, F. Zárate-Mondragón, J. M. Cadena-León, *Revista de Gastroenterol. de Mexico*, **80**, (8), 13 (2015).
9. B. Hanusch, K. Sinningen, F. Brinkmann, S. Dillenhöfer, M. Frank, K. H. Jöckel, T. Lücke, *Int. J Mol. Sci.*, **23** (4), 2136 (2022).
10. L. Cantoro, A. Di Sabatino, C. Papi, G. Margagnoni, S. Ardizzone, P. Giuffrida, D. Giannarelli, A. Massari, R. Monterubbianesi, M.V. Lenti, *J. Crohn's Colitis.,***11**, 975 (2017).
11. D. H. Kim, J. H. Cheon, *Immune Netw.*, **17**, 25 (2017).
12. N. A. Molodecky, I. S. Soon, D. M. Rabi, W. A. Ghali, M. Ferris, *Gastroenterol.*, **142**, 46 e42 (2012).
13. G. G. Kaplan, *Gastroenterol. Hepatol.*, **12**, 720 (2015).
14. G. P. Christophi, R. Rong, P. G. Holtzapple, P. T. Massa, S. K. Landas, *Inflamm. Bowel Dis.*, **18**, 2342 (2012).
15. T. Tian, Z. Wang, J. Zhang, *Oxid. Med. Cell. Longev.*, **2017**, 4535194 (2017).
16. R. D'Incà, R. Cardin, L. Benazzato, I. Angriman, D. Martines, G. Sturniolo, *Inflamm. Bowel Dis.,* **10**, 23 (2004).
17. H. E. Hamouda, S. S. Zakaria, S. A. Ismail, M. A. Khedr, W. W. Mayah, *World J.. Gastroenterol.*, **17**, 2417 (2011).
18. E. Ozhegov, E. Zhivotova, O. Lebedko, M. Fleishman, S. Alexeenko, S. Timoshin, *Bull. Exp. Biol. Med.*, **152**, 420 (2012).
19. M. Panayotova, *Trakia J. Sci.*, **21**, (4), 375 (2023).
20. P. Goycheva, K. Petkova-Parlapanska, E. Georgieva, Y. Karamalakova, G. Nikolova, *Int. J. Mol. Sci.*, **24** (17), 13541 (2023).
21. K. Szczeklik, W. Krzyściak, D. Cibor, R. Domagała-Rodacka, J. Pytko-Polończyk, T. Mach, D. Owczarek, *Polish Arch. Intern. Med.*, **128**, 362 (2018).
22. M. Koláček, J. Muchová, M. Dvořáková, Z. Paduchová, I. Žitňanová, I. Čierna, Z. Országhová, D. Székyová, N. Jajcaiová-Zedníčková, L. Kovács, *Free Radic. Res.,* **47**, 624 (2013).
23. M. Krzystek-Korpacka, P. Kempiński, A. Bromke, K. Neubauer, *Diagnost.,* **10** (8), 601 (2020).
24. I. M. Balmus, A. Ciobica, A. Trifan, C. Stanciu, *Saudi J. Gastroenterol: Official J. Saudi Gastroenterol. Assoc.,* **22** (1), 3 (2016).
25. L. Lih-Brody, S. R. Powell, K. P. Collier, G. M. Reddy, R. Cerchia, E. Kahn, S. Gary, *Dig. Dis. Sci.,* **41**, 2078 (1996).
26. V. Witko-Sarsat, M. Friedlander, C. Capeillère-Blandin, T. Nguyen-Khoa, A. T. Nguyen, J. Zingraff, P. Jungers, B. Descamps-Latscha, *Kidney Int.*, **49**, 1304 (1996).
27. R. L. Levine, D. Garland, C. N. Oliver, A. Amici, I. Climent, A. G. Lenz, B. W. Ahn, S. Shaltiel, E. R. Stadtman, *Meth. Enzymol.*, **186**, 464 (1990).
28. O. Erel, *Clin. Biochem.*, **37**, 277 (2004).
29. K. Yokoyama, K. Hashiba, H. Wakabayashi, K. Hashimoto, K. Satoh, T. Kurihara, N. Motohashi, H. Sakagami, *Anticancer Res.,* **24** (6), 3917 (2004).
30. C. Luceri, E. Bigagli, S. Agostiniani, F. Giudici, D. Zambonin, S. Scaringi, F. Ficari, M. Lodovici, C. Malentacchi, *Antiox.,* **8** (9), 378 (2019).

31. V. Correa-Salde, I. Albesa, *Biomed. Pharmacother.*, **63**, 100 (2009).
32. F. Xie, S. Sun, A. Xu, S. Zheng, M. Xue, P. Wu, J.H. Zeng, L. Bai, *Cell Death. Dis.*, **5**, e1006 (2014).
33. X. Xu, S. Sun, F. Xie, J. Ma, J. Tang, S. He, L. Bai, *Antioxid. Red. Sign.,* **27**, 37 (2017).
34. N. Escobales, M. Crespo, *Curr. Vasc. Pharmacol.*, (2005).
35. P. Pacher, J. S. Beckman, L. Liaudet, *Physiol. Rev.*, **87** (1), 315 (2007).
36. I. Maor, T. Rainin, A. Lanir, A. Lavy, *Dig. Dis. Sci.*, **53**, 2208 (2008).
37. B. Beltran, P. Nos, F. Dasí, M. Iborra, G. Bastida, M. Martínez, J. E. O'Connor, G. Sáez, I. Moret, J. Ponce, *Inflammat. Bowel Dis.*, **16** (1), 76 (2010).
38. E. Georgieva, Y. Karamalakova, R. Miteva, H. Abrashev, G. Nikolova, *Toxics*, **9** (12), 317 (2021).
39. H. Abrashev, J. Ananiev, E. Georgieva, *J. Clin. Med.*, **12** (5), 1842 (2023).

Possible application of green algae as emulsifiers in foods and nutritional supplements

I. K. Pehlivanov[1], Kr. T. Nikolova[2]*, I. V. Milkova[3], M. G Marudova[4], V. D. Gandova[5], A. Ts. Gerasimova[6], G. D. Gencheva[7], I. I. Minchev[3], V. Y. Andonova[1]

[1]Department of Pharmaceutical Technologies, Medical University of Varna, Faculty of Pharmacy, 84 Tzar Osvoboditel Blvd., 9002 Varna, Bulgaria

[2] Department of Physics and Biophysics, Medical University of Varna, Faculty of Pharmacy, 84 Tzar Osvoboditel Blvd., 9002 Varna, Bulgaria

[3]Department of Nutrient and Catering, University of Food Technologies, Economic Faculty, 26 Maritza Blvd., 4002 Plovdiv, Bulgaria

[4]Department of Physics, University of Plovdiv "Paisii Hilendarski", Faculty of Physics and Technology, 24 Tzar Asen Str., 4000 Plovdiv, Bulgaria

[5]Department of Analytical and Physical Chemistry, University of Food Technologies, Technological Faculty, 26 Maritza Blvd.,4002 Plovdiv, Bulgaria

[6] Department of Chemistry, Medical University of Varna, Faculty of Pharmacy, 84 Tzar Osvoboditel Blvd., 9002 Varna, Bulgaria

[7]Department of Chemistry and Biochemistry, Medical University of Pleven, Faculty of Pharmacy,1 Saint Kliment Ohridski Str., 5800 Pleven, Bulgaria

The high protein content (43.4 %) and the ability of dietary fiber in *Spirulina (Arthrospira platensis*) to retain water or vegetable oil make the alga suitable for use as an emulsifier in colloidal or emulsion systems. This study aimed to investigate the influence of *Spirulina (Arthrospira platensis)* (4%, 8%, 12%) as emulsifier on the physical and thermodynamic stability of model emulsions by determining parameters such as Gibbs energy, enthalpy, and entropy. Thermodynamic stability was estimated spectrophotometrically, and physical stability was determined by the Kozin method. It was shown that increasing the *Spirulina* concentration leads to a decrease in Gibbs free energy and an increase in the physical stability of all emulsions (20%, 40%, 60% oil phases) that are finely dispersed and microscopically determined. The highest percentage of retained emulsion (100 %) was at 12 % *Spirulina* with an oil phase content of 40 % or 60 %. From a rheological point of view, emulsions with *Spirulina* at 20 % oil phase showed plastic body behavior, and those with 40 % and 60 % oil phase showed pseudo-plastic behavior.

Keywords: emulsions, *Spirulina*, microscopic determinations, thermodynamic parameters.

INTRODUCTION

Oil-in-water emulsions are often used in pharmaceutical and food technology. Sunflower oil is the most preferred ingredient for developing emulsions due to its high thermal stability, relatively long shelf life, and wide distribution in Europe [1]. The choice of an appropriate emulsifier plays a crucial role in the stability of the emulsion, ensuring a longer shelf life for the product. Vegetable proteins have a proven emulsifying capacity [2]. *Spirulina* is a source of proteins (40-60 %), carbohydrates (1-3 %), and lipids (25-40 %) [3]. Spirulina extracts are widely used in the cosmetic industry, and their inclusion in suitable pharmaceutical dosage forms for therapeutic purposes is being studied [4]. Due to their amphiphilic nature, proteins are quickly adsorbed and easily rearrange at the oil/water interface. The highly elastic protein film formed on the oil droplets maintains the repulsive forces between them and increases the emulsion stability [5].

The present study aims to investigate the influence of *Spirulina (Arthrospira platensis)* (4 %, 8 %, 12 %) on emulsions' physical and thermodynamic stability.

MATERIALS AND METHODS:

Materials

The model emulsions were prepared using *Spirulina* as an emulsifier and sunflower oil as an oil phase. *Spirulina (Arthrospira platensis)* was taken from a bioreactor in Varvara, Bulgaria, and sunflower oil "Kaliakra" was purchased from the supermarket. All other reagents were of analytical grade.

Preparation of model emulsion

Nine model emulsions were made to assess the effect of oil concentrations (20 %, 40 %, 60 %) and *Spirulina* concentrations (4 %, 8 %, 12 %) on the stability of oil-in-water emulsions. The protein concentration was investigated for used microalgae; in our case, it is about 44 % [6]. The composition of model emulsions is presented in Table 1, and the scheme for their preparation is given in Figure 1. All emulsions were prepared as follows: *Spirulina* was added to distilled water (pH = 7.0), and the mixture was homogenized at 1000 rpm (ISOLAB Laborgeräte GmbH, Germany) for 3 minutes. Then, with continuous homogenization, the oil phase was added, and homogenization continued for another 5 minutes.

Water holding capacity

Water holding capacity (WHC) was determined using the method of Chau and Huang [7]. 1 g of the sample was homogenized with 10 mL of distilled water, and stored for 24 h at a temperature of 23-25 °C. It was centrifuged (2500G, 30 min), and the amount of the supernatant was measured. WHC was defined as mL of retained water from 1 g of sample.

Oil holding capacity

Oil-holding capacity (OHC) was determined according to the method of Chau and Huang [7]. The 1 g sample was homogenized with vegetable fat (1:10) and stored for 30 min at a temperature of 23-25 °C. It was centrifuged (2500G, 30 min), and the amount of the supernatant was measured. OHC was defined as mL of retained fat from one g of sample.

Microscopic studies

The microscopic analysis performed to determine the distribution of oil globules in the model emulsions with the oil phase of vegetable sunflower oil (20, 40, and 60 %) and *Spirulina* (4, 8, and 12 %) as an emulsifier was carried out with a Levenhuk MED D30T digital microscope, using the Dino Capture 2.0 plugin, version 1.2 .0. and a PC sample Window Management Bar.

Determination of physical stability of emulsions

Emulsion stability was determined by Kozin [8] using a Nahita 2640 centrifuge. A five g emulsion sample was placed in a 10 cm³ graduated centrifuge tube. Centrifugation was performed at angular velocity 314 rad.s⁻¹ for 20 min. The amount of retained emulsion was used to determine the stability of the emulsion *versus* separated water and oil phases.

Table 1. Composition of model emulsions with *Spirulina (Arthrospira platensis)* emulsifier

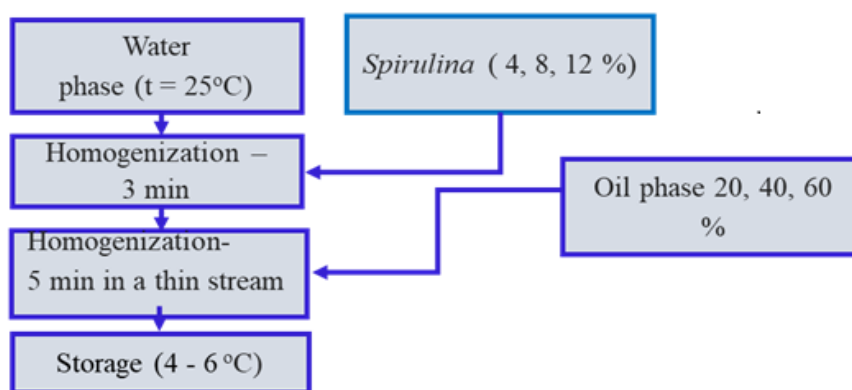| Sample	1	2	3	4	5	6	7	8	9
Emulsifier, % *(Spirulina (Arthrospira platensis))*	4	4	4	8	8	8	12	12	12
Oil phase (OP), % (sunflower oil)	20	40	60	20	40	60	20	40	60
Dispersion medium, % (water)	76	56	36	72	52	32	68	48	28

Figure 1. Technology for emulsion preparation.

Determination of the dispersity of emulsions

The method for determining dispersity was developed in [9]. Five g of the prepared emulsion was placed in a 50 cm³ beaker and diluted with distilled water in a 100 cm³ volumetric flask. Two cm³ was taken from the prepared mixture with a pipette and transferred to a volumetric flask of 50 cm³, and water was added to the mark and shaken, achieving a sample dilution of 1:500. A cuvette with a length path of 1.0 cm was used for measuring the transmission coefficient of the solution at a wavelength λ=540 nm relative to a control cuvette with distilled water. The amount of transmitted light determines the dispersion of the emulsion.

Thermodynamic stability of emulsions

The Gibbs free energy was calculated from equation 1.

$$\Delta G = -RTlnK \qquad (1),$$

where R is the universal gas constant (R = 8.314 J/(K×mol)) and T is the absolute temperature (K). The experimental calculation of the equilibrium constant K was conducted by the "dilution method" described by Kendrow *et al.* [10]. Dilutions were made to each model sample with increasing volume concentrations from 0.2 to 1.0 % (v/v) in steps of 0.2. The optical density measurement's wavelength was determined from the absorption spectrum for the sample with the highest concentration. This was the wavelength at which the corresponding solution had maximum absorption. The equilibrium constant is the angular coefficient of dependence A=f(C).

The measurements were conducted by using a spectrophotometer (Genesys 10UV Thermo Scientific, Massachusetts, USA). The research was carried out with a cuvette of 1 cm path length at λ= 620 nm.

In addition to the Gibbs energy, the enthalpy and entropy were calculated from equations 2 and 3.

$$\frac{dlnK}{d(\frac{1}{T})} = \frac{-\Delta H}{R} \qquad (2),$$

$$\Delta S = \frac{(\Delta H - \Delta G)}{T} \qquad (3),$$

where ΔH is enthalpy (kJ×mol⁻¹), ΔS is entropy (kJ×K⁻¹×mol⁻¹).

Rheology

The rheological measurements were performed at (20 ± 1) °C using Thermo Scientific HAAKE Viscotester 550 (Germany). The analyses were conducted in an SV DIN coaxial cylinder sensor at shear rates ranging from 0.0123 s⁻¹ to 1000 s⁻¹. The data for the shear stress as a function of the share rate

for each model were investigated. The instrument software application performed the mathematical modeling.

Statistical analysis

The data on the three parallel measurements of investigated parameters were processed to obtain the mean value and the standard deviation (SD). Dispersion analysis was used to compare the mean values with a significance level of $p < 0.05$. A nonlinear model was obtained by the IBM SPSS Statistic 26 computer program, USA.

RESULTS AND DISCUSSION

The type of dietary fiber (soluble and insoluble) consumed affects human physiology. Soluble and insoluble dietary fiber content determines water and vegetable oil holding capacity.

Our study showed that *Spirulina* has a WHC and OHC of 1.1 g/g and 1 g/g, respectively. This fact confirms the thesis by Suzuki *et al.* [11] that algae are suitable stabilizers of colloidal and emulsion systems.

The main characteristics (emulsion stability and dispersity) of emulsions with oil phase (OP) from vegetable sunflower oil 20, 40, and 60 % and emulsifier *Spirulina* 4, 8, and 12 % were investigated.

Table 2 presents the results of the Kozin test for physical stability of model emulsions with OP of vegetable sunflower oil (20 %, 40 %, and 60 %) and *Spirulina* content of 4, 8, and 12 % as an emulsifier.

Table 2. Physical stability of emulsions.

	Separated phase, ml			Retained emulsion, %
	O	W	E	
1	-	0.5	3.5	46.70
2	-	0.8	3.7	40.00
3	-	0.5	5.0	26.67
4	-	1.0	3.0	57.13
5	-	0.5	4.0	43.81
6	-	-	6.2	27.09
7	-	0.3	0.2	93.30
8	-	-	-	100.00
9	-	-	-	100.00

Increasing the amount of *Spirulina* increased the percentage of retained emulsion, regardless of the OP content. At 12 % *Spirulina* as emulsifier and 40 and 60 % OP, emulsion stability was 100 %. At 20 % OP and 12 % emulsifier, emulsion stability is high – about 93 %. Therefore, when developing emulsions with 20%, 40%, and 60% OP vegetable sunflower oil, it is appropriate to use 12 % *Spirulina* as an emulsifier.

The dispersity of O/W emulsions with the emulsifier freshwater algae *Spirulina (Arthrospira platensis)* with 20 %, 40 %, and 60 % OP of vegetable sunflower oil was determined, and the extinction values (E, %) were measured. The results are presented in Table 3.

Table 3. Dispersion of model emulsions with emulsifier *Spirulina (Arthrospira platensis)* (SP) and Oil Phase (OP) from vegetable sunflower oil.

Emulsifier/oil phase ratio			
Sample (SP/OP)	1	4	7
E,%	0.075	0.085	0,087
Sample (SP/ OP)	2	5	8
E,%	0,106	0.124	0.129
Sample (SP/ OP)	3	6	9
E,%	0.168	0.228	0.640

The optical density (extinction) values increased with an increase in the amount of *Spirulina (Arthrospira platensis)* as an emulsifier (Table 3) and the OP from 20 % to 40 % or 60 %. This trend was most pronounced in the 60 % emulsions with 4 %, 8 %, and 12 % *Spirulina (Arthrospira platensis)*. The optical density of emulsions with 12% *Spirulina (Arthrospira platensis)* as an emulsifier and 60 % OP were 3.8 times higher than those with 4 % emulsifier. Model emulsions 3, 6, and 9 with 12 % emulsifier and 20 %, 40 %, and 60 % OP are the most dispersed.

Microscopic analysis established the distribution of oil globules in model emulsions with OP of vegetable sunflower oil 20 %, 40 %, and 60 % and *Spirulina (Arthrospira platensis)* (4 %, 8 %, and 12 %). Microscopic observation was carried out 10 minutes after the preparation of the emulsions. The addition of *Spirulina* reduces the size of the oil globules in the emulsions, and as its concentration increases, the fine dispersion of the emulsions increases. The results are presented in Figure 2.

Fig. 2 shows that the prepared emulsions are polydisperse systems – their particles have different sizes.

As the *Spirulina* content increased to 12 % and the OP increased to 40 % and 60 %, small-sized oil globules predominated. The uniform distribution of tiny oil droplets facilitates the adsorption of the protein molecules of the microalgae by the lipid globules, which prevents their coalescence and, therefore, leads to the destabilization of the model emulsion. A similar fact was described by Hebishy *et al.* (2017) [12].

Samples with 4 % *Spirulina* and OP 20 % and 40 % sunflower oil have larger sizes and, therefore, are unstable as the oil globules interact and coalescence is observed.
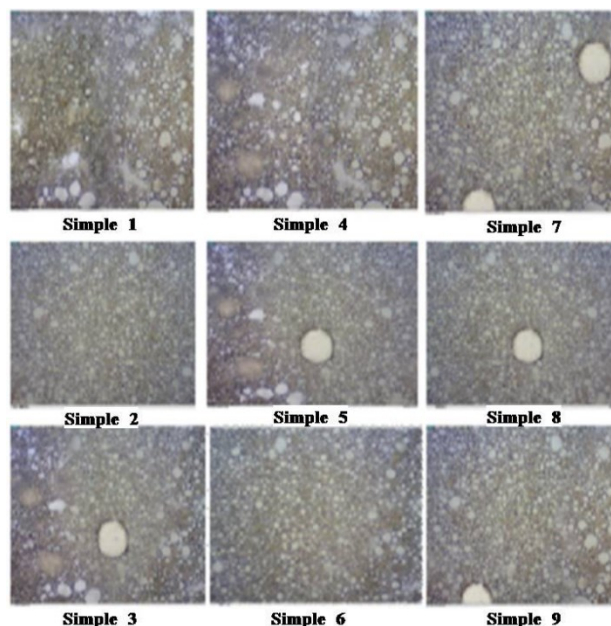

Figure 2. Microscopic analysis of model emulsions.

Sunflower oil was chosen for the OP of the developed emulsions, as it contains medium-chain fatty acids (C16:0 to C18:0). Taha and others (2018) [13] noted that the lower molecular weight of medium-chain triglycerides reduced surface tension more effectively contributing to forming a stable emulsion. The choice of vegetable oil is essential for the characteristics of the emulsion and its stability since the above properties depend on the physicochemical characteristics (viscosity, solubility, surface tension) of the oil [14].

The model emulsions' thermodynamic parameters, such as Gibbs free energy, enthalpy, and entropy, were calculated using equations 1-3. The results are presented in Table 4. The content of *Spirulina* increases, and the Gibbs free energy decreases. This parameter is used as a criterion for evaluating the thermodynamic stability of emulsions. At a negative value of the G parameter, spontaneous emulsification occurs. The more negative the free energy value, the more thermodynamically stable is the emulsion, according to Mehta and Kaur (2011) [16]. Increasing the concentration of sunflower oil increases the stability of the emulsions and leads to more negative Gibbs free energy values. Therefore, the emulsion system with the highest content of *Spirulina* (12 %) possessed the highest Gibbs modulus-free energy. Thus, the most incredible thermodynamic samples are also physically stable. Comparable results have been observed for other food emulsions [12, 16].

The conclusion made above is also confirmed by Figure 3, representing the dependence of Gibbs free energy on the concentration of *Spirulina* as an emulsifier and the oil content of the emulsion.

Table 4. Thermodynamic parameters - free Gibbs energy, enthalpy, and entropy. Samples with 4 % *Spirulina* and OP 20 % and 40 % sunflower oil have larger sizes and, therefore, are unstable as the oil globules interact and coalescence is observed.

Sample	$\Delta G \pm SD$ [kJ mol^{-1}]	$\Delta H \pm SD$ [kJ mol^{-1}]	ΔS [kJ mol^{-1} K^{-1}]
1	-5.28±0.05	-19.64±1.05	-0.048±0.002
2	-4.97±0.14	-19.50±1.11	-0.049±0.002
3	-6.48±0.54	-20.16±1.24	-0.046±0.002
4	-5.19±0.94	-19.60±0.76	-0.048±0002
5	-5.23±0.74	-19.62±0.49	-0.048±0.001
6	-5.63±0.64	-19.79±0.89	-0.048±0.001
7	-7.17±2.04	-20.46±1.32	-0.045±0.002
8	-7.03±1.24	-20.40±1.34	-0.045±0.001
9	-6.00±1.34	-19.95±1.07	-0.046±0.001
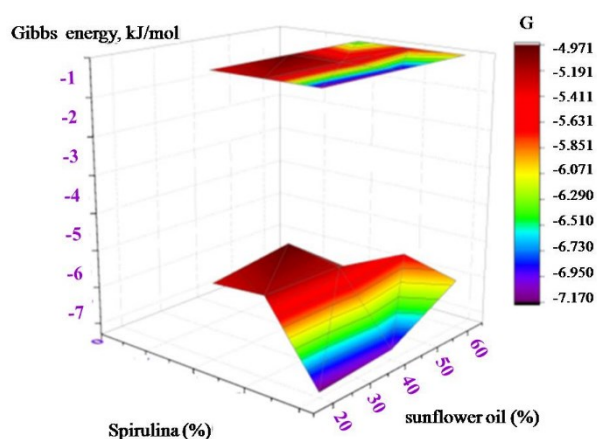
Figure 3. Graphical dependence between the Gibbs free energy and mass % O/W of emulsion prepared with *Spirulina*.

Enthalpy determines the thermal effect of emulsion systems. The negative value of enthalpy indicates that the processes are defined as exothermic. Entropy is related to the phase separation of the emulsion system and is a measure of its disorder. In the studied samples, the entropy shows shallow negative values.

Except for the amount of emulsifier, the results show that the amount of sunflower oil also affects the emulsion stability. Emulsions prepared with lower *Spirulina* concentrations and more significant amounts of the oil phase were characterized by higher Gibbs energy values. When the emulsifier amount increased, the emulsions' stability according to the resulting Gibbs energies was better, in addition to a smaller amount of oil phase. This is associated with the emulsifier nature that leads to forming of a particular emulsion. The free water binds to the emulsifier and leads to gelling processes. Because of the connection of water with the emulsifier, the

system's viscosity probably increases, which is another criterion for stability and explains the more excellent stability of the respective emulsions. To confirm the statement, rheological tests were carried out at 200 °C. From a rheological point of view, emulsions with 20 % oil phase had plastic behavior, and those with 40 % and 60 % oil phase had pseudo-plastic behavior. Results are presented in Figure 4.
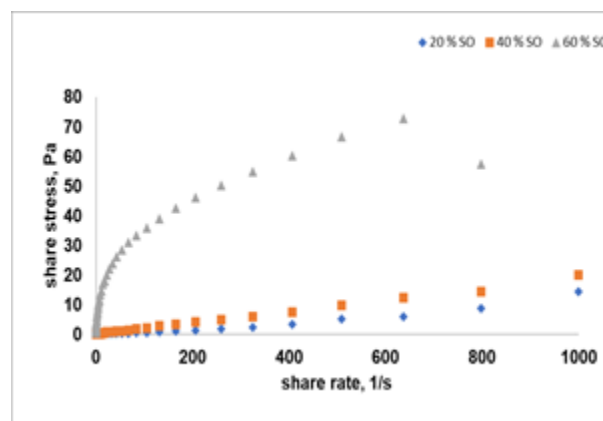

Figure 4. Dependence between share stress and share rate for model emulsions with *Spirulina* as an emulsifier.

CONCLUSIONS

Spirulina platensis has excellent potential for use in the food industry as a stabilizer and in the pharmaceutical industry as an emulsifier to enrich food products and replace synthetic substances in supplements. In developing emulsion systems in food and pharmaceutical technologies, concentrations of 12 % *Spirulina* as an emulsifier with 20, 40, and 60 % oil phase of vegetable sunflower oil can be recommended for high emulsion stability.

REFERENCES

1. D. B. Konuskan, M. Arslan, A. Oksuz, *Saudi J. Biol. Sci.*, **26**, 340 (2019).
2. J. P. Singh, A. Kaur, N. Singh, *J. Food SciTechnol.*, **53**, 1269 (2016).
3. H. Volkmann, U. Imianovsky, J. L. Oliveira, E. S. Sant'Anna, *Brazilian Journal of Microbiology,* **39**, 98 (2008).
4. S. P. Ferreira, L. Souza-Soares, J. A. V. Costa, *Revista de Ciencias Agrarias,* **36**, 275 (2013).
5. C.V. Nikiforidis, A. Matsakidou, V. Kiosseoglou, *RSC. Adv.* **4**, 25067 (2014).
6. I. Milkova, P. Radusheva, Kr. Nikolova, I. Minchev, P. Denev, D. Buhalova, I. Bodurov, T. Jovchev,

National science conference 15 years Pharmacy, Medical University – Plovdiv, 221 (2018).

7. L. Cv. Liucheng, Chi-Fai Chau, Ya-Ling Huang, *J. Agric. Food Chem.,* **51 (9)**, 2615 (2003).
8. N. I. Kozin, *Tech.&Scie.*, **5,** 249 (1966).
9. R. Govin, J.G. Leder, *Journal of Food Science,* **5,** 718 (1971).
10. C. Kendrow, J.C. Baum, C. J. Marzzacco, *J. ChemEduc*., **86,** 1330 (2009).
11. M. Suzuki, Y. Mizuno, Y. Matsuo, M. Masuda, *Phytochemistry*, **43**, 121 (1996).
12. E. Hebishy, A. Zamova, M. Buffa, A. Blasco-Moreno, A. Trujillo, *Processes* **5(6)**, 1 (2017), https://doi.org/10.3390/pr5010006.
13. A. Taha, T. Hu, Z. Zhang, A.M. Bakry, I. Khalifa, S. Pan, H. Hu, *UltrasonSonochem.*, **49**, 283 (2018).
14. D. J. McClements, Food emulsions: principles, practices, and techniques. CRC Press, (2016).
15. S. K. Mehta, G. Kaur, *Intech. Open, Rijeka*, 381 (2011).
16. V. Gandova, D. Balev, *Int. J. Inn. SciEngTechnol.,* **3**, 293 (2016).

Application of non-destructive fast methods for quality assessment of sunflower oil

I. P. Bodurov[1*], K. T. Nikolova[2], A. P. Viraneva[1], A. V. Grigorov[1]

[1]*University of Plovdiv "Paisii Hilendarski", Faculty of Physics and Technology, 24 Tzar Asen str., 4000 Plovdiv, Bulgaria*

[2]*Medical University "Prof. Dr. Paraskev Stoyanov" - Varna, Faculty of Pharmacy, 55 Marin Drinov Str., 9002 Varna, Bulgaria*

The sunflower oil is pressed from the seeds of the sunflower plant (*Helianthus annuus*). It contains high amounts of the essential fatty acid, linoleic acid. Sunflower oil is commonly consumed in foods. The quality of sunflower oil depends on the quality of the sunflower seeds to be processed, the storage conditions of the seeds before pressing and the refining conditions. The standard chemical methods used to determine the chemical content of the oils are usually time-consuming, labor-intensive and expensive. Therefore, we have tested four physical methods measuring refractive indices and their dispersion curves, color parameters, UV-VIS spectroscopic and fluorescence spectra that are related to the chemical structure and composition of the sunflower oils. The refractive indices of the samples were measured using a laser refractometer at wavelengths of 405 nm, 447 nm, 532 nm and 656 nm. The dispersion curves and the dispersion parameters were approximated using one-term Sellmeier model. The color parameters were obtained using a Lovibond PFX 880 spectrophotometer. The values for the refractive indices were compared to these, obtained by a standard method using the Abbe refractometer. These methods are fast, easy to perform and do not require any additional chemical agents. Four groups of sunflower oils – cold pressed, oil with added antioxidants and commercially refined and nonrefined sunflower oil, were investigated.

Keywords: refractive index, fluorescence, sunflower oil, quality assesment

INTRODUCTION

Sunflower oil is a popular vegetable oil derived from the seeds of the sunflower plant (*Helianthus annuus*) [1]. It is used for various purposes, including food and cosmetics.

Sunflower oil is a major source of high-quality edible oil, contributing to about 87% of vegetable oil production worldwide [2]. It is primarily produced for the development of high-oil varieties, which require fertile soil, adequate rainfall, and suitable environmental conditions. The global sunflower oil market is driven by the fluctuating prices of other vegetable oils, such as palm oil and soybean oil, and is in high demand in developing countries due to its healthier and more affordable alternatives to many counterparts [3].

Sunflower oil quality can be influenced by various factors, including: genotype and environment: Sunflower oil quality and yield depend on the plant genotype and its interaction with the environment [4]. Different sunflower cultivars have been developed to produce oils with specific fatty acid profiles, such as high stearic or high palmitic acid cultivars [5].

Temperature during the plant cycle: The effect of temperature during the plant cycle, from anthesis to maturity, on the fatty acid composition of

sunflower oil has been reported to change the oleic/linoleic acid (O/L) ratio, known as unsaturation ratio, in the oil [5].

Seed quality and treatment: Seed quality, seed treatment prior to extraction, extraction method, and processing conditions can affect the properties and composition of sunflower oil [6].

Blending with other oils: Blending sunflower oil with other edible vegetable oils, such as linseed oil, grapeseed oil, and coconut oil, can improve its quality characteristics, such as acidity and stability to autoxidation.

In summary, sunflower quality assessment can involve various techniques and methods, depending on the specific goals and requirements of the assessment. These assessments can help improve the understanding of sunflower cultivation, production, and the quality of sunflower-based products. The objective of the present work is to study the capabilities of a group of physical methods for fast quality evaluation of the sunflower oils.

MATERIALS AND METHODS

Materials

Four types of commercially available sunflower oils – cold pressed, oil with added antioxidants and commercially refined and nonrefined sunflower oil, were chosen for analysis and their characteristics

* To whom all correspondence should be sent:
E-mail: *bodurov@uni-plovdiv.bg*

were compared. The samples were measured immediately after opening the bottle to avoid accelerated oxidation processes.

Refractive index measurement

The refractive index values of the samples investigated were determined by a laser refractometer and a standard Abbe refractometer. The measurements by Abbe refractometer were performed at a temperature of 20 °C with an accuracy of $\pm 1 \times 10^{-4}$.

The refractive index values of the samples were measured using a laser refractometer with a total experimental uncertainty of less than 2×10^{-4} by the method of the disappearing diffraction pattern for four laser wavelenghts – 405 nm, 445 nm, 532 nm and 635 nm at a temperature of 20 °C. The data obtained from the refractive index measurement at four laser wavelengths were used for the construction of dispersion curves using the one-term Sellmeier model for the fundamental absorption band [7].

Fluorescence spectroscopy

BroLight BIM-6002 fiber-optic spectrometer with spectral sensitivity in the range of 200-1100 nm was used to measure the fluorescence spectra of sunflower. An optical fiber of 200 μm diameter was used for more light on the probe and measurement of fluorescent and scattered light. A collimator with a 5 mm aperture lens was used to capture more light and direct it to the receiver. Using a 200 μm entrance slit, the resolution was approximately 8 nm. The sources used to measure the fluorescence spectra were light emitting diodes (LEDs) emitting light at wavelengths of 245 nm, 265 nm, 275 nm, 295 nm, 375 nm, 395 nm, 405 nm, 410 nm, 415 nm and 435 nm. Measurements at 395 nm were performed, since the fluorescence intensity at the indicated wavelength was strongest for the relatively weak fluorescence signal at an excitation time of about 100 ms.

Color parameters measurement

The color parameters for the sunflower oil samples were determined in a CIELab colorimetric system after preliminary tempering of the samples. VISIONlite ColorCalc software package and Helios Omega spectrophotometer with 10 mm cuvette were used.

Luminance L and color characteristics a and b in a CIELab colorimetric system, color coordinates X,Y,Z and chromaticity coordinates x, y in a XYZ colorimetric system were determined. For the case of

the present study, CIELab is more informative, as it is designed for small color differences.

The color intensity C_{ab} and hue angle h_{ab} can be determined according to the following dependencies:

$$C_{ab} = \sqrt{a^2 + b^2} \qquad (1)$$
$$h_{ab} = \operatorname{arctg}(b/a) \qquad (2)$$

RESULTS AND DISCUSSION

Fluorescence spectroscopy is proving to be a fast, easy and possibly non-destructive technique for the analysis of sunflower oil. With the increase in the price of sunflower oil in Bulgaria and the ever-increasing imports, the creation of libraries of fluorescence spectra is useful for the development of methods to assess the quality, authenticity and geographical origin of sunflower oil.

Most samples have a characteristic peak at around 580 nm associated with oxidation as a result of exposure to temperature changes during transport, storage, bottling or as a result of exposure to direct sunlight. The fluorescence spectra are presented in Fig. 1.
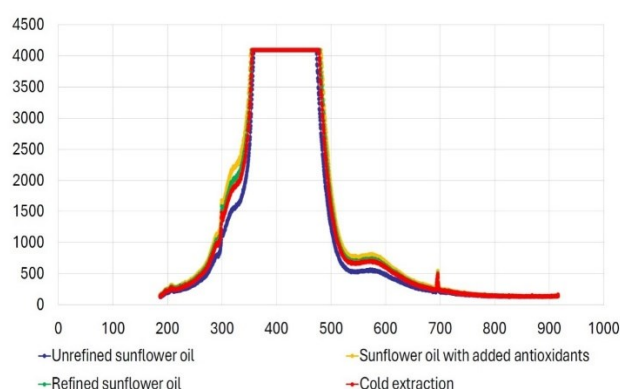

Fig. 1. Fluorescence spectra of sunflower oil samples

Two fluorescence maxima are clearly distinguishable:

- Peak I with maximal intensity in the range 580-590 nm;
- Peak II with maximal intensity around 696 nm.

Peak I can be attributed to the oxidation of the fatty acids and tocopherols [8], while Peak II displays a low intensity between 304 and 387 a.u. and can be linked to pigments like carotenoids and chlorophyll [9]. The positions of the peaks of the different samples match almost completely and differ only in intensity. The only type of oil that displays a shift of 10 nm in Peak I is the sunflower oil with added antioxidants. The aforementioned peak is linked to the oxidation of the samples, with refined sunflower oil with added antioxidants possesing the highest value of 758 a.u., followed by regular

155

refined sunflower oil with a value of 732 a.u. This latter result can be attributed to the fact that during the refining process a major part of the minor components that possess antioxidant effects in the sunflower oil (including vitamin E) are lost. This is linked to the high procentage of polyunsaturated fatty acids contained within vegetable oils [10]. Unrefined sunflower oil possesses the lowest intensity of Peak I (535 a.u.). This can be due to its production procedure preserving the compounds that possess antioxidant effects, which in turn leads to its lower oxidation.

Good positive corelation was found between the intensities of the flourescence peaks (caused by the pigments and the oxidising compounds ($I_{696} = 0.69 * I_{581} - 83.52$)) with the determination coefficient $R^2 = 0.73$. Similar correlation for olive oil is reported by Kyriakidis and Skarkalis [11].

The color measurements of both colorimetric systems (XYZ and CIELab) show that the color parameters of the second colorimetric system (meant for detection of small color differences) are more useful for both customers and analysers. Within the color range of the colorimetric system CIELab, the color parameters a* and b* can be given in polar coordinates by calculating the color C and hue h, which are linked to the perseption of the human eye. The color shade is considered a qualitative attribute dwhen determining the color.

All samples have high brightness. The distribution of color parameters in the samples according to the CIELab colorimetric system is presented in Fig. 2 and all values are listed in Table

1. The color of the sunflower oil is due to carotenoids and chlorophyll pigments [12]. For all samples parameter a has low values, and if the error in the measurement apparatus is taken into account, for refined samples the parameter approaches negative values. This observation strongly confirms the Moyano thesis which states that the parameter a is positive for unrefined and cold-pressed oils and negative for olive oils and refined sunflower oil [13].
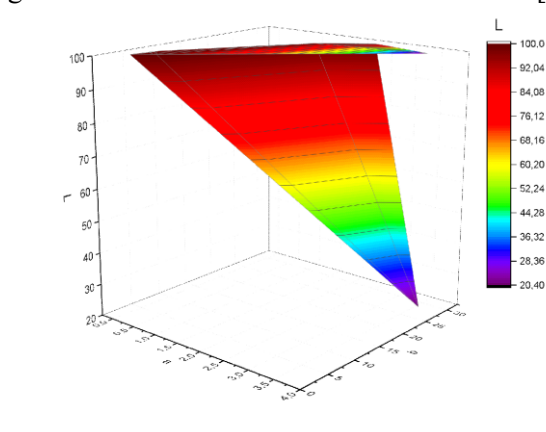

Fig. 2. Dependence between brightness and color parameter in CIELab colorimetric system

All samples have similar high luminosity, with the exception of the cold-pressed one. Similar fact has been reported by O'Brien [14]. The positive b component is attributed to the yellow color of the samples, caused by the presence of carotenoids [15]. The hue of the samples splits them in two groups: those with hue angle close to $90°$ (for refined samples) and those with angle between $82°$ and $85°$ (for unrefined and cold-pressed samples).
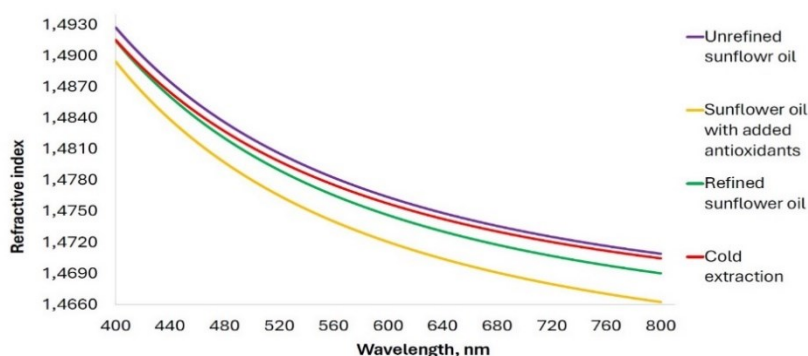
Table 1. Color parameters of sunflower oils

Sample	x	y	X	Y	Z	L	a	b	C	h
Cold extraction	0.53	0.446	3.7	3.1	0.2	20.5	3.6	28	28.3	82.7
Unrefined sunflower oil	0.481	0.427	114.7	101.9to	22.1	100	2.4	29.9	30	85.4
Biser	0.457	0.411	119.1	107.2	34.5	100	0.2	6.1	6.1	88.5
Sunflower oil with added antioxidants	0.458	0.413	108.1	97.2	30.4	98	0.2	7.6	7.6	88.6

Fig. 3. Refractive index dispersion curves of the sunflower oil samples

Table 2. Refractive indices measured by Abbe refractometer at 20 °C

Sample	Cold extraction	Unrefined sunflower oil	Refined sunflower oil	Sunflower oil with added antioxidants
Refractive index	1.4730	1.4718	1.4730	1.4690

According to the search results, the refractive indices of sunflower oil are as follows: 1.461 - 1.468 below 20 ºC, 1.461 – 1.4735 at 20°C [16].

It is important to note that the refractive index of sunflower oil can vary depending on factors such as temperature and specific type of sunflower oil being used. Using the Sellmeier's coefficients obtained from the refractive index data the dispersion curves of the refractive index were calculated for all samples in the spectral range (400-800) nm and plotted in Fig. 3.

It was found that the values of the refractive index for sunflower oil with added antioxidants are significantly lower than for the other investigated oils. These changes also can be associated with oxidation as a result of exposure to temperature changes during transport, storage, bottling or as a result of exposure to direct sunlight.

The refractive indices of the samples measured by using a standard Abbe refractometer are presented in Table 2.

It can be seen from the results shown in Table 2 that the sunflower oils with added antioxidants has the lowest refractive index value compared to other samples.

CONCLUSION

These initial studies imply that all offered physical techniques are connected and may be helpful in quickly identifying and evaluating the sunflower oil quality.

REFERENCES

1. B. S. Adeleke, O. O. Babalola, *Food Sci. Nutr.*, **8**, 4666 (2020).
2. B. Iegorov, O. Kananykhina, T. Turpurova, *Grain Products and Mixed Fodder's* (2022).
3. N. Potori, A. Stark, *Studies in Agricultural Economics*, **117**, 126 (2015).
4. W. P. Li, H. B. Shi, K. Zhu, Q. Zheng, Zh. Xu, *Agronomy Journal*, **109**, 2499 (2017).
5. A. R. Neto, A. M. Rauen de Oliveira Miguel, A. L. Mourad, E. A. Henriques, R. M. Vercelino Alves, *Crop Breed. Appl. Biotechnol.*, **16** (3), 197 (2016).
6. U. S. Pal, R. K. Patra, N. R. Sahoo, C. K. Bakhara, M. K. Panda, *Journal of Food Science and Technology*, **52** (7), 4613 (2015).
7. I. Bodurov, T. Yovcheva, S. Sainov, *Optica Applicata,* **45**, 199 (2015).
8. K. A. Omwange, D. F. Al Riza, Y. Saito, T. Suzuki, Y. Ogawa, K. Shiraga, et al., *Food Control*, **124**, Article 107906 (2021*)*.
9. N. Dupuy, Y. Le Dreau, D. Ollivier, J. Artaud, C. Pinatel, J. Kister, *Journal of Agricultural and Food Chemistry*, **53**, 9361 (2005).
10. B. Berra, R Gaspeli,. In: Third International Congress on the Biological Value of Olive Oil, Chania, Crete, Greece, 427 (1980).
11. N. B. Kyriakidis, P. Skarkalis, *Journal of AOAC International*, **83** (6), 1435 (2000)
12. F. Ramos-Escudero, M. L. González-Miret, A. Viñas-Ospino, M. Ramos Escudero, *J. Food Sci. Technol.*, **56**(11), 4901 (2019). doi: 10.1007/s13197-019-03960-x. Epub 2019 Jul 26. PMID: 31741514; PMCID: PMC682888
13. M. J. Moyano, A. J. Meléndez-Martínez, J. Alba, F. J. Heredia, *Food Res Int.,* **41**, 505 (2008). doi: 10.1016/j.foodres.2008.03.007.
14. R. D. O'Brien, Fats and oils: formulating and processing for applications, Boca Raton, Taylor & Francis, 2009, p. 680.
15. L. M. Giacomelli, M. Mattea, C. D. Ceballos, *J. Am. Oil Chem. Soc.*, **3**, 303 (2006). doi: 10.1007/s11746-006-1204-0.
16. S. J. Xu, X. K. Li, *Journal of Innovative Optical Health Sciences*, **14** (01), art. no. 2140010 (2021).

Effect of different hydrocolloids on Ca (II) – alginate beads containing extracts from *Arthrospira platensis*

N. T. Petkova[1], Kr. T. Nikolova[2*], G. D. Gentscheva[3,4], A. Ts. Gerasimova[5],
D. G. Kovacheva[4], N. K. Panova[2], St. At. Vladimirova[6]

[1]*Department of Organic Chemistry and Inorganic Chemistry, University of Food Technologies, Technological Faculty, 26 Maritza Blvd., 4002 Plovdiv, Bulgaria*

[2]*Department of Physics and Biophysics, Medical University of Varna, Faculty of pharmacy, 84 Tzar Osvoboditel Blvd., 9002 Varna, Bulgaria*

[3]*Department of Chemistry and Biochemistry, Medical University - Pleven, Faculty of Pharmacy, 1 Saint Kliment Ohridski Str., 5800 Pleven, Bulgaria*

[4]*Institute of General and Inorganic Chemistry, Bulgarian Academy of Sciences, Acad. Georgi Bonchev Str., Bl. 11, 1113 Sofia, Bulgaria*

[5]*Department of Chemistry, Medical University of Varna, Faculty of Pharmacy, 84 Tzar Osvoboditel Blvd., 9002 Varna, Bulgaria*

[6]*Institute of Physical Chemistry, Bulgarian Academy of Sciences, Acad. Georgi Bonchev Str., Bl. 11, 1113 Sofia, Bulgaria*

Alginate was applied in food matrix, and pharmaceutical products for efficient encapsulation of bioactive compounds or as a drug carrier. In the current study phycocyanin isolated from dry *Arthrospira platensis/Spirulina* was encapsulated in alginate beads. The aim of the current research was to evaluate the effect of different hydrocolloids (inulin, pectin and guar) at different pH values and temperatures on phycocyanin content in the alginate beads. The alginate microspheres were formed with 1% sodium alginate, 6% sucrose, 1% phycocyanin, and selected hydrocolloids, as neutral polysaccharides (inulin and guar) and anionic heteropolysaccharides (pectin). Moreover, the diameter of alginate-phycocyanin beads with or without hydrocolloids was evaluated. The addition of sucrose and inulin in a concentration of 6 % to alginate-phycocyanin beads stored at 25 and 37 °C showed the highest content of phycocyanin. The phycocyanin loss was minor at pH 6 and pH 9, respectively, especially when 0.8% pectin or 6% inulin was added to the alginate matrix. XRD patterns of all beads showed amorphous humps situated at different angles, depending on the particulate type of the hydrocolloid. The current research evaluates the potential of alginate beads with phycocyanin, as well as with pectin, guar and inulin to be used in food and pharmaceutical products.

Keywords: Ca (II) - alginate beads, phycocyanin, hydrocolloids, supplements

INTRODUCTION

Alginate is often used to create biodegradable microspheres that can be used to encapsulate unstable substances used in pharmaceuticals and food technology. In this way, unstable substances are protected from the pH of the environment in which they are used and/or from the action of enzymes contained in them [1]. As an anionic polysaccharide consisting of various ratios of L-guluronic and D-mannuronic acids linked by glycosidic bonds, alginate also has some disadvantages [2]:

- low encapsulation efficiency of the transported substance;
- rapid release of charged molecules.

The mentioned disadvantages are caused by the high porosity of the gel, which leads to leakage of the included medicinal products or phytopreparations from the alginate beads. The development of alginate microspheres with different hydrocolloids improving their properties, becomes more and more urgent task with the increasingly frequent use of novel drug delivery systems in pharmaceutical technologies. Microspheres - carriers of phytopreparations or medicinal substances, are essential for the transport and release of the substance at the target site with a controlled rate and good bioavailability [3]. Moreover, the addition of different hydrocolloids increases the stability of alginate gel and enhances the encapsulation process [4, 5]. Incorporation of natural polymers to alginate beads such as pectin [6], chitosan [7], inulin, cellulose, gelatin [8, 9] is an advantage not only due to their abundance in nature and the associated low price of the product, but also to the fact that they are low-toxic, biodegradable and biocompatible [10, 11]. The current research is aimed to evaluate the

* To whom all correspondence should be sent:
E-mail: *kr.nikolova@abv.bg*

effect of different hydrocolloids (inulin, pectin, and guar) at different pH values and temperatures on phycocyanin content in alginate beads.

MATERIALS AND METHODS

Materials

Sodium alginate with M-block 61%, G-block 39 %, and M/G ratio of 1.55 (Sigma-Aldrich, Munich, Germany), $CaCl_2$ and sucrose (Sigma-Aldrich, Munich, Germany). Inulin (Raftiline®HPX Beneo, Orafti, Belgium) with degree of polymerization DP = 25. Citrus pectin with a medium degree of esterification (DE = 70.6 %) originating from Spain. Guar gum was supplied from Orion (Bulgaria).

Phycocyanin extract

Dry *Arthrospira platensis* was purchased from the bioreactor (Varvara, Bulgaria). Phycocyanin was extracted in ultrasonic bath (IsoLab, Wertheim, Germany) at frequency 40 kHz, temperature 40 °C for 1 h [12]. The obtained water extract was filtered and lyophilized.

Preparation of Ca(II)-alginate beads with phycocyanin and different hydrocolloids

The calcium alginate beads encapsulated with phycocyanin and different hydrocolloids were prepared by the method of Petrova et al. [13] with slight modification. The resulting suspension of 1 % sodium alginate, 6% sucrose and 1 % phycocyanin was heated at 40 ºC for 3 min and homogenized with a laboratory Homogenizer IKA T18 (IKA – Werke GmbH & Co. KG, Staufen, Germany) for 2 min. Four different samples with 6% sucrose were prepared as follows:

A) control sample 1% alginate + 1% phycocyanin;

B) 1% alginate + 1% phycocyanin + 6.0 % inulin;

C) 1% alginate + 1% phycocyanin + 0.8% pectin;

D) 1% alginate + 1% phycocyanin + 0.6% guar.

To remove air bubbles, the obtained suspension was placed in the fridge for 60 min. The alginate beads were prepared as liquid solutions and were transferred into a syringe and dropped into a cold 2 % water solution of $CaCl_2$ at a temperature of 7 ºC. The obtained Ca(II)-alginate beads with phycocyanin and different hydrocolloids were filtered, washed twice with distilled water, and placed in containers with distilled water for further use.

Release of phycocyanin

24 hours after preparation, the absorption spectrum of the water with which the beads were flooded, was measured in order to determine the most suitable formulation for retaining phycocyanin.

Equal amounts of microspheres were placed in two different media at two different temperatures 25 ºC and 37 ºC - 25 mL acetate buffer with pH 6.0 and 25 mL ammonium buffer solution pH 9.0. The working solutions are obtained by mixing 25 pieces of the corresponding beads with 25 mL of a buffer solution with the corresponding pH. One series of solutions is left at 25 °C, and the other series of solutions is tempered for 30 min at 37 °C. The samples were taken 30 min after the establishment of thermal equilibrium maintained by a water bath.

The absorption spectra of the samples were measured in the visible range using a UV-VIS spectrophotometer. The phycocyanin content in the solution was determined according to the formula [14]:

$$phycocyanin(mg\ mL^{-1}) = \frac{A_{615nm} - 0.474 \times A_{652nm}}{5.34} \quad (1)$$

Average particle size

The average diameter and shape of the alginate microspheres were determined with a stereomicroscope SZ61 TR (Evident Corporation, Nagano, Japan). The spheres were observed in a bright field with reflected light at a 10 × objective and 4.5 × eyepiece magnification. Photos were taken with a 5Mp Wi-Fi camera Olympus EP50. The dimensions of the alginate spheres were determined using EPview software.

Morphology

For SEM and X-ray analyses the spheres were left to dry in open air at room temperature for 2 weeks.

The morphology of the dried alginate microspheres was examined using scanning electron microscopy (SEM) on a scanning electron microscope JEOL JSM-6390 (Tokyo, Japan). Samples were mounted on a metal holder using a sticky carbon band with increased conductivity and coated with gold. Accelerating voltage 20 kV, magnification ×10000 in secondary electrons.

X-ray analysis

Patterns of the alginate microspheres were collected within the range from 5.3 to 80° 2θ with a constant step 0.02° 2θ and counting time 52.5 sec./step on Bruker D8 Advance diffractometer (Germany) with Cu K_α radiation and LynxEye detector. Phase identification was performed with the Diffracplus EVA using ICDD-PDF2 (2014) database.

RESULTS AND DISCUSSION

The dimensions of 20 alginate spheres of each type were determined using an optical microscope. Table 1 presents the mean diameter ± standard deviation.

Table 1. Characterization of the size of alginate beads with phycocyanin.

Formulation	Polysaccharide concentration, %	Length ± SD μm	Width ± SD μm
Sample A	Alginate 1	3791 ± 236	3661 ± 101
Sample B	Alginate 1 - Inulin 6.0 %	3466 ± 203	1978 ± 116
Sample C	Alginate 1 - Pectin 0.8 %	4486 ± 624	4485 ± 626
Sample D	Alginate 1 - Guar 0.6 %	3749 ± 103	3726 ± 103

The shape of the beads is shown in Figure 1.
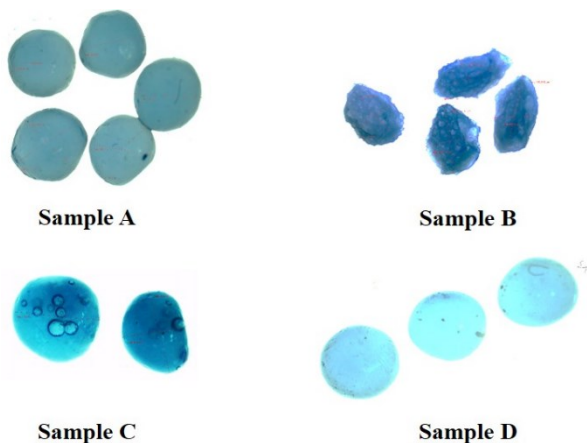
Figure 1. Shape of the alginate beads imaged with an optical reflection microscope.

The control samples with alginate and phycocyanin, as well as with alginate, phycocyanin, and guar (sample D), have an almost spherical shape, and a smooth surface with slight "wrinkles" on it. The samples with phycocyanin, alginate and pectin (sample C), similar to the above-mentioned samples, have a smooth surface and a spherical shape, but air bubbles are clearly observed under the surface layer of the beads. This can be related to the increasing viscosity of the sample when pectin is added. The alginate-phycocyanin-inulin samples (sample B) were irregularly, star-shaped, and were much smaller than the other beads.

The relatively large size and spherical shape is determined by the low concentration of calcium dichloride (2%) in the preparation of the alginate spheres. A low concentration of calcium leads to a higher water content in the gel and a limitation of

gelation [15]. As the concentration of calcium dichloride increases, the size of the spheres decreases due to an increase in cross-linking [16].

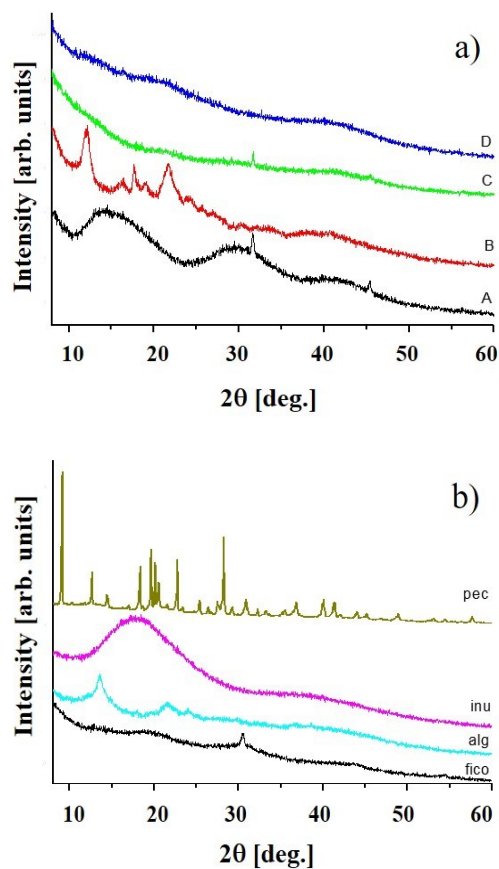The X-ray spectra of the investigated samples are presented in Figure 2.

Figure 2. X-ray spectra of b) starting substances and a) alginate spheres with additives respectively: A) control sample 1 % alginate + 1 % phycocyanin; B) 1 % alginate + 1 % phycocyanin + 6.0 % inulin; C) 1 % alginate + 1 % phycocyanin + 0.8 % pectin; D) 1 % alginate + 1 % phycocyanin + 0.6 % guar.

In the X-ray pattern of citrus pectin, peaks of highly crystalline residues of glucose (ICDD-PDF#00-24-1964) and glucose-hydrate (ICDD-PDF#00-30-1736) are observed, while inulin shows a typical amorphous pattern consisting of one "hump" with a maximum at around 18.5 º 2θ.

Na-alginate is characterized by a semi-crystalline diffraction pattern with the strongest peaks at 13.4º, 21.5º and 24.1º 2θ, which correspond to G(110), G(200)+M(020) and M(200) reflections from G and the M-blocks of the alginate structure [17, 18].

The pattern of phycocyanin comprises an amorphous component and a very small amount of a crystalline phase identified as (Na, K) Cl (ICDD-PDF#01-075-0303).

The X-ray pattern of the alginate spheres with phycocyanin (A) shows amorphous peaks, which

indicates that interaction of the two components has occurred. A small amount of crystalline phase identified as NaCl was also detected (ICDD-PDF#01-080-3939).

The X-ray pattern of the sample with alginate, phycocyanin, and inulin (Sample B) presents a semi-crystalline sample in which the alginate peaks are preserved, perhaps indicating the stronger interaction of phycocyanin with inulin.

In the sample of phycocyanin, alginate, and pectin (C), as well as in that of phycocyanin, alginate, and guar (D), amorphous diffraction patterns are observed. A small amount of crystalline NaCl (ICDD-PDF#01-080-3939) was also detected in the phycocyanin, alginate, and pectin samples.
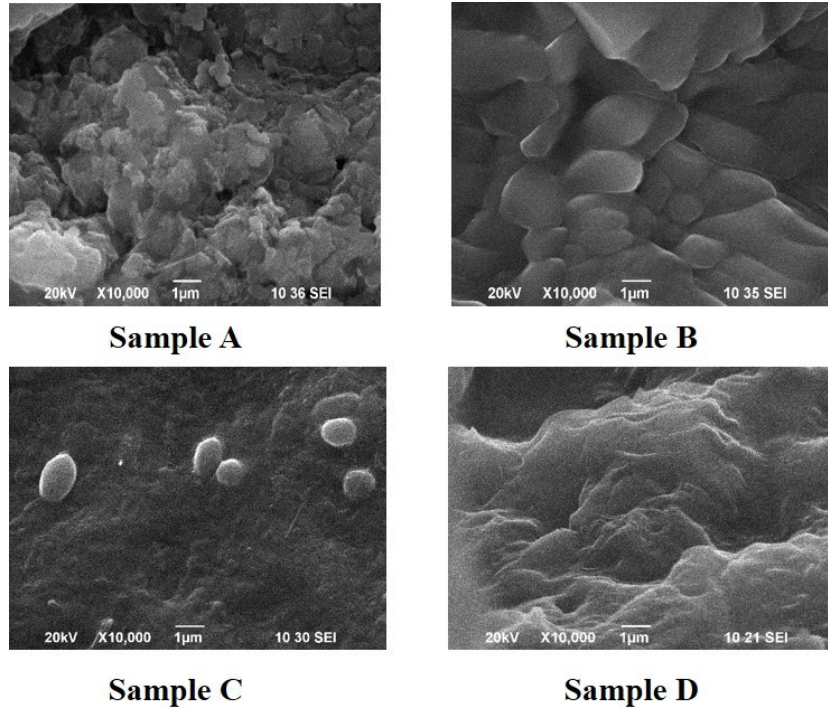
Figure 3. Morphological structure of the surface of the alginate beads.
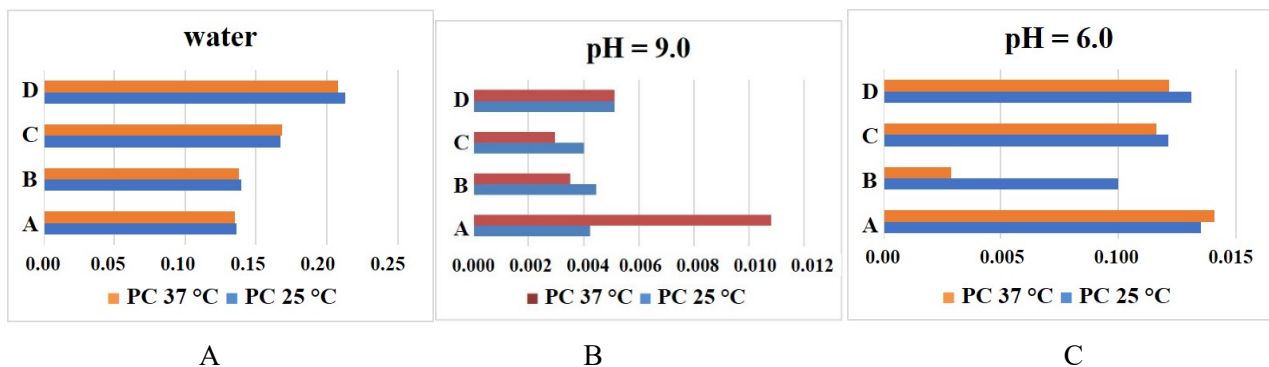
Figure 4. Release of phycocyanin from alginate microspheres.

More detailed information on the morphological structure of the surface of the spheres was obtained from scanning electron microscopy (SEM) of the dried samples. The results are presented in Figure 3. After drying at room temperature, the microspheres lose their spherical shape, and their surface looks different depending on the constituents of the spheres. Sample A is characterized by a rough surface morphology, which is made up of irregularly shaped particles aggregated into larger structural motifs with gaps (pores) between them. In sample B, the particles are larger with a slightly elliptical shape with smooth edges and adhere to each other. The surfaces of samples C and D are smoothed, without clearly defined particles, and in sample C, spherical particles are also observed above the surface, probably as a result of the transformation of air bubbles during the drying of the sample.

The results of phycocyanin release are shown in Figure 4.

161

The release of phycocyanin in an aqueous environment after a 24-hour stay of the alginate pearls was investigated to study the possibility of using them in smoothies or juices as a functional additive. In aqueous media, the release of phycocyanin at room and body temperature was almost the same for the control sample and that with added inulin, followed by that with pectin. The retention of the substance by alginate spheres with guar is the weakest.

With the ammonium buffer, except for the control, for all other samples the release of phycocyanin after 30 minutes at a temperature of 37 °C was weaker than at a room temperature of 25 °C.

In the case of the acetate buffer, the weakest phycocyanin loss was observed in the samples with inulin at 37 °C. Therefore, inulin incorporated in alginate beads fixed well phycocyanin into alginate-inulin matrices.

CONCLUSION

From the obtained results can be seen that inulin addition to alginate gel stabilized phycocyanin in the matrix and preserved it at all pH and water solutions. Therefore, this polysaccharide is proper as an encapsulating agent for phycocyanin together with alginate. In water solutions, the concentration of phycocyanin can reach 0.2 mg/ml when guar is used together with alginate. The most efficient encapsulating agent is 1 % alginate and 1 % alginate with 6 % inulin (Sample B). At pH 9 most efficient are pectin and inulin added to 1 % alginate (Samples B and C), while at pH 6 the phycocyanin is retained better in 1 % alginate and 6 % inulin (Sample B).

REFERENCES

1. S. Onal, F. Zihnioglu, *Artif. Cells Blood Substit. Imm. Biotech.,* **30 (3),** 229 (2002).
2. A. Halder, S. Maiti, B. Sa, *International J. of Pharmaceutics,* **302 (1–2),** 84 (2005).
3. S. Gujral, S. Khatri, *IJAPBC,* **2,** 2277 (2013).
4. R. Bhagwat, I. Vaidhya, *Int. J. Pharm. Sci. Res.,* **4,** 970 (2013).
5. I. Petrova, N. Petkova, A. Slavchev, T. Petrova, *Mater. Sci. Eng.,* 1031 (2021).
6. V. Pillay, M. P. Danckwerts, Z. Muhiddino, R. Fassihi, *Drug Development and Industrial Pharmacy,* **31,** 91 (2005).
7. Y. Murata, K. Tsumoto, K. Kofuji, S. Kawashima, *Chem. Pharm. Bull.,* **51,** 218 (2003).
8. P. F. Almeida, A. J. Almeida, *J. Control. Rel.,* **97,** 431 (2004).
9. M. S. Hamid Akash, K. Rehman, S. *Chen. Polym. Rev.,* **55,** 371 (2015).
10. K. M. Z. Hossain, U. Patel, I. Ahmed, *Prog. Biomater.,* **4,** 1 (2015).
11. P. Singh, D. Prakash, B. Ramesh, N. Singh, T. T. Mani, *Ind. J. Novel Drug Delivery,* **3,** 70 (2011).
12. I. Minchev, N. Petkova, I. Milkova-Tomova, *Biointerface Research in Applied Chemistry,* **11(2),** 9296 (2021).
13. I. Petrova, N. Petkova, A. Slavchev, T. Petrova, *IOP Conf. Series: Materials Science and Engineering,* 1031 (2021).
14. A. Bennett, L. Bogorad, *J. Cell Biol.,* **58,** 419 (1973).
15. J. R. Rodrigues, R. Lagoa, *J. of Carbohydrate Chem.,* **25,** 219 (2006).
16. H. Daemi, M. Barikani, *Scientia Iranica,* **19,** 2023 (2012).
17. S. Bhagyaraj, I. Krupa, *Molecules,* **25(3),** 435 (2020).
18. J. Fabia, C. Z. Slusarczyk, A. Gawlowski, *Fibres. Text. East Eur.,* **13,** 114 (2005).

Physicochemical profile of colostrum from Bulgarian White Dairy breed goats - first day after birth

S. Stoycheva*, L. Mondeshka

Agricultural Academy-Sofia, Research Institute of Mountain Stockbreeding and Agriculture, 281 Vasil Levski Str., 5600 Troyan, Bulgaria

Colostrum is the first food that mammals receive immediately after birth. Its unique chemical composition and qualities distinguish it from milk and make it an indispensable source of nutrients and passive immunity for the newborns. The most intense changes in the composition and properties of colostrum are observed in the first twenty-four hours after birth, and by the fifth day its biochemical and physicochemical parameters reach values characteristic of milk. Both interspecies and interbreed differences in the colostrum composition have been found.

Bulgarian White Dairy breed (BWD) is the only goat breed created in Bulgaria. It was created in the Research Institute of Mountain Stockbreeding and Agriculture of Troyan (RIMSA), by crossbreeding of local white goats and Saanen bucks. It is perfectly adapted to the climatic conditions of Bulgaria.

The purpose of the present study was to observe the changes in the physicochemical parameters that occurred during the first twenty-four hours in the colostrum of goats of the Bulgarian White Dairy breed. The research work was conducted in the Meat and Milk Laboratory at the Research Institute of Mountain Stockbreeding and Agriculture of Troyan.

For the twenty-four-hour period of the study, a reliable decrease of the indicators was reported, such as protein (14.97-5.33%), total solids (26.47-15.71%), solid- non-fat (SNF) (20.46- 10.88%), density (1.0443-1.0356 g/ml^3), acidity (35-20°T), milk fat (6.67-5.19%) and calcium (Ca) (0.240-0.145 mg/%). In contrast, the lactose (2.99-4.19%) and pH (6.2-6.33) showed an increase in their values. The obtained results are within the optimal limits for this animal species and are the first reported for BWD breed.

Keywords: colostrum, goats, physicochemical parameters, Bulgarian White Dairy breed

INTRODUCTION

Colostrum is the first food that mammals receive immediately after birth. Its unique chemical composition and qualities distinguish it from milk and make it an indispensable source of nutrients and passive immunity for the newborns. Both interspecies and interbreed differences in the colostrum composition have been found.

The most intense changes in the composition and properties of colostrum are observed in the first twenty-four hours after birth, and by the fifth day its biochemical and physicochemical parameters reach values characteristic of milk (Sánchez-Macías *et al.* [1]; Dimov *et al.* [2]). The changes that have occurred are a consequence of physiological processes that are most strongly influenced by factors such as health status, mother's diet, sequence of lactation [1], number of kids born (Knight and Peaker [3]), etc. Knowing the changes that occur during the colostrum and the entire lactation period and establishing milk quality criteria will guarantee a better quality

of the final products (Raynal-Ljutovac *et al.* [4]). According to Salem *et al.* [5], as the main nutritional component of colostrum and milk, milk proteins are essential, not only for the nutrition and growth of the offspring, but also in various technological aspects such as heat treatment, coagulation and rate of digestion.

Bulgarian White Dairy goat breed (BWD) was created in the RIMSA of Troyan, by crossbreeding of local white goats and Saanen bucks, it is the only breed of goats created in Bulgaria. Animals of this breed are perfectly adaptable to the climatic conditions of Bulgaria and represent the largest part of the goats raised in our country.

To date, in the available literature there is no information on the colostrum composition, milked on the first day after birth, in goats of BWD breed.

The purpose of the present study was to observe the changes in the physicochemical parameters that occurred during the first twenty-four hours in the colostrum of goats of the Bulgarian White Dairy breed.

---

* To whom all correspondence should be sent:
E-mail: s.e.stoycheva@abv.bg

MATERIAL AND METHODS

The study was conducted in the goat farm of the Experimental Base of the Research Institute of Mountain Stockbreeding and Agriculture of Troyan, located in the foot-hill of the Central Balkan Mountain, at 380 m above sea level.

The colostrum analyzed for the present study was obtained from twenty clinically healthy goats of BWD breed during the period of kidding. The samples were milked at the first and twenty-fourth hour after birth, as each of them was placed in an individual container of 200 ml and transported to the Meat and Milk Laboratory at the Laboratory complex of RIMSA-Troyan. The physicochemical analysis includes a total of nine indicators, of which milk fat, protein, lactose, solids, solid-not-fat were analyzed on a MilkoScan FT 120 Foss Electric device, and the samples were previously tempered to 40°C in a water bath to homogenize them. The obtained results are expressed in percentages (%).

Acidity and calcium (Ca) were determined by standard titration methods. Colostrum density was measured by weight method, at a sample temperature of 20°C, and reported in g/cm^3. Active acidity (pH) was determined using a pH meter 3110 SET 2- Wissenschaftlich-Technische Werkstatten.

The statistical processing was done using JMP v.7 software package. The results were presented as means and standard deviations (SD). Means were compared through t-test.

RESULTS AND DISCUSSION

Table 1 shows the chemical composition of colostrum at both time points of its obtaining.

Table 1. Chemical composition of colostrum from BWD goats in the period of 24h *postpartum*.

Indicators, %	1h		24 h		Sig.
	Mean	SD	Mean	SD	
Fat	6.67	2.16	5.19	1.75	*
Protein	14.97	2.23	5.33	1.48	***
Lactose	2.99	0.62	4.19	0.33	***
TS	26.47	4.02	15.71	2.73	***
SNF	20.46	2.07	10.88	1.26	***

* p < 0.5; *** p < 0.001

Protein

During the first twenty-four hours after birth (Table 1), the protein content in the colostrum decreased by 9.64% (p < 0.001). According to Arguello *et al.* [6], when the amount of colostrum or milk increases, the total protein content decreases, and this is most pronounced in dairy breeds such as the Bulgarian White Dairy goat. The values we report are a consequence of this physiological process and correspond to what has been described in studies in different breeds (Keskin *et al.* [7]; Moreno-Indias *et al.* [8]; Romero *et al.* [9]; Hodulová *et al.* [10]; Soloshenko *et al.* [11], Paramasivam *et al.* [12]). Kosum *et al.* [13] found in Saanen goats a decrease by 4.46% in the protein amount in the colostrum in the first 24 hours. For Majorera goats, [6] reported a reliable decrease in total protein during the first two days after birth. Again, in Majorera goats that gave birth to twins, [1] found that protein decreased by 45% in the 48-h period after birth. The high amount of protein during the first hours after birth is explained by the higher content of immunoglobulins, leukocytes, lactoferrin, lysozyme, growth hormones, some amino acids, etc. (Pellegrini *et al.* [14]; Rashid *et al.* [15]). Rachman *et al.* [16] reported a drastic drop in lactoferrin levels in the first 48 hours after birth in three goat breeds in Indonesia.

Lactose

Lactose is the main carbohydrate that the newborns receive with colostrum It is absorbed faster than fat [6]. In the present study, an increase was observed in the milk sugar content in the colostrum of BWD goats by 1.2% (p < 0.001) for the studied twenty-four-hour period (Table 1). That corresponds to the results obtained in the study on the colostrum of various goat breeds, in Majorera goats [1, 6], in Murciano-Granadina goats [9], etc.

[15] studied the colostrum composition of Beetal goats and found that when passing into milk, the lactose amount increased from 2.93% on the first day to 3.8% on the second day and 4,4% on the third day. Lactose favors the intestinal absorption of calcium, magnesium, phosphorus and vitamin D3 (Chilliard *et al.* [15, 17]). According to Olechnowicz and Sobek [9, 18], lactose concentration follows the pattern of milk production, as it increases immediately after birth, it reaches a peak and then decreases.

Total solids

The content of the total solids in the colostrum obtained at the first hour after birth was 10.76% (p < 0.001) more than the same obtained at the 24th hour (Table 1). The present findings correspond with the results of [10] in Czech White Shorthair goats, the authors reported a 10% decrease in colostrum total solids, as well as Elmaz *et al.* [19] in Honamli goats. [9] reported the highest total solids values for Murciano-Granadina goats in the first hour after birth and a decrease of 10% up to the 24th hour. Hadjipanayiotou [7, 20] reported that the total solids content of colostrum of Damascus goats was the

highest on the first day and decreased gradually until the third day.

*The solid-not-fat (*SNF) includes protein, lactose and minerals and is a relatively more constant quantity than total solids [2]. In the present study, SNF of colostrum decreased by 9.28% (p < 0.001) at the twenty-fourth hour compared to the first hour after birth (Table 1). The decrease in values in the present study is in agreement with that reported for other goat breeds. Marounek *et al.* [21] reported for the colostrum of White shorthaired goats, SNF of 16.03% at the first hour and 13.24% at the 24th hour. In Majorera goats, [1] found a decrease in the percentage of solid-not-fat from 13.87% after birth to 10.90% 24 hours later.

Fats

For the colostrum in the present study, a slight decrease in the percentage of fat content of 1.48%, (p > 0.5) was reported (Table 1). In Saanen goats, [13] reported a decrease in fat content from 8.27% to 6.76% in the first 24 hours, where as it was up to 5.79% at the 48th hour. A similar decrease in the amount of fat in colostrum during the first 24 hours after birth was also reported by [19] in goats of Honamli breed, by [10] in Czech White Shorthairs and Kráčmar *et al.* [22] in Brown Short-haired breed. In contrast to the present study,[6] found an increase in fat in the colostrum at 24 hours after birth, and this contradiction could be explained by the fact that all cisternal milk was removed on the first day.
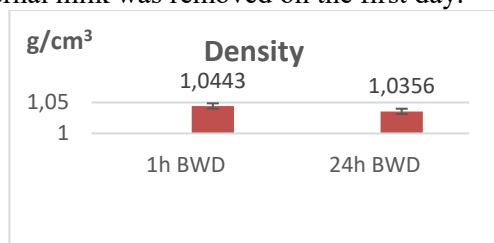
Figure 1. Mean density values (g/cm^3) of colostrum from BWD goats at the 1st h and 24th h after birth.

Figure 1 presents the decrease in colostrum density values for the first 24 hours after birth. According to [9], colostrum density drops sharply around the 12th hour after birth and continues to decline more smoothly until the 156th hour. For the Murciano-Granadina goat breed, the author reported a decrease from 1.0528 to 1.0303 g/cm^3 at 156th hour, as colostrum density was 1.0377 g/cm^3 at the 24th hour, which coincides with the present findings. Tôrres Vilar *et al.* [23] in Saanen goats in Brazil, under similar climatic conditions to Bulgarian, reported a decrease from 1.0530 at the first hour to 1.0280 g/cm^3 at the 24th hour.

There is a direct interconnection between the colostrum density, the change in the amount of fat

and the milk composition, i.e. the higher the content of solids of the colostrum, the higher the density (Prasad *et al.* [24]).

We found values of 35ºT at the first hour after birth and 20ºT at 24th h for the titratable acidity of BWD goat colostrum (Fig. 2) The present finding is in agreement with [9] for Murciano-Granadina goats and [23] for Saanen goats and although our results are slightly lower, the trend towards a decrease in acidity is the same and we attribute the differences to interbreed differences.
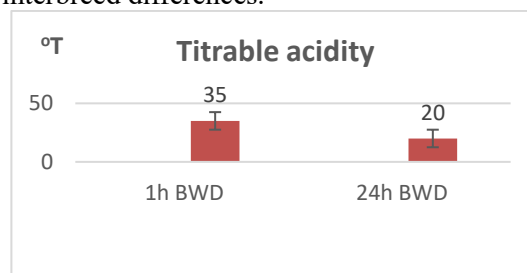

Figure 2. Mean values for the titratable acidity (ºT) of colostrum from BWD goats at 1st h and 24th h after birth.

Titratable acidity is determined immediately after milking and indicates the presence of phosphates, citrates, proteins and gases in the milk. In the milk of different species of animals, it varies within narrow limits, as in goat's milk, it is around 15-16°T. The primary acidity depends on the animal's health condition, nutrition and the lactation period, at the beginning of lactation, colostrum has a very high acid degree, then it enters the above limits and by the end of the lactation period it falls below 15°T [2].

[23] reported a very high correlation between colostrum protein content and titratable acidity (r = 0.9) and confirmed the theory of Mariani *et al.* [25] that lower percent protein results in lower titratable acidity.
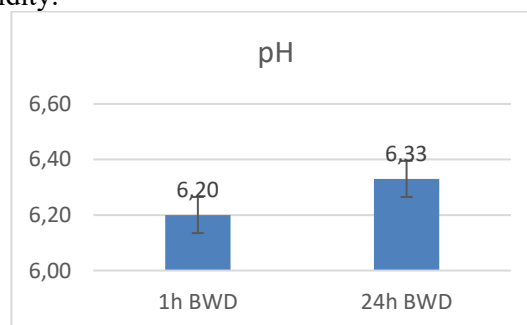

Figure 3. Mean pH values of colostrum from BWD goats at 1st h and 24th h after birth.

The active acidity (pH) of milk decreases more slowly than the titratable one, which is due to the buffering properties of milk, which are determined by the content of protein substances and salts [2]. In the present study, a slight increase was observed in average pH values from 6.2 at the first hour to 6.3

twenty-four hours later (Fig. 3). [23] reported pH 6.40 in colostrum at the first hour and pH 6.68 at the 24th hour for Majorera goat breed. In a similar study, [9] indicated a slight increase in the first twenty-four hours from pH 6.58 to pH 6.62. Similar to the data published by [1], again no significant variation in values was observed.
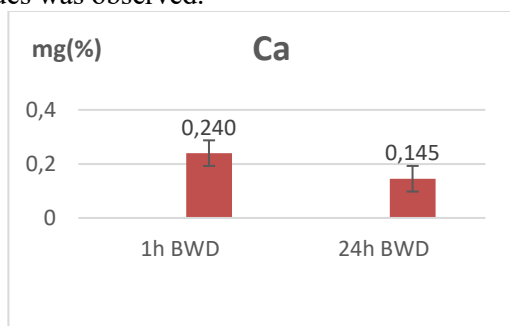

Figure 4. Average Ca values (mg/%) of colostrum from BWD goats at 1st h and 24th hour after birth.

The amount of Ca (Fig. 4) in colostrum from BWD goats at the first hour after birth was 0.239 mg/%, and at the twenty-fourth hour it was 0.145 mg/%. The calcium content in fresh goat's milk is found in the ionic, molecular and colloidal-dispersed state. Its amount in milk is relatively constant. The increased or decreased content of calcium in milk depends on the health of the animals, the lactation period and their nutrition [2].

CONCLUSIONS

The composition of colostrum from goats of BWD breed changes significantly during the first 24 hours after birth. A reliable decrease in the indicators was found: protein-(14.97-5.33%), total solids (26.47-15.71%), SNF (20.46-10.88%), density (1.0443-1.0356g/cm^3), acidity-(35-20°T), milk fat (6.67-5.19%) and calcium (Ca)-(0.240-0.145mg/%). In contrast, the lactose (2.99-4.19%) and pH (6.2-6.33) indicators showed an increase in values.

The obtained results are within the optimal limits for this animal species and are the first reported for BWD breed. Future research in this direction will enrich the knowledge about the composition and properties of colostrum from the most widely spread goat breed in Bulgaria and will benefit farmers.

REFERENCES

1. D. Sánchez-Macías, I. Moreno-Indias, N. Castro, A Morales-de la Nuez, A. Argüello, *J. Dairy Sci.,* **97**(1), 10 (2014).
2. N. Dimov, Q. Shalichev, P. Mineva, Dairying, State publishing house for agricultural literature, Sofia, 1975.
3. C. H. Knight, M. Peaker, *Q. J. Exp. Physiol.,* **67**(1), 165 (1982).
4. K. Raynal-Ljutovac, P. Gaborit, A. Lauret, *Small Rumin. Res.*, **60**(1), 167 (2005).
5. S. A Salem, I. E. A. Elsayed, F. A. Salama, N.H. Soliman, *Tropical and Subtropical Agroecosystems*, **11**(1), 29 (2009).
6. A. Arguello, N. Castro, S. Álvarez, J. Capote, *Small. Rumin. Res.*, **64**(1-2), 53 (2006).
7. M. Keskin, Z. Güler, S. Gül, O. Biçer, *J. Appl. Res.* **32**(1), 25 (2007).
8. I. Moreno-Indias, D. Sánchez-Macías, N. Castro, A. Morales-de la Nuez, L. E. Hernández-Castellano, J. Capote, A. Argüello, *Small Rumin. Res.*, **103**, 220 (2012).
9. T. Romero, M. C. Beltrán, M. Rodríguez A. Martí De Olives, M. P. Molina, *J. Dairy Sci.*, **96**(12), 7526 (2013).
10. L. Hodulová, L. Vorlová, R. Kostrhounová, *Acta Veterinaria Brno*, **83** (10), 15 (2014).
11. K. I. Soloshenko, I. V. Lych, I. M. Voloshyna, L. V. Shkotova, *Biopolymers and Cell.*, **36**(3), 197 (2020).
12. S. Paramasivam, B. Ramkumar,·U.Chinnaiyan, S. Polaki, D. Vegulada, P. Ranganathan, P. Ramasamy, *Journal of Food Measurement and Characterization* (2023). https://doi.org/10.1007/s11694-023-02033-0
13. N. Koşum, T. Taşkın, Ö. Kınık, Ç. Kandemir, E. Akan, *J. Anim. Prod.*, **59**(1), 1-8 (2018).
14. O. Pellegrini, F. Remeufa, M. Rivemale, *Lait,* **74**(6), 425 (1994).
15. A. A. Rashid, M. Yousaf, A. M. Salaryia, S. Ali, Pak. *J. Biochem. Mol. Biol.*, **45**(3), 113 (2012).
16. A. B. Rachman, R. R. A. Maheswari, M. S. Bachroem, *Procedia Food Science*, **3**, 200 (2015).
17. Y. Chilliard, A. Ferlay, J. Rouel, G. Lamberet, *J. Dairy Sci.*, **86**(5), 1751 (2003).
18. J. Olechnowicz, Z. Sobek, *J. Anim. Feed Sci.*, **17**(1), 41 (2008).
19. O., Elmaz, F. Taşçı, A. A. Akbaş, M. Saatcı, *Animal & Food Sciences Journal Iasi,* 157 (2022).
20. M. Hadjipanayiotou, *Small Rumin. Res.*, **18**(3), 255 (1995).
21. M. Marounek, L. Pavlata, L. Mišurová, Z. Volek, R. Dvorák, *Czech J. Anim. Sci.*, **57**, 28 (2012).
22. S., Kráčmar, S. Gajdůšek, J. Kuchtík, P. Jelínek, B. Minařík, *Acta Univ. Agri. et Silvi. Mendelianae Brunensis*, **5**, 91 (2002).
23. A. L. Tôrres Vilar, R. Germano Costa, P. Marques de Souza, A. Nunes de Medeiros, R. de Cássia Ramos do Egypto Queiroga, M. Ferreira Fernandes, R. Bras, *Zootec.*, **37**(9), 1674 (2008).
24. H. Prasad, P. S. Sengar, *Small Rumin. Res.*, **45**(1), 79 (2002).
25. P. Mariani, M. Pecorari, E. Fossa, S. Fieni, *Sci. Tecn. Lat.,* **32**, 222 (1981).

Synthesis and antioxidant activity of benzazole-based hybrids

M. Bachvarova[1], D. Kirkova[2], Y. Stremski[1*], E. Suyleyman[1], S. Statkova-Abeghe[1],
M. Docheva[2]

[1]Paisii Hilendarski University of Plovdiv, Faculty of Chemistry, Dept. of Organic Chemistry, 24,"Tzar Assen" Str. Plovdiv 4000, Bulgaria
[2]Tobacco and Tobacco Products Institute, Agricultural Academy, Markovo 4108, Bulgaria

The preparation of benzazole derivatives with a phenolic fragment in the second position is of great interest to the synthetic community. These compounds have been applied as antioxidants in medicine but also in the food and cosmetic industry as preservatives. Some phenols such as resorcinol have high toxicity and different methods for their structure modification are often studied and announced. Molecular hybridization with the introduction of a benzazole substituent in the aromatic ring of resorcinol would lead to enhanced oxidative stability and radical scavenging activity. The results showed more active profiles of benzothiazole-containing derivatives than benzimidazole ones.

Keywords: Multifunctional molecules, resorcinol, quercetin, benzazole hybrids, radical scavenging activity, α-amidoalkylation

INTRODUCTION

Benzimidazole ring is an important pharmacophore used widespread in medicine [1]. This privileged structure has an important biological significance based on a varied range of biological properties, such as antioxidant [1-3], antimicrobial [4], anti-inflammatory [5], antifungal [4], etc. The literature reports have shown remarkable antiproliferative [6-8] and antitumor activities [2, 3] of 2-phenylbenzimidazole compounds. The antiproliferative effect of a series of benzimidazole-based compounds has been tested on Colo-38 human skin cancer melanoma cells. Compound *1* (Figure 1), shows the highest antiproliferative effect at low micromolar concentration (IC$_{50}$ = 6.20 μM) [7].
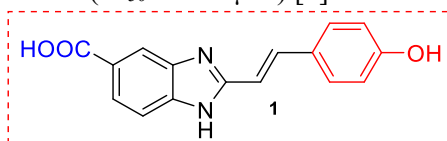

Figure 1. Phenol-containing hybrid *1*

Photoprotectors including various sunscreens are important since they reduce a large number of skin diseases caused by UV radiation [9]. Some synthetic benzazole compounds have proved potential application as UV-protectors in cosmetics [7, 8, 10, 11]. In this regard, 2-phenyl-1*H*-benzimidazole-5-sulfonic acid *2* (PBSA, Figure 2) is one of the UVB filters used most commonly in cosmetics for sun protection, having an excellent safety profile. Another example is Oxisol *3* (Figure 2), as well as the disodium salt of phenyl-dibenzimidazole tetrasulfonate *4* (known as Neo Heliopan, Figure 2), which absorb mainly in the UVA range. Neo Heliopan is water-soluble, photostable and safe, with extremely low skin penetration. In addition, the 2-aryl benzimidazole compounds *5* showed satisfactory SPF values tested *in vitro* compared to the commercial PBSA filter [7].
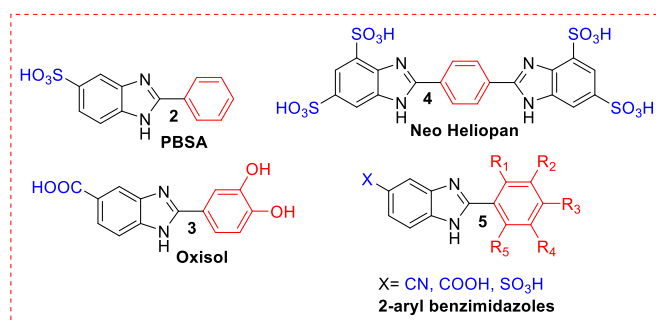

Figure 2. Benzimidazole-based UV-filters

---

* To whom all correspondence should be sent:
E-mail: *stremski@uni-plovdiv.net*

According to the authors, the most promising 2-arylbenzimidazole-5-sulfonic acids (compounds *6* and *7*), as well as 2-styryl-benzimidazole *1* show broad-spectrum solar protection against UVA and UVB rays [7].
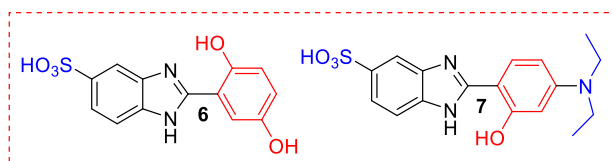

Figure 3. 2-arylbenzimidazole-5-sulfonic acids *6*, *7*

Many polyphenols isolated from plants, including flavonoids, are reported to have significant photoprotective effects on the skin and act as weak UV-filters. In addition, they have antioxidant, anti-inflammatory and anticarcinogenic profiles. The presence of hydroxyl groups and aromatic fragments in the structure improves their capability of absorbing UV light in a wide range of wavelengths, which determines their properties [12]. Recent research suggested that polyphenols may be an effective source of skin protection from the effects of UV rays (UVA и UVB) [13].

A validated and standardized method for *in vitro* assessment of UVA protection is described in ISO 24443:2021 [14], while the assessment of UVB protection is still not clearly investigated. The method proposed by Diffey-Robson for *in vitro* estimation of the SPF parameter in 1989 has been widely and successfully applied [15]. Djuidje *et al.* recently reported for the synthesis of various 2-substituted benzimidazoles, structural analogues of phenylbenzimidazole sulfonic acid (PBSA). The isosteric modification approach was used by the authors to design and investigate the structure-activity relationship of benzimidazole derivatives. The compounds showed good antifungal activity against *M. gypseum, M. canis, T. mentagrophytes, T. tonsurans* and *E. floccosum* with IC_{50} values in the range of 0.97–3.80 µg/ml. The authors concluded that series of 2-heteroaryl benzimidazoles could be privileged for the development of new multifunctional molecules, useful for the treatment of multifactorial diseases [16].

In the last decade, the design and synthesis of novel multifunctional benzazole molecules with antioxidant activity similar to the polyphenols has been of interest among the scientific community [7]. A series of newly synthesized 2-aryl benzimidazoles (*5*, Figure 2) were estimated for their antioxidant potential. DPPH, FRAP and ORAC assays were used for the evaluation of radical scavenging activity of the synthesized

168

compounds and their structure-activity relationship depending on the number and position of hydroxyl groups in the 2-aryl moiety. The presence of diethylamino group or 2-styryl group is associated with good antioxidant potential. Also, it was observed that the presence of sulfonic acid group at the 5-position of the benzimidazole core was the least favourable, while derivatives containing 5-cyano- or 5-carboxy-groups showed moderate to high antioxidant activity [7].

High antioxidant activity for benzazole compounds containing resorcinol in their structure, represented by the general formula (Figure 4) has been also reported [3]. Racane *et al.* compared the DPPH and ABTS radical scavenging assays, in terms of evaluating the antioxidant activity of a series of 2-aryl benzimidazole and benzothiazole compounds. Benzimidazole compounds were found to exhibit higher radical scavenging activity compared to benzothiazole analogues *via* the ABTS method [3].
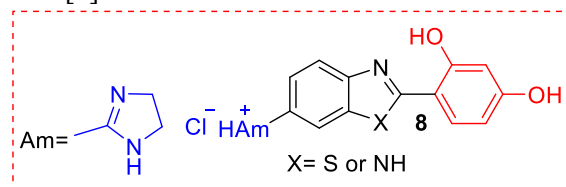

Figure 4. Benzazole-resorcinol hybrids *8*

In recent studies, we reported the synthesis of some 2-hydroxyphenyl benzothiazolines following an accessible reaction of α-amidoalkylation [17]. In addition, the results for their antimicrobial activity gave good lead for further structure optimisations. Furthermore, we proposed the synthesis of novel quercetin hybrids with potent radical scavenging activity [18], and also possibility for modification of a benzimidazole ring with resorcinol [19].

In this study, we have applied our efficient protocol to synthesize benzazole-resorcinol hybrids [17, 19], exploring their radical scavenging potential. Assessing their ability to neutralize free radicals is particularly relevant for potential use in cosmetics, addressing both aesthetic concerns and skin health. Positive results could position these compounds as promising candidates for further cosmetic research, contributing to the development of skincare products with enhanced antioxidant and protective properties. This study aligns with the ongoing quest for multifunctional molecules in cosmetic science.

MATERIALS AND METHODS
Reagents and equipment

The starting reagents, solvents and materials were provided by commercial suppliers (Merck).

Melting points were determined on a Kruss M5000 melting point meter. HRMS spectral measurements were performed on a Bruker mass spectrometer. IR spectra were measured on an ALPHA II FT-IR spectrometer. NMR spectra were measured on a Bruker Avance AV600 spectrometer at the Institute of Organic Chemistry with Centre of Phytochemistry-BAS, Sofia. Deuterated dimethyl sulfoxide or chloroform were used as NMR solvents. The absorbance of free radical scavenging assay was measured by a Spectroquant Pharo 300, UV/Vis spectrophotometer.

Materials

A suitable approach for the preparation of benzazole-resorcinol hybrids through one-pot reaction was applied and optimized (Scheme 1) [17, 19]. The reactions completion was monitored by thin layer chromatography (TLC). All synthesized compounds were purified by column chromatography on silica gel with a mixture of petroleum/diethyl ether as eluents. The expected structure of the compounds was spectrally confirmed by 1D ^{1}H, ^{13}C{^{1}H}-NMR, 2D HSQC-NMR, IR and HRMS spectra and published in our previous studies [17, 19].

Methods

ABTS free radical scavenging assay. The procedure to determine the radical scavenging activity of the new synthesized compounds by using ABTS$^{\bullet+}$, follows the original method of Re *et al.* [20] with slight modifications: 7 mM ABTS and 2.45 mM $K_2S_2O_8$ dissolved in water, were mixed in equal amounts 1:1 (v/v), and the mixture was allowed to stay for 14 – 16 hours for stabilization [20]. The stability of undiluted ABTS$^{\bullet+}$ is at least 1 week, stored in a refrigerator. The resulting free radical cation was diluted with pure methanol to reach an absorbance of 0.7±0.02, which was measured spectrophotometrically at 734 nm. Sample loading relative to ABTS free radical was 0.1:0.9 (0.3 ml analyte + 2.7 ml ABTS$^{\bullet+}$). The time required for the reaction to proceed was 10 min at room temperature in the dark, after which the absorbance of the sample analysed was measured.

The stability of the undiluted ABTS$^{\bullet+}$ is a minimum of 1 week in refrigerated storage. In the present studies, stock solutions of the substances were prepared at a concentration of 1 mg/ml. From these, solutions of lower concentrations were made by dilution with methanol. A plot of % inhibition (RSA%) *versus* concentration of each substance was plotted and the IC$_{50}$ values for each substance were found in μg/ml (ppm) and converted to μM.

RESULTS AND DISCUSSION

As a result of molecular hybridization, a benzazole fragment was successfully combined with resorcinol by applying an intermolecular reaction of α-amidoalkylation. The electrophilic *N*-acyliminium reagents were generated *in situ* and the subsequent reaction with resorcinol according to Scheme 1 led to final products *12*, *13*.

The main purpose of this work after the obtaining of benzazole-rezorcinol hybrids was to develop an effective method for examination of their radical scavenging activity.

To determine the radical scavenging activity of the newly synthesized compounds, we applied the ABTS method, building on our previous experience. In earlier studies of the radical scavenging activity of natural phenols [21], we found that gallic acid (IC$_{50}$ = 37.7±1.25 μM) and pyrogallol (IC$_{50}$ = 22.7±1.45 μM) exhibited the highest radical scavenging activity, while catechol (IC$_{50}$ = 111.2±0.5 μM) exhibited the lowest one. The ABTS assay resulted in comparable and reproducible results. In this regard, the radical scavenging activity of the synthetic 2-aryl benzothiazolines was measured under the same conditions in a medium containing free radical cations of ABTS [21]. As a result, benzothiazole derivatives containing pyrogallol (IC$_{50}$ = 45.9±6.21 μM) and resorcinol (*12a* IC$_{50}$ = 55.6±0.51 μM), (*12b* IC$_{50}$ = 46.3±6.21 μM) fragments showed activity similar to the gallic acid and resorcinol (48.2±4.9 μM). Table 1 represents the radical scavenging activity data examined for compounds *12a, b* and *13a, b* and resorcinol.
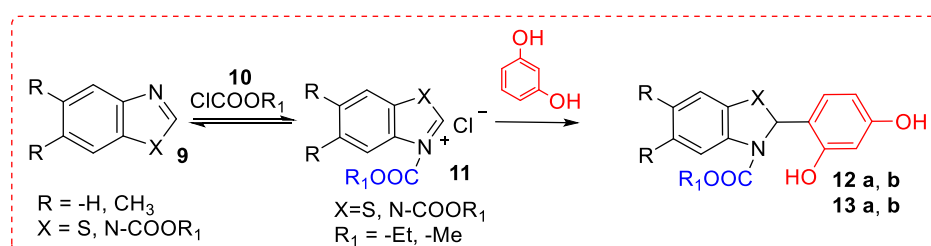
Scheme 1. Synthesis of 2-(2,4-dihydroxyphenyl)benzazolines

Table 1. Radical scavenging activity of 2-aryl benzazoles by the ABTS-method

Compound	MW	IC$_{50}$ µM	Structure
Resorcinol	110.11	48.2±4.9	
12a X = -S, R = -H, R$_1$ = -Et [17]	317.36	55.6±0.5	
12b X = -S, R = -H, R$_1$ = -Me [17]	303.33	46.3±6.2	
13a X = -NCOOR$_1$, R = -H, R$_1$ = -Et [19]	372.38	88.9±4.0	
13b X = -NCOOR$_1$, R = -Me, R$_1$ = -Et [19]	400.43	71.6±4.0	

Table 2. Radical scavenging activity of quercetin hybrids by the ABTS-method [18]

Compound	MW	IC$_{50}$ µM	Structure of Qct-hybrids
Quercetin (Qct)	302.24	48.0±4.4	
Rutin	610.52	95.3±4.5	
14a X = -S, R = -H, R$_1$ = -Et	509.49	49.8±3.5	
14b X = -S, R = -H, R$_1$ = -Me	495.46	50.0±3.5	
15 X = -NCOOR$_1$, R = -H, R$_1$ = -Et	564.50	58.3±3.5	
16a X = -NCOOR$_1$, R = -Me, R$_1$ = -Et	592.56	62.4±3.5	
16b X = -NCOOR$_1$, R = -Me, R$_1$ = -Me	564.50	55.1±3.5	

Moreover, we also reported the radical scavenging activity of the novel 2-substituted benzazole-quercetin hybrids (*14a, b - 16a, b*). In the 2-substituted benzazole-quercetin hybrids, no significant differences in the activity of the compounds were observed depending on the hetero part of the molecule (Table 2). The benzimidazole-resorcinol derivatives *13a* and *13b* showed lower activity than 1*2a* and *12b* containing a benzothiazole fragment, but close to the natural compound - rutin.

The activity of *12a* and *12b* was comparable to the quercetin hybrids, pure quercetin and resorcinol. The new benzazole-resorcinol hybrids demonstrated good radical scavenging potential. From them *12b* was with the highest activity (Table 1). The results achieved in this work give lead for future investigations based on the explanation of the mechanism of interactions with the free radical, also the reasons for differences in the activity caused by the presence of hydroxyl groups.

CONCLUSION

A molecular hybridization method was successfully demonstrated for the preparation of resorcinol hybrids containing benzothiazole, benzimidazole and 5,6-dimethylbenzimidazole fragment by applying an earlier introduced *one-pot* intermolecular reaction of *α*-amidoalkylation. The resulting compounds have high radical-scavenging ability. The radical scavenging activity of 2-(2,4-dihydroxyphenyl)-*N*-carboxymethyl-benzothiazol-ines *12b* - IC$_{50}$ - 46.3±6.2 µM is comparable to that of resorcinol and quercetin. The radical scavenging activity of the resorcinol hybrids is higher than that of rutin. Two assays, such as ABTS and DPPH were compared to evaluate the radical scavenging activity of synthetic benzazole compounds. The ABTS method is more sensitive than the DPPH. The results are promising and give good lead for potential application in cosmetics.

REFERENCES

1. B. Narasimhan, D. Sharma, P. Kumar, *Med. Chem. Res.,* **21**, 269 (2012).
2. L. Racané, K. Butković, I. Martin-Kleiner, M. Kralj, G. Karminski-Zamola, M. Hranjec, *Croatica Chemica Acta*, **92**(2), 181 (2019).

3. M. Racané, N. Sedić, M. Ilić, S. Aleksić, G. Kraljević Pavelić, *Med. Chem.,* **17**, 57 (2017).

4. N. Phan, T. Huynh, H. Nguyen, Q. Le, Q. T. Nguyen, K. Ngo, T. Nguyen, K. Ton, K. Thai, T. Hoang, *ACS Omega*, **8**(31), 28733 (2023).

5. R. Veerasamy, A. Roy, R. Karunakaran, H. Rajak, *Pharmaceuticals, MDPI*, **14**(7), (2021).

6. M. Karpińka, J. Matysiak, A. Niewiadomy, *Archives of Pharmacal Research,* **34**(10), 1639 (2011).

7. A. Baldisserotto, M. Demurtas, I. Lampronti, M. Tacchini, D. Moi, G. Balboni, S. Pacifico, S., Vertuani, S. Manfredini, V. Onnis, *Bioorganic Chemistry*, **94**, (2020).

8. R. Barbari, C. Tupini, E. Durini, E. Gallerani, F. Nicoli, I. Lampronti, A. Baldisserotto, S. Manfredini, *Molecules*, **28**(1), (2023).

9. D. Fivenson, N. Sabzevari, S. Qiblawi, J. Blitz, B. Norton, S. Norton, *Int. J. Women's Dermatol.*, **7**, 45 (2021).

10. G. Nitulescu, D. Lupuliasa, I. Adam-Dima, G. Nitulescu, *Multidisciplinary Digital Publishing Institute (MDPI).* **10**(4), (2023).

11. A. Bino, A. Baldisserotto, E. Scalambra, V. Dissette, D. Vedaldi, A. Salvador, E. Durini, S. Manfredini, S. Vertuani, *Journal of Enzyme Inhibition and Medicinal Chemistry*, **32**(1), 527 (2017).

12. J. Nichols, S. Katiyar, *Arch. Dermatol. Res.,* **302**, 71 (2010).

13. H. Sies, W. Stahl, *Annu. Rev. Nutr.,* **24**, 173 (2004).

14. ISO 24443:2021, Cosmetics. Determination of sunscreen UVA photoprotection *in vitro*, (2021).

15. B. Diffey, J. Robson. *J. Soc. Cosmet. Chem.,* **40**, 127 (1989).

16. E. Djuidje, E. Durini, S. Sabrina Sciabica, E. Serra, J. Balzarini, S. Liekens, S. Manfredini, S. Vertuani, A. Baldisserotto, *Molecules*, **25**, 4324 (2020).

17. Y. Stremski, D. Kirkova, S. Statkova-Abeghe, P. Angelov, I. Ivanov, D. Georgiev, *Synthetic Communications*, 3007 (2020).

18. D. Kirkova, Y. Stremski, S. Statkova-Abeghe, M. Docheva, *Molbank*, (1), M1329, 202 (2022).

19. Y. Stremski, M. Bachvarova, D. Kirkova S. Statkova-Abeghe, *Molbank*, (1), M1602 (2023).

20. R. Re, N. Pellegrini, A. Proteggente, A. Pannala, M. Yang, C. Rice-Evans, *Free Radicals in Biology and Medicine*, **26**, 1231 (1998).

21. D. Kirkova, S. Statkova-Abeghe, M. Docheva, Y. Stremski, S. Minkova, *Bulg. Chem. Commun.,* **52** (Special issue D), 196 (2020).

Secondary metabolites from tobacco and different natural herbs, extracted by maceration with polar solvents

D. Kirkova[1]*, M. Docheva[1], L. Stoyanova[1,2], Y. Stremski[2], S. Statkova-Abeghe[2], V. Petrova[2], Y. Kochev[1]

[1]Tobacco and Tobacco Products Institute, Agricultural Academy, Markovo 4108, Bulgaria
[2] Department of Organic Chemistry, University of Plovdiv "Paisii Hilendarski", 24 Tsar Asen Str., 4000 Plovdiv, Bulgaria

Tobacco (*N. tabacum* L.) is an annual plant belonging to the family *Solanaceae*, genus *Nicotiana*. The first information of the use of tobacco as a medicinal plant data back to 1492. After the isolation of the alkaloid nicotine from tobacco leaves in 1828 and the establishment of its addictive effect, the medical world ceased to use tobacco as a treatment. Several centuries later, scientific research has resumed and it is again directed towards a detailed study of the biologically active substances in tobacco and its alternative use in medicine, bio-engineering and biotechnology. Organic tobacco is a new industrial plant product that is grown on certified bio fields, without using conventional fertilizers and plant protection preparations. The nicotine content is significantly lower than that of tobacco grown under conventional conditions. It is of interest to study the quantitative and qualitative composition of some secondary metabolites in organic tobacco extracts, like total phenolic content, obtained by maceration with different polar solvents, and the comparison with selected medicine plants extracts - thyme, hawthorn, horsetail, nettle, and dandelion. Our research found that bio tobacco has a high content of phenolic acids close to the content of phenolic acids in thyme and is higher than that of the medicinal plants horsetail, dandelion, hawthorn and nettle. Bio tobacco extracts have high antioxidant activity determined by ABTS, DPPH, HPSA, FRAP, CUPRAC methods, similar to that of thyme extracts activty. Bio tobacco extracts have significantly higher antioxidant activity than hawthorn, nettle, horsetail and dandelion extracts.

Keywords: bio tobacco, medical herbs, total phenolic content, antioxidant activity

INTRODUCTION

The plants are able to synthesize many different secondary metabolites [1,2]. Secondary metabolites are directly related to its adaptive properties to the environment [3]. The secondary metabolites such as phenolic acids, flavonoids, and terpenoids are responsible for the antioxidant potential in medicinal plants, which is expressed in the ability to bind to free radicals and "neutralize" their action [1].

The utilization of medicinal plants in folk and official medicine dates back centuries. In connection with the growing potential for the use of medicinal plants, there is an interest in scientific research related to the qualitative and quantitative composition of biologically active substances in medicinal plants, including their antioxidant activity, preclinical and clinical research on the quality and action [3].

Tobacco (*N. tabacum* L.) is an annual plant belonging to the family *Solanaceae*, genus *Nicotiana*. The traditional use of tobacco is to make tobacco products for smoking. As a plant tobacco is also characterized by a large number of secondary metabolites - alkaloids, polyphenols, coumarins, isoflavonoids, carotenoids, terpenes, etc. [4-9]. The

plant dates back to 1492. After the isolation of the alkaloid nicotine from tobacco leaves in 1828 and the establishment of its addictive effect, the medical world ceased to use tobacco as a treatment [10]. Several centuries later, scientific research has resumed and it is again directed towards a detailed study of the biologically active substances in tobacco and its alternative use in medicine [11]. Heretofore, more than 15 individual components of the phenolic acids and flavonoids have been identified in tobacco and tobacco waste. The largest amounts are phenolic acids - chlorogenic, neochlorogenic and cryptochlorogenic acids, and flavonoids - rutin and nicotiflorin. Caffeic acid, scopoletin, scopolin, quercetin were found in relatively smaller amounts [12, 13].

At the Tobacco and Tobacco Products Institute, Bulgaria a procedure for growing tobacco on a certified bio field has been developed for several years. There are already data on the main chemical composition of the Krumovgrad 58 bio tobacco variety, where the nicotine content is significantly lower compared to growing the same tobacco variety under conventional conditions [14].

In previous research, the polyphenolic content of different types, varieties, and lines of conventionally

---

grown tobacco was investigated [18]. It is of interest to study the polyphenolic content of bio tobacco and compare its phenolic profile with that of medicinal plants from Bulgaria. For this purpose, we selected 5 herbs from different genera and families - thyme, nettle, hawthorn, horsetail and dandelion.

MATERIALS AND METHODS

Plant material: The plant materials, hawthorn fruits (*Crataegus monogyna*), horsetail (*Equisetum arvense*), thyme (*Thymus spp*), nettle leaves (*Urtica dioica* L.) and dandelion root (*Taraxacum officinale*), were purchased from the commercial network from Plovdiv region, Bulgaria. Tobacco was grown in a certified experimental bio field - Gotse Delchev, of the Tobacco and Tobacco Products Institute.

Tobacco, horsetail, thyme, nettle leaves, dandelion root were ground into a fine powder, while hawthorn fruits were crumbled to a particle size of 2-3 mm.

Chemicals: All chemicals are of analytical grade quality and were purchased from Honeywall and Sigma Aldrich (USA).

Instruments: Spectrophotometer "Spectroquant Pharo 300", UV/Vis (Merck, USA)

Preparation of plant extracts: Dry plant powder (0.1 g) was extracted with 10 ml solvent (60 % methanol, 70 % ethanol, water and acetone) for 1h, 2h, 4h, 12h, 72h and 92h on static maceration. The extracts were filtered by a syringe filter and used for further analysis.

Determination of total phenolic content (TPC) by the Folin-Ciocalteu (FC) assay: The TPC of 60 % methanolic, 70 % ethanolic, aqueous and acetonic extracts was assessed using the FC method [16], with some modification [17]: 0.1 ml of plant extract (water, 60 % methanolic, 70% ethanolic and acetonic extract), 6 ml water and 0.5 ml 0.2 M FC reagent were placed into a test tube. After 4 minutes 3.4 ml of 7.5 % Na_2CO_3 was added. All samples and the blank were stored in the dark for 2 hours and then measured at 765 nm against the blank sample. The concentration of the phenolic compounds in the extracts was calculated using gallic acid as standard, and the results were expressed as milligrams gallic acid equivalents per gram extract (mg GAE/g).

Determination of antioxidant activity

1,1-diphenyl-2-picryl-hydrazyl (DPPH) assay. The DPPH scavenging capabilities of 60 % methanolic and 70 % ethanolic were evaluated using the free radical method that is reported by Docheva *et al*. [18]. This method measures the reaction of the antioxidants with stable DPPH free radicals. The absorbance is measured at 515 nm against a methanol.

2,2'-azino-bis(3-ethylbenzothiazoline-6-sulfonate) (*ABTS*) *assay*. The ABTS radical cation (ABTS$^{•+}$) scavenging activities of the 60 % methanolic and 70 % ethanolic solutions were evaluated according to the original method of Re *et al*. [19] with slight modifications by our previous study [20]. The ABTS$^{•+}$ cation radical developed from its reaction with ABTS (7 mM) in H_2O and $K_2S_2O_8$ (2.45 mM) at room temperature in the dark for 14-16 h. The absorbance at 734 nm was measured for each sample relative to methanol.

Hydrogen peroxide scavenging activity (HPSA) assay. HPSA of 60 % methanolic and 70 % ethanolic extracts was determined using 0.2 M phosphate buffer (PB, pH = 7.4) and H_2O_2 (2 mM dissolved in PB). 0.1 ml plant extracts, 0.6 ml H_2O_2 and 3.3 ml PB were placed into a test tube. After 10 minutes in the dark, the absorbance at 230 nm was measured for each sample.

Ferric reducing antioxidant power (FRAP) assay. The reducing power of the ferric (Fe^{3+}) ions of both extracts was measured using Benzie`s method [21] with slight modification reported by Docheva *et al*. [22]. The basis of this method is the reduction of Fe^{3+} to ferricyanide in stoichiometric excess relative to the antioxidants. In this method, the absorbance measurements of the samples are obtained at 593 nm against a blank.

Cupric reducing antioxidant power (CUPRAC) assay. The reducing power of the cupric ions (Cu^{2+}) of aqueous alcoholic extracts was determined according to Apak *et al*. [23] with slight modifications: to a test tube were added 1 ml $CuCl_2$ solution (10 mM dissolved in water), 1 ml of neocuproine alcoholic solution (7.5 mM dissolved in ethanol) and 1 ml of ammonium acetate buffer solution (1 M, pH=7), followed by mixing; 0.1 ml of herbal extract and 1 ml of water were added (total volume, 4.1 ml) and mixed well. The absorbance was measured at 450 nm for each sample after 30 min in the dark [17].

Antioxidant activity was determined using Trolox as reference standard and results were calculated as mM TE/g. The results of each sample were represented as the mean ± standard deviation of three independent replicates.

RESULTS AND DISCUSSION

Determination of TPC in plant extract by different solvents

Optimizing the method for extraction of phenolic compounds (TPC, TFC, and TTC) from medicinal plants has important and significant meaning to

future biomolecules for human health, pharmaceutical, and medicinal research. The extraction techniques, extraction time and the solvent selection are the main challenges toward the development of the technique for the qualitative and quantitative analysis of TPC in plant materials [24, 25].

Effect of extraction time by maceration

The most utilized classical methods for extraction of TPC are maceration, solid-liquid extraction, Soxhlet extraction, etc. [25]. In order to investigate the effect of extraction time on total phenolic content yield, the extraction time studied was from 1 to 96 h. A solvent of 60% methanol was used, which has been proven to ensure complete extraction of the total phenolic content in tobacco [26]. As shown in Figure 1 the maximum yield of TPC for tobacco, nettle, horsetail, dandelion, thyme is 1 h. whereas, for the complete extraction of TPC from hawthorn fruit, 72 hours of static maceration are required because of the response surface.

Effect of extraction solvent

The most common solvents used for the extraction of phenolic compounds from plant materials are methanol, ethanol, acetone, and their various aqueous mixtures of various concentrations [25, 27]. Hence, for an optimization method for TPC extraction from tobacco, hawthorn, nettle, horsetail, dandelion and thyme, four solvents with different polarities were used - 60 % methanol, 70 % ethanol, water and acetone. The effect of solvents in the extraction of the target compounds was investigated by the FC method for determination of TPC. The highest total phenolic content was reported in the extracts obtained by 60 % methanol (6.9±0.4 mg GAE/g dandelion – 36.8±2.5 mg GAE/g thyme), followed by 70 % ethanol (5.5 mg GAE/g dandelion – 37.6±2.6 mg GAE/g thyme) and water (25.5±1.7 mg GAE/g bio tobacco II class – 5.4±0.3 mg GAE/g dandelion). The expected lowest amount of phenolic compounds was extracted with pure acetone.

Bio tobacco has a high TPC, which is close to the TPC of thyme and higher than that of the medicinal plants horsetail, dandelion, hawthorn and nettle. The TPC of horsetail and dandelion extracts obtained by extraction with 60% MeOH, 70% EtOH and H_2O is three times lower than that of thyme and bio tobacco extracts and about two times lower than hawthorn and nettle extracts.

	Tobacco	Hawthorn	Nettle	Horsetail	Dandelion	Thyme
1 h	36,1	16,5	15,8	8,2	6,9	36,8
2 h	35,2	14,5	14,2	8,3	7,0	41,2
4 h	34,9	20,2	13,7	9,7	7,4	41,1
12 h	33,5	16,6	14,6	8,6	6,8	38,4
72 h	37,3	22,6	15,6	9,7	8,4	38,3
96 h	34,2	20,8	15,5	9,4	7,1	42,3
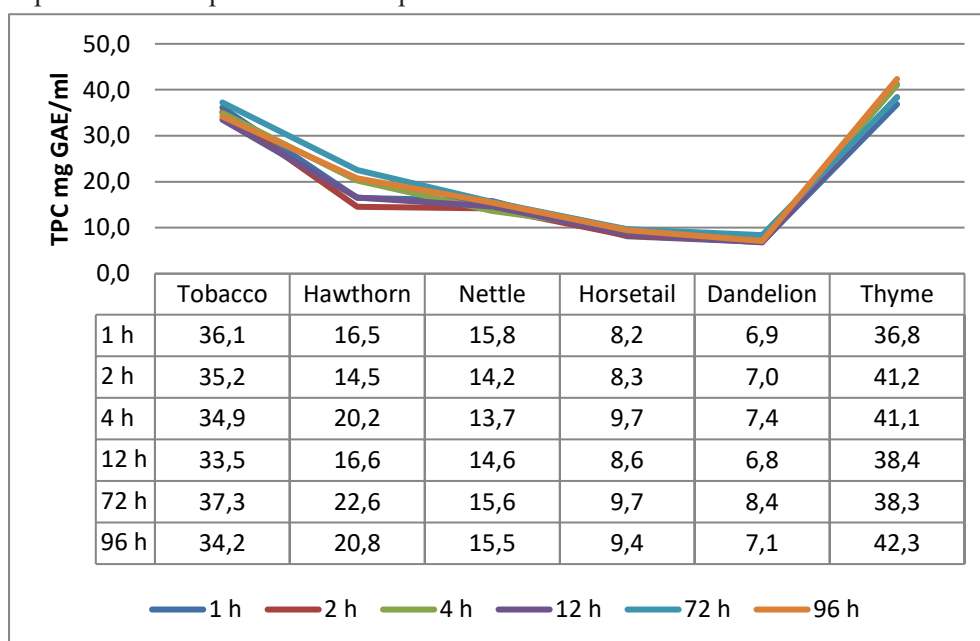
Figure 1. Optimization for extraction of TPC by maceration with 60% MeOH

Table 1. TPC of tobaccos and medicinal plants, obtained by different extractants, (mg GAE/g)

Plants	60 % MeOH	70 % EtOH	Acetone	H_2O
Bio tobacco I cl.	36.1±2.5	27.8±1.9	2.0±0.1	22.6±1.5
Bio tobacco II cl.	35.2±2.4	20.8±1.4	2.1±0.1	25.5±1.7
Hawthorn	22.6±1.5	14.5±1.0	2.8±0.2	10.6±0.7
Nettle	15.8±1.1	10.8±0.7	nd.	12.4±0.8
Horsetail	8.2±0.5	5.6±0.3	1.4±0.1	6.2±0.4
Dandelion	6.9±0.4	5.5±0.3	nd.	5.4±0.3
Thyme	36.8±2.5	37.6±2.6	3.6±0.2	25.1±1.7

Phenolic acids as secondary metabolites are mainly formed as a result of biotic or abiotic stress [3]. In this regard, the amount of phenolic acids varies in the same medicinal plant grown under different environmental conditions. Therefore, the comparison of the amount of total phenolic content is mainly informative in character. However, research shows that polar solvents such as butanol, methanol, ethanol or water-alcohol mixtures extract a greater amount of phenolic acids from hawthorn, dandelion, thyme compared to non-polar solvents – diethyl ether, hexane [28-30].

Determination of antioxidant activity of plant extracts

Phenolic compounds are very important plant constituents with free radical scavenging ability, because of their hydroxyl groups. It has been established that phenolic compounds are the major plant compounds with antioxidant activity, and this activity is due to their redox properties. They are a class of antioxidant agents that can absorb and neutralize free radicals [31]. For a better characterization of the extracts, different methods are used to determine the antioxidant activity, based on different reaction mechanisms - transfer of both a hydrogen atom and an electron includes the ABTS, HPSA and DPPH methods; transfers of one electron includes the CUPRAC and FRAP methods [32, 33].

The antioxidant activity of only 60 % methanolic and 70 % ethanolic extracts are investigated, because of the highest TPC. All the extracts show high antioxidant activity determined by methods of transfer of both a hydrogen atom and an electron – ABTS, DPPH and HPSA. The highest antioxidant activity of 60 % methanolic extracts is reported by the ABTS method (from 80.3±5.8 mM TE/g - dandelion to 590.6±41.3 mM TE/g - thyme),

followed by HPSA (from 42.2±2.7 mM TE/g - dandelion to 349.7±25.5mM TE/g - tobacco I class) and DPPH method (from 36.7±2.5 mM TE/g - dandelion to 428.0±29.9mM TE/g - thyme), illustrated in Table 2.

It is noteworthy that the extracts from different plants have different activity in relation to the different methods of transfer of both a hydrogen atom and an electron. Bio tobacco extracts exhibited equally high antioxidant activity determined by ABTS and HPSA; hawthorn, horsetail and dandelion - almost twice as much high activity determined by ABTS method compared to DPPH and HPSA, nettle – highest activity by HPSA, while thyme has highest activity determined by ABTS method.

The antioxidant activity determined by the ABTS method was higher compared to the DPPH method in the study of extracts of nettle [34] and thyme [35].

A significant difference in antioxidant activity was observed in transfer of one electron methods – FRAP and CUPRAC assays. The antioxidant activity determined by the CUPRAC method varies from 99.9±7.0 mM TE/g (dandelion) to 868.6±60.8 mM TE/g (thyme), and is twice higher than the antioxidant activity determined by the FRAP method - from 23.6±1.65 mM TE/g dandelion to 401.8±28.1mM TE/ g – thyme.

It is noteworthy that the difference in antioxidant activity between the FRAP and CUPRAC method for hawthorn, dandelion and thyme 60 % methanolic extracts is between two and three times, while for tobacco and nettle extracts – more than four times. This shows that there are substances in the methanolic extracts of tobacco and dandelion that have the ability to reduce Cu^{2+} to a greater extent than Fe^{3+}.

Table 2. Antioxidant activity of tobaccos and medicinal plant extracts, obtained by 60 % MeOH and 70 % EtOH, mM TE/g

Extract	DPPH	ABTS	HPSA	FRAP	CUPRAC
60 % MeOH					
Bio tobacco I cl.	262.5±18.5	367.9±25.7	349.7±25.5	197.0±13.7	801.7±56.1
Bio tobacco II cl.	249.3±17.4	344.0±24.1	318.7±23.0	192.3±13.4	807.3±56.3
Hawthorn	105.5±7.3	208.8±14.6	172.1±9.8	113.0±7.91	333.9±23.3
Nettle	107.8±7.3	148.5±10.3	197.8±13.6	95.0±6.6	470.6±32.9
Horsetail	54.0±3.7	86.3±6.0	113.7±7.9	30.1±2.1	103.3±7.2
Dandelion	36.7±2.5	80.3±5.8	42.2±2.7	23.6±1.65	99.9±7.0
Thyme	428.0±29.9	590.6±41.3	312.2±22.4	401.8±28.1	868.6±60.8
70 % EtOH					
Bio tobacco I cl.	260.2±18.2	284.2±19.8	483.2±33.8	182.1±12.7	865.9±60.6
Bio tobacco II cl.	213.2±14.9	296.1±20.7	400.8±28.0	172.6±12.0	759.8±53.1
Hawthorn	122.4±8.5	223.3±15.6	217.1±15.2	113.8±7.9	339.4±23.7
Nettle	64.5±4.5	130.1±9.1	195.2±13.6	56.5±4.0	238.8±16.7
Horsetail	28.0±1.9	70.3±4.9	109.9±7.7	22.7±3.9	127.4±8.9
Dandelion	31.8±2.2	72.3±5.1	60.6±4.2	17.0±1.2	113.5±77.9
Thyme	353.3±24.7	556.3±38.9	477.0±33.3	372.0±26.0	1064.0±74.2

The antioxidant activity of the ethanolic extracts is similar to that of the methanolic extracts – shown in Table 2. It is noteworthy that the antioxidant activity determined by ABTS method of bio tobacco ethanolic extracts (average 290.2 mM TE/g) is by about 60 mM TE/g lower than the methanolic extracts (average 355.9 mM TE/g). Antioxidant activity of tobacco and thyme ethanolic extracts determined by the HPSA method is by about 100 mM TE/g higher compared to the methanolic extracts. Bio tobacco methanolic and ethanolic extracts have similar high antioxidant activity to thyme extracts determined by ABTS, DPPH, HPSA, FRAP, CUPRAC methods, which is related to the high TPC. The lowest antioxidant activity is reported for the methanolic and ethanolic extracts of dandelion and horsetail, which have the lowest TPC.

CONCLUSION

The total phenolic content and antioxidant activity of bio tobacco extracts and of medicinal plants hawthorn, thyme, dandelion, nettle and horsetail are investigated. The highest yield of TPC by maceration for 1 hour is achieved. An exception is hawthorn fruit, which requires a maceration of 72 hours. No significant differences in TPC when extracted with 60 % methanol and 70 % ethanol are observed. Bio tobacco has a high content of phenolic acids and high antioxidant activity determined by ABTS, DPPH, HPSA, FRAP, CUPRAC methods, which is close to the content of phenolic acids and antioxidant activity in thyme.

Tobacco extracts are characterized with higher TPC and antioxidant activity compared to the medicinal plants horsetail, dandelion, hawthorn and nettle. The 70 % ethanol is a suitable solvent for extracting the maximum amount of phenolic compounds, and the obtained extracts can be used as potential antioxidants.

REFERENCES

1. R. Watson, Secondary metabolites of plants and their role: Overview, 2nd edn, 2014.
2. K. Pandey, S. Rizvi, *Oxidative Medicine and Cellular Longevity*, **2(5)**, 270 (2009).
3. A. Leitão, F. Enguita, in: Microbial Cell Factories Engineering for Production of Biomolecules, Elsevier, 2021, p. 51.
4. L. Nugroho, R. Verpoorte, *Plant Cell, Tissue and Organ Culture* **68(2)**, 105 (2002).
5. M. Docheva, M. Staikova, A. Stoilova, D. Dimanov, *Bulg. Chem. Commun.* **49** (Special Issue), 212 (2017).

6. V. Popova, Z. Petkova, T. Ivanova, M. Stoyanova, L. Lazarov, A. Stoyanova, T. Hristeva, M. Docheva, V. Nikolova, N. Nikolov, V. Zheljazkov, *Industrial Crops and Products*, **117**, 375 (2018).
7. V. Popova, T. Ivanova, A. Stoyanova, V. Georgiev, T. Hristeva, V. Nikolova, M. Docheva, N. Nikolov, S. Damyanova, *Trends in Phytochemical Research*, **2(1)**, 27 (2018).
8. V. Popova, T. Ivanova, A. Stoyanova, V. Nikolova, T. Hristeva, M. Docheva, N. Nikolov, I. Iliev, *Journal of Applied Biology and Biotechnology*, **7(5)**, 45 (2019).
9. T. Tso, Ideals, Inc, Beltsville, USA, 1990.
10. A. Charlton, *J. R. Soc. Med.*, **97**, 292 (2004).
11. X. Zou, B. Amrit, A. Rauf, M. Saeed, Y. Al-Awthan, M. Al-Duais, O. Bahattab, M. Khan, H. Suleria, *ACS Omega* **6(39)**, 25361 (2021).
12. K. Kishore, *Indian Journal of Drugs*, **2(21)**, 5 (2014).
13. A. Rodgman, The Chemical Components of Tobacco and Tobacco Smoke, Second edn. CRC Press. 2016.
14. M. Kasheva, H. Bozukov, M. Docheva, Y. Kochev, D. Kirkova, *Bulgarian Journal of Crop Science*, **58(4)**, 49 (2021).
15. M. Docheva, S. Dagnon, *C. R. Acad. Bulg. Sci.*, **68(2)**, 183 (2015).
16. V. Singleton, J. Rossi, *Am. J. Enol. Vinic.* **16 (48),** 144 (1965).
17. D. Bojilov, S. Manolov, B. Bozadzhiev, J. Stremski1, I. Ivanov, *Journal of International Scientific Publications*, **6**, 314 (2018).
18. M. Docheva, S. Dagnon, S. Statkova-Abeghe, *Nat. Prod. Res.,* **28(17)**, 1328 (2014).
19. R. Re, N. Pellegrini, A. Proteggente, A. Pannala, M. Yang, C. Rice-Evans, *Free Radic. Biol. Med.*, **26**, 1231 (1999).
20. D. Kirkova, S. Statkova-Abeghe, M. Docheva, Y. Stremski, S. Minkova, *Bulg. Chem. Commun*, **52** (Special issue D), 196 (2020).
21. I. Benzie, J. Strain, *Analytical Biochemistry*, **239**, 70 (1996).
22. M. Docheva, Y. Kochev, D. Kirkova, A. Stoilova, *Bulg. Chem. Commun,* **52** (Special Issue D), 149 (2020).
23. R. Apak, K. Güçlü, M. Ozyürek, S. Esin Karademir, E. Erçağ, *International Journal of Food Sciences and Nutrition*, **57(5-6)**, 292 (2006).
24. A. Salih, F. Al-Qurainy, M. Nadeem, M. Tarroum, S. Khan, H. Shaikhaldein, A. Al-Hashimi, A. Alfagham, J. Alkahtani, *Molecules,* **26(24),** 7454 (2021).
25. O. Alara, N. Abdurahman, C. Ukaegbu *Current Research in Food Science,* **4**, 200 (2021).
26. S. Dagnon, A. Edreva, *Beitr. Tabakforsch. Int.,* **20 (5),** 355 (2003).
27. A Khoddami, A. Wilkes, T. Roberts, *Molecules,* **18**, 2328 (2013).
28. H. Bahri, C. Benkirane, B. Tazi, *Academia Journal of Medicinal Plants*, **7(2)**, 030 (2019).
29. A. Khan, K. Arif, B. Munir, S. Kiran, F. Jalal, N. Qureshi, S. Hassan, G. Soomro, A. Nazir, A. Ghaffar, M. Tahir, M. Iqbal, *Pol. J. Environ. Stud.*, **28(1)**, 497 (2019).
30. M. Roby, M. Sarhan, K. Selim, K. Khalel, *Industrial Crop and Products*, **43**, 827 (2013).
31. A. Adedapo, F. Jimoh, A. Afolayan, *Acta Pol. Pharm.,* **68(1)**, 83 (2011).
32. I. Munteanu, C. Apetrei, *Int. J. Mol. Sci.* **22(7),** 3380 (2021).
33. İ. Gulcin, *Archives of Toxicology* **94**, 651 (2020).
34. Z. Kukric, L, Topalic-Trivunovic, B. Kukavica, S. Matos, S. Pavicic, M. Boroja, A. Savic, *Aptere*, **43**, 1 (2012).
35. M. Mzid, S. Khedir, M. Salem, W. Regaieg, T. Rebai, *Pharmaceutical Biology*, **55(1)**, 775 (2017).

Polyphenol content in tobacco (*N. tabacum* L.) and antioxidant activity

M. Docheva[1], D. Kirkova[1]*, L. Stoyanova[1,3], V. Dureva[1], R. Dimova[1], D. Dimitrova[1, 2], M. Bachvarova[2], E. Syuleyman[2]

[1]*Tobacco and Tobacco Products Institute, Agricultural Academy, Markovo 4108, Bulgaria*
[2] *University of Plovdiv "Paisii Hilendarski", Department of Organic Chemistry, 24 Tsar Asen Str., 4000 Plovdiv, Bulgaria*
[3]*University of Plovdiv "Paisii Hilendarski", Department of Chemical Technology, 24 Tsar Asen Str., 4000 Plovdiv, Bulgaria*

The aim of the present work is to determine the content of polyphenols in tobacco varieties and to investigate the antioxidant activity in tobacco extracts. Bulgarian tobacco varieties from the Basmi and Kabakulak variety groups produced conventionally and biologically, were used. Two types of extracts were investigated - crude extracts obtained by four solvents - 100% CH$_3$OH, 60% CH$_3$OH, H$_2$O, and 96% C$_2$H$_5$OH, and purified extracts obtained by further purification of crude 60% methanolic extract using two techniques - solid phase extraction (SPE) and resin purification, Tobaccos from the variety group Basmi, conventionally grown, have a higher polyphenol content compared to the tobaccos from variety group Kabakulak. No significant difference was observed in the polyphenol contents of in conventionally and organically grown tobaccos of the same variety. The content of phenolic compounds in crude extracts by various solvents decreased in the following order: 60% CH$_3$OH>H$_2$O>100% CH$_3$OH>96% C$_2$H$_5$OH. The crude and purified tobacco extracts showed high antioxidant activity determined by ABTS, FRAP and DPPH assays. The total phenolic content and antioxidant activity of 60% crude methanolic extracts were close to the SPE purified and resin-purified tobacco extracts.

Key words: tobacco extracts, polyphenol content, total phenolic content, antioxidant activity

INTRODUCTION

Polyphenol compounds are secondary metabolites found mainly in plants [1]. They have a great variety of biological functions, some polyphenols act as antioxidants based on their ability to form delocalized unpaired electrons, stabilizing the formed phenoxyl radical after reaction with lipid radicals [2].

Tobacco (*N. tabacum* L.) is a plant containing a large number of chemical substances, including polyphenols. Depending on the type and variety of tobacco, the method of drying and storage, more than 4,500 individual chemical substances have been identified [3]. The cultivation of tobacco in Bulgaria over the last few years has been divided into two agricultural practices: in the conditions of organic production and conventional production [4].

The aim of the present work is to determine the polyphenol content in conventionally and organically grown Bulgarian tobacco varieties and to investigate the antioxidant activity in the obtained crude and purified extracts.

MATERIALS AND METHODS

Material

Dry leaves of tobacco variety Basmi– conventionally and organically (bio) grown and tobacco variety Kabakulak – conventionally grown, were used as a material. The cultivars are from the collection of the Tobacco and Tobacco Products Institute, Plovdiv, Bulgaria. The description of the analyzed tobaccos is presented in Table 1.

Reagents and equipment

2,2-Diphenyl-1-picrylhydrazyl (DPPH), 2,2'-azino-bis (3-ethylbenzothiazoline-6-sulfonic acid) (ABTS), 100 % CH$_3$OH, 96 % C$_2$H$_5$OH, gallic acid, 6-hydroxy-2,5,7,8-tetramethyl-chroman-2-carboxylic acid (Trolox), sodium carbonate, hydrochloric acid, 2M Folin-Ciocalteu`s phenol reagent were purchased from Sigma-Aldrich, USA. All chemicals and solvents were of HPLC grade.
Liquid chromatograph equipped with a binary pump, UV/VIS detector and analytical column "Kromasil" C$_{18}$, 5 μm, 150 mm, Perkin Elmer LC 290, USA. UV/VIS spectrophotometer "Spectroquant Pharo 300".

---

* To whom all correspondence should be sent:
    E-mail: *desislavaa894@gmail.com*

Table 1. Description of analyzed tobaccos

Growth	Tobacco variety	Sort	Class	Harvest	Designation
Conventional	Basmi	Krumovgrad 58	I	2020	Sample A1
			II	2020	Sample A2
		Krumovgrad 78 C	I	2020	Sample B1
			II	2020	Sample B2
	Kabakulak	Han Tervel 39	I	2020	Sample C1
			II	2020	Sample C2
		Hanski 277	I	2020	Sample D1
			II	2020	Sample D2
Bio	Basmi	Krumovgrad 58	I	2019	Sample AB1
			II	2019	Sample AB2
		Krumovgrad 58	I	2020	Sample AB3
			II	2020	Sample AB4
		Nevrokop1146	I	2020	Sample NB1
			II	2020	Sample NB2

Methods

Preparation of crude extracts: Dry tobacco powder (0.2 g) was extracted with 10 ml H_2O, 100 % CH_3OH, 60 % CH_3OH, 96 % C_2H_5OH for 30 min on a shaker. The extracts were filtered by a syringe filter and used for further analysis.

Preparation of resin-purified tobacco extracts: Resin-purified tobacco extracts were prepared using the method previously reported by Docheva and Dagnon [5].

Preparation of purified tobacco extracts by solid phase extraction (SPE-purified tobacco extracts): SPE-purified tobacco extracts were prepared using the method previously reported by Dagnon and Edreva [6].

Determination of polyphenol content using HPLC: The quantitative determination of polyphenols in tobaccos was carried out by the method described by Dagnon and Edreva [6].

Determination of total phenolic contents (TPC) using the Folin-Ciocalteu (FC) method: The amount of TPC was based on the FC method [7] with some modifications [8]: 0.1 ml tobacco extract (water, 100 % methanolic, 60% methanolic and 96 % ethanolic extracts), 6 ml H_2O and 0.5 ml 0.2 M FC reagent were added. After 4 min 3.4 ml 7.5 % Na_2CO_3 is added. All the samples and the blank were stored in the dark for 2 h, and then the absorbance was measured at 765 nm against the blank sample - 0.1 ml solvent, 6 ml H_2O and 0.5 ml 0.2 M FC reagent. The concentration of the phenolic compounds in the extracts was calculated using gallic acid as standard, and the results were expressed as milligrams gallic acid equivalents per gram extract (mg GAE/g).

2,2'-Azino-bis (3-ethylbenzothiazoline-6-sulfonic acid) (ABTS) radical scavenging method: The

ABTS free radical scavenging activity was determined by the method previously reported by Kirkova *et al.* [9].

2,2-Diphenyl-1-picrylhydrazyl (DPPH) free radical scavenging method: The DPPH radical scavenging activity was determined as reported by Docheva *et al.* [10].

Ferric reducing antioxidant power method (FRAP): The FRAP assay was conducted according to the original method reported by Benzie and Strain [11] and modified by Docheva *et al.* [12].

Antioxidant activity was determined using Trolox as standard and the results were calculated as mM TE/g. Assays were performed in triplicate and data were presented as mean values ± standard deviation.

RESULTS AND DISCUSSION

Polyphenol content in different tobaccos determined by HPLC

The polyphenol complex in tobacco mainly included phenolic acids and flavonoids. The main contribution to the amount of phenolic acids is due to chlorogenic acid (ChA), neochlorogenic acid (NChA) and cryptochlorogenic acid (CrChA), while to flavonoids – rutin (Rut) and nicotiflorin (NF). Gallic acid, caffeic acid, sinapic acid, coumarin, myricetin 3-*O*-galactoside, neoeriocitrin, (+)-catechin, scopoletin and others were found in smaller amounts [6]. Full extraction of the polyphenols in tobacco was achieved with 60 % CH_3OH [6].

The content of the main components in the polyphenol complex of the analyzed tobaccos is presented in Figure 1. The content of ChA varied widely - from 3.65±0.37 mg/g (Sample D2) to

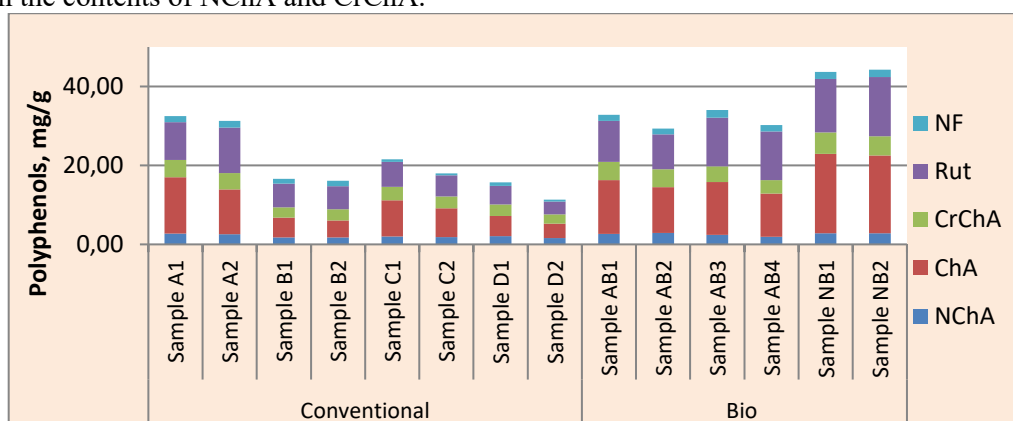20.15±2.02 mg/g (Sample NB1). Less variation was observed in the contents of NChA and CrChA.

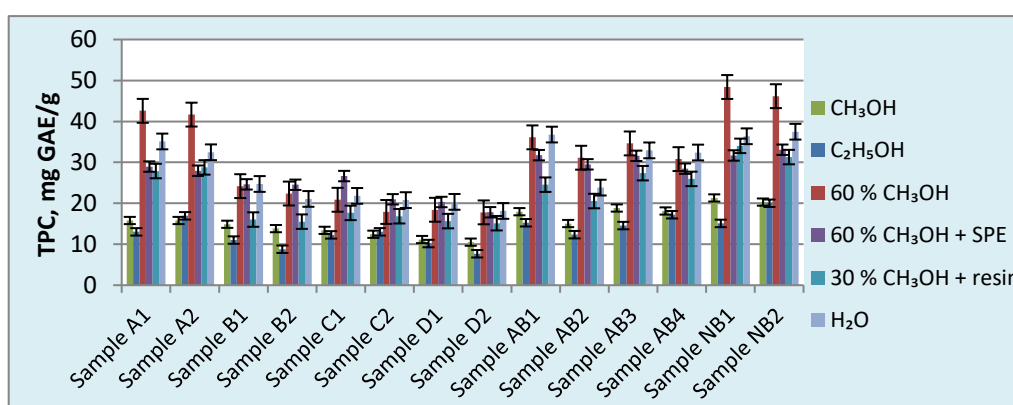**Figure 1.** The main components in the polyphenol complex in tobaccos, mg/g

Figure 2. Total phenolic content in tobacco extracts, mg GAE/g

The content of Rut varied between 3.27±0.33 mg/g (Sample D2) and 14.94±1.49 mg/g (Sample NB1). The amount of NF did not exceed 1.91±0.19 mg/g (Sample AB3 and Sample NB1). The polyphenol content in variety Krumovgrad 58 - Sample A1 and Sample A2 (average 32.49±0.89 mg/g) was twice as much as that in Krumovgrad 78 C - Sample B1 and Sample B2 (average 16.36±0.38 mg/g). The tobacco variety Han Tervel 39 - Sample C1 and Sample C2 (average 19.77±2.51 mg/g) was with higher polyphenol content compared to the variety Hanski 277 – Sample D1 and Sample D2 (average 13.50±3.10 mg/g).

Tobaccos from variety group Basmi, conventionally grown (Samples A1, A2, B1 and B2), were characterized with relatively higher polyphenolic content (average 24.11±8.97 mg/g) to the tobaccos of variety group Kabakulak, conventionally grown, Samples C1, C2, D1 and D2 (average 16.63±4.29 mg/g).

Polyphenol content in the organic tobacco variety Nevrokop was average 43.96±0.45 mg/g and was higher than in the organic tobacco variety Krumovgrad 58 (average 31.90±3.13 mg/g). No significant difference in the polyphenol contents in

the variety Krumovgrad 58, conventional production and organic production was observed. Statistically, no difference was noticed in the polyphenol contents between the different classes of tobacco from the same variety, as well as between the different harvests – see Fig. 1.

Spectrophotometric determination of TPC in tobacco

The TPC determined by FC method is presented in Figure 2. It is noteworthy that the TPC shows higher content than the phenolic acids determined with HPLC (Figs. 1 and 2). These results can be explained with the selectivity of the definable components – with HPLC only chlorogenic acid and its isomers can be identified. The TPC determined the entire range of phenolic acids and some flavonoids [13]. The differences were also due to the different standards that were used – Rut for HPLC and gallic acid for spectrophotometric analysis.

Figure 2 shows that solvents with different polarities extract different amounts of the TPC. The quantity of TPC decreased in the following order: 60% CH_3OH >H_2O>100 % CH_3OH >96 % C_2H_3OH. The TPC in the extracts obtained with 60 % CH_3OH,

varied between 17.80±1.25 mg GAE/g (Sample D2) and 48.40±3.39 mg GAE/g (Sample NB1) and were close to the TPC in the water extracts - 18.13±0.54 mg GAE/g (Sample D2) and 37.50±2.63 mg GAE/g (Sample NB2). The TPC in 100 % methanolic extracts (from 10.51 ±0.73 mg GAE/g – Sample D2 to 21.31±1.48 mg GAE/g – Sample NB1) showed approximately twice as low results compared to the 60 % methanolic extracts (from 17.79 ±1.26 mg GAE/g – Sample D2 to 48.40±5.52 mg GAE/g – Sample NB1) and water extracts (from 18.13 ±1.29 mg GAE/g – Sample D2 to 36.37±4.31 mg GAE/g – Sample NB1). The ethanolic extracts were characterized with the lowest TPC (from 8.80 ±0.62 mg GAE/g - Sample B2 up to 17.20±1.20 mg GAE/g - Sample AB4).

The selective extraction with solvents of different polarity was used to extract not only the target compounds, but also other substances with similar polarity. Two techniques to purify extracts containing phenolic compounds were applied - solid-phase extraction (SPE) and resin purification.

The TPC of tobacco extracts, obtained by SPE ranged from 17.80±1.27 mg GAE/g (Sample D2) to 33.10±2.32 mg GAE/g (Sample NB2), while the TPC of the resin-purified tobacco extracts varied from 15.10 ±1.06 mg GAE/g (Sample D2) to 34.00±2.38 mg GAE/g (Sample NB). The TPC was comparable to that of extracts obtained by extraction with 60% CH_3OH – see Fig. 2.

It is notable that purified extracts from Samples A1, A2, NB1 and NB2 obtained by SPE and resin purification showed a reduction in total phenolic content of about 15 mg GAE/g, compared to the 60 % methanolic extracts.

The investigated crude and purified extracts from Bulgarian tobacco varieties had a significantly higher content of phenolic acids compared to tobacco extracts from Pakistan, where the TPC varied between 4.85±0.08 mg GAE/g and 24.82±0.07 mg GAE/g [13]. In tobacco leaves from Tunisia, the polyphenols varied between 14.46 mg GAE/g and 23.05 mg GAE/g [14].

Antioxidant activity of tobacco extracts

Three different methods (ABTS, DPPH, and FRAP) were applied to identify the antioxidant activity of tobacco crude and purified extract. DPPH and ABTS are stable free radicals that can determine the free radical scavenging capacity of antioxidants [15]. The FRAP method can measure the antioxidant and reduction abilities of plant extracts according to their ability to reduce Fe^{3+} to Fe^{2+} [16].

ABTS method. Antioxidant activity of tobacco extracts, determined by ABTS method, is shown in

Figure 3. The average antioxidant activity of crude 60% methanolic extracts obtained from tobacco variety Kabakulak (Samples C1, C2, D1 and D2) was 157.1±6.3 mM TE/g - lower than the antioxidant activity of tobacco variety Basmi ecotype Krumovgrad tobacco extracts – average 259.3±19.8 mM TE/g. No significant difference in the antioxidant activity of tobaccos from the variety group Basmi, conventionally (251.7±19.8 mM TE/g) and organically (264.4±19.8 mM TE/g) grown was observed. The antioxidant activity of the water extracts varied between 135±9.45 mM TE/g (Sample D2) and 363.9±25.47 mM TE/g (Sample A2) and was similar to that of 60% methanol extracts. It is notable that water extracts obtained from conventionally produced (Samples A1 and A2) and from biologically produced (Samples AB3, AB4, NB1, and NB2) tobaccos had higher activity than 60 % methanolic extracts, despite the lower total phenolic content (Figure 3).

The antioxidant activity of the crude methanolic extracts varied from 61.70±4.93 mM TE/g (Sample D1) to 97.30±6.32 mM TE/g (Sample NB1). The ethanolic extracts had the lowest antioxidant activity, although approximately the same amount of TPC with the methanolic extracts. In crude tobacco extracts obtained from conventionally produced tobacco and organic tobacco no significant difference in antioxidant activities was observed (Fig. 3).

The antioxidant activity of the SPE-purified tobacco extracts ranged from 124.00±8.68 mM TE/g (Sample D2) to 239.00±16.73 mM TE/g (Sample NB2) and was higher than that. of the resin-purified extracts (from 87.90±6.15 mM TE/g Sample D2 to 180.00±12.60 mM TE/g Sample NB1). The antioxidant activity of the SPE-purified tobacco extracts was not significantly different from the crude 60% methanolic extracts. The data obtained indicate that the purification of the tobacco extracts did not affect the increase of the antioxidant activity.

DPPH method. Antioxidant activity determined by DPPH assay showed the highest activity in crude 60% methanolic extracts (from 91.3±6.4 mM TE/g Sample D2 to 263.60±18.40 mM TE/g Sample NB1), followed by methanolic extracts (between 31.30±2.20 mM TE/g Sample D2 and 166.10±11.60 mM TE/g Sample NB1) and ethanolic extracts (ranging from 19.10±1.30 mM TE/g Sample D2 to 71.69±5.00 mM TE/g Sample NB1) – see Fig. 4.

The antioxidant activity of purified SPE tobacco extracts ranged from 96.00±6.70 mM TE/g (Sample D2) to 241.90±16.80 mM TE/g (Sample NB1), and it was close to the antioxidant activity of crude 60% methanolic extracts.
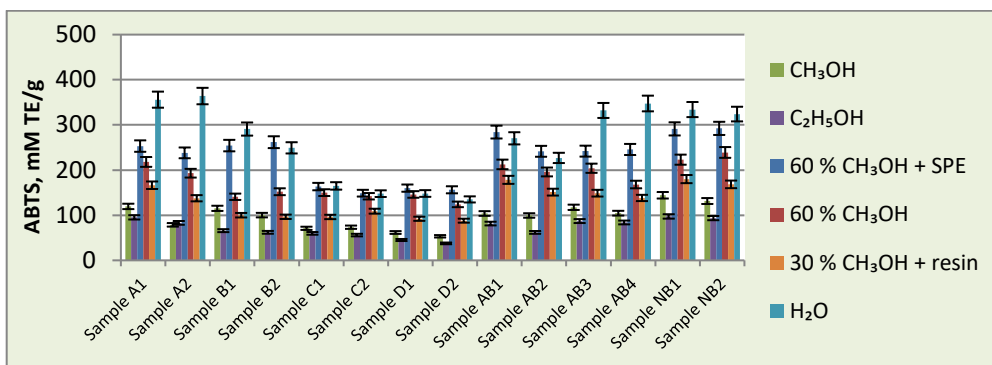
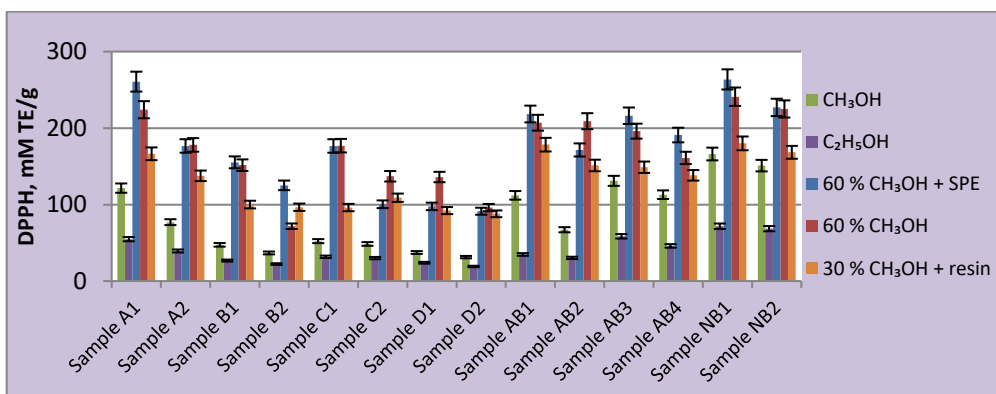**Figure 3.** Antioxidant activity of tobacco extracts, determined by ABTS assay, mM TE/g

Figure 4. Antioxidant activity of tobacco extracts, determined by DPPH assay, mM TE/g
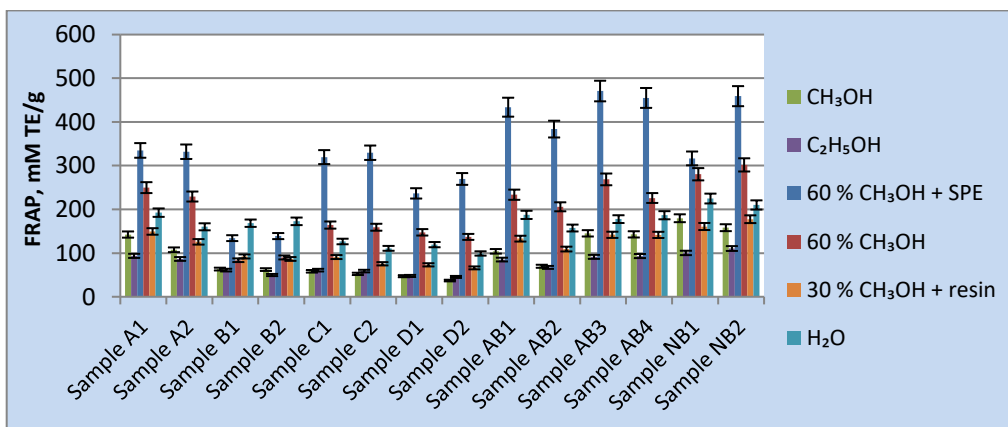

Figure 5. Antioxidant activity of tobacco extracts, determined by FRAP assay, mM TE/g

It is noteworthy that resin-purified extracts obtained from tobaccos of variety group Kabakulak (Sample C1, Sample C2, Sample D1 and Sample D2) had lower antioxidant activity compared to the SPE-purified extracts. The obtained data can be explained by the fact that through the purification with resin, some of the substances contained in tobacco, which have the ability to react with free radicals, were removed. In the resin-purified extracts obtained from conventionally and organically produced variety group Basmi, the antioxidant activity ranged from 60.00±4.20 mM TE/g (Sample B2) to 215.90±15.10 mM TE/g (Sample NB2) and was close to resin-purified extracts (Fig. 4).

The crude and purified tobacco extracts, obtained from variety group Basmi tobaccos, grown under organic conditions (Samples AB1, AB2, AB3, AB4, NB1, and NB2), showed higher antioxidant activity determined by the DPPH method compared to that of conventionally grown tobaccos from variety groups Basmi and Kabakulak.

FRAP method. The results of FRAP assay are presented in Figure 5. The antioxidant activity of crude tobacco extracts decreased in the following order: 60% CH_3OH, H_2O, 100 % CH_3OH and C_2H_5OH. Despite approximately the same amount of TPC in the 60 % methanolic extracts and in the water extracts (Fig. 2), the difference in antioxidant activity was between two and three times (Fig. 5).

The obtained data show that 60% methanolic extracts also contain other substances, which are capable of reducing Fe^{3+} to Fe^{2+}. The antioxidant activity of crude methanolic and ethanolic extracts was approximately the same, which is comparable with TPC.

It is noteworthy that the difference in the antioxidant activity of the SPE-purified tobacco extracts from 83.60 ± 5.80 mM TE/g (Sample B1) to 301.80 ± 21.10 mM TE/g (Sample NB2) was twice as high as the resin-purified tobacco extracts from 66.10 ± 4.60 mM TE/g (Sample D2) to 177.50 ± 12.40 mM TE/g (Sample NB2), despite approximately the same TPC. Tobacco extracts obtained from tobacco variety group Basmi organically grown (Samples AB1, AB2, AB3, AB4, NB1, and NB2) exhibited higher activity, tested by FRAP method, than conventionally produced tobaccos from the variety group Basmi and Kabakulak.

CONCLUSION

Tobaccos from the variety group Basmi (Krumovgrad and Nevrokop) had higher content of phenolic compounds than tobaccos from the variety group Kabakulak (Han Tervel 39 and Hanski 277). No statistically significant difference between conventionally and organically produced tobaccos of variety group Basmi and between classes was observed. Crude 60% methanolic and SPE-purified tobacco extracts, obtained from Bulgarian tobacco varieties conventionally and organically grown, showed strong antioxidant potential.

REFERENCES

1. O. Alara, N. Abdurahman, C. Ukaegbu, *Curr. Res. Food Sci.,* **4 (3),** 200 (2021).
2. M. Andersen, K. Markham, Flavonoids: chemistry, biochemistry and applications, Boca Raton, FL: CRC Press, Taylor & Francis Group, 2006.
3. A. Rodgman, A. Perfetti, The Chemical Components of Tobacco and Tobacco Smoke, 2nd edn., CRC Press; Boca Raton, Florida, 2013.
4. M. Kasheva, H. Bozukov, M. Docheva, Y. Kochev, D. Kirkova, *BJCS*, **58 (4)**:48 (2021).
5. M. Docheva, S. Dagnon, *C. R. Acad. Bulg. Sci.*, **68 (2),** 183 (2015).
6. S. Dagnon, A. Edreva, *Beitr. Tabakforsch. Int.,* **20 (5)**: 355 (2003).
7. V. Singleton, J. Rossi, *Am. J. Enol. Vinic.,* **16 (48)**:144 (1965).
8. D. Bojilov, S. Manolov, B. Bozadzhiev, J. Stremski, I. Ivanov, *J. Int. Sci. Publ.,* **6**, 314 (2018).
9. D. Kirkova, S. Statkova-Abeghe, M. Docheva, Y. Stremski, S. Minkova, *Bulg. Chem. Commun.*, **52** (Special issue D), 196 (2020).
10. M. Docheva, S. Dagnon, S. Statkova-Abeghe, *Nat. Prod. Res.,* **28 (17),** 1328 (2014).
11. I. Benzie, J. Strain, *Analyatical Biochemistry*, **239,** 70 (1996).
12. M. Docheva, Y. Kochev, D. Kirkova, A. Stoilova, *Bulg. Chem. Commun.,* **52** (Special Issue D), 149 (2020).
13. X. Zou, B. Amrit, A. Rauf**,** M. Saeed, Y. Al-Awthan, M. Al-Duais, O. Bahattab, M. Khan, H. Suleria**,** *ACS Omega,* **6 (39),** 25361 (2021).
14. S. Nasr, S. Aazza, W. Mnif, M. Miguel, *J. Appl. Pharm. Sci,* **4 (08),** 23 (2014).
15. Molnar, M.; I. Jerković, D. Suknović, B. Rajs, K Aladić, D. Šubarić, S. Jokić, *Molecules*, **22 (3),** 348 (2017).
16. J. Nilsson, D. Pillai, G. Onning, C. Persson, A. Nilsson, B. Akesson, *Mol. Nutr. Food Res.*, **49,** 239 (2005).

In vitro and *in vivo* evaluation of the multifaceted physiological roles and biochemical pathways of lignin- and morin-based formulations

M. R. Toneva[1], D. G. Ivanova[1], M. T. Tzanova[2], Z. L. Yaneva[1*]

[1]Department of Pharmacology, Animal Physiology, Biochemistry and Chemistry, Faculty of Veterinary Medicine, Trakia University, Students Campus, 6000 Stara Zagora, Bulgaria
[2]Department of Biological Sciences, Faculty of Agriculture, Trakia University, Students Campus, 6000 Stara Zagora, Bulgaria

Owing to the inherent chemical complexity of natural bioactive compounds, the identification of their molecular targets and biochemical mechanisms of action has always been a challenge in front of biomedical sciences. The present study reviews recent approaches, which combine *in vitro* evaluation and *in vivo* screening of potential physiological activities of the plant-derived bioactive molecules lignin and morin and formulations on their basis. The aim is to assess the potential of the hetero polymer and the flavonoid as platforms for the design of portfolios of innovative pharmacological products aimed for therapy and supportive care. Collectively, the significance of advanced research in this area with special emphasis on the main challenges associated with toxicity issues and other undesirable health consequences resulting from the direct administration of both natural substances was also advocated.

Keywords: lignin, morin, biological activity, *in vitro*, *in vivo*

INTRODUCTION

Natural bioactive compounds play a crucial role for human well-fare due to their diverse pharmacological activities such as antidiabetic, antipyretic, anticancer, antidiuretic, anti-atherosclerotic, antioxidant, antimicrobial, etc., which determine their therapeutic applicability for treatment of many diseases [1]. Flavonoids are the most abundant and ubiquitously found phenols in nature [2, 3].

The benefits of natural polymers in the biomedical field have been thoroughly investigated. Various homogeneous and heterogeneous biopolymers and their biocomposites have attracted much attention for biomedical applications including wound healing, drug delivery [4], tissue engineering, and biosensors due to their unique features and bioactivities [5].

Lignin is one of the most common structural biopolymers in plant cells [6]. It is produced by oxidative coupling of three phenolic alcohols: coniferyl, p-coumaril, sinapyl alcohol in the cell walls. The process is catalyzed by the enzyme peroxidase [7]. In recent years, lignin has been applied as a source for the development of: nanoparticles, nanotubes, hydrogels, sunscreen lotions and 3D printed materials used in biomedicine [8]. The heterobiopolymer is characterized by low cytotoxicity, good stability, biocompatibility, biodegradability, presence of phenolic and aliphatic hydroxyl groups in its structure [9], ability to be modified by targeting molecules [7, 10], antioxidant activity, antimicrobial potential, low proinflammatory effects, nonhemolytic activity [8, 11-13], and reducing serum cholesterol activity [14].

Morin belongs to the class of plant flavonoids, which represent a family of natural plant-derived dietary bioactive compounds with polyphenolic nature found in vegetables, fruits, juices and herbs. They have different biological functions like antioxidant properties and oxygen radical scavenging potential [15-18]. Morin hydrate is a bioflavonol characterized with a hydroxyl group at the 3-position and comprised of a flavone (2-phenyl-1-benzopyran-4-one) backbone. It is a 7-hydroxyl flavonol that contains three additional hydroxy substituents at positions 2′, 4′, and 5. Morin in pure form is a bitter, yellow-colored stable compound that is relatively neutral and insoluble in water. It is an isomeric form of quercetin. Both natural flavonoids could be differentiated from each other based on the B-ring's hydroxylation pattern, which is "ortho" in quercetin and "meta" in morin [19]. Morin belongs to the *Rosaceae, Moraceae* and *Fagaceae* families. Major sources are *Morus alba* L. (white mulberry), *Psidium guajava* (guava), *Maclura pomifera* (guava leaves), *Maclura tinctoria* (old fustic), Osage orange), *Allium cepa*

---

* To whom all correspondence should be sent:
E-mail: *zvezdelina.yaneva@trakia-uni.bg*

(onion), *Psidium guajava* L. (guava leaves), *Maclura tinctoria* (old fustic), *Malus pumila* (apple skin), *Prunus dulcis* (almond), *Chlorophora tinctoria* (figs), *Castanea sativa* (sweet chestnut), *Artocarpus heterophyllus* (jack fruit), tea, red wine, coffee, seaweed and cereal grains [15, 19]. It possesses various physiological properties, such as anti-allergic, anti-arthritis, anti-cancer, anti-mutagenic, anti-diabetic, anti-inflamatory, anti-microbial, hepatoprotective, neuroprotective, antioxidant, hypouremic, nephroprotective, gastroprotective, cardioprotective and others [15, 20]. Morin also performs a systemic protective activity, reducing the negative side effects of some drugs without interfering with their action. It is suitable for long-term administration at low doses without exhibiting toxicity [20].

In this respect, the present study reviews recent approaches which combine *in vitro* evaluation and *in vivo* screening of potential physiological activities of the plant-derived bioactive molecules lignin and morin and formulations on their basis. The aim is to assess the potential of the hetero polymer and the flavonoid as platforms for the design of portfolios of innovative pharmacological products aimed for therapy and supportive care.

Novel lignin-based nanoformulations and their physiological activities

Alkali lignin nanoparticles (ALNP) and dioxane lignin nanoparticles (DLNP) were synthesized by Kamal *et al*., 2022 [21] from two different lignin sources, namely alkaline softwood lignin (AL) and hardwood dioxane lignin (DL) extracted from subabul stems using a nanoprecipitation method. It was established that DLNP and ALNP possess higher antioxidant activity compared to DL and AL. DLNP offers higher protection for *E. coli* from UV rays, compared to ALNP. A good anticancer effect was observed in various cytological tests and animal experiments with alkaline lignin, the bioactive molecule resveratrol (RSV) and Fe_3O_4 magnetic nanoparticles [22]. *In vitro* experiments show increased release of resveratrol from the magnetic RSV-loaded lignin nanoparticles (AL/RSV/Fe_3O_4 NPs), reduced tumor size and higher accumulation of administered drugs. There is a reduction of side effects of the administered drugs, compared to the freely administered dosage forms. This formulation is potentially useful for the administration of poorly soluble drugs.

Another scientific group synthesized synthetic lignin which was applied to two human cell lines (breast adenocarcinoma, MCF7 and normal fetal lung fibroblasts, MRC5). Inhibition of cell growth

was observed in both cell lines after 4 hours, while a better sensitivity of cancer cells compared to fetal lung fibroblasts was observed after 72 hours of administration in lower doses [23].

Alqahtani *et al*. (2019) [24] established that curcumin-loaded lignin nanoparticles show high mechanical strength and significant encapsulation efficiency (92%). *In vitro* tests proved stability of the nanoformulations in gastric fluid and slow release of the formulations in intestinal conditions. Besides, *in vivo* pharmacokinetic experiments displayed that curcumin-encapsulated nanoparticles increase the bioavailability of curcumin ten times as compared to free curcumin and proved the applicability of the lignin nanoformulations for oral administration of drug molecules with poor bioavailability and low solubility.

Our research team studied the antimicrobial activity of two- and three-component morin/chitosan/lignin formulations. The combination of morin-chitosan and morin-lignin showed a 100% increase in the inhibitory activity against *S. aureus* compared to the pure components. The combination of morin-chitosan-lignin showed an inhibitory effect on all the tested bacterial strains, with the highest antimicrobial potential against *S. aureus*, and the lowest against *B. cereus* and *E. coli*. The hypothetical mechanisms by which chitosan–morin–lignin combined systems can inhibit microbial growth include: electrostatic interactions between microbial cell surfaces causing cell wall disruption and intracellular component leakage; adhesion and penetration of the morin–polymer combinations into the cell membrane imposing sequential negative effects on protein synthesis processes; chelation of fundamental nutrients and essential metals; ROS production and cell surface pH reductions resulting in mediated bacterial apoptosis [25].

Toxicity of chitosan-coated lignin nanoparticles was tested by Stine *et al*. (2021) [26] and Ravishankar *et al*. (2019) [27]. Binding of chitosan to nanoparticles enhances their adsorption to biological samples through electrostatic adhesion. The newly synthesized nanoparticles were applied directly to the developing zebrafish embryo with the enzymatically removed chorion, and to the chorionic membrane of the embryo. Embryo lethality and sublethal endpoints were monitored. Higher mortality and sublethal endpoints were observed in embryos treated with chitosan-lignin nanoparticles compared to plain lignin and control groups in the concentration of 320 µg/ml. The study proved that chitosan-loaded lignin nanoparticles were more toxic than regular lignin particles [26]. It was established that gels based on chitosan and alkaline

lignin are non-toxic to mesenchymal stem cells *in vitro* and to zebrafish up to 100 μg/ml *in vivo*. When the gel was applied to NIH 3T3 mouse fibroblast cells, they showed good cell migration, suggesting that the gel could be used in wound healing [27].

The bioactivities of binary hydroxypropyl methyl cellulose (HPMC) /lignin) and three-component systems (HPMC/lignin/chitosan) studied by Alzagameem *et al*. (2019) were affected by lignin concentration. The systems displayed higher antioxidant and antimicrobial activity at 5% concentration, while the biopotentials decreased at 30%. Besides, the antimicrobial activity of lignin depending on its source increased in the order: softwood organosolution > softwood kraft > grass organosolution. Testing the films against spoilage bacteria that grow at low temperatures, revealed the activity of HPMC/lignin 1 (extracted by H_2SO_4 at pH = 2 for 90 - 180 min at room temperature) and HPMC/lignin/chitosan films against both *Brochothrix thermosphacta* and *Pseudomonas fluorescens* [28].

Cardioprotective activity of morin

The cardioprotective effects of morin have been proven by numerous studies. One of these was done by daily administration of morin (40 mg/kg) for 30 days. Albino Wistar rats were then injected subcutaneously with isoproterenol (85 mg/kg) every 24 hours for 2 days. The study of Al-Numair *et al*. (2014) [29] established that isoproterenol (ISO)-induced myocardial infarction (MI) in rats led to increased levels of lipid hydroperoxide (LOOH) and thiobarbituric acid reactive substances (TBARS) in plasma and heart and a decrease in catalase (CAT), superoxide dismutase (SOD), glutathione peroxidase (GPx) and glutathione-S-transferase (GST), reduced levels of glutathione (GSH) and vitamin E and C. The treatment of the rats with morin provoked a significant return to approximately normal levels of the above parameters.

Deoxycorticosterone acetate (DOCA)-induced salt hypertension in male Wistar rats and antihypertensive and antioxidant effects of morin were studied by Prahalathan *et al*., 2011 [30]. Rats showed significant increase in systolic and diastolic blood pressure, heart rate, and in thiobarbituric acid and lipid hydroperoxide levels. Reduction of SOD, CAT, glutathione peroxidase, glutathione, vitamin C and vitamin E was observed. The administration of morin (50 mg/kg) daily for six weeks returned the parameters to approximately normal levels.

Another scientific team investigated the inter-actions between morin and different drugs. The combination of diltiazem (15 mg/kg, oral) and morin (1.5–7.5 mg/kg, oral) in rats increased the bioavailability of diltiazem by 1.4 to 1.8 times. The combination of etoposide (6 mg/kg, oral) and morin (15 mg/kg, oral) in rats increased the bioavailability of etoposide by 1.4 times. It was established that in isoproterenol-induced myocardial infarction and doxorubicin cardiac fibrosis, morin restored the mitochondrial function, improved the antioxidant and mitochondrial enzymes and decreased apoptosis [17].

Neuroprotective effects of morin

Morin executes a significant neuroprotective action by affecting various mechanisms. There are studies, which provide evidence that morin ameliorates neuroinflammation and oxidative stress in Alzheimer's Wistar rats. *In vitro* studies show that morin can exert anti-amyloidogenic activity reversibly and specifically by binding to the amyloid fibril structure of Aβ instead of to the monomers of Aβ. Morin has been shown to form complexes with Cd (II) and exhibit strong antioxidant activity *in vitro* [18].

Thangarajana *et al*. (2018) induced lead acetate (PbAc) intoxication and subsequent oxidative stress in the rat brain. Oxidative stress, memory impairment, and motor deficits were observed. Rats, that were treated with morin, showed significant recovery of the abnormal changes. Histopathological sections of the cerebral cortex, hippocampus and cerebellum showed neuronal loss in PbAc rats and their recovery with the morin administration [31].

Khamchai *et al*. (2020) administered 30 mg/kg morin by intraperitoneal injection before ischemia, during ischemia, and at reperfusion in rats in brain injury and blood-brain barrier (BBB) disruption. The results showed a significant reduction in the production of reactive oxygen species, lipid peroxidation, blood-brain barrier damage and neutrophil infiltration, inflammation and apoptosis by reducing brain infarct size, ameliorated cerebral damage and increased protein expression. The data obtained displayed that morin exerts protective effect against cerebral and blood-brain barrier damage by attenuating inflammation, oxidative stress and apoptosis [32].

Sharma *et al*. (2017) investigated the effect of intranasal delivery of morin hydrate-loaded microemulsion for the management of Alzheimer's disease. After intranasal delivery, the brain and blood drug concentrations were found to be higher for morin-loaded microemulsion as compared to pure morin. Significant reduction was observed in the pharmacodynamic parameters after intranasal

administration of the flavonoid-loaded micro-emulsion as compared to control group. 21 days of morin-loaded microemulsion treatment resulted in significantly enhanced memory in Wistar rats [33].

Zhang *et al.* (2010) induced Parkinson's disease in mouse. They studied the neuroprotective effects of morin on 1-methyl-4-phenylpyridinium ion (MPP+)-induced apoptosis in neuronal differentiated PC12 cells and a 1-methyl-4-phenyl-1,2,3,6-tetrahydropyridine mouse model of Parkinson disease. Application of morin (5-50 μmol/L) significantly reduced the loss of cell viability, apoptosis and ROS formation. Morin (20 to 100 mg/kg) attenuates behavioral deficits, dopaminergic neuronal death and striatal dopamine depletion. The obtained data suggest that morin has neuroprotective actions *in vitro* and *in vivo* and may be used as a therapeutic agent for the treatment of neurodegenerative diseases [34].

Hepato-protective effects of morin

Hepato-protective effects of morin could be attributed to increase in superoxide dismutase, hemoxygenase-1, glutathione-S-transferase, catalase, glutathione peroxidase and decrease in liver transaminase, hepatocyte death, total cholesterol, triacylglycerol, formation of ROS, etc.

Li *et al.* (2019) induced acute hepatotoxicity with CCl_4 in pathogen-free male C57BL/6 mice, which provoked reduced liver transaminase levels and hepatocyte death, attenuated liver histopathological changes and inflammatory response. The administration of morin orally lead to hepatoprotective effect by blocking TREM-1-mediated inflammatory response in macrophages and reducing oxidative stress by modulating the regulator of cellular resistance to oxidants Nrf2/HO-1 pathway in the liver [35].

Mondal *et al.* (2022) compared the hepatoprotective effect of free administered morin and morin-encapsulated chitosan nanoparticles in chronic arsenic poisoning of the liver. The flavonoid-loaded nanoformulation was four times more effective compared to pure morin. Administration of the nanoaprticles reduced serum levels of ALT, AST, ALP and tissue arsenic deposition, inhibited the formation of ROS and increased the levels of SOD), GSH, CAT, GST, (GPx), hemoxygenase-1 (HO-1) and NADPH quinone oxidoreductase 1 (NQO1) [36]. Kamal *et al.* (2022) reported that morin significantly protected the rats against paracetamol-induced hepatotoxicity associated with alterations in the plasma total cholesterol, triacylglycerol, and HDL-C levels, as well as liver ALT, AST, ALP, LDH, protein thiol,

GSH, SOD, CAT, MDA, and tumor necrosis factor-alpha levels. The histological results showed that morin protected the liver tissues against the toxic effect of paracetamol [37].

Photoprotective properties of morin

Tran *et al.* (2022) encapsulated morin in liposomal vesicles to improve the photoprotective properties of the flavonoid. It was established that morin was a strong scavenger of DPPH radicals, displayed a remarkable ROS inhibitory ability, and protected keratinocytes against dust particles by downregulating the expression of matrix metalloproteinase-1 (MMP-1). Water solubility of liposomal morin was significantly improved as compared to the free form of morin due to a reduction in the particle size of the liposomes, which increased dermal absorption. Based on the findings obtained, it was suggested that morin-loaded liposomes can be used for various topical antiaging applications [38]

Potential of morin against induced lung injury

Tianzhu *et al.* (2014) studied the anti-inflammatory activity of morin on acute lung injury using lipopolysaccharide-induced acute lung injury mouse model [39]. The experimental results displayed that morin treatment significantly depressed inflammatory cell numbers in the bronchoalveolar lavage fluid, decreased lung NLRP3 inflammasome protein level, and improved SOD activity and inhibited myeloperoxidase activity. Histological investigations established that morin considerably inhibited neutrophils in lung tissue compared with control group, which proved the protective effect of the flavonoid on lipopolysaccharide-induced acute lung injury in mice [39]. The potential of morin against induced lung injury from cigarette smoke was investigated by Cai *et al.* (2018). The obtained results showed that morin significantly inhibited lung pathological changes, myeloperoxidase (MPO) activity and MDA levels. The levels of total cells, macrophages, neutrophils and the production of inflammatory cytokines were also suppressed by the flavonoid. The results indicate that morin may be used as a potential drug for cigarette smoke-induced lung injury [40].

Obviously, morin exhibits advantageous therapeutic effects against acute lung injury, however, the mechanism of its action remains unclear. Recently, a scientific team established considerable increase of inflammation and pyroptosis in the lung tissue of mice with lipopolysaccharide-induced acute lung injury.

187

According to the study, the flavonoid blocked the activation of the TLR4/TRAF6/NF-κB pathway, synergically inhibited the entry of p65 into the nucleus, inhibited caspase-1 activation and protected the GSDMD protein from cleavage [41].

Anti-diabetic effects of morin

Streptozotocin (STZ)-induced diabetes mellitus has been studied by many scientists. Naziret *et al.* (2021) conducted an *in vivo* experiment displaying a significant restoration of changes in fasting blood glucose levels and body weight loss, as well as lowering cholesterol, LDL, triglyceride levels and increasing HDL after morin administration. Significantly increased antioxidant enzymes such as GPx, GSH and % DPPH inhibitory activity, while reduced level of lipid peroxidation Malondialdehyde (MDA) values in pancreatic homogenates of diabetic rats were established. Morin demonstrated high antioxidant, antidiabetic and antibacterial potential, making it a suitable therapeutic agent for the treatment of diabetes mellitus and bacterial infections [42]. The study of Vanitha *et al.* (2014) reported that morin reduced blood glucose and improved serum insulin levels, decreased glucose-6-phosphatase and fructose-1,6-bisphosphatase, increased hepatic hexokinase and glucose-6-phosphate dehydrogenase activity in diabetic rats. The bioflavonoid was found to be effective in preserving the normal appearance of pancreatic islets, as well as in preserving insulin-positive cells in STZ-rats. These findings indicate that morin has beneficial effect in diabetes by regulating carbohydrate metabolic enzyme activities [43]. Protective effect of morin on trabecular bone of healthy and diabetic rats with diabetic osteopenia was investigated by Abuohashish *et al.* (2013). Significant bone loss, damage to trabecular bone microarchitecture, density and other morphometric parameters were associated with the disease. Serum levels of glucose, IL-1β, IL-6, and TNF-α were significantly increased, while the levels of insulin and GSH were decreased in diabetic rats. These serum changes returned to normal values after 5 weeks of morin treatment. These results reveal the protective effect of morin against diabetes-induced osteopenia [44]. Antiosteoarthritic properties of morin *in vitro* and *in vivo* were studied by Chen *et al.* (2012). Morin inhibited the expression of matrix metalloproteinase MMP-3 and MMP-13 and increased the expression of tissue inhibitors of metalloproteinase TIMP-1 in interleukin-1b-induced rat chondrocytes. *In vivo* study in a rat model demostrated that morin suppressed cartilage degradation [45].

Profit of morin/lignin combinations

Our team created different formulations based on morin. Combination of morin-chitosan and morin-lignin showed a 100% increase in inhibitory activity against *S. aureus* compared to the pure components. The combination of morin-chitosan-lignin showed an inhibitory effect on all the tested bacterial strains, with the highest degree occurring against *S. aureus*, and the weakest against *B. cereus* and *E. coli*. The hypothetical mechanism of action includes electrostatic interactions between microbial cell surfaces, adhesion and penetration of the morin–polymer combinations into the cell membrane, chelation of fundamental nutrients and essential metals. The lower rate of *in vitro* release of morin from flavonoid-encapsulated lignin microparticles, as well as the lack of gastric mucosal irritation, proved the advantages for p.o. application of our newly synthesized microparticles compared to directly applied morin. A significant antioxidant and radical scavenging ability of the particles has been demonstrated [46].

CONCLUSIONS AND FUTURE PROSPECTS OF LIGNIN- AND MORIN-BASED FORMULATIONS BIOMEDICAL APPLICABILITY

After extensive research we can conclude that lignin is characterized with low cytotoxicity, biodegradability, good stability and low pro-inflammatory effect. As disadvantages of lignin, we can point out the variability in its composition, poor binding and delivery of hydrophilic drugs. In conclusion, based on new scientific research on the antioxidant, antimicrobial, antiproliferative, anticancer, antiviral and antifungal activities of lignin, we may say that it can be used as a vehicle of various agents in biomedicine.

Direct administration of morin has a number of disadvantages, such as poor water solubility, resulting in low oral bioavailability, very short plasma half-life (30 min) after intravenous injection, rapid metabolism, degradation and elimination from the body, hindering its potential contribution to the prevention and treatment of various diseases. It is sensitive to the solvent used and pH, being highly unstable at basic conditions and metastable in acidic and neutral media. Diverse scientific studies have reported *in vitro* and *in vivo* cardioprotective, neuroprotective, nephroprotective, hepatoprotective, anticancer, gastroprotective, pulmonary, and antidiabetic activities of the natural bioflavonoid morin.

Future perspectives for modern scientific research are related to challenges of designing

natural delivery systems for polyphenols, ensuring effective integration of bioactive molecules and their protection from degradation along their physiological distribution pathways and reaching their area of therapeutic action. Another important task for scientists is the determination of a safe and effective dose for the treatment of various acute and chronic diseases.

In summary, to date the available information on lignin and morin and their overall impact on experimental animals is still scarce, but it is a prerequisite for subsequent trials proving their effectiveness against various diseases.

REFERENCES

1. K. Shrinet, R. K. Singh, A.K. Chaurasia, A. Tripathi, A. Kumar, Chapter 17 - Bioactive compounds and their future therapeutic applications, in: R. P. Sinha, D.-P. Häderveds (eds.), Natural Bioactive Compounds, Academic Press, 2021, p. 337.
2. Z. Yaneva, D. Ivanova, *Antioxidants (Basel)*. **9**(12), 1180 (2020).
3. Z. Yaneva, D. Ivanova, M. Toneva, M. Tzanova, V. Marutsova, N. Grozeva, *Int. J. Mol. Sci*., **24**, 16268 (2023).
4. D. Ivanova, M. Toneva, E. Simeonov, B. Nikolova, S. Semkova, G. Antov, Z. Yaneva, *Pharmaceutics*, **15**, 1067 (2023).
5. G. Widhiantara, A. Permatasari, W. Rosiana, N. Sari, M. Sandhika, P. Wiradana, M. Jawi, *Journal of Applied Pharmaceutical Science*, **13**(01), 042 (2023).
6. M. Karimi, H. Zare, A. Bakhshian, N. Yazdani, M. Hamrang, E. Mohamed, *Nanomedicine*, **11**(5), 513 (2016).
7. P. Parchi, O. Vittorio, L. Andreani, P. Battistini, N. Piolanti, S. Marchetti, *Front, Aging Neurosci*., **8**, 1 (2016).
8. J. Domínguez-Robles, A. Carcamo-Martínez, S. Stewart, R. Donnelly, E. Larraneta, M. Borrega, *Sustainable Chemistry and Pharmacy*, **18,** 100320 (2020).
9. N. Lewis, E. Yamamoto, *Annu. Rev. Plant. Physiol. Plant. Mol. Biol*., **41**, 455 (1990).
10. K. Radotić, M. Mićić, M. Jeremić, *Ann. NY Acad. Sci.* **1048**, 215 (2005).
11. F. Verdini, E. Gaudino, E. Canova, S. Tabasso, P. Behbahani, G. Cravotto, *Molecules*, **27**, 3598 (2022).
12. D. Vieira, L. Gamarra, *Einstein (São Paulo),* **14**(1), 99 (2016).
13. M. Vinardel, M. Mitjan, *Int. J. Mol. Sci,*, **18**, 1219 (2017).
14. M. J. Ernsting, M. Murakami, A. Roy, S.-D. Li, *J. Controlled Release*, **172**, 782 (2013).
15. R. Zhang, K. Kang, S. Kang, J. Park, J. Hyun, *Basic & Clinical Pharmacology & Toxicology*, **108**, 63 (2011).
16. N. Shen, T. Wang, Q. Gan, S. Liu, L. Wang, B. Jin, *Food Chemistry*, **383,** 132531 (2022).
17. J. Khan, P. Deb, S. Priya, K. Medina, R. Devi, S. Walode, M. Rudrapa, *Molecules*, **26**(13), 4021 (2021).
18. J. Li, M. Sun, X. Cui, C. Li, *Int. J. Mol. Sci.*, **23**, 10020 (2022).
19. S. Rajput, X. Wang, H. Yan, *Biomedicine & Pharmacotherapy*, **138**, 111511 (2021).
20. A. Caselli, P. Cirri, A. Santi, P. Paoli, *Current Medicinal Chemistry*, **23**, 1 (2016).
21. S. Yearlaa, K. Padmasree, *Journal of Experimental Nanoscience*, **11**(4), 289 (2016).
22. L. Dai, R. Liu, L.-Q. Hu, Z.-F. Zou, C.-L. Si, *Sustainable Chem. Eng*., **5**, 8241 (2017).
23. L. Andrijevic, K. Radotic, J. Bogdanovic, D. Mutavdzic, G. Bogdanovic, *J. BUON*, **13**(2), 241 (2008).
24. M. Alqahtani, A. Alqahtani, A. Al-Thabit, M. Roni, R. Syed, *Journal of Materials Chemistry B*, **7**, 4461 (2019).
25. Z. Yaneva, G. Beev, N. Rusenova, D. Ivanova, M. Tzanova, D. Stoeva, M. Toneva, *Antibiotics (Basel)*, **11**(5), 650 (2022).
26. J. Stine, B. Harper, C. Conner, O. Velev, S. Harper, *Nanomaterials*, **11**, 111 (2021).
27. K. Ravishankar, M. Venkatesan, R. Desingh, A. Mahalingam, B. Sadhasivam, R. Subramaniyam, R. Dhamodharan, *Materials Science and Engineering: C*, **102**, 447 (2019).
28. A. Alzagameem, S. Klein, M. Bergs, X. Tung Do, I. Korte, S. Dohlen, C. Hüwe, J. Kreyenschmidt, B. Kamm, M. Larkins, M. Schulze, *Polymers*, **11**(4), 670 (2019).
29. K. Al-Numair, G. Chandramohan, M. Alsaif, C. Veeramani, A. El Newehy, *Afr. J. Tradit. Complement. Altern. Med*., **11**(3), 14 (2014).
30. P. Prahalathan, S. Kumar, B. Raja, *Metabolism,* **61**(8), 1087 (2012).
31. S. Thangarajana, A. Vedagiria, S. Somasundaramb, R. Sakthimanogaran, M. Murugesana, *Neurotoxicology and Teratology*, **66**, 35 (2018).
32. S. Khamchai, W. Chumboatong, J. Hata, C. Tocharus, A. Suksamrarn, J. Tocharus, *Scientific Reports,* **10**, 13379 (2020).
33. D. Sharma, M. Singh, P. Kumar, V. Vikram, N. Mishra, *Artificial Cells, Nanomedicine, and Biotechnology*, **45**(8), 1620 (2017).

34. Z. Zhang, X. Cao, N. Xiong, H. Wang, J. Huang, S. Sun, T. Wang, *Acta Pharmacologica Sinica*, **31**, 900 (2010).

35. X. Li, Q. Yao, J. Huang, Q. Jin, B. Xu, F. Chen, C. Tu, *Frontiers in Pharmacology*, **10**, 1089 (2019).

36. S. Mondal, S. Das, P. Mahapatra, K. Saha, *Nanoscale Adv.*, **4**, 2857 (2022).

37. G. Kamal, M. Nasr, M. Hussein, A. Aziz, A. Fayed, *Biomedical Research and Therapy,* **9**(9), 5260 (2022).

38. H. Tran, C. Yang, T. Wu, F. Yen, *Antioxidants*, **11**, 1183 (2022).

39. Z. Tianzhu, Y. Shihai, D. Juan, *Inflammation*, **37**(6), 1976 (2014).

40. B. Cai, X. Gan, J. He, W. He, Z. Qiao, B. Ma, Y. Han, *International Immunopharmacology*, **63**, 198 (2018).

41. J. Yu, Z. Nie, D. Feng, L. Zhang, Y. Bai, H. Zhang, J. Zhao, W. Pan, *Research Square*, online first (2023).

42. N. Nazir, M. Zahoor, M. Nisar, I. Khan, R. Ullah, A. Alotaibi, *Molecules*, **26**, 4464 (2021).

43. P. Vanitha, C. Uma, N. Suganya, E. Bhakkiyalakshmi, S. Suriyanarayanan, P. Gunasekaran, S. Sivasubramanian, K. Ramkumar, *Environmental Toxicology and Pharmacology*, **37**, 326 (2014).

44. H. Abuohashish, S. Al-Rejaie, K. Al-Hosaini, M. Parmar, M. Ahmed, *Diabetology & Metabolic Syndrome*, **5**, 5 (2013).

45. W. Chen, P. Hu, J. Bao, L. Wu, *Experimental Biology and Medicine*, **237**, 380 (2012).

46. D. Ivanova, M. Toneva, E. Simeonov, B. Nikolova, S. Semkova, G. Antov, Z. Yaneva, *Pharmaceutics*, **15**, 1067 (2023).

Instructions about Preparation of Manuscripts

General remarks: Manuscripts are submitted in English by e-mail. The text must be prepared in A4 format sheets using Times New Roman font size 11, normal character spacing. The manuscript should not exceed 15 pages (about 3500 words), including photographs, tables, drawings, formulae, etc. Authors are requested to use margins of 2 cm on all sides.

Manuscripts should be subdivided into labelled sections, e.g. INTRODUCTION, EXPERIMENTAL, RESULTS AND DISCUSSION, etc. **The title page** comprises headline, author(s)' names and affiliations, abstract and key words. Attention is drawn to the following:

a) **The title** of the manuscript should reflect concisely the purpose and findings of the work. Abbreviations, symbols, chemical formulae, references and footnotes should be avoided. If indispensable, abbreviations and formulae should be given in parentheses immediately after the respective full form.

b) **The author(s)'** first and middle name initials and family name in full should be given, followed by the address (or addresses) of the contributing laboratory (laboratories). **The affiliation** of the author(s) should be listed in detail (no abbreviations!). The author to whom correspondence and/or inquiries should be sent should be indicated by an asterisk (*) with e-mail address.

The abstract should be self-explanatory and intelligible without any references to the text and containing up to 250 words. It should be followed by keywords (up to six).

References should be numbered sequentially in the order, in which they are cited in the text. The numbers in the text should be enclosed in brackets [2], [5, 6], [9−12], etc., set on the text line. References are to be listed in numerical order on a separate sheet. All references are to be given in Latin letters. The names of the authors are given without inversion. Titles of journals must be abbreviated according to Chemical Abstracts and given in italics, the volume is typed in bold, the initial page is given and the year in parentheses. Attention is drawn to the following conventions: a) The names of all authors of a certain publications should be given. The use of "et al." in the list of references is not acceptable; b) Only the initials of the first and middle names should be given. In the manuscripts, the reference to author(s) of cited works should be made without giving initials, e.g. "Bush and Smith [7] pioneered...". If the reference carries the names of three or more authors it should be quoted as "Bush et al. [7]", if Bush is the first author, or as "Bush and co-workers [7]", if Bush is the senior author.

Footnotes should be reduced to a minimum. Each footnote should be typed double-spaced at the bottom of the page, on which its subject is first mentioned. **Tables** are numbered with Arabic numerals on the left-hand top. Each table should be referred to in the text. Column headings should be as short as possible but they must define units unambiguously. The units are to be separated from the preceding symbols by a comma or brackets. Note: The following format should be used when figures, equations, etc. are referred to the text (followed by the respective numbers): Fig., Eqns., Table, Scheme.

Schemes and figures. Each manuscript should contain or be accompanied by the respective illustrative material, as well as by the respective figure captions in a separate file. As far as presentation of units is concerned, SI units are to be used. However, some non-SI units are also acceptable, such as °C, ml, l, etc. Avoid using more than 6 (12 for review articles) figures in the manuscript. Since most of the illustrative materials are to be presented as 8-cm wide pictures, attention should be paid that all axis titles, numerals, legend(s) and texts are legible.

The authors are required to submit the text with a list of three individuals and their e-mail addresses that can be considered by the Editors as potential reviewers. Please note that the reviewers should be outside the authors' own institution or organization. The Editorial Board of the journal is not obliged to accept these proposals.

The authors are asked to submit **the** final text (after the manuscript has been accepted for publication) in electronic form by e-mail. The main text, list of references, tables and figure captions should be saved in separate files (as *.rtf or *.doc) with clearly identifiable file names. It is essential that the name and version of the word-processing program and the format of the text files is clearly indicated. It is recommended that the pictures are presented in *.tif, *.jpg, *.cdr or *.bmp format. The equations are written using "Equation Editor" and chemical reaction schemes are written using ISIS Draw or ChemDraw programme.

EXAMPLES FOR PRESENTATION OF REFERENCES

REFERENCES

1. D. S. Newsome, Catal. Rev.–Sci. Eng., 21, 275 (1980).
2. C.-H. Lin, C.-Y. Hsu, J. Chem. Soc. Chem. Commun., 1479 (1992).
3. R. G. Parr, W. Yang, Density Functional Theory of Atoms and Molecules, Oxford Univ. Press, New York, 1989.
4. V. Ponec, G. C. Bond, Catalysis by Metals and Alloys (Stud. Surf. Sci. Catal., vol. 95), Elsevier, Amsterdam, 1995.
5. G. Kadinov, S. Todorova, A. Palazov, in: New Frontiers in Catalysis (Proc. 10th Int. Congr. Catal., Budapest (1992), L. Guczi, F. Solymosi, P. Tetenyi (eds.), Akademiai Kiado, Budapest, 1993, Part C, p. 2817.
6. G. L. C. Maire, F. Garin, in: Catalysis. Science and Technology, J. R. Anderson, M. Boudart (eds.), vol. 6, Springer Verlag, Berlin, 1984, p. 161.
7. D. Pocknell, GB Patent 2 207 355 (1949).
8. G. Angelov, PhD Thesis, UCTM, Sofia, 2001, pp. 121-126.
9. JCPDS International Center for Diffraction Data, Power Diffraction File, Swarthmore, PA, 1991.
10. CA 127, 184 762q (1998).
11. P. Hou, H. Wise, J. Catal., in press.
12. M. Sinev, private communication.
13. http://www.chemweb.com/alchem/articles/1051611477211.html.

Texts with references which do not match these requirements will not be considered for publication!!!

CONTENTS